# Photodegradation Illuminated

## New Analytical Tools for Studying Photochemical Processes

Iris Groeneveld

# Photodegradation Illuminated

## New Analytical Tools for Studying Photochemical Processes

Iris Groeneveld

2023

**Photodegradation Illuminated**

New Analytical Tools for Studying Photochemical Processes


| | |
|---|---|
| ISBN: | 978-94-6483-079-8 |
| DOI: | 10.5463/thesis.214 |
| Printing: | Ridderprint, The Netherlands |
| Cover design: | Eline Groeneveld |
| Credits chapter pages: | Van Gogh Museum, Amsterdam (Vincent van Gogh Stichting) |

VRIJE UNIVERSITEIT

# Photodegradation Illuminated

## New Analytical Tools for Studying Photochemical Processes

ACADEMISCH PROEFSCHRIFT

ter verkrijging van de graad Doctor of Philosophy aan
de Vrije Universiteit Amsterdam,
op gezag van de rector magnificus
prof.dr. J.J.G. Geurts,
in het openbaar te verdedigen
ten overstaan van de promotiecommissie
van de Faculteit der Bètawetenschappen
op woensdag 28 juni 2023 om 15.45 uur
in een bijeenkomst van de universiteit,
De Boelelaan 1105

door

Iris Groeneveld

geboren te Werkendam

| | |
|---|---|
| promotoren: | prof.dr. G.W. Somsen |
| | prof.dr. M.R. van Bommel |
| copromotor: | dr. F. Ariese |
| promotiecommissie: | prof.dr. A.M. Rijs |
| | prof.dr. S. Woutersen |
| | prof.dr. W.P. de Voogt |
| | dr. I.D. van der Werf |
| | prof.dr. M.J. Melo |

## Private and institutional partners







## Academic partners



The work in this thesis was financially supported by the TooCOLD project, which is funded by the TTW Open Technology Programme, (partly) financed by the Dutch Research Council (NWO), project number 15506.

kijk eens naar buiten

kun je het ruiken?

kun je het zien?

kun je het voelen?

een universum vol atomen en moleculen die langs mekaar krioelen

bewegen en zijn

bloemen kleuren

mensen geuren

klanken laten klinken

natuurwetten die ervoor zorgen dat sommige dingen drijven

en andere zinken

althans hier op aarde

elders werkt het weer anders

en ik zei natuurwetten

maar het is natuurlijk eigenlijk weer anders

want de natuur heeft geen wetten

die haar dingen bemoeilijkt of oplegt

en die wetten zijn slechts onze observatie van hoe het allemaal werkt

of hoe wij denken dat het werkt

want het is allemaal perceptie

kijk eens naar buiten

en vertel me wat je echt ziet

– Pepijn Lanen

To invent something,
all you need is imagination and a big pile of junk

– some famous scientist

# Table of Contents

# Preface

At first glance, the study of light-induced degradation, cultural heritage, food products, and water purification may not seem to have much in common. Yet for all fields, there is a divide between the public perception and the fascinating detailed reality of the science behind the scenes. The work presented here focuses on bridging the gap between these areas through analytical chemistry.

Personally, I believe that analytical chemistry builds the fundament of most scientific discoveries. They are the eyes, nose, and ears of the scientific community. Using our analytical tools, we can define constituents, chemical behavior and characteristics on a molecular level; something we cannot do using our physical senses. But most importantly, besides it being loads of fun, it enables us to answer the most important questions that may influence our future for the better.

From November 2017 to June 2018, I was fortunate enough to be given an inside look at the conservation work performed at the Ateliergebouw of the Cultural Heritage Agency of The Netherlands. It immediately sparked my interest in the science behind cultural heritage, which lead to my application and acceptance for a PhD in this field. The past 4+ years have been chaotic, fun, stressful, educational, and challenging, but above all, it has been an amazing experience during which I have learned and grown incredibly much. Now, I hope to provide a similarly illuminating experience by presenting insight into the development of new analytical tools for studying photochemical processes.

This dissertation is the culmination of several years of hard work and dedication. I am deeply grateful to the many individuals who have contributed to the successful completion of this project. It would not have been possible without these individuals' help and support; for that, I am forever grateful.

Iris Groeneveld

## PS

I have hidden a small surprise on the cover of this book.
Now, it is time for you to do your own research:

*“I don't need the sun, but I still emit light,*
*In the darkness, I glow, oh what a sight!*
*Absorbing photons, energy I store,*
*Releasing it slowly, what am I, you implore?*
*A molecule with a special task,*
*To degrade and shine, as it were,*
*A photodegradable glow, in the dark lure!”*

# CHAPTER 1

Introduction

# The nature of light

Light is a type of electromagnetic radiation that travels through space at a speed of nearly 300,000 km per second. It is a form of energy that can be transmitted through a vacuum, meaning that it does not necessarily require a medium, e.g., air or water. Light is often described as a wave, but it can also exhibit properties of particles, called photons. This dual nature is also known as wave-particle duality.

The wave nature of light is characterized by its wavelength, which is the distance between two successive peaks or troughs of the wave, whereas the particle nature of light is described by quantum mechanics, which explains how light can be absorbed or emitted in discrete packets of energy, i.e., photons. The energy of a photon is related to the frequency of the corresponding wave, which is the number of times the wave oscillates per second. The higher this frequency, the higher the energy of the photons. Because of that, the energy ($E$) of a photon is directly proportional to the product of the frequency ($\nu$) of the wave and Planck's constant ($h$) (Eq. 1.1). The frequency can in turn be described by the speed of light in vacuum ($c = 3 \cdot 10^8$ m s$^{-1}$) and the wavelength ($\lambda$) [1].

$$E = h\nu = \frac{hc}{\lambda} \qquad \text{(Eq. 1.1)}$$

Photons from light with short wavelengths, e.g., gamma and X-rays, and ultraviolet (UV) light, are of higher energy compared to photons from light with long wavelengths, e.g., infrared (IR) and microwaves. This range of energies can be displayed in the form of a spectrum, called the electromagnetic spectrum, shown in Fig. 1.1.

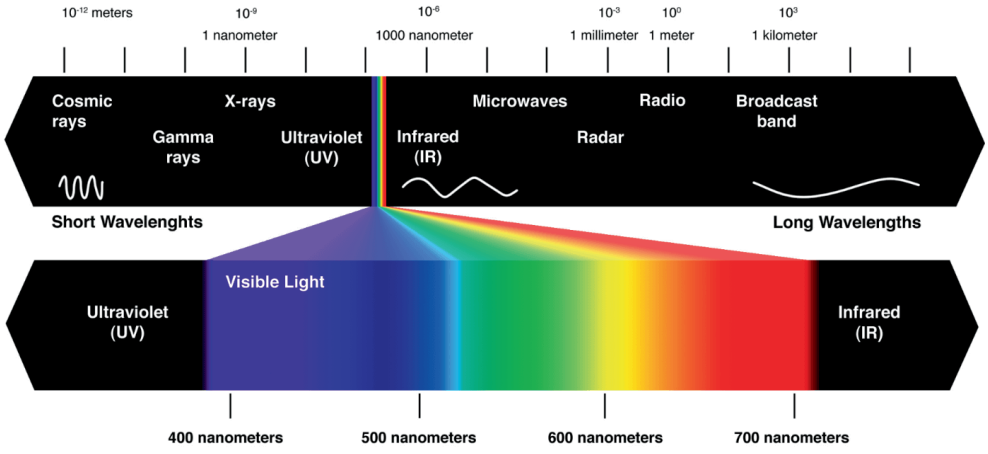


Figure 1.1. The electromagnetic spectrum from gamma and cosmic rays to radio waves. The solar spectrum predominantly consists of UV, visible and infrared light [2].

Radiation originating from the sun essentially contains only a small part of the electromagnetic spectrum, as shown in Fig. 1.2. The relatively small portion of light with wavelengths below 300 nm is absorbed by the Earth's atmosphere and will never reach the surface of the Earth. The part of the spectrum from the sun that reaches Earth is roughly between 300 nm and 1 mm and is divided into three ranges: UV, visible (Vis), and IR radiation [1]. UV is of the shortest wavelength (100-400 nm) and, therefore, of the highest photon energy, thus potentially the most damaging. Vis light falls within the range of approximately 400-700 nm, and IR light contains wavelengths from 700 nm to >1 mm. The colors in the Vis light spectrum are determined by the wavelength, with shorter wavelengths appearing blue or violet and longer wavelengths appearing red.

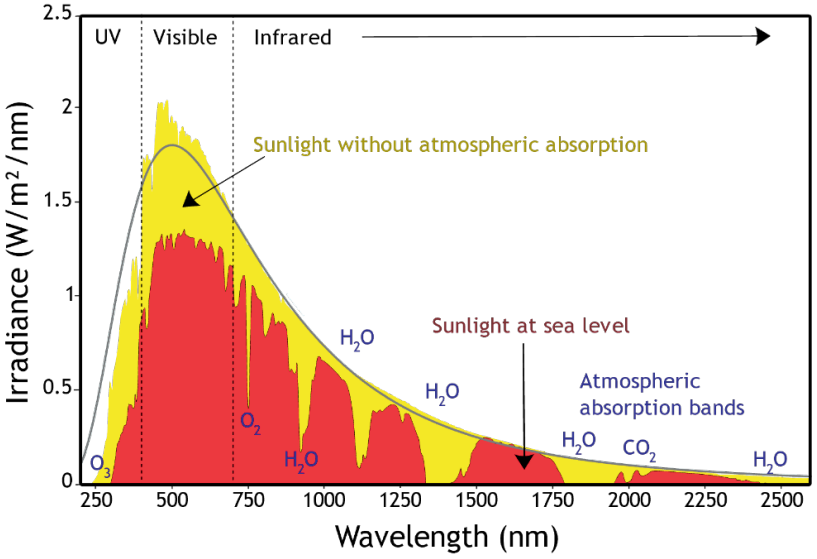


Figure 1.2. The solar spectrum before absorption by the Earth's atmosphere (yellow) and the observed sunlight at sea level after absorption by atmospheric gases (red), which includes, e.g., ozone ($O_3$), oxygen ($O_2$), water ($H_2O$), and carbon dioxide ($CO_2$). Credit: Robert A. Rohde, via Wikimedia Commons (adapted).

# Matter illuminated

The next logical question to ask oneself is how light interacts with matter. Whether light is absorbed, transmitted, reflected, or scattered partly depends on the molecular structure of a compound and can be illustrated by an absorption spectrum, as is shown for the red dye Eosin Y in Fig. 1.3. The part of the spectrum that is reflected instead of absorbed determines the colors observed by the human eye. For example, the absorbance by Eosin Y is mostly between 420 and 570 nm, which corresponds to the blue and green parts of the Vis light, meaning that the remainder of the light will be reflected and shades of orange and red will be visible to the human eye.

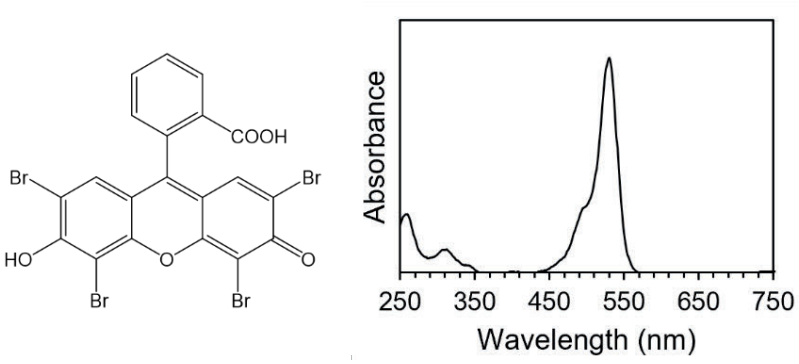


Figure 1.3. The molecular structure of the red/pink dye Eosin Y and its absorption spectrum.

We could say that the interaction between light and matter colors our world. Unfortunately, light may also affect the colors we perceive negatively, meaning that molecules may lose their physical and chemical properties as a result of the absorption of photons. After absorption of a photon, the molecule can be brought from the ground state ($S_0$) into the first or second excited singlet state ($S_1$, $S_2$) by promotion of an electron to a higher energy level, which is best described by the Jablonski diagram in Fig 1.4 [3]. After internal conversion (IC) and/or vibrational relaxation (VR) to the lowest vibrational state of $S_1$, the excess energy can be lost by non-radiative relaxation (e.g., molecular or atomic collisions), or by emitting a photon of lower energy than the absorbed photon, which is called fluorescence. Although less common, non-radiative relaxation by intersystem crossing (ISC) to the excited triplet state ($T_1$) can also occur, followed by relaxation to $S_0$ by non-radiative decay or emission of a photon, i.e., phosphorescence [3]. The process of phosphorescence is rather slow (ms to s) compared to fluorescence (ns to μs) because there is a change in electron spin multiplicity from $T_1$.

The loss of excess energy can also take place by cleavage of bonds or chemical reactions with neighboring molecules, which may occur from $S_1$ or $T_1$, although more likely from $T_1$ as this state has a longer lifetime. We speak of photodegradation or light-induced degradation (LID) when the properties of the compound of interest are lost as a result of these photochemical processes. Such photoreactions can be divided into type 1 and type 2 reactions. Type 1 photoreactions are defined as 'direct', meaning that they occur upon excitation of the compound of interest. Type 2 photoreactions occur through a photosensitizer, which is a photoexcited molecule that produces a chemical change in a second molecule. These reactions are therefore called 'indirect' photoreactions. A common mechanism for type 2 photoreactions is the formation of reactive singlet state oxygen ($^1O_2$) after quenching of the photoexcited molecule by triplet oxygen ($^3O_2$) [5]. It is, therefore, of interest for the food industry to wrap foodstuffs in anoxic environments,

especially when the packaging is transparent. Museums may decide to use oxygen-free displays for this reason, although difficult to achieve [6,7].

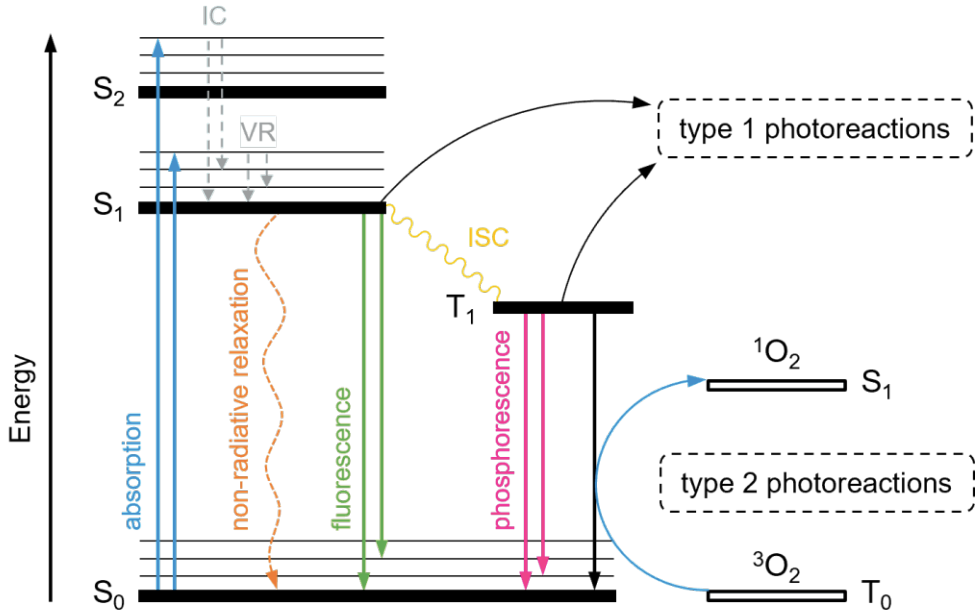


Figure 1.4. Jablonski diagram representing the different energy transitions a molecule may undergo after absorption of a photon, including type 1 and type 2 photoreactions. Molecular energy levels are represented by filled bars and those of oxygen by empty bars. $S_0$=ground singlet state, $T_0$=ground triplet state, $S_1$=first excited singlet state, $S_2$=second excited singlet state, $T_1$=first excited triplet state, IC=internal conversion, VR=vibrational relaxation, ISC=intersystem crossing. Adapted with permission from [4].

## Photodegradation in day-to-day life

As mentioned, photodegradation is the process by which a substance is broken down or decomposed by the action of light. As will be clear after reading the work in this thesis, photodegradation may have negative as well as positive effects. An example of a negative influence that may be familiar is the fading of old pictures that hung on the wall for years, combined with the mark that is left on the wall after removing the picture (like when Monsieur Gustave and Zero removed *'Boy with Apple'* by Van Hoytl from the walls of Schloss Lutz in *The Grand Budapest Hotel)*. Also the photodegradation of foodstuffs, e.g., nutrients such as vitamins or food coloring, is perceived as undesirable. An example is the change in color of margarine as a result of photooxidation of Bixin, an unstable compound that rapidly changes color from yellow to orange under the influence of light [8].

There are also examples in daily life where light is applied deliberately to degrade molecules. Photodegradation can be an important process in the degradation of pollutants and other harmful substances, e.g., the use of high-energy UV sources for water purification [9]. A medical example can be found in tattoo removal, where a high-energy pulsed laser decomposes the ink in the dermis [10].

It may not be perceived as such, but cultural heritage can also be considered a part of day-to-day life. To keep cultural heritage accessible to anyone, it should be conserved and preserved as well as possible. Unfortunately, light also plays an important role in this [11]. Many natural and synthetic colorants are light-sensitive and may fade within several years due to photodegradation, as is the case for a large portion of the work by the postimpressionist painter Vincent van Gogh. Researchers have found that the yellow pigments in *'Zonnebloemen'*, the violet walls in *'De Slaapkamer',* and the purple flowers in *'Veld met Irissen bij Arles'* (Fig. 1.5) have been and are still fading into less brilliant colors [12–15].


Figure 1.5. Color reconstruction of *'Veld met Irissen bij Arles'*, Vincent van Gogh (1853 – 1890), Arles, May 1888 [15].

For example, the Irises from Fig. 1.5 were described by Van Gogh as purple but look bluer nowadays. Van Gogh created purples by combining red and blue paints. It was found that the fading of the light-sensitive red dye Eosin Y caused the discoloration from purple to light blue as the blue paint was more stable, which is also illustrated on the cover of this thesis [14]. Knowing this, researchers were able to create a digital reconstruction that shows what the painting must have looked like right after it was finished (Fig. 1.5).

## Artificial light aging

To put this in a more scientific light: in order to prevent or employ the effects of LID, the photodegradation mechanisms and kinetics must be understood. This is generally done by mimicking a real-world situation by artificial light aging, meaning that the object or compound of interest is exposed to high-intensity light in much shorter time frames to create a similar light dose (J $cm^{-2}$).

Artificial light aging is typically performed in a specialized chamber or machine that is designed to simulate the effects of long-term exposure to sunlight. The process can be used to test a wide range of materials, including plastics, rubber, textiles, coatings, and food products. There are different techniques available for doing so, each with its own advantages and disadvantages. Two common techniques to evaluate the stability of colorants in solid materials (e.g., textiles, paints) applied in cultural heritage are the Xenotest [16] and MicroFading Tester (MFT) [17,18].

The Xenotest consists of a casing with a Xenon-arc lamp, resembling the spectrum of the sun, surrounded by several sample holders that rotate around the lamp's axis for homogeneous irradiation. Parameters such as humidity, temperature, and illuminance can be controlled and it is, therefore, a straightforward and versatile technique. The obtained result is assessed for the degree of fading. The MFT (Fig. 1.6) was designed for art objects that can be placed directly under a microscope, e.g., drawings, textiles, and paintings, to predict the light stability of an object when exposed to common museum light levels for longer periods [19]. This makes the use of reconstructions no longer necessary. The instrument is coupled to a high-intensity light source and contains lenses to focus the light into a small light spot (≈0.3 mm). During irradiation, the probe containing the lenses collects the reflected light, which is recorded by a spectrophotometer to identify the color change in the spot in real-time. An advantage of the MFT is that it is only micro-destructive, therefore, the spot is generally too small to be detected with the naked eye.

Nevertheless, both the Xenotest and the MFT do not necessarily provide chemical information on the photodegradation process. They assess the extent of fading of colo-

rants by comparing the irradiated sample with the blue wool standard [18]. Chemical analysis can be performed, but this is rather time-consuming and requires preparative steps that may break down the parent compound and/or degradation products and may exhibit different specificities towards the range of compounds, making the results less reliable [20]. Additionally, sample complexity, inhomogeneity, and low sample concentrations make chemical analysis challenging for these approaches.

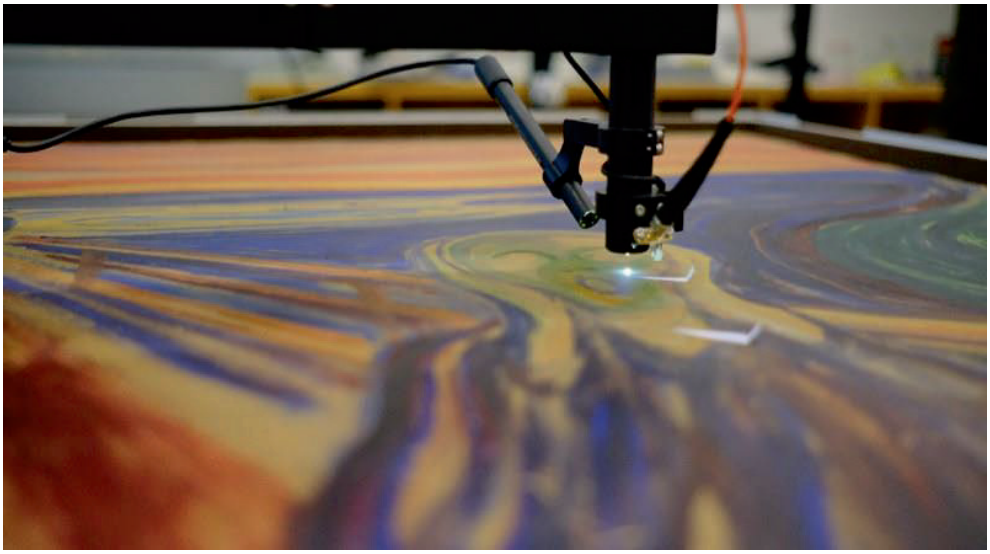

Figure 1.6. MicroFading Tester on *'The Scream'* by Edvard Munch (1863–1944). Photo by Tomasz Lojewski.

A third, somewhat different, method for studying photodegradation is the irradiation of compounds in solution [21,22]. In general, a solution of the compound of interest is prepared and stored in a vial or a beaker, which is then exposed to a light source for a prolonged period of time. The advantage of this straightforward approach is that the set-up is relatively flexible: any solvent or light source could be used, and no sample preparation or extraction procedure is needed for chemical analysis such as liquid chromatography. This makes it more attractive to use as a method for studying photodegradation over time. However, caution must be taken with the interpretation of the results, as photodegradation in solution does not always reflect photodegradation on a substrate [20].

The abovementioned light aging methods share two disadvantages: (i) in all cases, to be able to determine photodegradation kinetics, samples must be taken manually over time, potentially changing conditions, such as the optical path length; and (ii) the methods are relatively labor intensive, making them prone to errors. To solve these limitations, on-line

coupling of the photodegradation system to analytical instruments may be the way to go.

## Analytical chemistry as a tool for studying photodegradation

Many analytical techniques could be of assistance in studying the exact molecular processes during and after photodegradation. A technique that is closely related to measuring molecular properties by means of light is spectroscopy. Spectroscopy comes from the Latin word *'spectrum'*, meaning *'appearance, image'*, and the Greek word *'skopein'*, meaning *'to view, observe'*. Spectroscopy studies the electromagnetic radiation produced by a system (e.g., pure compound, mixture, or physical object) or the interaction between matter and radiation, usually in a non-destructive manner. Especially the latter statement is crucial when a system should be monitored over time without disrupting the system. Spectroscopy would, therefore, be a suitable candidate for monitoring photodegradation processes in-situ. Several spectroscopic methods could be used to observe molecular structure changes, including UV/Vis absorbance, IR, (X-ray) fluorescence, or Raman spectroscopy.

However, during photodegradation, multiple new molecular species may be formed and spectroscopy measurements will show spectra that represent a mixture of many molecular species. Therefore, by spectroscopy alone it may be difficult to determine which compounds are being formed, thus additional techniques are needed. Resolving these questions would require separation of the photodegraded mixture by, e.g., liquid chromatography (LC), followed by an additional detection technique of the separated compounds, such as diode array detection (DAD) or mass spectrometry (MS) [23–28].

## The TooCOLD project

The work in this thesis took place in the context of a multidisciplinary project resulting from a collaboration between Vrije Universiteit Amsterdam and the University of Amsterdam and several external partners.

The project *'Toolbox for studying the Chemistry Of Light-induced Degradation'* (TooCOLD, TTW 15506) aims to provide new insights to protect works of art, improve water purification systems, and ensure the quality and safety of foodstuffs. This is done by developing a so-called toolbox where advanced analytical instruments are combined with light-exposure technology and data analysis techniques to provide insight into the photodegradation mechanisms of many different components.

The research project was divided into three different parts:

(i) Development of a robust and efficient light-exposure cell with spectroscopic monitoring, which can be easily adjusted to study a wide range of parameters that can affect photodegradation mechanisms. The work thereof is described in this thesis.

(ii) Integration of the developed light exposure cell in a two-dimensional LC set-up with the aim to extract pure compounds from mixtures with consecutive irradiation and analysis of degradation products. For more information about this topic, please see the thesis of Mimi J. Den Uijl: *"Under the Influence of Light – New Chromatographic Tools for Elucidating Photodegradation Mechanisms"* (ISBN: 978-94-6458-538-4).

(iii) Development of innovative data-analysis methodology to analyze the data as a whole to take advantage of the relational information between different steps of the degradation processes. For more information about this topic, please see the work by Rick Helmus et al. [29,30].

## Aims and thesis outline

Before the start of this project, common approaches for studying photodegradation often differentiated between the actual light exposure and the chemical analysis of the formed photodegradation products. This makes the study to effect of light on complex mixtures rather challenging and the high level of sample handling increases the risk of contamination and introduction of human error. This work aimed to develop a fully automated and efficient light-exposure system for the study of LID of components in solution, incorporating real-time monitoring of the photodegradation process. This was done in the first place by designing a light cell with in-situ absorption spectroscopy, which was later coupled to LC-DAD-MS. The system was then tested for several compounds of which the photodegradation mechanisms are already well studied in the literature. The compounds selected for this were Eosin Y, Crystal Violet, and Riboflavin.

To understand photodegradation mechanisms and to define requirements for an ideal photodegradation set-up, **Chapter 2** describes the most important parameters that influence the photodegradation of dyes and pigments. These include the irradiation source, light intensity and time, the effect of oxygen, temperature, the effects of catalysts, as well as the dye or pigment concentration. Additionally, a comparison was made between photodegradation in solution and on substrates and specific parameters that may affect the processes in these media.

**Chapter 3** reviews liquid core waveguides (LCWs) as a possible solution for the design of light-exposure cells. They allow simultaneous illumination and optical assessment of liquid samples and, therefore, constitute one way of combining photoreactor design with on-line or in situ analytical detection methods. This chapter aimed to assess the differences between different types of LCWs with regards to (freedom of) design, the degree of light attenuation, the range of transmittable wavelengths, compatibility with analytical techniques, current challenges, and applicability to photodegradation studies.

To analyze photodegradation products that may vary greatly with regard to chemical properties, a generic analysis method for colorants and their degradation products must be available to apply to irradiated samples. The development of such a method is described in **Chapter 4**, where an LC-DAD approach using an ion pairing agent in the mobile phase is proposed for the analysis of natural and synthetic dyes.

**Chapter 5** describes the design and characterization of an LCW set-up for online sample irradiation and the study of photodegradation, including in-situ absorbance spectroscopy. This chapter aimed to evaluate the overall performance of the new LID cell by assessing its transmission characteristics, the absolute photon flux achieved in the LCW, and its capacity to study solute degradation in the presence of oxygen. The potential of the LID set-up for light-exposure studies was studied by monitoring the degradation of the dyes Eosin Y and Crystal Violet.

Based on the system described in Chapter 5, Da Vinci Laboratory Solutions B.V., one of the private partners in the TooCOLD project, built a prototype. **Chapter 6** evaluates this integrated and fully automated system for the study of LID, comprising a liquid handler, an irradiation source, and an LCW exposure cell with dedicated optics and spectrograph, coupled on-line to LC-DAD. The analytical performance of the new system was investigated by assessing linearity, the limit of detection and repeatability of the in-situ absorbance detection, sample recovery and carryover, and overall repeatability of light-induced degradation monitoring and use of the system, with Riboflavin as the test compound. The applicability of the system was studied by recording a photodegradation time profile of Riboflavin.

Gas permeability is a unique property of the LCW in the developed LID set-up and would enable the study of the effect of oxygen on photodegradation. The aim of **Chapter 7** was to assess the oxygen- and nitrogen-gas permeability of the LCW and to evaluate the usefulness of this characteristic to deoxygenate samples inside the LID cell. As proof of principle, the role of oxygen on the LID of Riboflavin and Eosin Y was investigated under oxic and anoxic conditions. Analysis was done by on-line LC-MS to achieve identification and relative quantification of photodegradation products.

Monitoring the photodegradation process by spectroscopy was an important goal of the TooCOLD project. In-situ absorbance spectroscopy was established, and in **Chapter 8** also the feasibility of implementing Raman spectroscopy for studying photodegradation is explored. Four aspects were studied: (i) off-line surface enhanced Raman spectroscopy (SERS) using silver colloids of photodegradation products after LC fractionation of a dye sample irradiated in the LCW, (ii) the characteristics and applicability of leaning pillar chips placed inside a microfluidic device for SERS detection, (iii) on-chip SERS analysis during the photodegradation of Crystal Violet, and (iv) the use of carbon paper as a gas-permeable SERS substrate.

**Chapter 9** provides the conclusions from this thesis, discusses remaining challenges, and describes perspectives for further improvements and implementation of the developed methods in practice.

Finally, the work described in this thesis is summarized in English and in Dutch in **Chapter 10**.

# References

[1] D.H. Sliney, What is light? The visible spectrum and beyond, Nature Eye. 30 (2016) 222–229. https://doi.org/10.1038/eye.2015.252.

[2] J.L. Morton, Electromagnetic spectrum, (2020). https://www.colormatters.com/color-and-science/electromagnetic-color (accessed November 15, 2022).

[3] D. Frackowiak, The Jablonski diagram, J Photochem Photobiol B. 2 (1988) 399. https://doi.org/10.1016/1011-1344(88)85060-7.

[4] S.J. Beech, S. Noimark, K. Page, N. Noor, E. Allan, I.P. Parkin, Incorporation of crystal violet, methylene blue and safranin O into a copolymer emulsion; the development of a novel antimicrobial paint, RSC Adv. 5 (2015) 26364–26375. https://doi.org/10.1039/C5RA01673H.

[5] C. Michelin, N. Hoffmann, Photosensitization and Photocatalysis - Perspectives in Organic Synthesis, ACS Catal. 8 (2018) 12046–12055. https://doi.org/https://doi.org/10.1021/acscatal.8b03050.

[6] Museum Kaap Skil, 17th century wedding dress unveiled, (2022). https://kaapskil.nl/en/latest/news/17th-century-wedding-dress-unveiled/ (accessed November 26, 2022).

[7] A. Serrano, A. Brokerhof, B. Ankersmit, M. van Bommel, From the bottom of the sea to the display case: A study into the long-term preservation of archaeological maritime silk textiles in controlled atmosphere, J Cult Herit. 45 (2020) 91–100. https://doi.org/10.1016/J.CULHER.2020.04.004.

[8] M.A. Montenegro, A.D.O. Rios, A.Z. Mercadante, M.A. Nazareno, C.D. Borsarelli, Model Studies on the Photosensitized Isomerization of Bixin, J Agric Food Chem. 52 (2004) 367–373. https://doi.org/https://doi.org/10.1021/jf0349026.

[9] M. Valentí-Quiroga, R. Gonzalez-Olmos, M. Auset, J. Díaz-Ferrero, Study of the Photodegradation of PBDEs in Water by UV-LED Technology, Molecules. 26 (2021). https://doi.org/10.3390/MOLECULES26144229.

[10] E.F. Bernstein, Laser Tattoo Removal, Semin Plast Surg. 21 (2007) 175–192. https://doi.org/10.1055/S-2007-991186.

[11] R.M. Ion, A. Nuta, A.A. Sorescu, L. Iancu, Photochemical Degradation Processes of Painting Materials from Cultural Heritage, Photochemistry and Photophysics - Fundamentals to Applications. (2018). https://doi.org/10.5772/INTECHOPEN.76169.

[12] L. Monico, K. Janssens, E. Hendriks, F. Vanmeert, G. van der Snickt, M. Cotte, G. Falkenberg, B.G. Brunetti, C. Miliani, Evidence for Degradation of the Chrome Yellows in Van Gogh's Sunflowers: A Study Using Noninvasive In Situ Methods and Synchrotron-Radiation-Based X-ray Techniques, Angewandte Chemie International Edition. 54 (2015) 13923–13927. https://doi.org/10.1002/ANIE.201505840.

[13] E. Hendriks, L. Jansen, J. Salvant, É. Ravaud, M. Eveno, M. Menu, I. Fiedler, M. Geldof, L. Megens, M. van Bommel, C.R. Johnson, D.H. Johnson, A comparative study of Vincent van Gogh's Bedroom series, in: Studying Old Master Paintings: Technology and Practice, 2011: pp. 237–243.

[14] E. Kirchner, I. van der Lans, F. Ligterink, M. Geldof, A. Ness Proano Gaibor, E. Hendriks, K. Janssens, J. Delaney, Digitally reconstructing Van Gogh's Field with Irises near Arles. Part 2: Pigment concentration maps, Color Res Appl. 43 (2018) 158–176. https://doi.org/10.1002/COL.22164.

[15] E. Kirchner, M. Geldof, E. Hendriks, A.N.P. Gaibor, K. Janssens, J. Delaney, I. van der Lans, F. Ligterink, L. Megens, T. Meedendorp, K. Pilz, M. Geldof, E. Hendriks, A.N.P. Gaibor, K. Janssens, J. Delaney, I. van der Lans, F. Ligterink, L. Megens, T. Meedendorp, K. Pilz, Recreating Van Gogh's original colors on museum displays, Electronic Imaging. 31 (2019) 1–6. https://doi.org/10.2352/ISSN.2470-1173.2019.14.COLOR-077.

[16] L.F.C. Friele, A Comparative Study of Natural and Xenotest Exposure Condition: for Measuring Fading and Degradation, Journal of the Society of Dyers and Colourists. 79 (1963) 623–631. https://doi.org/10.1111/J.1478-4408.1963.TB02522.X.

[17] P.M. Whitmore, X. Pan, C. Bailie, Predicting The Fading of Objects: Identification of Fugitive Colorants Through Direct Nondestructive Lightfastness Measurements, Journal of the American Institute for Conservation. 38 (1999) 395–409. https://doi.org/10.1179/019713699806113420.

[18] P.M. Whitmore, C. Bailie, S.A. Connors, Micro-fading tests to predict the result of exhibition: progress and prospects, Studies in Conservation. 45 (2000) 200–205. https://doi.org/10.1179/SIC.2000.45.SUPPLEMENT-1.200.

[19] G. Patin, R.G. Erdmann, F. Ligterink, J.G. Neevel, K.J. van den Berg, E. Hendriks, An enhanced optical micro-fading device, J Cult Herit. 57 (2022) 276–285. https://doi.org/10.1016/J.CULHER.2022.08.012.

[20] M.J. den Uijl, A. Lokker, B. van Dooren, P.J. Schoenmakers, B.W.J. Pirok, M.R. van Bommel, Comparing different light-degradation approaches for the degradation of crystal violet and eosin Y, Dyes and Pigments. 197 (2022) 109882. https://doi.org/10.1016/J.DYEPIG.2021.109882.

[21] D. Confortin, H. Neevel, M. Brustolon, L. Franco, A.J. Kettelarij, R.M. Williams, M.R. van Bommel, Crystal violet: Study of the photo-fading of an early synthetic dye in aqueous solution and on paper with HPLC-PDA, LC-MS and FORS, J Phys Conf Ser. 231 (2010) 012011. https://doi.org/10.1088/1742-6596/231/1/012011.

[22] A. Alvarez-Martin, S. Trashin, M. Cuykx, A. Covaci, K. de Wael, K. Janssens, Photodegradation mechanisms and kinetics of Eosin-Y in oxic and anoxic conditions, Dyes and Pigments. 145 (2017) 376–384. https://doi.org/10.1016/j.dyepig.2017.06.031.

[23] P.I. Hora, P.J. Novak, W.A. Arnold, Photodegradation of pharmaceutical compounds in partially nitritated wastewater during UV irradiation, Environ Sci (Camb). 5 (2019) 897–909. https://doi.org/10.1039/c8ew00714d.

[24] M. Shamsipur, B. Hemmateenejad, N.J. Jahani, K.M. Majd, Liquid chromatographic-mass spectrometric monitoring of photodegradation of diphenylamine using experimental design

methodology, J Photochem Photobiol A Chem. 299 (2015) 62–68. https://doi.org/10.1016/j.jphotochem.2014.12.002.

[25] F. Sabatini, I. Degano, M. van Bommel, Investigating the in-solution photodegradation pathway of Diamond Green G by chromatography and mass spectrometry, Coloration Technology. 137 (2021) 456–467. https://doi.org/10.1111/COTE.12538.

[26] R. Liu, Q. Jin, G. Tao, L. Shan, Y. Liu, X. Wang, LC-MS and UPLC-quadrupole time-of-flight MS for identification of photodegradation products of aflatoxin B1, Chromatographia. 71 (2010) 107–112. https://doi.org/10.1365/s10337-009-1354-y.

[27] A. Manhita, V. Ferreira, H. Vargas, I. Ribeiro, A. Candeias, D. Teixeira, T. Ferreira, C.B. Dias, Enlightening the influence of mordant, dyeing technique and photodegradation on the colour hue of textiles dyed with madder - A chromatographic and spectrometric approach, Microchemical Journal. 98 (2011) 82–90. https://doi.org/10.1016/j.microc.2010.12.002.

[28] B.W.J. Pirok, G. Moro, N. Meekel, S.V.J. Berbers, P.J. Schoenmakers, M.R. van Bommel, Mapping degradation pathways of natural and synthetic dyes with LC-MS: Influence of solvent on degradation mechanisms, J Cult Herit. 38 (2019) 29–36. https://doi.org/10.1016/J.CULHER.2019.01.003.

[29] R. Helmus, T.L. ter Laak, A.P. van Wezel, P. de Voogt, E.L. Schymanski, patRoon: open source software platform for environmental mass spectrometry based non-target screening, J Cheminform. 13 (2021) 1–25. https://doi.org/10.1186/s13321-020-00477-w.

[30] R. Helmus, B. van de Velde, A.M. Brunner, T.L. ter Laak, A.P. van Wezel, E.L. Schymanski, patRoon 2.0: Improved non-target analysis workflows including automated transformation product screening, J Open Source Softw. 7 (2022) 4029. https://doi.org/10.21105/JOSS.04029.

# CHAPTER 2

## Parameters that affect the photodegradation of dyes and pigments in solution and on substrate – An overview

## Abstract

It has been known for many years that dyes and pigments are subject to light-induced degradation, or photodegradation, when exposed to light. It is the very reason why some beverages or medicines are wrapped in light-tight packaging materials, and why museums cover their windows with UV-blocking filters. The exact chemistry of light-induced degradation can be quite complex. Why and how are these dyes and colorants affected by light? How fast do these processes occur? Are there ways to prevent this from happening in a straightforward and durable way? These were and still are questions that are relevant to the many fields where colorants are applied. In order to support these questions, we have tried to provide a broad overview of the research that has already been conducted on the photodegradation of dyes and pigments and the analysis of photodegradation products. In those papers, the most important parameters that were discussed are the influence of the irradiation source, intensity and time, the presence or absence of oxygen, temperature, the effects that catalysts have, as well as the dye or pigment concentration. Additionally, we have investigated the differences found for photodegradation in solution and on substrates and specific parameters that may affect the processes in these media.

**Publication**

Parameters that affect the photodegradation of dyes and pigments in solution and on substrate – An overview

Iris Groeneveld, Maria Kanelli, Freek Ariese, Maarten R. van Bommel

*Dyes and Pigments*, **2023**, 210, 110999, DOI: 10.1016/j.dyepig.2022.110999

## 2.1 Introduction

Energy in the form of light induces physical and chemical changes to most organic compounds [1–4]. Inks, foods, pharmaceuticals, cosmetic products and polymers are only a few examples of materials that undergo degradation under the influence of light, also called light-induced degradation or photodegradation [5–7]. Among them, organic colorants are of great interest, as they are often used for the decoration of various products, thereby playing a decisive role in marketing and art. Photodegradation can have both a positive and a negative impact. On the one hand it can be responsible for fading colors in (historical) art objects, the loss of color and valuable nutrients in foodstuffs, the fading of cosmetics, and the degradation of functional active components in pharmaceuticals [3,8–10]. On the other hand, photodegradation can also be implemented as a straightforward way to disinfect and purify wastewater generated from textiles, printing and paper industries [6,11]. A famous example of undesirable photodegradation in historical objects can be found in the painting *Sunflowers* by Van Gogh, depicted in Fig. 2.1A, from which it is evident that the yellow colors are fading.

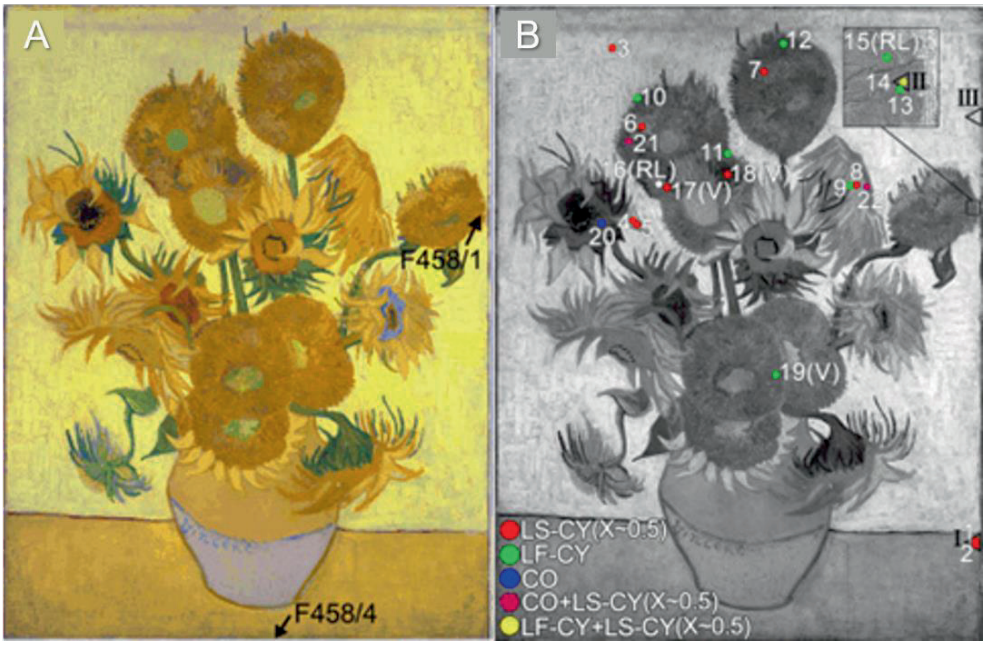


Figure 2.1. (A) Photograph of *Sunflowers* by Van Gogh (Arles, 1889; Van Gogh Museum, Amsterdam) with sample spots shown. (B) Raman distribution of different types of chrome yellows, with the light-sensitive pigments indicated by LS-CY (red). Adapted with permission from [12] (Copyright 2015 Wiley-VCH Verlag GmbH & Co. KGaA).

Researchers have found that the reason for the darkening of these once bright chrome yellow pigments is through the $Cr^{VI} \rightarrow Cr^{III}$ reduction in the light-sensitive sulfur-rich chrome yellows ($PbCr_{1-x}S_xO_4$), depicted as bright red dots in the Raman map in Fig. 2.1B [12]. The findings of studies like these will eventually result in a more accurate, safe and controlled strategy for the light exposure of historical objects. In addition, it will inform art historians but also the wider public about the original appearance of objects of art which is of relevance to understand the intention of the artist.

To better understand how these photodegradation processes occur or to ensure product quality, light stability testing is often performed using accelerated ageing to estimate within a shorter amount of time the long-term effects at the expected light levels. However, most studies focus on the visual effect, i.e., fading, but less on the degradation mechanisms, which are key to a better understanding of photodegradation. Not only for increasing the shelf life of consumer products and preserving artwork, but for example also for reducing the amount of (unknown) chemicals released into the environment.

## 2.1.1 Photochemistry of dyes and pigments

Colorants can interact with light in multiple ways. After a molecule absorbs a photon and is brought into the excited state, it can lose the excess energy by following several different pathways. These include physical processes that cause the relaxation of the molecule back to the ground state, as well as photochemical reactions that lead to the degradation of the molecule and the formation of new products [13]. Two main classes of photochemical reactions are distinguished depending on the photon-absorbing molecule and are illustrated in Fig. 2.2: (i) direct photochemical reactions, i.e., the dye molecules (D) are brought into the excited state (D)* and undergo intra- or intermolecular reactions after absorption of a photon, and (ii-v) indirect photochemical reactions, i.e., photons are absorbed by a photosensitizer (S) after energy transfer (ii) or by a photocatalyst (C) after oxidation (iii) or reduction (iv) of the catalyst, or by photochemically induced hydrogen atom transfer (v), which in turn excites the dye molecule [14].

### Direct photochemical reactions

When light is absorbed by the dye itself, several protective pathways may be followed to lose the excess energy: (i) by emitting a photon (fluorescence or phosphorescence), (ii) through non-radiative relaxation e.g., vibrational relaxation, and molecular or atomic collisions, or (iii) by molecular reactions i.e., photoreactions. In the situation where photoreactions take place, two distinct pathways are possible: (a) intramolecular interactions occur, i.e., the photoexcited dye decomposes without further reactions with other substances, or (b) intermolecular reactions, i.e., the dye molecule may react with

other substances present in the system. Both mechanisms result in photodegradation [15]. In the first case, the dye molecules must be chemically unstable in their photoexcited form and decompose through dissociation, intramolecular rearrangement reactions, or redox processes [13].

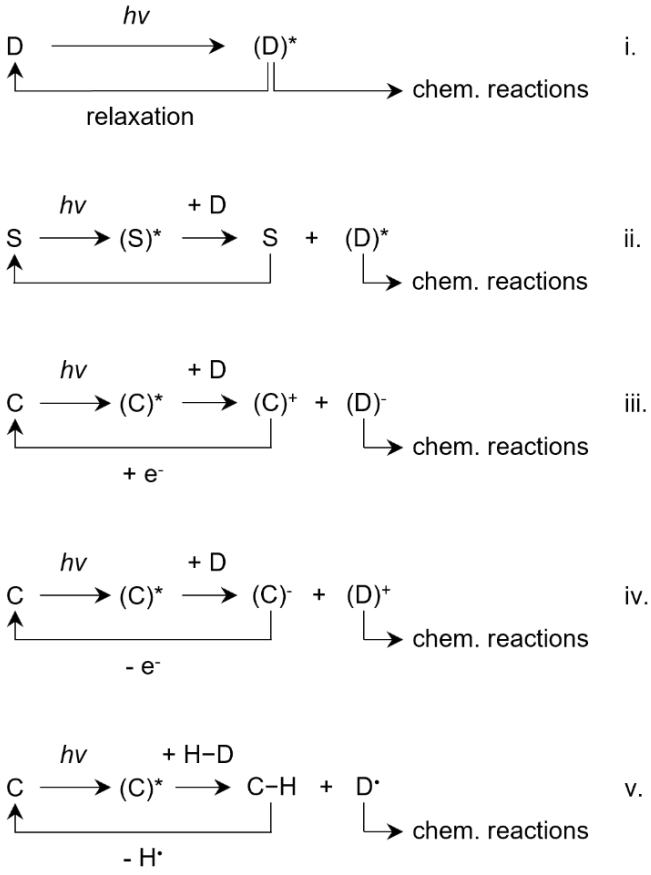


Figure 2.2. An overview of possible direct (i) and indirect (ii–v) photodegradation pathways. D = dye, S = photosensitizer, C = catalyst. Adapted with permission from [14] (Copyright 2018 American Chemical Society).

In the second case, the photoexcited dye molecules are chemically unstable only if other reactive substances are present in the system [15]. In both cases, the photochemical reactions are initiated from the singlet or triplet excited state ($^1$D*, $^3$D*) of the dye molecules. The lifetime of $^3$D* is much longer (μs) compared to the lifetime of $^1$D* (ns), and for many compounds the former is therefore assumed to be more reactive.

**Indirect photochemical reactions**

Photosensitizers are generally compounds with high absorption coefficients and low activation energies and are often in the same phase as the compound to be researched [14]. When excited, they either react directly with the neighboring dye or pigment or they react with molecular oxygen ($^3O_2$) to create singlet oxygen ($^1O_2$), which then becomes the reactive species. It goes without saying that photosensitizers can also include dyes. Examples of dyes that create $^1O_2$ through $^3D^*$ and, thus, behave like photosensitizers are Green 8 (a pyrene dye), Chlorophyllin (a chlorophyll dye), Red 22 (a xanthene dye) and Green 5 (an anthraquinone dye) [16].

Besides photosensitizers photocatalysts can be used, which are classified as homogeneous or heterogeneous, depending on whether the reactants and the photocatalysts exist in the same or in different phases, respectively. The most commonly employed homogeneous photocatalysts include ozone ($O_3$) and photo-Fenton systems with iron (Fe) and hydrogen peroxide, whereas in heterogeneous photocatalysis transition metal oxide particles, such as titanium dioxide ($TiO_2$) and tin oxide ($SnO_2$) as well as semiconductors are most often used [17]. Pigments and coatings often contain metals that can behave as a catalyst, for example, $TiO_2$ [18], aluminum oxide ($Al_2O_3$) [19], or iron oxide ($Fe_2O_3$) [20]. Section 2.4 goes into more detail of the exact reaction mechanisms of photocatalysis.

## 2.1.2 Aim of the review

Photodegradation is significantly influenced by a number of different factors. These parameters may affect both the kinetics and the photochemical mechanism, thereby affecting the degradation products formed as well as the extent of fading of dyes and pigments. To understand the changes occurring to artworks and to develop proper mitigation strategies, the chemical processes and kinetics should be known. There are many papers published describing these mechanisms including the analytical methods used to obtain them, however, a clear overview of the parameters that influence those mechanisms is still missing. Hence, this work is an attempt to provide such an overview, describing what can be found in existing literature across a variation of application areas and how these processes have been studied using various analytical detection methods. The discussed parameters include the type and the intensity of the irradiation source, the influence of oxygen, temperature, catalysts and dye concentration. This is followed by a comparison between in-solution and on-substrate photodegradation, where we describe the matrix-specific parameters as well. Afterwards, an overview of how these photodegradation products are generally analyzed is provided, and finally, all findings are discussed and summarized in the conclusions.

## 2.2 Parameters influencing photodegradation of dyes and pigments



Photodegradation of organic colorants is a dynamic process that is influenced by a number of different parameters, both internal and external. Internal factors are inherent to the compound under investigation and comprise the chemical structure and the physical state of the dye (e.g., absorption spectrum and polarity), as well as the properties of other substances present in the system (e.g., catalysts). External factors include the spectral distribution and intensity of the light source, the presence or absence of oxygen, temperature, humidity, pH, the type of solvent or substrate, and the concentration of dye. All these parameters are extensively reviewed in this chapter and are also depicted in Fig. 2.3.

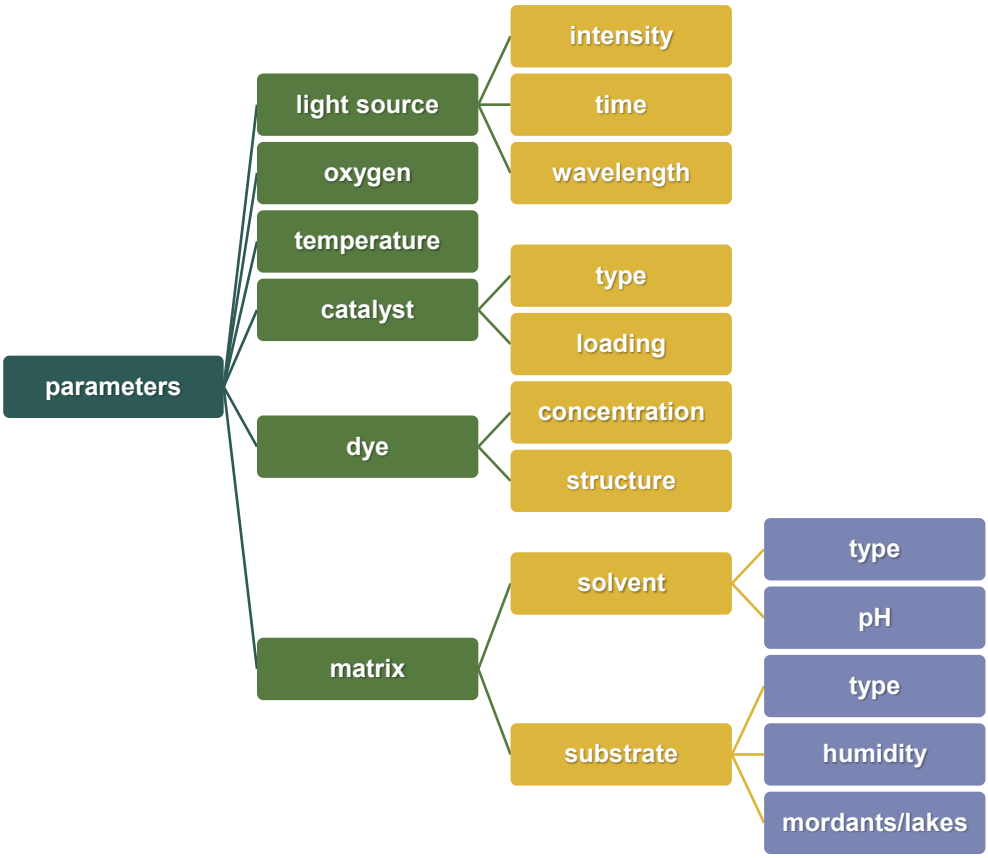


Figure 2.3. Overview and classification of the discussed parameters that influence the photodegradation of dyes and pigments.

### 2.2.1 Irradiation source

The light stability of dyes and pigments is usually evaluated under accelerated test conditions using commercial light sources. However, depending on the light source used, both the intensity and the wavelength of irradiation may lead to different results.

**Intensity**

Light of higher intensities leads to higher photodegradation efficiencies and accelerated reaction rates, as more photons are introduced into the system [21–26]. An important definition that can be used to quantify and compare the light stability between compounds, is the quantum yield of photodegradation: the number of absorbed photons leading to a molecular reaction relative to the total number of photons absorbed [27]. A high quantum yield is characterized by a high likelihood of a reaction taking place after absorption of a photon. The opposite is true for low quantum yields, where the chance of a reaction is low following absorption of a photon and the absorbed energy is more likely to be converted to heat or emitted a fluorescence. However, there is no universal relationship that describes the influence that light intensity has on the photofading process. Jamal et al. [22] found that the photodegradation efficiency of Reactive Blue 13, a mono-azo dye, in aqueous solution is directly proportional to the applied intensity of the light source. In contrast, Lachman et al. [25] showed that for several water-soluble organic dyes the degree of increased photofading in tablets depended on the dye and did not follow any particular pattern: the acceleration in the fading rate ranged from 1.5-fold for indigotin to 240-fold for alizarin cyanine green F.

In the case of photocatalysis it was shown that photofading also correlates with light intensity [28–32]. Ollis et al. [33] showed that: (i) at low light intensities the relationship is linear, because the quantum efficiency (the number of photons transformed relative to the number absorbed) is a constant, meaning that the rate varies with intensity, (ii) at intermediate light intensities beyond a certain value, the rate depends on the square root of the light intensity, whereas (iii) at high light intensities the photodegradation rate is independent of the light intensity and remains constant.

**Time**

As it would be expected, the photodegradation efficiency of organic colorants increases with an increased exposure time. Many light-induced degradation studies make use of artificial ageing based on the reciprocity principle to investigate the sensitivity of colorants as a way of relating the exposure doses (intensity*time) acquired from accelerated ageing to the ones typically encountered in a museum environment [34–37]. These photometric measurements are often extrapolated to estimate the time required

to reach a specific degree of damage. A popular approach makes use of a MicroFading tester (MFT), which can be applied directly on the art object [38,39]. The MFT consists of a probe containing several lenses to focus a high energy light source into a small spot (≈0.3 mm) to induce accelerated light ageing. Advances are still being made to the set-up, indicating that this method is of interest to many [40,41]. The use of an MFT takes little time and the result can be followed in real-time. However, there is concern regarding the validity of the results from MFT studies due to the large difference between the light intensities of MFT (5 Mlux) and those typically present in galleries (<200 lux) [42–44]. According to the reciprocity principle, similar photodegradation efficiencies are caused by the same light dose, i.e., using either high irradiation intensities for shorter periods of time or lower intensities for longer periods of time. This principle is indeed valid for most light stable colorants, however, deviations from the reciprocity principle proportional to the illumination intensity have been observed for organic colorants with a lower lightfastness. This is shown by the work of Hoyo-Meĺendez et al. [45], who demonstrated that silk samples dyed with the lightfast dye cochineal followed the reciprocity principle at all light intensities tested (0.5-4 Mlx), whereas the less light stable dyes Pomegranate and Turmeric only followed the reciprocity principle at low light intensities (0.1-0.5 Mlx). Their study showed that reciprocity failure is mainly correlated to the use of high intensity lamps, however, they also state that the physical state of the dye (e.g., aggregate formation) may positively influence the dye's lightfastness, which seems to be the case for cochineal. Therefore, in the case of photosensitive dyes and pigments, light intensity should be kept at low levels when studying the photodegradation to avoid inappropriately relating the exposure doses of normal and accelerated ageing.

### Wavelength

The nature of the incident light plays a major role in the photodegradation of dyes. Unstable dyes typically fade more easily under Visible (Vis) radiation, whereas dyes of high light fastness usually require UV radiation as it is of higher energy [46]. To fully comprehend how photodegradation is influenced by the irradiation wavelength, two main factors should be considered: (i) the absorption spectrum of the dye and (ii) how damaging the light is that is being absorbed. Typically, light of shorter wavelengths provides higher levels of energy capable of breaking bonds, thus leading to higher photodegradation efficiencies and increased reaction rates. This has indeed been observed for several organic dyes and pigments [21,47–50]. Nonetheless, the dependence of the wavelength on photodegradation is also related to the absorption spectrum of the irradiated compound. For photons to be absorbed, the spectrum of the irradiation source should overlap with the absorption spectrum of the dye or the photosensitizer/catalyst [15]. This explains why some colorants experience higher

degrees of photodegradation when exposed to light of longer wavelengths if this matches the absorption spectrum better [51]. However, no direct correlation between the fading rate and the color of the dye has been found, as this also depends on many other factors, such as the medium, binding agent, and other additives [52–54].

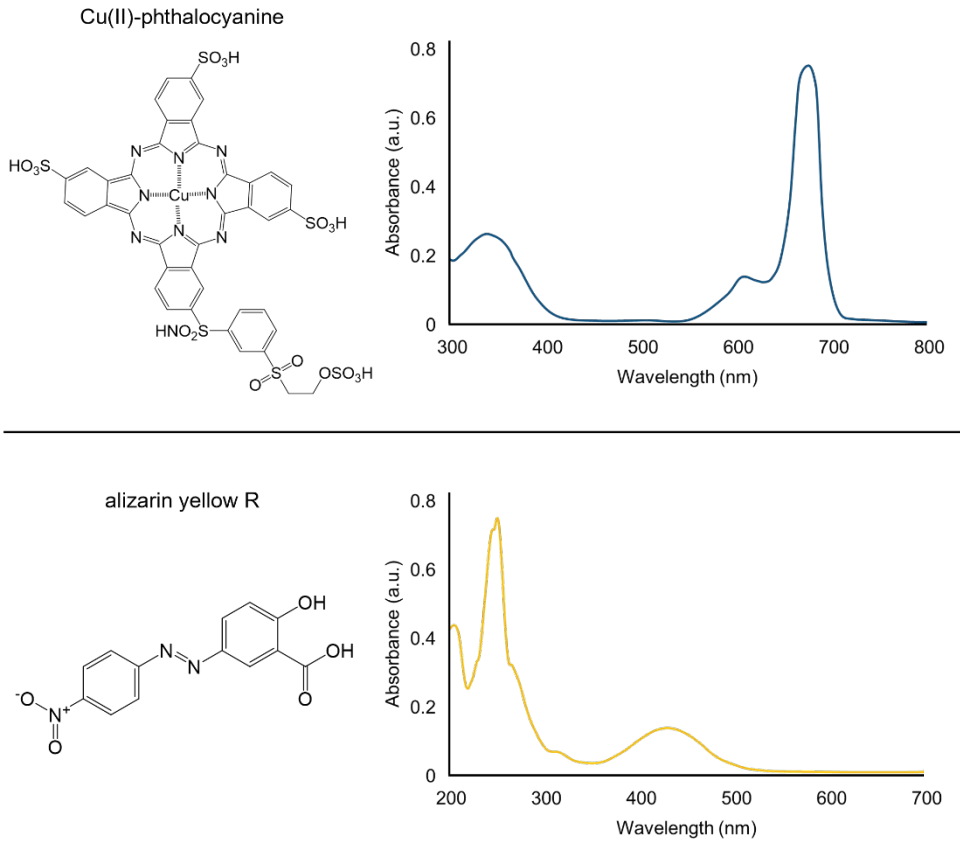


Figure 2.4. Molecular structures and absorption spectra of Cu(II)-phthalocyanine and alizarin yellow R. Adapted with permission from [55] (Copyright 2015 Taylor & Francis) and [56] (Copyright 2012 Elsevier).

Batchelor et al. [57] showed that both UV and Vis light induce the photodegradation of azo dyes and phthalocyanines under solar lighting conditions, however, in the case of azo dyes the Vis fraction was the most important, while for phthalocyanines the UV portion was dominant. This difference can be attributed to the fundamentally different structures of the dye classes, resulting in different photochemistry. Both azo dyes and phthalocyanines absorb UV and Vis light as can be seen in Fig. 2.4, but the chemical structure of the phthalocyanine is much stronger compared to the azo dye, meaning that more energy (i.e., UV light) is needed to initiate photodegradation. There may be an additional explanation for this difference. Compounds that predominantly absorb light of

longer wavelengths, thus lower energy, such as Cu(II)phthalocyanine, have lower $S_1$ and $T_1$ states compared to compounds that mainly absorb in the UV region. As a result, the lifetime of the triplet excited state is shorter, which also decreases the time for the compound to undergo chemical reactions with neighboring molecules. Additionally, it was found that oxygen is required in the photodegradation of these specific dyes with Vis light, but not with UV light, again indicating that the photofading mechanism can be different depending on the irradiation wavelength.

The illumination wavelength may not only affect the photodegradation rate, but also the photodegradation mechanism. This is because the absorption bands of a compound may be related to different chemical subgroups of the molecule. Therefore, by irradiating at different wavelengths it is possible to excite different chromophores of the molecule. For example, Ahmad et al. [21] showed that intramolecular photoaddition of Riboflavin into cyclodehydroriboflavin is enhanced under UV irradiation, whereas under Vis light mostly photoreduction of Riboflavin into formylmethylflavin, lumiflavin and lumichrome takes place. Nevertheless, the measurements in both of these studies were performed only by spectroscopic techniques, therefore, the identification of the various photodegradation products is questionable. Alvarez-Martin et al. [58] used both spectroscopic and chromatographic techniques and demonstrated that by irradiation with wavelengths close to the main absorbance band of the red pigment Eosin Y the photodegradation reaction was faster by a factor of >20.

### 2.2.2 Oxygen

Different photochemical reactions are observed depending on the presence or absence of free molecular oxygen [59–63]. Under anaerobic conditions, $^3D^*$ can either be reduced or oxidized, depending on the presence of a reducing or oxidizing agent, respectively. When both agents are present in the system, the reaction mechanism is determined by the nature of the reagents and the environmental or experimental conditions. Under aerobic conditions, interaction between $^3D^*$ and $O_2$ (the latter normally being in the triplet ground state) takes place through an energy transfer process, resulting in the formation of $^1O_2$, provided that no reducing agent is present. This highly reactive oxygen allotrope leads to further decomposition and fading of the organic dye. Less commonly, $^3D^*$ may also react with $O_2$ via an electron transfer process, generating radical superoxide ions ($O_2^{\cdot-}$). When a reductant is also present in an aerobic system, competition takes place.

Obviously, the presence or absence of oxygen plays a major role in the photodegradation process of dyes and pigments. Multiple studies have shown that in most cases of organic colorants, a decrease in oxygen concentration leads to lower photodegradation rates, however, a complete halt to the fading process has not been observed [48,57,64–

71]. This might be due to other degradation processes occurring simultaneously (e.g., reduction in presence of a reducing agent). The degree of influence that oxygen has on the degradation rate has been found to depend on both the structure of the colorant and the solvent or substrate, which was demonstrated in an extensive study conducted by Arney et al. [61]. In their work, different trends were observed for different samples: some faded at rates that varied linearly with oxygen concentration, whereas others faded at rates that varied linearly with the square root of the oxygen concentration. Additionally, in proteinaceous substrates, where photodegradation mainly proceeds via reduction pathways, oxygen may have less of an influence on photodegradation. Saito et al. [70] observed lower photodegradation rates for six natural dyes on both silk and cotton substrates in the absence of oxygen, however, the overall influence of oxygen was more pronounced in the case of the cotton (cellulosic) substrates, thus confirming this hypothesis.

Contrary to what is typically observed, Schwen et al. [72] showed that diazacyanine blue and diazacyanine yellow dyed textiles degraded quicker under anaerobic conditions. The same trend was observed for Basic Blue 3 on silk and wool, also proteinaceous substrates. Arney et al. [61] demonstrated that the vermillion azo pigment follows the same tendency when applied as an oil pigment onto a glass slide. Blaisdell [73] found that oxygen inhibits the photodegradation of two azo dyes in isopropyl solution, due to a photosensitized oxidation of the solvent.

Furthermore, as would be expected, oxygen can also influence the mechanism of the photodegradation reaction. Alvarez-Martin et al. [58] investigated the photodegradation of Eosin Y in aqueous solution under aerobic and anaerobic conditions and found that oxygen affects both the rate and the mechanism of the reaction (Fig. 2.5). In particular, in the presence of oxygen, photodegradation followed a fast oxidative pathway where the breakdown of the chromophore resulted in complete loss of color. In contrast, in the absence of oxygen a slower debromination process took place, which led to less pronounced photofading, since the chromophore remained essentially intact. These results combined prove that it is impossible to draw generalized conclusions and detailed investigation of the fading reactions of different dyes and in different media is crucial in order to understand how the reaction mechanisms proceed.

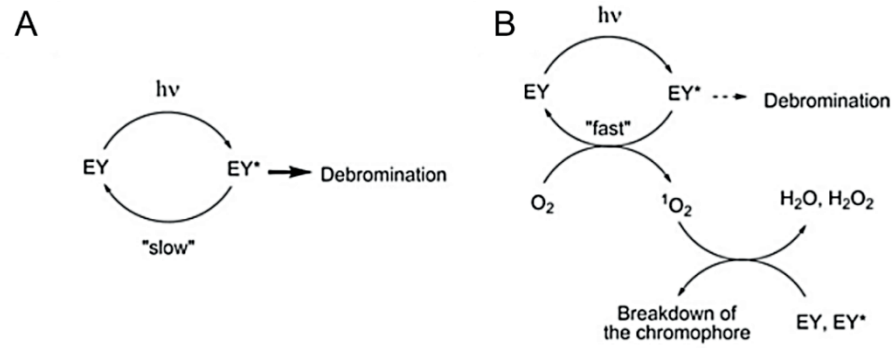


Figure 2.5. (A) Under anaerobic conditions a relatively slow debromination process takes place from the triplet excited state of Eosin Y (EY*), while under aerobic conditions (B) a second, faster process takes place resulting in the breakdown of the chromophore after generation of $^1O_2$ by EY*. Reprinted with permission from [58] (Copyright 2017 Elsevier).

### 2.2.3 Temperature

In general, temperature has been found to have relatively little effect on the photofading process of organic dyes and pigments. As would be expected, a rise in temperature increased the fading rate, but to a lesser extent compared to other parameters [24,50,74,75]. The pathways of the photodegradation process have not been found to be altered by differences in the temperature. This is an unexpected observation when considering that an increase in temperature leads to more energy, therefore reactions with higher activation energies could become preferable. However, since the thermal energies involved are small compared to the energies absorbed in the form of photons, the changes are rather insignificant.

Photodegradation of organic colorants on fiber substrates was shown to be influenced by temperature in two different ways. On the one hand, a change in temperature in such substrates almost invariably causes a change in moisture content. In particular, an increase in temperature leads to lower moisture levels in the fiber material, thus reducing the degree of photodegradation. On the other hand, however, it was shown that heat breaks down aggregated dye particles and that this may a reversible process [76]. Giles et al. irradiated dyed cellophane films in a heated atmosphere, but included 'cooling down' breaks in between where the sample was stored in a cold and dark environment. They found that the optical density increased linearly with temperature as a result of the breakdown of aggregates when irradiated in a heated atmosphere but saw a decrease in optical density after the cooling down period, indicating reaggregation of dye particles. The breakdown of aggregates increases the surface area accessible for photochemical reactions, therefore increasing photodegradation. These opposing effects both depend

on the type of the fiber substrate, as some fiber substrates can absorb greater amounts of moisture or promote aggregation to a higher extent, thereby being more susceptible to temperature than others.

In aqueous solutions, an increase in temperature results in lower concentrations of dissolved molecular oxygen, indicating that the influence of temperature and oxygen may be interrelated. Not many studies have assessed this effect, however, neither the photodegradation pathway nor the fading efficiency have been found to show any change in such systems [24].

In heterogeneous photocatalytic systems, temperature was found to have an indirect effect on the photodegradation of dyes. In particular, low temperatures favor the adsorption of the dye onto the catalyst, which is a spontaneous exothermic process. Nevertheless, in this case the adsorption of the degradation products is also enhanced, thus reducing the number of active sites on the catalyst. In contrast, high temperatures lead to an increase in the mobility of the dye molecules, therefore increasing the kinetic energy. However, the enhanced kinetic energy of the dye molecules may also allow them to escape from the photocatalyst surface, without being subjected to photodegradation. This effect was demonstrated by Barakat et al. [77] who showed that the morphology of the catalyst is very relevant when studying the effect of temperature on the photodegradation of dyes. They compared the photodegradation of rhodamine B at different temperatures with silver (Ag) doped $TiO_2$ nanoparticles and Ag doped $TiO_2$ nanofibers. For the nanoparticles, higher temperatures increased the photodegradation rate, whereas a rise in temperature had a negative effect when nanofibers were used. This was explained due to the super activity of the nanofiber surface compared to the nanoparticles. Unfortunately, very few studies [78–81] have evaluated the effect of temperature on the photodegradation of dyes in such systems.

### 2.2.4 Catalysts

Catalysts can be added to increase the photodegradation rate and the process is strongly influenced by both the type and amount of catalyst used. A photocatalyst enhances the photodegradation rate by generating reactive radical species on its surface after irradiation with light of energy higher than the bandgap of the catalyst. Upon irradiation, electrons are excited to the conduction band, which generates positive holes ($h^+$) in the valance band of the photocatalyst. Subsequently, adsorbed oxygen and water molecules are transformed into highly reactive superoxide ions and hydroxyl radicals, respectively, which react with and ultimately lead to the decomposition of adsorbed organic dyes [82,83].

In photocatalytic systems, organic colorants may fade completely upon light irradiation, whereas for some photodegradation reactions efficiency levels off after a while [78,84,85]. This is probably due to blockage of multiple active sites on the catalyst surface, which might occur over time and is dependent on the type of catalyst [86].

### Type of catalyst

The intrinsic properties of the catalyst significantly influences the photodegradation efficiency of dyes for heterogeneous systems. Such properties include the light absorption range, the redox potential, the charge separation efficiency and the stability of the catalyst. Therefore, some catalysts show higher activity towards the decolorization of organic dyes under identical environmental conditions due to differences in these inherent properties. For instance, zinc oxide (ZnO) was found to be more efficient for the removal of several different organic dyes from water compared to $TiO_2$ [87–89], which is due to its broader absorption spectrum [85].

Unfortunately, single-component materials, such as ZnO and $TiO_2$, typically cannot satisfy the requirement of large redox potential and broad light absorption range simultaneously. Therefore, the investigation of new heterostructure systems that can improve the overall photocatalytic efficiency has become increasingly popular throughout the last decades. The outstanding properties of heterostructure catalysts are a result of the synergistic effect, electronic interaction, and strain effect, which will be different from that of pure materials [90]. For instance, Saeed et al. [86] demonstrated that titanium dioxide supported palladium ($TiO_2$/Pd) and titanium dioxide supported platinum ($TiO_2$/Pt) nanoparticles show higher photocatalytic activity compared to pure $TiO_2$ nanoparticles, with the effect being more pronounced in the case of $TiO_2$/Pd. El-Bahy et al. [91] reported that lanthanide ions can enhance the photodegradation efficiency of $TiO_2$ and found that gadolinium (III) doped titanium dioxide ($Gd^{3+}$/$TiO_2$) nanoparticles result in a higher photocatalytic activity towards Direct Blue 53. Alzahrani [92] showed that the photodegradation of Eosin Y was significantly higher when using Ag doped magnetic nanoparticles (Ag-$Fe_3O_4$) compared to pure magnetic nanoparticles ($Fe_3O_4$) and Paul et al. [93] found the same trend for Ag doped graphitic carbon nitride (Ag-g$C_3N_4$) towards methylene blue, crystal violet and Rose Bengal. It is evident that advanced technologies have led to the production of new systems, able to transcend difficulties of previous photocatalysts, resulting in more effective and efficient photodegradation.

### Catalyst loading

Another factor that has been shown to affect the rate and efficiency of the photofading reaction is the photocatalyst loading. As it would be expected, an increase in the amount

of catalyst leads to higher photodegradation efficiencies and increased reaction rates as more active sites are provided for adsorption of dye molecules. In fact, the initial reaction rates were found to increase proportionally with the amount of the catalyst [83,94]. Nonetheless, beyond a certain critical point, both the rate and efficiency of the photodegradation reaction either level off [28,86] or even begin to drop [84,91,95–97]. For heterogenic photocatalysis this can be explained by an increase in the suspension's turbidity, which leads to more dominant light scattering phenomena, resulting in limited light absorption by the photocatalyst surface. Moreover, Herrmann [83] illustrated that the optimum photocatalyst loading depends on the initial solute concentration, therefore, the higher the initial dye concentration, the higher the optimum amount of photocatalyst required for its photodegradation. Thus, an optimum amount of photocatalyst does exist and should be determined first, not only to ensure efficient photodegradation, but also to avoid unnecessary use of catalyst excess.

### 2.2.5 Dye concentration

It was shown that photodegradation is strongly influenced by the amount of organic dye or pigment present in a solution or on a substrate. For dyes adsorbed onto substrates, dye concentration is closely related to aggregation. The higher the dye concentration, the greater the average size of the dye aggregates, thus, the lower the relative surface area accessible to environmental factors that lead to photofading. Therefore, an increase in dye concentration leads to an increase in aggregation, resulting in slower photofading rates. This is indeed evidenced by several studies investigating various organic colorants on paper, textiles and other synthetic materials [57,98–101]. Apart from an increase in aggregation, increased dye concentrations may also lead to higher absorption on the surface and weaker interactions between the substrate and the organic colorant, resulting again in lower reaction rates, which is further elaborated in section 3.2.1 [98,102]. Batchelor et al. [57] investigated the photodegradation of low and high concentrations (light and dark shades) of reactive dyes on cotton fibers and determined the color change before and after irradiation using a Datacolor SF600 Spectrophotometer. They found that the amount of color fading due to photodegradation was linear with time for both dark and light shades, but that the percentage of dye lost was greater for the lighter shades.

In heterogeneous photocatalytic systems the initial dye concentration is shown to have a strong influence on the photodegradation mechanism. It was found that an increase in the dye concentration leads to reduced photodegradation efficiencies and lower reaction rates. Numerous experiments have been performed both for different classes of organic dyes and with different catalysts, all supporting the aforementioned statement

[28–30,86,89,91,103,104]. An explanation for this effect lies in the rate-limiting step of the formation of hydroxyl radicals on the photocatalytic surface. In particular, as the initial dye concentration increases while the irradiation intensity remains constant, fewer photons will reach the catalyst surface due to absorbance by the dye molecules, therefore, fewer reactive radicals are produced by the catalyst, leading to slower photodegradation rates [105].

The effect of dye concentration on in-solution photodegradation in absence of catalysts has been studied less. Research has shown that at low dye concentrations the photodegradation process of xanthene dyes erythrosine and phloxine B follows first-order kinetics, while at higher dye concentrations a more complex reaction mechanism may be involved. In particular, self-catalysis becomes more significant with increased concentration, resulting in higher reaction rates [24,106]. Strongly concentrated solutions also result in slower degradation rates due to high absorption at the top or edges of the sample, resulting in few photons reaching the main portion of the solution. This was demonstrated by Groeneveld et al. when studying the photodegradation of Riboflavin in a 12-cm long liquid core waveguide cell [107].

## 2.3 In-solution versus on-substrate

Dye photofading in solution does not always mirror dye photofading on a surface. The properties of substrates (e.g., proteinaceous, cellulosic, synthetic matrix) and those of solvents (e.g., proton accepting or donating) may influence the photodegradation process of dyes significantly. In fact, it has been shown that dye molecules can exist as different tautomers depending on the medium, meaning that interactions between the dye and the medium molecules can lead to different dye structures, even without photoirradiation [108,109]. Nevertheless, solution or gel phase systems can sometimes be used as simple models to evaluate the kinetics and mechanisms of photochemical reactions of organic based colorants in solid samples [59]. Confortin et al. [110] demonstrated that crystal violet produced the same photodegradation products both in solution and on paper (Fig. 2.6), indicating that it follows the same or a similar photofading mechanism regardless of these media. Sousa et al. [59] found that the major degradation product of indigo in liquids, and in cellulose or collagen gels was isatin, which was in line with the analysis of blues from millenary Andean textiles (200 BC to 200 DC). They propose that the photodegradation rates found for indigo in water could be representative for that in historical artefacts.

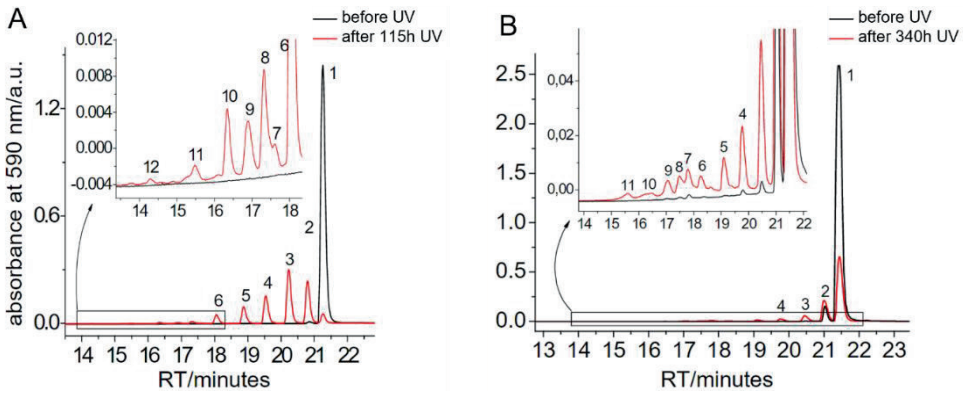


Figure 2.6. Comparison of degradation products from crystal violet (peak 1) samples irradiated (A) in aqueous solution or (B) on paper by Confortin using liquid chromatography with photodiode detection (LC-DAD). The same degradation products (peaks 2–12) were found in both media after exposure to UV light, although in higher concentrations and within a shorter irradiation time for crystal violet in solution. Adapted with permission from [110] (Copyright 2010 IOPscience).

Furthermore, it has been found that the rate of photochemical reactions in solution is typically greater due to the enhanced mobility of dye molecules in solution [71,102,111]. However, Abbott et al. [112] reported that the photodegradation of Acid Red 52 and Direct Blue 1 was much faster on paper and cotton (both cellulosic matrices) compared to in-solution degradation. In addition, the UV-Vis absorption spectra showed significant differences when the dyes were dissolved in water or when they were deposited on a substrate. It is worth repeating that the fading rate depends also on the dye concentrations, and this effect was remarkably slower for the substrate compared to the solutions. Other photodegradation parameters that can be related to the matrix are the type of solvent or substrate, the pH of the solution, the presence of mordants in substrates and the humidity of the environment, which are discussed below.

## 2.3.1 Solvent

**Type of solvent**

Properties of the solvent, such as its proticity and polarity, affect the solubility of different compounds through intermolecular interactions with the dissolved substances. Such interactions could eventually result in the formation of products that may lead to incorrect conclusions when used as a model for on-substrate photodegradation. For textile dyes, dimethyl sulfoxide (DMSO) was found to be particularly appropriate for the extraction of dyes that bind to the textile fiber through hydrophobic interactions (i.e., vat dyes and direct dyes) [113]. However, Pirok et al. [114] showed that the presence of DMSO accelerated the photodegradation reaction of Eosin Y and carminic acid; it was

found to interact with the carboxylic acid groups of all molecules present in the solution. Therefore, the use of DMSO as an extraction solvent of organic dyes from textile for light-induced degradation studies should be investigated as it may affect the composition of the degradation products, which would hamper the use as a model for photofading studies on textiles.



The influence of DMSO on photodegradation reactions as well as ethanol was evidenced by a different study. Ethanol is a common solvent of ink compositions, rendering it very relevant for document dating purposes. Brezová et al. [115] studied the effect of water, ethanol and DMSO on the photodegradation mechanism of six triarylmethane dyes, methylene blue, and Eosin Y both under aerobic and anaerobic conditions. The results showed that even under anaerobic conditions reactive oxygen species were formed for all dyes dissolved in ethanol and DMSO, indicating that the initial presence of oxygen is less important when these solvents are used for photodegradation studies. However, this may be different for aqueous solutions. It was found that reactive oxygen species were formed by crystal violet, methylene blue, malachite green oxalate and Acid Green 16 in oxygen-saturated aqueous solutions, whereas under anaerobic aqueous conditions these species were only formed by crystal violet.

The polarity of the solution environment also plays an important role in the photostability of photochromic organic dyes. Photochromic dyes are characterized by a reversible change of color upon exposure to light, which is a result of a change in chemical structure depending on the environment. In particular, it was found that photodegradation of photochromic dyes in tetrahydrofuran (THF) was faster compared to benzene, due to the higher polarity of THF, which stabilized the unstable open colored form of the dye molecules, promoting the photodegradation of this specific dye [102]. Furthermore, an increase in the water content of the solvent showed an increase of the fading rate of azo dyes, which may be due to the formation of radical hydroxyl species or may result in an enhanced contribution to the excited state of intra-molecular charge-transfer forms, followed by photoreduction to hydrazyl radicals, which have a lower stability in water [116]. It is clear that the effect of the solvent in the photodegradation process of organic colorants is strongly associated with the structure of the dye, therefore, to fully comprehend its influence, it is important that future studies evaluate the photofading reactions of different organic colorants in various solvents and media.

**pH**

Photodegradation in solution may be significantly influenced by the solution pH or other reducing agents. Redox active groups can be protonated or deprotonated in acidic or alkaline pH, respectively, resulting in different forms, which may be less susceptible to

photodegradation. Seixas de Melo et al. [117] studied keto and leuco-forms of indigotin derivatives in solution and found differences in the preferred relaxation pathways from the excited state to the ground state. They also suggested a difference in excited-state geometry, which ultimately may lead to a different photochemistry for the two forms.

The effects of the pH are different for many dyes depending on their chemical structure and pKa value. In general, charged molecules are more prone to initiate a photodegradation reaction. Therefore, the photodegradation of acidic dyes, such as carminic acid, alizarin and phycocyanin has been shown to increase at pH values higher than their pKa, where these molecules are mostly negatively charged [47,48,65]. Similarly, the photofading rate of the basic dye methylene blue was found to increase at pH values lower than its pKa, where the molecule exists almost entirely in the cation form [118]. It is also worth noting that changes in the pH leading to protonation or deprotonation may induce alterations in the conjugated system of the organic dyes, thereby changing their absorption spectrum [47,65,119,120], which should be taken into account when performing light-induced degradation studies in solution.

In heterogeneous photocatalytic systems, photodegradation is indirectly influenced by the solution pH, depending on both the solid catalyst and the dissolved dye. In particular, pH affects the electrostatic interactions between the molecules on the surface of the photocatalyst and the dye molecules, thus, the adsorption capacity of the catalyst is altered. Several photocatalytic materials, such as $TiO_2$ and g-$C_3N_4$, display amphoteric characteristics [121,122]. Therefore, at a lower pH protonation of the photocatalyst will take place, leading to a positively charged surface, whereas at higher pH values a negatively charged surface will be formed. In the former case, anionic dyes are electrostatically attracted, thus highly adsorbed onto the catalyst surface, thereby being successfully subjected to photodegradation. However, the adsorption of cationic dyes is hindered due to electrostatic repulsion; the reverse is true in the latter case at higher pH. In summary, high adsorption capacities, and therefore high photodegradation efficiencies and reaction rates, are observed when cationic or anionic dyes are adsorbed on the catalyst surface at alkaline or acidic pH, respectively.

### 2.3.2 Substrate

When photodegradation of organic colorants is taking place on a substrate, several different factors need to be considered before evaluating the fading efficiency and reaction mechanism of organic colorants. Such factors include the type of substrate (e.g., synthetic, proteinaceous or cellulosic), its complexity when heterogeneous systems are present and its susceptibility towards photodegradation, interactions with the

organic colorant, humidity, and the presence of mordants; a substance used to bind dyes to fabrics and to convert a dye into a pigment.



### Type of substrate

The type of substrate may have a strong influence on the photodegradation mechanism. Cumming et al. [123] showed that photodegradation of dyes on proteinaceous substrates (e.g., wool, silk, gelatin) is more likely to follow a reduction pathway with the histidine side chains of the protein substrates acting as reducing agents, whereas on non-protein substrates (e.g., cellulose, cotton, nylon) oxidation is more probable. This observation was further supported by several other studies [70,76]. Nevertheless, this should not be seen as an absolute statement, as oxidation and reduction can both take place on protein and non-protein substrates, as substrate matrices themselves are also susceptible to photodegradation. Proteinaceous substrates can photo-oxidize through specific amino acids after absorbing UV light [124], resulting in significant deterioration and yellowing of the matrix [125]. Cellulosic substrates, on the other hand, such as cotton and paper are found to be less photolabile, therefore, photo-oxidation of these substrates is less common [126].

Additionally, another major factor that may affect the photodegradation of dyes is the hydrophobicity of the substrate. As example, direct dyes show higher lightfastness on hydrophilic substrates (e.g., cotton) [127], whereas disperse and basic dyes are found to have higher lightfastness on hydrophobic fabrics (e.g., polyester) [72,128,129]. Both observations can be easily explained. On the one hand, hydrophilic media have a high porosity and moisture regain, thus, leading to higher levels of aggregation of hydrophobic direct dyes. Aggregation is known to improve the lightfastness of dyes, due to the reduced surface area accessible to environmental parameters that induce photodegradation, as previously mentioned in section 2.5 [130]. On the other hand, hydrophobic substrates cause a decreased rate of photofading due to the low diffusion rate of moisture to the location of the dye, an effect known as the ‘diffusion-restriction effect’ [76]. Therefore, it is evident that the mechanism of photodegradation reactions of organic dyes varies with the species of dyes and substrates and is difficult to be generalized.

### Humidity

The humidity of the environment was found to have a significant effect on the lightfastness of dyes adsorbed onto substrates. It has been shown that the fading of textile dyes and inks was faster under damp conditions, therefore, an increase in relative humidity greatly reduces the lightfastness of dyes except for colorants with high dye diffusion, which is predicted to be the case for hydrophilic dyes [50,57,70,75,76,131,132].

Ambient humidity may have a different impact depending on the paint system, i.e., oil vs. watercolor. Rader Bowers et al. [133] found that carminic acid watercolor is more affected by ambient humidity than oil paint. They suggest that this is because of higher mechanical cracking of the watercolor and increased surface area for interactions of the pigment with air. However, it may also be due to differences in absorptivity: water is clearly less absorbed by oils compared to paper. The effect of high relative humidity on oil lakes is observed as an increased formation of dicarboxylic acids and a higher degree of hydrolysis, followed by evaporation of free fatty acids [134]. Harrison et al. [135] observed an increased formation of epsomite ($MgSO_4 \cdot 7H_2O$) crystals on the surface of cadmium yellow and French ultramarine oil paints upon light exposure at 75% relative humidity. This study highlights the importance of minimizing exposure to elevated levels of light and humidity to prevent these types of degradation processes.

Giles et al. [76] demonstrated that a reduction in the relative humidity can decelerate the fading process in two ways: (i) by slowing down the access of moisture to the dye molecules, and (ii) by facilitating the breakdown of large dye aggregates. Additionally, textile fibers are known to swell due to absorbed moisture, which enables air to penetrate the intermolecular pores more readily and allowing it to participate in the photochemical reactions [136]. Therefore, the influence of humidity may be closely related with the influence of oxygen, although currently no study proves that oxidative pathways are more likely in high relative humidity environments.

Humidity is also closely associated with perspiration, which is a factor to consider for clothing textiles. In humid conditions sweat evaporates slowly due to the inability of the surrounding air to hold more water vapor. Therefore, under high humidity conditions sweat tends to accumulate more. Unfortunately, besides lower lightfastness, photochemical reactions of dyes on garments induced by perspiration could produce potentially harmful substances (e.g., aromatic amines and heavy metals), which could directly contact one's skin [137]. The extent of influence that perspiration has on the photodegradation of organic colorants depends on their molecular structure and on the pH of perspiration. Several studies were performed on the effect of perspiration on several reactive dyes on cotton fabrics, including anthraquinone, monoazo, disazo and phthalocyanine dyes. Anthraquinone reactive dyes showed the best photostability in both acidic and alkaline perspiration, whereas Cu-complex azo reactive dyes were the most photosensitive [138,139]. Furthermore, structures involving the monochlorotriazine reactive group showed high stability, whereas vinyl sulfone reactive groups were the least photostable [138]. The fading rate of chlorotriazinyl reactive dyes was higher in acidic than in alkaline perspiration; the reverse was true for vinyl sulphonyl reactive dyes [139,140]. The fading was caused by interaction with other compounds, such as L-

histidine, sodium chloride and glucose, and the pH. The effect of the pH is probably due to changes in the hydrolytic stability of the dye-fiber bonding.

### Mordants



A mordant or dye fixative is a material used to bind dyes onto fabrics by creating a coordination complex with the dye, which then attaches to the fabric. The lightfastness of organic colorants is significantly influenced by both the mordant and the mordanting method. In fact, a study on 18 yellow natural dyes concluded that the structure of the dye is not as important as the mordant in determining the lightfastness of colored textiles [141]. This may be true for structurally similar dyes, however, chemically different structures probably show more pronounced effects. The most commonly used mordants are tannic acid, certain salts of aluminum (Al), chromium (Cr), copper (Cu), Fe and tin (Sn). In general, better lightfastness can be achieved with Cr, Cu and Fe salts used as mordants, whereas a lower photostability is observed for Sn and Al salts [34,141–144]. Additionally, the mordant bath concentration and the dyeing procedure also have an influence on the lightfastness of organic dyes. In particular, the uptake by the fibers is not directly proportional to the mordant bath concentration: at high concentrations the relative amount of mordant absorbed is lower [144]. Moreover, compared to post-mordanting, the pre-mordanting method, where the substrate is first treated with the mordant and then with the dye, leads to fibers with higher amounts of metal ions, therefore stronger color hues and as a result higher lightfastness [144]. In any case, the overall stability of dyes on fabric substrates strongly depends on the stability of the formed complexes of the dye, the fiber and the mordant.

### Lake pigments

Lake pigments are pigments that are synthesized by precipitating a dye with a coordination metal also called a substrate. Both the type of the coordination metal and the metal to dye ratio can result in different colors compared to the uncoordinated dye [71,145,146]. Anselmi et al. demonstrated this in their work on geranium lakes where they studied the coloring properties of mono- and bimetallic Eosin Y lakes with Al and Pb as the coordination metal [147]. A difference in perceived hue of color means that a slight shift in the absorbance spectrum has taken place, therefore, possibly altering the photodegradation mechanism as explained in section 2.1.3. The Eosin Y-metal coordination was also proven to be different for Al or Pb [148]. This was explained by Beltran et al. who showed that Pb-lakes show unidentate or bidentate bridging coordination, while Al lakes mostly presented a bidentate bridging coordination with Eosin Y. These different interactions may determine the reactivity of the complexes, thus also their lightfastness.

The type of metal used for lake pigments may also influence oxidation behavior of the chromophores in the paint layers leading to the degradation of the substrate. This was shown by Thomas et al. who studied the photodegradation of watercolor drawings based on madder lake pigments applied on paper. They found a strong correlation between the degradation of the paper substrate and the presence and type of the coordination metal. The relationship between the metal content and the color change was less clear, although the presence of oxygen may play an important role there. The work by Liu et al. suggests that the photodegradation of iron gall ink and other iron-containing pigments is increased in the absence of oxygen, because these anaerobic conditions interrupt an important charge transfer transition from $Fe^{II}$ to $Fe^{III}$ in the coordination process with the dye [60]. However, Bowers et al. [71] showed that the photodegradation of carmine Al lakes stabilized under anaerobic conditions, which strengthens the conclusion that the effect of the coordination metal depends very much on the type and the coordination with the dye.

The paint medium, i.e., oil or watercolor, may also affect the photodegradation of lake pigments in different ways. Watercolors are known to be particularly sensitive to light, however, it was found that this is dependent on the type of mordant used [145]. Rader Bowers et al [133] compared the photodegradation of carminic acid in water solutions, and in oil and watercolor lake pigments. They found that carmine watercolors were less sensitive to oxygen than oils. Another interesting outcome of this study was that the photodegradation rate of carminic acid in solution closely resembled that of oil paints under anoxic conditions, suggesting that in-solution photodegradation could be used as a model system to study photodegradation in oil paints. The similarity in effects was attributed to the fluid nature of partially dried oil paints, representing a comparable gas permeability as in-solution degradation. It would be interesting to see whether the photodegradation mechanisms in oil and watercolor paints show the same trends amongst other dyes as well.

## 2.4 Analytical methods applied to the analysis of photodegradation products

The effect of different parameters on the photofading process of organic colorants, as well as the characterization of their degradation products can be assessed using various analytical techniques. However, the selection of the most beneficial and suitable method depends both on the application field and the aim of the study. For instance, research in the field of cultural heritage faces practical issues due to the complexity and varying levels of degradation as well as the extremely low amount of sample material available.

Furthermore, dyes and pigments used in cultural heritage objects are generally deposited on paper or textiles, therefore, minimally invasive analytical methods are required for their analysis. In contrast, studies on the photodegradation of organic dyes for the purification of wastewater are always performed in aqueous solutions and large sample volumes are usually available. Ideally, the selected analytical method should be sensitive enough to measure low concentrations of both the organic colorants and their degradation products and should also be rapid and robust to allow for the large number of measurements needed to evaluate the various parameters that affect photodegradation. Therefore, in this section the benefits and weaknesses of the most applied analytical methods are reviewed and discussed.

The assessment of color change or fading due to photodegradation is often performed using colorimetry or lightfastness test standards as is depicted in Table A-1 in Appendix A [34,46,48,49,66,68–70,72,75,76,99,126,129,138–140,142–144]. Colorimetry is a technique used to quantify a color perceived by the human eye. This is achieved by deriving spectra to physical coordinates of color perception, which correlates human color vision with wavelengths in the Vis electromagnetic spectrum. The derived spectra are then used to calculate color differences (ΔE) prior to and after photoirradiation of the colored samples, thereby facilitating the evaluation of the photofading degree. Lightfastness test standards, on the other hand, are used to assess the extent of photodegradation for dyeing of textile fabrics, plastics or other materials and manufacturing paints or printing inks. The most commonly used standards are the Blue Wool Scale, the Grey scale and the scale defined by the American Standard Test Measure (ASTM). Testing is typically performed by exposing the dye samples and the standards to controlled sunlight or artificial light generated by a Xenon arc lamp followed by a comparison among them to identify the degree of color fading. Unfortunately, both colorimetry and lightfastness test standards provide information only about the extent of color change and results may be subject to interpersonal error; additional analytical tools must be applied for acquiring data on the kinetics or the characterization of degradation products.

As it can be clearly seen from Table A-1, UV-Vis spectroscopy is the golden standard for analytically measuring the light stability of organic colorants. Most often, absorption and reflectance spectroscopy are being implemented to evaluate the effects of different parameters as the amount of light absorbed or reflected is indicative of the amount of coloring matter present in the sample. In addition, such methods are generally fast and easy to replicate. However, the absorption and reflectance spectra of organic molecules are strongly dependent upon the matrix composition and the optical absorption wavelength may shift as the chemical structure of the dye is changing during

photodegradation [47,119,120]. Other spectroscopic techniques, such as Raman, fiber optics reflectance spectroscopy (FORS) and fluorescence spectroscopy have also been applied for dye analysis, especially in works of art and cultural heritage artifacts due to their capability of acquiring structural information in a non-invasive way [65,71,110,149,150]. Nevertheless, the relatively low sensitivity of these techniques as well as the distortion of the signal caused by such complex mixtures render the identification of photodegradation and by-products extremely difficult. Additionally, even in samples with sufficiently high dye concentrations and no contaminants present, the degradation products often cannot be distinguished from the parent molecule, as they show very similar spectra. Hence, for the unambiguous identification of the degradation products, which allows for the elucidation of the mechanism of the photochemical reactions, mass spectrometry (MS) is usually a requirement. Indeed, MS provides information on the mass-to-charge ratio of both the molecular ion of the dye and its fragments, resulting in more reliable identification, while simultaneously offering very high sensitivity and selectivity. Direct MS methods, such as laser desorption ionization (LDI), matrix-assisted laser desorption ionization (MALDI), direct analysis in real-time (DART) and surface acoustic wave nebulization (SAWN) have been implemented as straightforward tools for the characterization of organic colorants on textiles and paper [50,98,151–154]. These techniques are minimally invasive due to the small sample sizes, require limited sample pre-treatment, and allow for the rapid determination of photodegradation products. Nevertheless, the lack of separation prior to the introduction of the sample in the MS leads to very complex mass spectra and may induce severe ion suppression effects, thus obstructing proper identification. To overcome these issues, separation techniques such as liquid chromatography (LC), gas chromatography (GC) or capillary electrophoresis (CE) coupled to MS have been extensively applied [51,58,65,71,114,124,144,155]. Most natural and synthetic colorants are non-volatile organic compounds; therefore, GC methods have rarely been implemented, due to the extra time-consuming derivatization step required for their analysis, even though excellent repeatability and reproducibility can be achieved [156]. On the contrary, CE and especially LC techniques constitute the most exploited separation methods for dye analysis. CE provides high resolution analysis while requiring very small sample sizes and low running costs, whereas LC-MS is a very robust combination that allows for the reliable characterization of almost any complex mixture. However, these separation techniques require that the analytes are extracted from the original materials using a solvent, which ideally should not intervene with the photodegradation process of the organic colorants.

Considering the advantages and disadvantages of the various analytical tools currently available, it becomes clear that a complete light-induced degradation study of organic colorants must incorporate complementary analytical techniques. Indeed, a more recent approach combines spectral information with MS data to achieve a better understanding of the photodegradation process [50,58,65,71,98,110,113,124,157,158]. This way the advantages of the two methods are enhanced, leading to more reliable results. An example of this approach can be found in the implementation of LC coupled to both photodiode array detection (DAD) and electrospray ionization MS (ESI-MS) [113]. DAD allows for the simultaneous acquisition of multiple absorbance spectra across the UV to Vis wavelength range, rendering it very efficient for light absorbing samples. The application of LC hyphenated with a combination of DAD and MS as detection systems led to improved separation of similar sample components and increased the detection limit, resulting in a more comprehensive understanding of the dye compositions. We have shown an example of such hyphenated systems for studying photodegradation mechanisms in a previously published article where a light reactor cell based on a liquid core waveguide (LCW) with in situ absorption spectroscopy was coupled on-line to LC-DAD [107]. Later, the same light reactor cell was coupled to 2D-LC, where the first LC separation was used to separate and isolate Riboflavin from a multivitamin B complex inside the light reactor cell, after which the degradation products of the light exposed Riboflavin were subjected to the second LC separation with DAD detection [159].

## 2.5 Discussion and conclusions

Degradation by light is a ubiquitous phenomenon that affects a wide range of materials, organic colorants being among them. A more comprehensive understanding of the photodegradation process is needed with the constant development of new synthetic dyes. In the present literature study, we have extensively reviewed the influence of different experimental and environmental parameters on the photodegradation of organic colorants across a variation of work fields. The wide variety of parameters and structurally different organic colorants that are evaluated under different experimental conditions applied in each study make it extremely difficult to render reliable comparisons. Additionally, most photodegradation studies focused on the effect of a limited number of parameters on a selection of organic dyes and pigments. We did not find a single study taking into consideration the entirety of the different parameters that influence photodegradation on a wide range of structurally different organic colorants. Such a study – even though rather complex – could allow for more universally applicable conclusions and a more complete understanding of the photofading process.

Based on the currently available literature, several conclusions can be drawn concerning the effect of the different parameters affecting the photodegradation process:

- An increase in the dose (intensity*time) leads to more pronounced photodegradation due to a higher photon input. The effect of the wavelength is associated with the structure of the dye and the absorption spectrum of the absorbing photosensitizer, catalyst or dye and has a strong influence on the mechanism of the photochemical reactions taking place.

- Oxygen is of paramount importance, as it strongly affects the pathways of the photodegradation reaction. A decrease in oxygen concentration usually leads to lower photofading effects, however, the extent of influence is closely related with the chemical structure of the dye and the matrix. In situations where $^3D^*$ is quenched by oxygen to create $^1O_2$ the photofading rate may actually decrease under aerobic conditions (e.g., Riboflavin).

- Temperature increase influences the photofading efficiency of organic colorants, however, to a lower extent compared to other parameters. A rise in temperature may reduce the degree of photodegradation by reducing the moisture content of the substrate or increase the degradation rate by breaking down dye aggregates, providing more surface area for irradiation. In solution an increased temperature may lead to more movement, thus higher kinetic energy of the dye molecules, leading to faster reaction rates, while photocatalysis is preferred at lower temperatures since this increases adsorption to the catalyst's surface, although this strongly depends on the photocatalytic activity of the catalyst.

- In heterogeneous photocatalytic systems, enriched photocatalysts show higher catalytic activity compared to single-component materials. There is an optimum amount of catalyst that leads to higher photodegradation efficiencies and increased reaction rates.

- A rise in dye concentration leads to aggregated dye molecules adsorbed onto substrate matrices, which reduces photofading. Increased dye concentrations result in more pronounced dye-dye interactions in the absence of a catalytic system, however, it also results in more absorption at the surface, meaning that less light reaches deeper lying molecules. In-solution photocatalytic degradation is also impeded by an in increase in dye concentration.

- Dye photodegradation in solution is not always identical with dye photodegradation on a substrate as the reaction mechanisms may differ. The rate of photochemical reactions in solution is usually greater than that on substrate, because of the

increased mobility of e.g., dye molecules, catalysts and oxygen and due to the fact that the light distribution in a solution is more homogenic assuming proper mixing.

- The effect of solvent is strongly associated with the structure of the dye. Both the type of solvent and the pH can affect or temporarily change the chemical structure of the dye, thereby altering its susceptibility towards light. Solvents such as DMSO may also act as oxidizing agents. The effect of the pH is mostly dependent on the pKa of the dye or pigment.

- The type of substrate has a strong influence on the photochemical reactions taking place. Where proteinaceous substrates mostly lead to reduction processes, non-proteinaceous substrates favor oxidation reactions. A rise in relative humidity promotes photodegradation and might also be closely related to the influence of oxygen, whereas mordants improve the lightfastness of organic colorants on solid substrates. On the other hand, mordants or metals present in lake pigments may act as photocatalysts or oxidizing agents, which increases the photofading process.

Regarding the analytical methods that have been implemented for the assessment of the effect of the different parameters, a clear trend was observed. The use of MS for the identification of the photodegradation products, as well as the incorporation of separation techniques, such as LC, which allow for the chemical analysis of complex mixtures, have become increasingly popular in recent years. An even more recent approach combines the advantages of two orthogonal techniques, thereby leading to an improved understanding of the photofading process [158]. Other approaches often include spectroscopic techniques, colorimetry, and lightfastness test standards, which are relatively easy to implement, but provide less specific information. Hence, further work in this field could focus on the simultaneous evaluation of the influencing factors and the characterization of the degradation products, which allow for the more detailed elucidation of the photochemical processes.

# References

[1] B.P. DiMento, R.P. Mason, Factors controlling the photochemical degradation of methylmercury in coastal and oceanic waters, Mar Chem. 196 (2017) 116. https://doi.org/10.1016/J.MARCHEM.2017.08.006.

[2] B. Kobin, S. Behren, B. Braun-Cula, S. Hecht, Photochemical Degradation of Various Bridge-Substituted Fluorene-Based Materials, Journal of Physical Chemistry A. 120 (2016) 5474–5480. https://pubs.acs.org/doi/full/10.1021/acs.jpca.6b02127 (accessed July 28, 2022).

[3] R.-M. Ion, A. Nuta, A.-A. Sorescu, L. Iancu, Photochemical Degradation Processes of Painting Materials from Cultural Heritage, Photochemistry and Photophysics - Fundamentals to Applications. (2018). https://doi.org/10.5772/INTECHOPEN.76169.

[4] W. Hu, D. Liu, S. Su, L. Ren, H. Ren, L. Wei, S. Yue, Q. Xie, Z. Zhang, Z. Wang, N. Yang, L. Wu, J. Deng, Y. Qi, P. Fu, Photochemical Degradation of Organic Matter in the Atmosphere, Adv Sustain Syst. 5 (2021) 2100027. https://doi.org/10.1002/ADSU.202100027.

[5] K.O. Gorshkova, I.I. Tumkin, L.A. Myund, A.S. Tverjanovich, A.S. Mereshchenko, M.S. Panov, V.A. Kochemirovsky, The investigation of dye aging dynamics in writing inks using Raman spectroscopy, Dyes and Pigments. 131 (2016) 239–245. https://doi.org/10.1016/j.dyepig.2016.04.009.

[6] P.I. Hora, P.J. Novak, W.A. Arnold, Photodegradation of pharmaceutical compounds in partially nitritated wastewater during UV irradiation, Environ Sci (Camb). 5 (2019) 897–909. https://doi.org/10.1039/c8ew00714d.

[7] A. Micheluz, E.M. Angelin, J.A. Lopes, M.J. Melo, M. Pamplona, Discoloration of Historical Plastic Objects: New Insight into the Degradation of β-Naphthol Pigment Lakes, Polymers 2021, Vol. 13, Page 2278. 13 (2021) 2278. https://doi.org/10.3390/POLYM13142278.

[8] J. Verduin, Photodegradation Products And Their Analysis In Food, Food Sci Nutr. 6 (2020) 1–16. https://doi.org/10.24966/FSN-1076/100067.

[9] V. Andrisano, R. Gotti, A. Leoni, V. Cavrini, Photodegradation studies on Atenolol by liquid chromatography, J Pharm Biomed Anal. 21 (1999) 851–857. https://doi.org/10.1016/S0731-7085(99)00223-X.

[10] V. Andrisano, R. Ballardini, P. Hrelia, N. Cameli, A. Tosti, R. Gotti, V. Cavrini, Studies on the photostability and in vitro phototoxicity of Labetalol, Eur J Pharm Sci. 12 (2001) 495–504. https://doi.org/10.1016/S0928-0987(00)00218-9.

[11] X.Z. Li, M. Zhang, Decolorization and biodegradability of dyeing wastewater treated by a TiO2-sensitized photo-oxidation process, Water Science and Technology. 34 (1996) 49–55. https://doi.org/10.1016/S0273-1223(96)00786-X.

[12] L. Monico, K. Janssens, E. Hendriks, F. Vanmeert, G. van der Snickt, M. Cotte, G. Falkenberg, B.G. Brunetti, C. Miliani, Evidence for Degradation of the Chrome Yellows in Van Gogh's Sunflowers: A Study Using Noninvasive In Situ Methods and Synchrotron-Radiation-Based X-ray Techniques,

Angewandte Chemie International Edition. 54 (2015) 13923–13927. https://doi.org/10.1002/ANIE.201505840.

[13] A.T. Peters, H.S. Freeman, Physico-Chemical Prinsiples of Color Chemistry, Blackie Academic & Professional, 1996.

[14] C. Michelin, N. Hoffmann, Photosensitization and Photocatalysis - Perspectives in Organic Synthesis, ACS Catal. 8 (2018) 12046–12055. https://doi.org/https://doi.org/10.1021/acscatal.8b03050.

[15] H.C.A. Van Beek, P.M. Heertjes, Fading by light of organic dyes on textiles and other materials, Studies in Conservation. 11 (1966) 123–132. https://doi.org/10.1179/sic.1966.016.

[16] F. Vázquez-Ortega, I. Lagunes, Á. Trigos, Cosmetic dyes as potential photosensitizers of singlet oxygen generation, Dyes and Pigments. 176 (2020) 108248. https://doi.org/10.1016/J.DYEPIG.2020.108248.

[17] C.H. Wu, C.L. Chang, Decolorization of Reactive Red 2 by advanced oxidation processes: Comparative studies of homogeneous and heterogeneous systems, J Hazard Mater. 128 (2006) 265–272. https://doi.org/10.1016/j.jhazmat.2005.08.013.

[18] M. Dell'Edera, C. lo Porto, I. de Pasquale, F. Petronella, M.L. Curri, A. Agostiano, R. Comparelli, Photocatalytic TiO2-based coatings for environmental applications, Catal Today. 380 (2021) 62–83. https://doi.org/10.1016/J.CATTOD.2021.04.023.

[19] P. Karlsson, A.E.C. Palmqvist, K. Holmberg, Surface modification for aluminium pigment inhibition, Adv Colloid Interface Sci. 128–130 (2006) 121–134. https://doi.org/10.1016/J.CIS.2006.11.010.

[20] M. Müller, J.C. Villalba, F.Q. Mariani, M. Dalpasquale, M.Z. Lemos, M.F.G. Huila, F.J. Anaissi, Synthesis and characterization of iron oxide pigments through the method of the forced hydrolysis of inorganic salts, Dyes and Pigments. 120 (2015) 271–278. https://doi.org/10.1016/J.DYEPIG.2015.04.026.

[21] I. Ahmad, Q. Fasihullah, F.H.M. Vaid, Effect of light intensity and wavelengths on photodegradation reactions of Riboflavin in aqueous solution, J Photochem Photobiol B. 82 (2006) 21–27. https://doi.org/10.1016/j.jphotobiol.2005.08.004.

[22] M.A. Jamal, M. Muneer, M. Iqbal, Photo-degradation of monoazo dye blue 13 using advanced oxidation process, Chemistry International. 1 (2015) 12–16. https://doi.org/10.31221/osf.io/dq46r.

[23] H. Li, Z. Xiong, X. Dai, Q. Zeng, The effect of perspiration on photo-induced chemical reaction of azo dyes and the determination of aromatic amine products, Dyes and Pigments. 94 (2012) 55–59. https://doi.org/10.1016/j.dyepig.2011.11.006.

[24] J.K.G. Karlsson, O.J. Woodford, R. Al-Aqar, A. Harriman, Effects of Temperature and Concentration on the Rate of Photobleaching of Erythrosine in Water, Journal of Physical Chemistry A. 121 (2017) 8569–8576. https://doi.org/10.1021/acs.jpca.7b06440.

[25] L. Lachman, C.J. Swartz, T. Urbanyi, J. Cooper, Color Stability of Tablet Formulations II: Influence of Light Intensity on the Fading of Several Water-Soluble Dyes, Journal of the American Pharmaceutical Association (Scientific Ed.). 49 (1960) 165–169. https://doi.org/10.1002/JPS.3030490312.

[26] F.W. Goodhart, H.A. Lieberman, D.S. Mody, F.C. Ninger, Stability of Certified Dyes in Tablets III, J Pharm Sci. 56 (1967) 63–67. https://doi.org/10.1002/JPS.2600560113.

[27] G. Gauglitz, Photophysical, Photochemical and Photokinetic Properties of Photochromic Systems, Photochromism: Molecules and Systems. (2003) 15–63. https://doi.org/10.1016/B978-044451322-9/50006-3.

[28] B. Neppolian, H.C. Choi, S. Sakthivel, B. Arabindoo, V. Murugesan, Solar/UV-induced photocatalytic degradation of three commercial textile dyes, J Hazard Mater. 89 (2002) 303–317. https://doi.org/10.1016/S0304-3894(01)00329-6.

[29] C.C. Liu, Y.H. Hsieh, P.F. Lai, C.H. Li, C.L. Kao, Photodegradation treatment of azo dye wastewater by UV/TiO2 process, Dyes and Pigments. 68 (2006) 191–195. https://doi.org/10.1016/j.dyepig.2004.12.002.

[30] V.K. Gupta, R. Jain, A. Nayak, S. Agarwal, M. Shrivastava, Removal of the hazardous dye-Tartrazine by photodegradation on titanium dioxide surface, Materials Science and Engineering C. 31 (2011) 1062–1067. https://doi.org/10.1016/j.msec.2011.03.006.

[31] C.M. So, M.Y. Cheng, J.C. Yu, P.K. Wong, Degradation of azo dye Procion Red MX-5B by photocatalytic oxidation, Chemosphere. 46 (2002) 905–912. https://doi.org/10.1016/S0045-6535(01)00153-9.

[32] J. Chanathaworn, C. Bunyakan, W. Wiyaratn, J. Chungsiriporn, Photocatalytic decolorization of basic dye by TiO2 nanoparticle in photoreactor, Songklanakarin Journal of Science and Technology. 34 (2012) 203–210.

[33] D.F. Ollis, E. Pelizzetti, N. Serpone, Photocatalyzed destruction of water contaminants, Environ Sci Technol. 25 (1991) 1522–1529. https://doi.org/10.1021/es00021a001.

[34] N. Kohara, C. Sano, Y. Magoshi, M.A. Becker, M. Yatagai, M. Saito, Degradation and Color Fading of Cotton Fabrics Dyed with Natural Dyes and Mordants, ACS Symposium Series. (2001) 74–85. https://doi.org/10.1021/bk-2001-0779.ch006.

[35] D. Saunders, J. Kirby, Light-induced Colour Changes in Red and Yellow Lake Pigments, 15 (1994) 79–97.

[36] R.L. Feller, Control of deteriorating effects of light upon museum objects, Museum International. 17 (1964) 57–98. https://doi.org/10.1111/j.1468-0033.1964.tb01570.x.

[37] D.G. Duff, R.S. Sinclair, D. Stirling, Light-induced Colour Changes of Natural Dyes, Https://Doi.Org/10.1179/Sic.1977.020. (1977) 161–169. https://doi.org/10.1179/SIC.1977.020.

[38] P.M. Whitmore, X. Pan, C. Bailie, Predicting The Fading of Objects: Identification of Fugitive Colorants Through Direct Nondestructive Lightfastness Measurements, Journal of the American Institute for Conservation. 38 (1999) 395–409. https://doi.org/10.1179/019713699806113420.

[39] P.M. Whitmore, C. Bailie, S.A. Connors, Micro-fading tests to predict the result of exhibition: progress and prospects, Studies in Conservation. 45 (2000) 200–205. https://doi.org/10.1179/SIC.2000.45.SUPPLEMENT-1.200.

[40] C. Pesme, A. Lerwill, V. Beltran, J. Druzik, Development of Contact Portable Microfade Tester to Assess Light Sensitivity of Collection Items, Journal of the American Institute for Conservation. 55 (2016) 117–137. https://doi.org/10.1080/01971360.2016.1154430.

[41] G. Patin, R.G. Erdmann, F. Ligterink, J.G. Neevel, K.J. van den Berg, E. Hendriks, An enhanced optical micro-fading device, J Cult Herit. 57 (2022) 276–285. https://doi.org/10.1016/J.CULHER.2022.08.012.

[42] V.L. Beltran, C. Pesme, S.K. Freeman, M. Benson, Microfading Tester - Light Sensitivity Assessment and Role in Lighting Policy, Los Angeles, 2021.

[43] A. Lerwill, C. Pesme, V. Beltran, J. Druzik, Investigating the Validity of Microfading Spectroscopy to Predict Photochemically Induced Color Change at Lower Light Levels, in: NIP & Digital Fabrication Conference, Portland: Society for Imaging Science and Technology, 2015: pp. 123–128.

[44] V. Beltran, J. Druzik, A. Lerwill, C. Pesme, An Examination of Light-Induced Color Change in Anoxia and Hypoxia Using the Microfading Tester, in: Research and Technical Studies Group Postprints, AIC Annual Meeting, San Francisco, 2014.

[45] J.M. Del Hoyo-Meléndez, M.F. Mecklenburg, An investigation of the reciprocity principle of light exposures using microfading spectrometry, Spectroscopy Letters. 44 (2011) 52–62. https://doi.org/10.1080/00387010903508572.

[46] K. McLaren, The Spectral Regions of Daylight which cause Fading, in: F.T.C.C. PUBLICATTON XVII, 1956.

[47] L. Jespersen, L.D. Strømdahl, K. Olsen, L.H. Skibsted, Heat and light stability of three natural blue colorants for use in confectionery and beverages, European Food Research and Technology. 220 (2005) 261–266. https://doi.org/10.1007/s00217-004-1062-7.

[48] K. Jørgensen, L.H. Skibsted, Light sensitivity of cochineal. Quantum yields for photodegradation of carminic acid and conjugate bases in aqueous solution, Food Chem. 40 (1991) 25–34. https://doi.org/10.1016/0308-8146(91)90016-H.

[49] H. Hattori, K. Yoshizumi, P.C. Crews, Wavelength sensitivity of AATCC Blue wool lightfastness standards under light radiation, Dyes and Pigments. 92 (2012) 936–941. https://doi.org/10.1016/j.dyepig.2011.05.015.

[50] C. Weyermann, D. Kirsch, C. Costa-Vera, B. Spengler, Photofading of ballpoint dyes studied on paper by LDI and MALDI MS, J Am Soc Mass Spectrom. 17 (2006) 297–306. https://doi.org/10.1016/j.jasms.2005.11.010.

[51] A.R. Fischer, P. Werner, K.U. Goss, Photodegradation of malachite green and malachite green carbinol under irradiation with different wavelength ranges, Chemosphere. 82 (2011) 210–214. https://doi.org/10.1016/j.chemosphere.2010.10.019.

[52] M.J. Melo, P. Nabais, M. Vieira, R. Araújo, V. Otero, J. Lopes, L. Martín, Between past and future: Advanced studies of ancient colours to safeguard cultural heritage and new sustainable applications, Dyes and Pigments. 208 (2022) 110815. https://doi.org/10.1016/J.DYEPIG.2022.110815.

[53] E. Guerra, F. Gosetti, E. Marengo, M. Llompart, C. Garcia-Jares, Study of photostability of three synthetic dyes commonly used in mouthwashes, Microchemical Journal. 146 (2019) 776–781. https://doi.org/10.1016/J.MICROC.2019.02.002.

[54] C. Harsito, A.R. Prabowo, S.D. Prasetyo, Z. Arifin, Enhancement stability and color fastness of natural dye: A review, Open Engineering. 11 (2021) 548–555. https://doi.org/10.1515/ENG-2021-0055/MACHINEREADABLECITATION/RIS.

[55] S. Aliouche, K. Djebbar, T. Sehili, Removal of an azo dye (Alizarin yellow) in homogeneous medium using direct photolysis, acetone/UV, H2O2/UV, /UV, H2O2//UV, and /heat, Desalination Water Treat. 57 (2016) 18182–18193. https://doi.org/10.1080/19443994.2015.1090915.

[56] M.A. Rauf, S. Hisaindee, J.P. Graham, M. Nawaz, Solvent effects on the absorption and fluorescence spectra of Cu(II)-phthalocyanine and DFT calculations, J Mol Liq. 168 (2012) 102–109. https://doi.org/10.1016/J.MOLLIQ.2012.01.008.

[57] S.N. Batchelor, D. Carr, C.E. Coleman, L. Fairclough, A. Jarvis, The photofading mechanism of commercial reactive dyes on cotton, Dyes and Pigments. 59 (2003) 269–275. https://doi.org/10.1016/S0143-7208(03)00118-9.

[58] A. Alvarez-Martin, S. Trashin, M. Cuykx, A. Covaci, K. De Wael, K. Janssens, Photodegradation mechanisms and kinetics of Eosin-Y in oxic and anoxic conditions, Dyes and Pigments. 145 (2017) 376–384. https://doi.org/10.1016/j.dyepig.2017.06.031.

[59] M.M. Sousa, C. Miguel, I. Rodrigues, A.J. Parola, F. Pina, J.S. Seixas De Melo, M.J. Melo, A photochemical study on the blue dye indigo: from solution to ancient Andean textiles, Photochemical & Photobiological Sciences. 7 (2008) 1353–1359. https://doi.org/10.1039/B809578G.

[60] Y. Liu, T. Fearn, M. Strlič, Photodegradation of iron gall ink affected by oxygen, humidity and visible radiation, Dyes and Pigments. 198 (2022) 109947. https://doi.org/10.1016/J.DYEPIG.2021.109947.

[61] J.S. Arney, A.J. Jacobs, R. Newman, The Influence of Oxygen on the Fading of Organic Colorants, Journal of the American Institute for Conservation. 18 (1979) 108–117. https://doi.org/10.1179/019713679806029020.

[62] H. Stapelfeldt, H. Jun, L.H. Skibsted, Fluorescence properties of carminic acid in relation to aggregation, complex formation and oxygen activation in aqueous food models, Food Chem. 48 (1993) 1–11. https://doi.org/10.1016/0308-8146(93)90213-Y.

[63] S. Nakagawa, K. Sakakibara, H. Gotoh, Novel degradation mechanism for triarylmethane dyes: Acceleration of degradation speed by the attack of active oxygen to halogen groups, Dyes and Pigments. 124 (2016) 130–132. https://doi.org/10.1016/j.dyepig.2015.09.006.

[64] C. Clementi, W. Nowik, A. Romani, F. Cibin, G. Favaro, A spectrometric and chromatographic approach to the study of ageing of madder (Rubia tinctorum L.) dyestuff on wool, Anal Chim Acta. 596 (2007) 46–54. https://doi.org/10.1016/j.aca.2007.05.036.

[65] H.Y. Jiang, X.D. Hu, J.J. Zhu, J. Wan, J.B. Yao, Studies on the photofading of alizarin, the main component of madder, Dyes and Pigments. 185 (2021). https://doi.org/10.1016/j.dyepig.2020.108940.

[66] C. Korenberg, The photo-ageing behaviour of selected watercolour paints under anoxic conditions, The British Museum: Technical Research Bulletin. 2 (2008) 49–57.

[67] L. Casella, M. Tsukada, Effects of low-oxygen environments in the light fading of six dyes present in the autochrome color screen, Journal of the American Institute for Conservation. 51 (2012) 159–174. https://doi.org/10.1179/019713612804860392.

[68] V.L. Beltran, J. Druzik, S. Maekawa, Large-scale assessment of light-induced color change in air and anoxic environments, Studies in Conservation. 57 (2012) 42–57. https://doi.org/10.1179/2047058411Y.0000000006.

[69] A. Lerwill, J.H. Townsend, J. Thomas, S. Hackney, C. Caspers, H. Liang, Photochemical colour change for traditional watercolour pigments in low oxygen levels, Studies in Conservation. 60 (2015) 15–32. https://doi.org/10.1179/2047058413Y.0000000108.

[70] M. Saito, C. Minemura, N. Nanashima, M. Kashiwagi, Color Fading Behavior of Anthraquinone Dyes Due to Environmental Conditions, Textile Research Journal. 58 (1988) 450–454. https://doi.org/10.1177/004051758805800804.

[71] L.M. Rader Bowers, S.J. Schmidtke Sobeck, Impact of medium and ambient environment on the photodegradation of carmine in solution and paints, Dyes and Pigments. 127 (2016) 18–24. https://doi.org/10.1016/J.DYEPIG.2015.12.012.

[72] G. Schwen, G. Schmidt, Some Experiments on the Effect of Dye, Fibre, and Atmosphere on Light Fastness, Journal of the Society of Dyers and Colourists. 75 (1959) 101–105. https://doi.org/10.1111/j.1478-4408.1959.tb02314.x.

[73] B.E. Blaisdell, The Photochemistry of Aromatic Azo Compounds in Organic Solvents, Journal of the Society of Dyers and Colourists. 65 (1949) 618–628. https://doi.org/10.1111/J.1478-4408.1949.TB02539.X.

[74] H. Kühn, The effect of oxygen, relative humidity and temperature on the fading rate of watercolors. reduced light-damage in a nitrogen atmosphere., Studies in Conservation. 12 (1967) 79–88. https://doi.org/10.1179/sic.1967.12.s1.011.

[75] K. McLaren, The Importance of Temperature and Relative Humidity in Light-fastness Testing, Journal of the Society of Dyers and Colourists. (1956) 527–537. https://doi.org/10.1111/j.1478-4408.1962.tb02457.x.

[76] C.H. Giles, G. Baxter, S.M.K. Rahman, Studies of High Fastness to Light in Coloring Matters in Hydrophilic Substrates, Http://Dx.Doi.Org/10.1177/004051756103101001. 31 (1961) 831–844. https://doi.org/10.1177/004051756103101001.

[77] N.A.M. Barakat, M.A. Kanjwal, I.S. Chronakis, H.Y. Kim, Influence of temperature on the photodegradation process using Ag-doped TiO2 nanostructures: Negative impact with the nanofibers, J Mol Catal A Chem. 366 (2013) 333–340. https://doi.org/10.1016/j.molcata.2012.10.012.

[78] Z. Shams-Ghahfarokhi, A. Nezamzadeh-Ejhieh, As-synthesized ZSM-5 zeolite as a suitable support for increasing the photoactivity of semiconductors in a typical photodegradation process, Mater Sci Semicond Process. 39 (2015) 265–275. https://doi.org/10.1016/j.mssp.2015.05.022.

[79] S. Mozia, A.W. Morawski, M. Toyoda, M. Inagaki, Application of anatase-phase TiO2 for decomposition of azo dye in a photocatalytic membrane reactor, Desalination. 241 (2009) 97–105. https://doi.org/10.1016/j.desal.2007.12.048.

[80] E.T. Soares, M.A. Lansarin, C.C. Moro, A study of process variables for the photocatalytic degradation of rhodamine B, Brazilian Journal of Chemical Engineering. 24 (2007) 29–36. https://doi.org/10.1590/S0104-66322007000100003.

[81] S. Zhou, A.K. Ray, Kinetic Studies for Photocatalytic Degradation of Eosin B on a Thin Film of Titanium Dioxide, Ind Eng Chem Res. 42 (2003) 6020–6033. https://doi.org/10.1021/ie030366v.

[82] Y.H. Chiu, T.F.M. Chang, C.Y. Chen, M. Sone, Y.J. Hsu, Mechanistic insights into photodegradation of organic dyes using heterostructure photocatalysts, Catalysts. 9 (2019). https://doi.org/10.3390/catal9050430.

[83] J.-M. Herrmann, Heterogeneous photocatalysis: fundamentals and applications to the removal of various types of aqueous pollutants, Catal Today. 53 (1999) 115–129. https://doi.org/10.1115/IMECE200743738.

[84] M. Naushad, G. Sharma, Z.A. Alothman, Photodegradation of toxic dye using Gum Arabic-crosslinked-poly(acrylamide)/Ni(OH)2/FeOOH nanocomposites hydrogel, J Clean Prod. 241 (2019) 118263. https://doi.org/10.1016/j.jclepro.2019.118263.

[85] S. Sakthivel, B. Neppolian, M. V. Shankar, B. Arabindoo, M. Palanichamy, V. Murugesan, Solar photocatalytic degradation of azo dye: Comparison of photocatalytic efficiency of ZnO and TiO2, Solar Energy Materials and Solar Cells. 77 (2003) 65–82. https://doi.org/10.1016/S0927-0248(02)00255-6.

[86] K. Saeed, I. Khan, T. Gul, M. Sadiq, Efficient photodegradation of methyl violet dye using TiO2/Pt and TiO2/Pd photocatalysts, Appl Water Sci. 7 (2017) 3841–3848. https://doi.org/10.1007/s13201-017-0535-3.

[87] C. Lizama, J. Freer, J. Baeza, H.D. Mansilla, Optimized photodegradation of reactive blue 19 on TiO2 and ZnO suspensions, Catal Today. 76 (2002) 235–246. https://doi.org/10.1016/S0920-5861(02)00222-5.

[88] N. Daneshvar, D. Salari, A.R. Khataee, Photocatalytic degradation of azo dye acid red 14 in water on ZnO as an alternative catalyst to TiO2, J Photochem Photobiol A Chem. 162 (2004) 317–322. https://doi.org/10.1016/S1010-6030(03)00378-2.

[89] S.K. Kansal, M. Singh, D. Sud, Studies on photodegradation of two commercial dyes in aqueous phase using different photocatalysts, J Hazard Mater. 141 (2007) 581–590. https://doi.org/10.1016/j.jhazmat.2006.07.035.

[90] D. Zheng, L. Yu, W. Liu, X. Dai, X. Niu, W. Fu, W. Shi, F. Wu, X. Cao, Structural advantages and enhancement strategies of heterostructure water-splitting electrocatalysts, Cell Rep Phys Sci. 2 (2021) 100443. https://doi.org/10.1016/J.XCRP.2021.100443.

[91] Z.M. El-Bahy, A.A. Ismail, R.M. Mohamed, Enhancement of titania by doping rare earth for photodegradation of organic dye (Direct Blue), J Hazard Mater. 166 (2009) 138–143. https://doi.org/10.1016/j.jhazmat.2008.11.022.

[92] E. Alzahrani, Photodegradation of Eosin y Using Silver-Doped Magnetic Nanoparticles, Int J Anal Chem. 2015 (2015). https://doi.org/10.1155/2015/797606.

[93] D.R. Paul, R. Sharma, P. Panchal, R. Malik, A. Sharma, V.K. Tomer, S.P. Nehra, Silver Doped Graphitic Carbon Nitride for the Enhanced Photocatalytic Activity Towards Organic Dyes, J Nanosci Nanotechnol. 19 (2019) 5241–5248. https://doi.org/10.1166/jnn.2019.16838.

[94] E.M. Saggioro, A.S. Oliveira, T. Pavesi, C.G. Maia, L.F.V. Ferreira, J.C. Moreira, Use of titanium dioxide photocatalysis on the remediation of model textile wastewaters containing azo dyes, Molecules. 16 (2011) 10370–10386. https://doi.org/10.3390/molecules161210370.

[95] D.R. Paul, R. Sharma, S.P. Nehra, A. Sharma, Effect of calcination temperature, pH and catalyst loading on photodegradation efficiency of urea derived graphitic carbon nitride towards methylene blue dye solution, RSC Adv. 9 (2019) 15381–15391. https://doi.org/10.1039/c9ra02201e.

[96] N. Soltani, E. Saion, M.Z. Hussein, M. Erfani, A. Abedini, G. Bahmanrokh, M. Navasery, P. Vaziri, Visible light-induced degradation of methylene blue in the presence of photocatalytic ZnS and CdS nanoparticles, Int J Mol Sci. 13 (2012) 12242–12258. https://doi.org/10.3390/ijms131012242.

[97] M.R. Sohrabi, M. Ghavami, Photocatalytic degradation of Direct Red 23 dye using UV/TiO2: Effect of operational parameters, J Hazard Mater. 153 (2008) 1235–1239. https://doi.org/10.1016/j.jhazmat.2007.09.114.

[98] C. Weyermann, D. Kirsch, C. Costa Vera, B. Spengler, Evaluation of the photodegradation of crystal violet upon light exposure by mass spectrometric and spectroscopic methods, J Forensic Sci. 54 (2009) 339–345. https://doi.org/10.1111/j.1556-4029.2008.00975.x.

[99] F.M. Tera, E.M. Osman, S.F. Ibrahim, M.N. Michael, Quantification of the light fastness of colored substrates by applying fading rate constant values, Egypt J Chem. 59 (2016) 1012–1027. https://doi.org/10.21608/ejchem.2016.1556.

[100] A.L. Forster, J.L. Bitter, S. Rosenthal, S. Brooks, S.S. Watson, Photofading in cotton fibers dyed using red, yellow, and blue direct dyes during examination with microspectrophotometry (MSP), Forensic Chemistry. 5 (2017) 72–78. https://doi.org/10.1016/j.forc.2017.06.006.

[101] N.S. Allen, M. Ledward, G.W. Follows, Photooxidation and stabilisation of mixed acid dyed nylon 6,6 film and fibres: influence of thermal history, delustrant and relationship with luminescent species, Polym Degrad Stab. 38 (1992) 95–105. https://doi.org/10.1016/0141-3910(92)90001-L.

[102] R. Pardo, M. Zayat, D. Levy, Effect of the chemical environment on the light-induced degradation of a photochromic dye in ormosil thin films, J Photochem Photobiol A Chem. 198 (2008) 232–236. https://doi.org/10.1016/j.jphotochem.2008.03.013.

[103] B. Neppolian, H.C. Choi, S. Sakthivel, B. Arabindoo, V. Murugesan, Solar light induced and TiO2 assisted degradation of textile dye reactive blue 4, Chemosphere. 46 (2002) 1173–1181. https://doi.org/10.1016/S0045-6535(01)00284-3.

[104] R.J. Davis, J.L. Gainer, G. O'Neal, I.-W. Wu, Photocatalytic decolorization of wastewater dyes, Water Environment Research. 66 (1994) 50–53. https://doi.org/10.2175/WER.66.1.8.

[105] K.M. Reza, A. Kurny, F. Gulshan, Parameters affecting the photocatalytic degradation of dyes using TiO2: a review, Appl Water Sci. 7 (2017) 1569–1578. https://doi.org/10.1007/s13201-015-0367-y.

[106] Y.S. Keum, J.H. Kim, Q.X. Li, Relationship between Singlet Oxygen Formation and Photolysis of Phloxine B in Aqueous Solutions, Journal of Photoscience. 10 (2003) 219–223.

[107] I. Groeneveld, I. Bagdonaite, E. Beekwilder, F. Ariese, G.W. Somsen, M.R. van Bommel, Liquid Core Waveguide Cell with In Situ Absorbance Spectroscopy and Coupled to Liquid Chromatography for Studying Light-Induced Degradation, Anal Chem. 94 (2022) 7647–7654. https://doi.org/10.1021/acs.analchem.2c00886.

[108] J. Oakes, S.N. Batchelor, S. Dixon, Azo dye location in textiles: A novel UV-vis approach, Coloration Technology. 121 (2005) 237–244. https://doi.org/10.1111/j.1478-4408.2005.tb00279.x.

[109] L.C. Abbott, S.N. Batchelor, L. Jansen, J. Oakes, J.R. Lindsay Smith, J.N. Moore, Spectroscopic studies of Direct Blue 1 in solution and on cellulose surfaces: effects of environment on a bis-azo dye, New Journal of Chemistry. 28 (2004) 815–821. https://doi.org/10.1039/B401055H.

[110] D. Confortin, H. Neevel, M. Brustolon, L. Franco, A.J. Kettelarij, R.M. Williams, M.R. Van Bommel, Crystal violet: Study of the photo-fading of an early synthetic dye in aqueous solution and on paper with HPLC-PDA, LC-MS and FORS, J Phys Conf Ser. 231 (2010). https://doi.org/10.1088/1742-6596/231/1/012011.

[111] L.C. Abbott, S.N. Batchelor, J.R. Lindsay Smith, J.N. Moore, Reductive reaction mechanisms of the Azo Dye Orange II in aqueous solution and in cellulose: From radical intermediates to products, Journal of Physical Chemistry A. 113 (2009) 6091–6103. https://doi.org/10.1021/jp9021147.

[112] L.C. Abbott, P. MacFaul, L. Jansen, J. Oakes, J.R.L. Smith, J.N. Moore, Spectroscopic and photochemical studies of xanthene and azo dyes on surfaces: Cellophane as a mimic of paper and cotton, Dyes and Pigments. 48 (2001) 49–56. https://doi.org/10.1016/S0143-7208(00)00091-7.

[113] J. Han, J. Wanrooij, M. van Bommel, A. Quye, Characterisation of chemical components for identifying historical Chinese textile dyes by ultra high performance liquid chromatography – photodiode array – electrospray ionisation mass spectrometer, J Chromatogr A. 1479 (2017) 87–96. https://doi.org/10.1016/j.chroma.2016.11.044.

[114] B.W.J. Pirok, G. Moro, N. Meekel, S.V.J. Berbers, P.J. Schoenmakers, M.R. van Bommel, Mapping degradation pathways of natural and synthetic dyes with LC-MS: Influence of solvent on degradation mechanisms, J Cult Herit. 38 (2019) 29–36. https://doi.org/10.1016/j.culher.2019.01.003.

[115] V. Brezová, J. Pigošová, B. Havlínová, D. Dvoranová, M. Ďurovič, EPR study of photochemical transformations of triarylmethane dyes, Dyes and Pigments. 61 (2004) 177–198. https://doi.org/10.1016/j.dyepig.2003.10.012.

[116] I. Bridgeman, A.T. Peters, Photochemical Degradation of Aminoazobenzene Disperse Dyes in Ethanolic Solution: Part I: Effect of Concentration, Water, and Temperature, Textile Research Journal. 44 (1974) 639–645. https://doi.org/10.1177/004051757404400901.

[117] J. Seixas De Melo, A.P. Moura, M.J. Melo, Photophysical and spectroscopic studies of indigo derivatives in their keto and leuco forms, Journal of Physical Chemistry A. 108 (2004) 6975–6981. https://doi.org/10.1021/JP049076Y/ASSET/IMAGES/LARGE/JP049076YF00007.JPEG.

[118] C. Minamoto, N. Fujiwara, Y. Shigekawa, K. Tada, J. Yano, T. Yokoyama, Y. Minamoto, S. Nakayama, Effect of acidic conditions on decomposition of methylene blue in aqueous solution by air microbubbles, Chemosphere. 263 (2021) 1–6. https://doi.org/10.1016/j.chemosphere.2020.128141.

[119] G. Favaro, C. Miliani, A. Romani, M. Vagnini, Role of protolytic interactions in photo-aging processes of carminic acid and carminic lake in solution and painted layers, Journal of the Chemical Society, Perkin Transactions 2. 2 (2002) 192–197. https://doi.org/10.1039/b104595b.

[120] Z. MacHatova, Z. Barbieriková, P. Poliak, V. Jančovičová, V. Lukeš, V. Brezová, Study of natural anthraquinone colorants by EPR and UV/vis spectroscopy, Dyes and Pigments. 132 (2016) 79–93. https://doi.org/10.1016/j.dyepig.2016.04.046.

[121] F. Cheng, H. Wang, X. Dong, The amphoteric properties of g-C3N4 nanosheets and fabrication of their relevant heterostructure photocatalysts by an electrostatic re-assembly route, Chemical Communications. 51 (2015) 7176–7179. https://doi.org/10.1039/c5cc01035g.

[122] I. Poulios, A. Avranas, E. Rekliti, A. Zouboulis, Photocatalytic oxidation of Auramine O in the presence of semiconducting oxides, Journal of Chemical Technology and Biotechnology. 75 (2000) 205–212. https://doi.org/10.1002/(SICI)1097-4660(200003)75:3.

[123] J.W. Cumming, C.H. Giles, A.E. McEachran, A Study of the Photochemistry of Dyes on Proteins and other Substrates, Journal of the Society of Dyers and Colourists. 72 (1956) 373–381. https://doi.org/10.1111/j.1478-4408.1956.tb02146.x.

[124] I. Degano, M. Biesaga, M.P. Colombini, M. Trojanowicz, Historical and archaeological textiles: An insight on degradation products of wool and silk yarns, J Chromatogr A. 1218 (2011) 5837–5847. https://doi.org/10.1016/j.chroma.2011.06.095.

[125] J.M. Dyer, S.D. Bringans, W.G. Bryson, Characterisation of photo-oxidation products within photoyellowed wool proteins: Tryptophan and tyrosine derived chromophores, Photochemical and Photobiological Sciences. 5 (2006) 698–706. https://doi.org/10.1039/b603030k.

[126] J. Thomas, J.H. Townsend, S. Hackney, M. Strlič, A chemiluminescence study of madder lakes on paper, Polym Degrad Stab. 95 (2010) 2343–2349. https://doi.org/10.1016/j.polymdegradstab.2010.08.024.

[127] G. Baxter, C.H. Giles, M.N. Mckee, N. Macaulay, The Influence of the Physical State of Dyes upon their Light Fastness, Order A Journal On The Theory Of Ordered Sets And Its Applications. (1955) 218–235.

[128] H.R. Chipalkatti, N.F. Desai, C.H. Giles, N. Macaulay, The Influence of the Substrate upon the Light Fading of Azo Dyes, Journal of the Society of Dyers and Colourists. 70 (1954) 487–501. https://doi.org/10.1111/j.1478-4408.1954.tb02006.x.

[129] N.S. Allen, J.F. McKellar, B. Mohajerani, Lightfastness and spectroscopic properties of basic triphenylmethane dyes: Effect of the substrate, Dyes and Pigments. 1 (1980) 49–57. https://doi.org/10.1016/0143-7208(80)80006-4.

[130] C.H. Giles, The fading of colouring matters, Journal of Applied Chemistry. (1965) 541–550. https://doi.org/10.1179/sic.1964.s002.

[131] N.S. Brommelle, The russell and abney report on the action of light on water colours, Studies in Conservation. 9 (1964) 140–152. https://doi.org/10.1179/sic.1964.024.

[132] M. Meissner, E. Baumann, R. Hofmann, The Role of Humidity Cycling in Accelerated Light Fastness Tests, IS&Ts International Conference on Digital Production Printing and Industrial Applications. (2003) 203–204.

[133] L.M. Rader Bowers, S.J. Schmidtke Sobeck, Impact of medium and ambient environment on the photodegradation of carmine in solution and paints, Dyes and Pigments. 127 (2016) 18–24. https://doi.org/10.1016/J.DYEPIG.2015.12.012.

[134] F. Modugno, F. di Gianvincenzo, I. Degano, I.D. van der Werf, I. Bonaduce, K.J. van den Berg, On the influence of relative humidity on the oxidation and hydrolysis of fresh and aged oil paints, Sci Rep. 9 (2019) 1–16. https://doi.org/10.1038/s41598-019-41893-9.

[135] J. Harrison, J. Lee, B. Ormsby, D.J. Payne, The influence of light and relative humidity on the formation of epsomite in cadmium yellow and French ultramarine modern oil paints, Herit Sci. 9 (2021) 1–17. https://doi.org/10.1186/S40494-021-00569-2/FIGURES/10.

[136] N.S. Allen, Photofading and light stability of dyed and pigmented polymers, Polym Degrad Stab. 44 (1994) 357–374. https://doi.org/10.1016/0141-3910(94)90095-7.

[137] K.J. Dodd, Health and safety legislation: Issues for the synthetic dyestuff industry in the UK, Review of Progress in Coloration and Related Topics. 32 (2002) 103–117. https://doi.org/10.1111/j.1478-4408.2002.tb00254.x.

[138] Y. Jia, L. Zhang, K. Liu, R. Chen, C. Zhang, J. Yin, W. Shen, J. He, Effects of the perspiration on the photo-fading of reactive dyes, Textile Research Journal. 89 (2019) 688–697. https://doi.org/10.1177/0040517517753639.

[139] D. Zhuang, L. Zhang, D. Pan, J. He, Fading of reactive dyes on cellulose under light and perspiration, Coloration Technology. 123 (2007) 80–85. https://doi.org/10.1111/j.1478-4408.2007.00066.x.

[140] S. Waheed, C.M. Ashraf, Stability of reactive dyes in sunlight changes in their colour coordinates, Journal of the Chemical Society of Pakistan. 25 (2003) 114–121.

[141] P.C. Crews, The influence of mordant on the lightfastness of yellow natural dyes, Journal of the American Institute for Conservation. 21 (1982) 43–58. https://doi.org/10.1179/019713682806028559.

[142] T. Padfield, S. Landi, The light-fastness of the natural dyes, Studies in Conservation. 11 (1966) 181–196. https://doi.org/10.1179/sic.1966.022.

[143] M. Yatagai, Y. Magoshi, M.A. Becker, C. Sano, H. Ikuno, N. Kohara, M. Saito, Degradation and color fading of silk fabrics dyed with natural dyes and mordants, ACS Symposium Series. 779 (2001) 86–97. https://doi.org/10.1021/bk-2001-0779.ch007.

[144] A. Manhita, V. Ferreira, H. Vargas, I. Ribeiro, A. Candeias, D. Teixeira, T. Ferreira, C.B. Dias, Enlightening the influence of mordant, dyeing technique and photodegradation on the colour hue of textiles dyed with madder - A chromatographic and spectrometric approach, Microchemical Journal. 98 (2011) 82–90. https://doi.org/10.1016/j.microc.2010.12.002.

[145] B.H. Berrie, Y. Strumfels, Change is permanent: Thoughts on the fading of cochineal-based watercolor pigments, Herit Sci. 5 (2017) 1–9. https://doi.org/10.1186/s40494-017-0143-4.

[146] A. Jimtaisong, Aluminium and calcium lake pigments of Lac natural dye, J. Pharm. Sci. 56 (2020) 18140. https://doi.org/10.1590/s2175-97902019000418140.

[147] C. Anselmi, D. Capitani, A. Tintaru, B. Doherty, A. Sgamellotti, C. Miliani, Beyond the color: A structural insight to Eosin-based lakes, Dyes and Pigments. 140 (2017) 297–311. https://doi.org/10.1016/J.DYEPIG.2017.01.046.

[148] V. Beltran, A. Marchetti, S. de Meyer, G. Nuyts, K. de Wael, Geranium lake pigments: The role of the synthesis on the structure and composition, Dyes and Pigments. 189 (2021) 109260. https://doi.org/10.1016/J.DYEPIG.2021.109260.

[149] M.J. Melo, A. Claro, Bright light: Microspectrofluorimetry for the characterization of lake pigments and dyes in works of art, Acc Chem Res. 43 (2010) 857–866. https://doi.org/10.1021/ar9001894.

[150] I. Geiman, M. Leona, J.R. Lombardi, Application of Raman Spectroscopy and Surface-Enhanced Raman Scattering to the Analysis of Synthetic Dyes Found in Ballpoint Pen Inks, J Forensic Sci. 54 (2009) 947–952. https://doi.org/10.1111/j.1556-4029.2009.01058.x.

[151] A. Astefanei, M. Van Bommel, G.L. Corthals, Surface Acoustic Wave Nebulisation Mass Spectrometry for the Fast and Highly Sensitive Characterisation of Synthetic Dyes in Textile Samples, J Am Soc Mass Spectrom. 28 (2017) 2108–2116. https://doi.org/10.1007/s13361-017-1716-x.

[152] R.A. Armitage, K. Jakes, C. Day, R.A. Armitage, K. Jakes, C. Day, Direct analysis in real time-mass spectroscopy for identification of red dye colourants in Paracas Necropolis Textiles Direct analysis in real time-mass spectroscopy for identification of red dye colourants in Paracas Necropolis Textiles, Sci Technol Archaeol Res. 1 (2016) 59–68. https://doi.org/10.1179/2054892315Y.0000000009.

[153] I. Degano, E. Ribechini, F. Modugno, M.P. Colombini, Analytical Methods for the Characterization of Organic Dyes in Artworks and in Historical Textiles, Appl Spectrosc Rev. 44 (2009) 363–410. https://doi.org/10.1080/05704920902937876.

[154] R.W. Jones, J.F. Mcclelland, Analysis of writing inks on paper using direct analysis in real time mass spectrometry, Forensic Sci Int. 231 (2013) 73–81. https://doi.org/10.1016/j.forsciint.2013.04.016.

[155] T. Watanabe, S. Terabe, Analysis of natural food pigments by capillary electrophoresis, J Chromatogr A. 880 (2000) 311–322. https://doi.org/10.1016/S0021-9673(00)00209-0.

[156] J. Poulin, A New Methodology for the Characterisation of Natural Dyes on Museum Objects Using Gas Chromatography–Mass Spectrometry, Studies in Conservation. 63 (2018) 36–61. https://doi.org/10.1080/00393630.2016.1271097.

[157] I. Groeneveld, S.E. Schoemaker, G.W. Somsen, F. Ariese, M.R. Van Bommel, Characterization of a liquid-core waveguide cell for studying the chemistry of light-induced degradation, Analyst. 146 (2021) 3197–3207. https://doi.org/10.1039/d1an00272d.

[158] B.W.J. Pirok, M.J. Den Uijl, G. Moro, S.V.J. Berbers, C.J.M. Croes, M.R. Van Bommel, P.J. Schoenmakers, Characterization of Dye Extracts from Historical Cultural-Heritage Objects Using State-of-the-Art Comprehensive Two-Dimensional Liquid Chromatography and Mass Spectrometry with Active Modulation and Optimized Shifting Gradients, Anal Chem. 91 (2019) 3062–3069. https://doi.org/10.1021/acs.analchem.8b05469.

[159] M.J. den Uijl, Y.J.H.L. van der Wijst, I. Groeneveld, P.J. Schoenmakers, B.W.J. Pirok, M.R. van Bommel, Combining Photodegradation in a Liquid-Core-Waveguide Cell with Multiple-Heart-Cut Two-Dimensional Liquid Chromatography, Anal Chem. 94 (2022) 11055–11061. https://doi.org/10.1021/acs.analchem.2c01928.

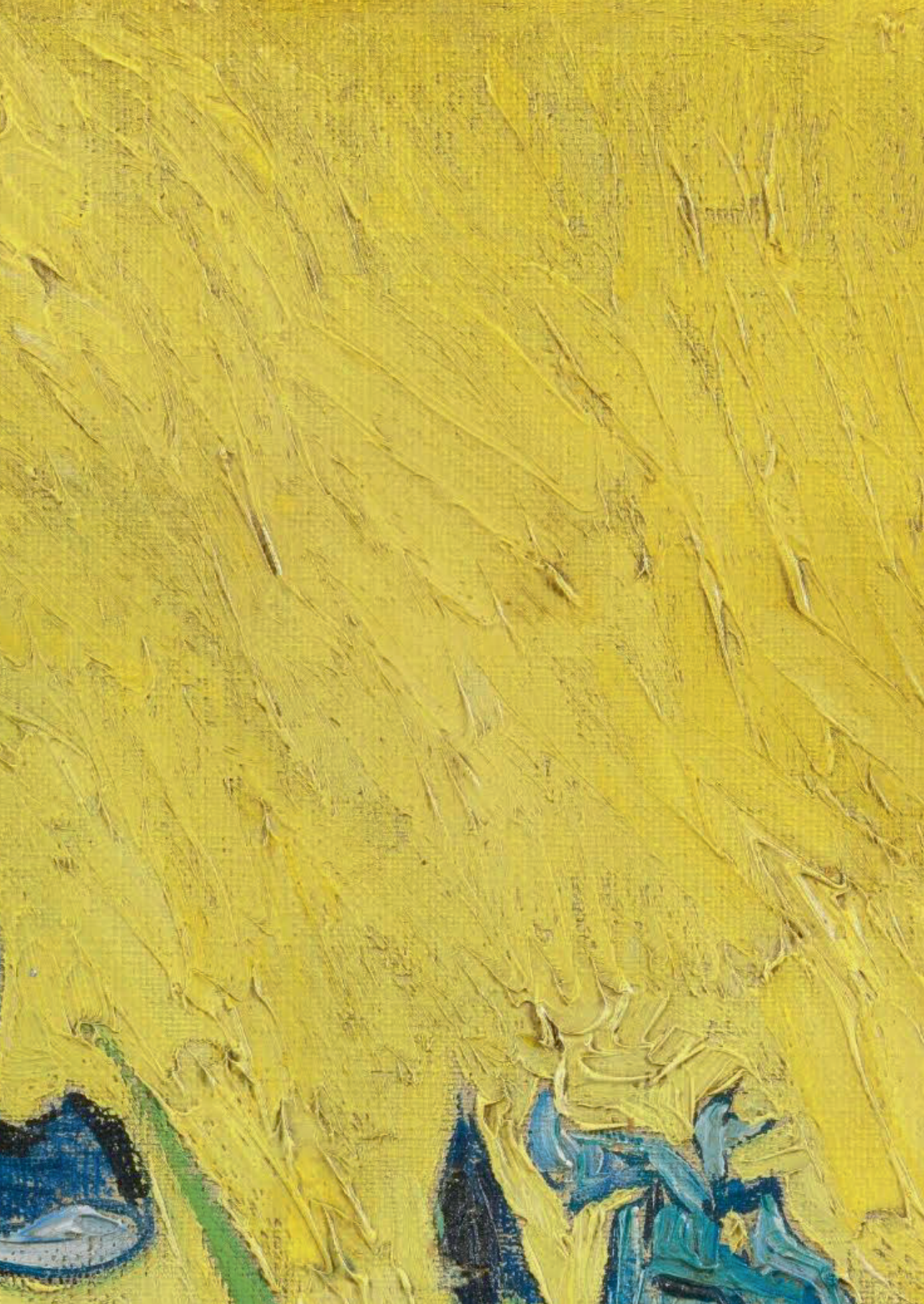

# CHAPTER 3

## Use of liquid-core waveguides as photochemical reactors and/or for chemical analysis – An overview

## Abstract

The study of photochemical reactions is of great importance in many fields including the pharmaceutical, food, and paint industry. Most of these photochemical processes are being studied to better understand how to apply them for a specific purpose or how unwanted effects can be prevented. Advances are still being made in photoreactor design, where in-situ detection of the involved reagents and products is an important development. Liquid-core waveguides (LCWs) allow simultaneous illumination and optical assessment of liquid samples and, therefore, constitute one way of combining photoreactor design with on-line or in-situ analytical detection methods. LCWs possess several interesting characteristics, such as low light loss, increased optical path length, and possibilities for coupling with spectroscopic techniques. The current review discusses the state-of-the-art of LCWs applied as photoreactors, for analytical detection, and their combinations. We discuss the differences between several total internal reflection (TIR)-based LCWs, including polymer and polymer-coated capillaries, and silica aerogels, and interference-based waveguides, including Bragg fibers, holey fibers, Kagomé fibers and anti-resonance reflecting optical waveguides (ARROWs). Assessed characteristics include the (freedom of) design, the degree of light attenuation, the range of transmittable wavelengths, gas permeability, compatibility with analytical techniques, current challenges, and applications.



**Publication**

Use of liquid-core waveguides as photochemical reactors and/or for chemical analysis – An overview

Iris Groeneveld, Amber Jaspars, Imran B. Akca, Govert W. Somsen, Freek Ariese, Maarten R. van Bommel

*J. Photochem. and Photobiol.*, **2023**, *14*, 100168, DOI: 10.1016/j.jpap.2023.100168

## 3.1 Introduction

Photochemistry in this review includes any chemical reaction or modification of a molecule initiated by visible (Vis) or UV light. Such processes generally start with the excitation of a molecule either directly upon absorption of a photon or indirectly upon energy transfer via a photoexcited photosensitizer or photocatalyst. There is an interest in studying and applying photochemistry for many areas, including medicine [1–4], water purification [5–7], food quality conservation [8–10], and cultural heritage [11–13], among many others. A photochemical reaction can be initiated on purpose, for instance in photochemotherapy where light is used to 'activate' a drug in combination with an oral or topical photosensitizer for the treatment of diseases [4], or for the purification process of drinking water, where high-intensity UV lamps are used to degrade potentially harmful chemicals [7]. If such a reaction leads to molecular fragmentation or loss of functional chemical properties, we usually speak of light-induced degradation or photodegradation. Photodegradation may also be an unwanted process. Examples are change of quality of taste and color of food products, appearance of harmful byproducts during irradiation of waste water, or color fading of paints [14,15].

### 3.1.1 Studying light-induced degradation – conventional approaches

Suitable analytical techniques allowing the detection of changes in the molecular structure must be available in order to probe and understand photochemical processes. Ideally, monitoring photochemistry is done in situ (i.e., in the reaction mixture) so that the chemical process can be studied in real-time and in a non-invasive manner, requiring as few analytical steps as possible. However, in practice, these conditions are difficult to meet. Traditionally, photochemical reactions are performed in relatively large batch reactors that can be difficult to homogenize and hard to irradiate in a homogeneous way. Distributing the available light over a large area implies a relatively low irradiance and therefore relatively long reaction times. Moreover, these approaches typically require sampling at specific time points in order to monitor the reaction off-line, making it labor intensive. One way to resolve some of the above-mentioned challenges is by decreasing the volume of the cells (photoreactors) to enhance irradiation efficiencies and to increase the reaction kinetics. On-line monitoring of the extent of degradation would have several practical advantages and circumvent some sources of error.

### 3.1.2 Optofluidics

A solution for in-situ monitoring of photochemistry has often been found in optofluidics, which is the field where fluids and optics are combined to (i) guide the direction of light by means of a fluid, or (ii) analyze fluids or compounds/particles in fluids by means of

light. Microfluidic optofluidics or lab-on-a-chip devices result in faster mixing of reagents and more efficient irradiation of the whole sample due to their small volumes. Monitoring of light-induced reactions can be achieved by coupling microfluidic photoreactors with analytical techniques, such as mass spectrometry (MS) [16], nuclear magnetic resonance (NMR) [17], liquid chromatography (LC) [18,19], and UV/Vis absorption [20,21], fluorescence [22] and Raman spectroscopy [23,24]. Sun et al. [2] presented a droplet microfluidic platform for continuous flow-based photochemical reactions with on-line analysis by electrospray ionization (ESI) MS. The generated droplets (5-10 nL) were irradiated in a continuous flow using a blue LED array that was placed above the microfluidic device. This enabled the simultaneous irradiation of up to 100 nL-sized reaction droplets at the picomolar level and a high analysis throughput of 0.3 samples $s^{-1}$. Azzouz et al. [7] developed a microfluidic flow reactor with zinc oxide nanowires as a photocatalytic nanomaterial for water purification. The samples were irradiated with a UV lamp (365 nm) for only 5 s at a distance of 10 cm from the 3-$cm^2$ microfluidic device, which resulted in degradation of up to 95%. The reduction of sample volumes in combination with microfluidic channels also comes with challenges. Irradiation of a sample in a flat, chip-based microreactor is generally performed by illumination perpendicular to the flow cell through some optical window, which could be inefficient due to scattering losses at the surface and focusing of the beam to match the size of the microreactor channel. In addition, higher limits of detection (LOD) may be the result when spectroscopic analysis is performed in a perpendicular fashion as a result of the short optical pathlength. Irradiation from within or along the inner volume of the photoreactor is a way to increase the irradiation efficiency and the light intensity received by the sample, enhancing the photochemical reaction rates and, therefore, shortening analysis times [25,26]. This way of irradiating also increases the optical path length for spectroscopic methods when the detector is positioned at the other, distal end of the photochemical cell, which results in higher sensitivity.

### 3.1.3 Liquid-core waveguides as photoreactors

The principle of waveguiding can be used to increase irradiation efficiencies in photochemical reaction cells [20,27]. Hollow waveguides are capillaries that can guide light along their axial direction, thereby completely irradiating a liquid sample if loaded inside the capillary core, making it a liquid-core waveguide (LCW). Waveguiding can be achieved by different principles [27]. A frequently used approach is the application of total internal reflection (TIR), where incoming light is guided along the length of the LCW due to differences in refractive index between the cladding material and the sample solution inside the core [28]. A second approach is based on the use of wave interferences to localize the electromagnetic wave, where multiple layers of materials

are used as cladding. This creates a refractive index profile in the cross-section of the waveguide, which initiates multiple reflections of the electric field, which can interfere constructively or destructively [29].

### 3.1.4 Waveguides and chemical analysis

Waveguides have been used to increase the detection sensitivity in absorbance-based methods [30]. The large optical path lengths ($L$) offers increased absorbance ($A$) as follows from Lambert-Beer's law (Eq. 1), where $\varepsilon$ is the molar absorption coefficient, $C$ the concentration, and $I_0$ and $I$ the intensity of the transmitted light in the absence and presence of the analyte, respectively [31,32].



$$A = log\left(\frac{I_0}{I_t}\right) = \varepsilon LC \qquad \text{(Eq. 3.1)}$$

The use of LCWs in combination with on- or in-line detection for studying photochemistry provides an interesting solution to the irradiation and detection limitations that are faced with microfluidic chips. With LCWs both irradiation and detection are along the axis of the waveguide, yielding improved illumination efficiency and detection sensitivity. Furthermore, in spite of the increased optical path length, the inner volume can remain low by using small diameter cores.

Several reviews have been published about specific types of waveguides for in-situ detection or sensing purposes, such as photonic crystal fibers [33–36], Bragg fibers [37] and anti-resonance reflecting optical waveguide (ARROW) fibers [38], and leaky waveguides [39]. Other authors discussed specific applications, e.g., fluorescence-based fiber optics or biosensors [40,41]. In 2008, Schmidt et al. [29] presented a review article on developments and the current status of LCWs in optofluidics. Four years later, Pasco et al. [42] described applications of LCWs in flow-based analysis techniques. In 2018, Pidenko *et al.* [43] published a review on the current state-of-the-art of biosensors based on various types of optical fibers loaded with a solution inside the hollow core. However, a comprehensive review on waveguides with in-situ or in-line spectroscopic techniques to study and monitor photochemical processes is currently lacking. Most recently (in 2019), Rehm et al. [44] provided an extensive overview on the developments of continuous flow photoreactors and their applications to photochemical synthesis. Waveguides were also mentioned as potential candidates, but coupling with analytical techniques was addressed only briefly.

Several reviews aim to point out the benefit of a certain type of waveguide in the field of photochemistry or analytical sciences. The purpose of this review is to report on the developments in both fields, with a focus on where photochemistry and spectroscopic

analysis are performed simultaneously. Here, we describe different types of waveguides that have been applied as microreactors in photochemistry and/or for analysis, with emphasis on the differences between several TIR-based (i.e., polymer and polymer-coated capillaries, and silica aerogels) and interference-based LCWs, including Bragg fibers, holey fibers, Kagomé fibers and ARROWs. The waveguides were assessed based on their design and flexibility of their design, optical loss, applicable wavelengths, compatibility with analytical techniques, applications, and current challenges.

## 3.2 Total internal-reflection liquid-core optical waveguides

In the second half of the 20th century, advances were made on LCW spectrophotometric cells with a longer path length for enhanced absorbance and sensitivity while maintaining small sample volumes. First, LCWs were often tubes made of quartz or glass coated with highly reflective metals containing a liquid core, based on the principle of reflection or TIR exploiting Snell's law (Eq. 2). This law describes the refraction ($\theta_2$) of a light beam with an angle of incidence ($\theta_1$) hitting the interface of two transparent media of different refractive indices ($n_1$, $n_2$) [45]:

$$\frac{sin(\theta_2)}{sin(\theta_1)} = \frac{n_1}{n_2} \qquad \text{(Eq. 3.2)}$$

TIR occurs when $n_2 > n_1$ and the angle of incidence is equal to or larger than the critical angle ($\theta_c$), which is determined by Eq. 3. To successfully exploit this effect, the core of the LCW (e.g., the solvent or sample solution) should have a higher refractive index (RI) than that of the cladding material [28].

$$sin\,\theta_c = n_2/n_1 \qquad \text{(Eq. 3.3)}$$

The conventional way of coupling light into an LCW is by focusing a collimated light beam into the core. Light entering the core at an angle larger than $\theta_c$ will be totally reflected at the core/cladding interface and transmitted along the liquid core, providing an efficient way of irradiating the whole sample inside the LCW [46].

Despite the fact that quartz and metal-coated tubes provided long-path LCWs, their high attenuation along the axis of these cells counteracted any benefit of the increased optical path length [47,48]. Since metal-coated tubes were designed to reflect light through any transparent core over large angles, they were independent of the RI of solvents. However, they were mostly suitable in the Vis, microwave, and infrared regions. Glass or quartz tubes worked on the principle of TIR, but in order for TIR to take place very high RI

solvents (e.g., bromobenzene [49], $n$ = 1.56) had to be used. Suitable materials with an RI lower than most solvents were not available at the time. This changed in 1989 when DuPont introduced the polymers Teflon AF 1600 and 2400, which have a lower RI ($n$ = 1.29) than that of water ($n$ = 1.33) [50]. Teflon AF is an amorphous copolymer of 2,2-bistrifluoromethyl-4,5-difluoro-1,3-dioxol (PDD) and tetrafluoroethylene (TFE) and is transparent for light above a wavelength of 200 nm [50,51]. Teflon AF tubes could be used for TIR-based waveguiding of light between 200 and 1600 nm using solvents such as methanol ($n$ = 1.329), acetonitrile ($n$ = 1.344) or hexane ($n$ = 1.375) [51]. This resulted in a significant leap forward for LCWs, as Teflon AF was moldable into tubing, films or coatings, resulting in chemically inert waveguides with low attenuation [52].



### 3.2.1 Polymer-coated capillaries

The first step of applying the new low-RI Teflon for LCWs was to coat fused silica capillaries externally with Teflon AF, producing the so-called type II LCWs that are compatible with a large range of solvents. In 1997, Altkorn et al. showed how a type II LCW could effectively replace fused silica-only LCWs [53].

A disadvantage of type II LCWs, however, is that TIR does not occur at the core/silica interface, but rather at the Teflon AF/silica and the Teflon AF/air interfaces (Fig. 3.1B). This resulted in light being trapped inside the cladding material and, therefore, leading to inefficient irradiation of the core solution. This could also lead to decreased analytical sensitivity when it is used for detection purposes, due to a high background signal originating from the stray light from the cladding [28]. Dasgupta et al. [54] described how the background signal can be rejected by applying an opaque coating to the tip of the capillary or by using a light collection fiber that is equal to or smaller than the core diameter of the LCW, such that it only collects light transmitted through the liquid core.

Type II LCWs are commercially available as long optical path length detector cells for UV-Vis absorbance spectroscopy. These optical flow cells have been used by Melchert et al. [55] for the determination of carbaryl pesticides in natural waters at concentrations as low as 200 µg $L^{-1}$ using a 100-cm long flow cell. The same flow cell was studied by Rocha et al. [56] for the analysis of phosphates in fresh waters, which was achieved after on-line photochemical conversion of organic phosphorus into orthophosphate. They used molybdenum blue as a color indicator for the total amount of orthophosphate in the fresh water samples reaching detection limits down to 2 µg $L^{-1}$, i.e., much lower than reported by Melchert et al. [55]. The detection is directly related to the absorption coefficient of the analyte. Therefore, more strongly absorbing compounds will result in lower detection limits. This also means that the concentration of the solution should be taken into consideration for photochemical reactions, as a too-high concentration will result in total

absorption of the light in the first few centimeters of the LCW, resulting in heterogenous and slower reaction rates along the length of the waveguide.

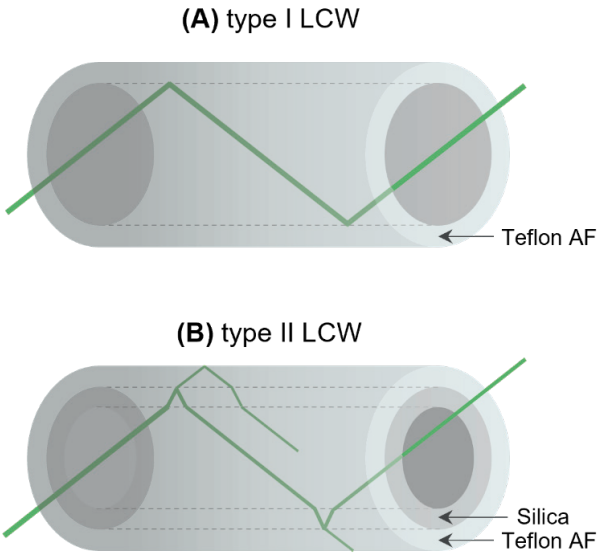


Figure 3.1. A simplified schematic of the path a photon with an incident angle at or larger than the critical angle may follow in (A) a type I or (B) type II LCW.

### 3.2.2 Polymer capillaries

In an attempt to prevent the background interferences that occur with type II LCWs, type I LCWs were produced, which consist of capillaries made entirely of Teflon AF, so that TIR will occur at the liquid/Teflon AF interface (Fig. 3.1A). The LCWs made of Teflon AF tubing show relatively high losses (dB $m^{-1}$) compared to other waveguides discussed in this review, e.g., holey and Kagomé fibers. The difference between the type I and type II Teflon AF waveguides is small with regards to optical loss, however, type I waveguides have the added benefit of gas permeability because there are no obstructing silica wall, which makes them interesting for studying (photo)reactions under oxic vs anoxic conditions. For photochemistry, the type I waveguides show more efficient irradiation of the core compared to type II waveguides, due to the differences in the TIR interface.

Teflon AF LCWs have been used frequently for trace analysis, for example in water and marine chemistry [28,57,58]. Other applications have been described, for example by Cheng et al. [32], who used a 9-cm long Teflon AF tube for the determination of organophosphorus pesticides in vegetables and fruits by absorbance spectroscopy, improving the LOD by a factor of 1000 compared to classical spectrophotometry. The large inner diameter (2.56 mm), leading to enhanced optical paths, as well as reduction

of noise both contributed to the LOD enhancement. Another example of long optical path length UV-Vis absorbance spectroscopy was provided by Rubles et al. [52], who developed and characterized the type I LCW for the use in a commercial spectrophotometer for measuring low light absorbance values of dilute aqueous solutions, reaching LODs as low as 3 mAU (equivalent to an optical density of 36 $\mu$AU $cm^{-1}$). Type I LCWs have also been used for fluorescence spectroscopy [59–61]. Liu et al. [61] developed a setup for capillary isoelectric focusing of naturally fluorescent or fluorescently labelled proteins with a fluorescence whole-column imaging detection system based on a type I LCW (Fig. 3.2). For excitation, the authors focused an argon-ion laser axially into the LCW capillary. The fluorescence signal that was transmitted through the Teflon AF walls was read across the whole LCW length (5.5 cm) by a CCD camera positioned at a 90° angle with respect to the LCW. When compared to a commercially available instrument with UV absorbance detection, the separation efficiency was similar, whereas the detection sensitivity was enhanced by 3-5 orders of magnitude. The enhanced detection was mainly attributed to the high quantum yields of the fluorescent proteins in combination with the highly advantageous signal-to-noise ratio obtained for fluorescence detection.



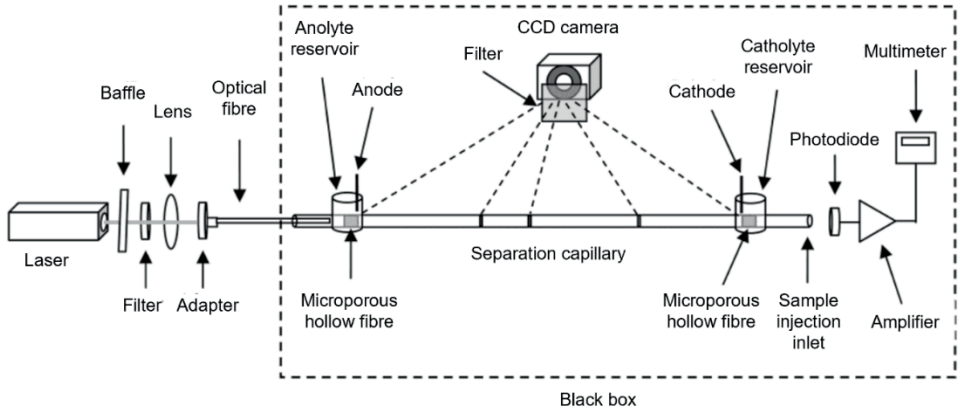


Figure 3.2. Schematic diagram of the instrumental setup by Liu et al. for capillary isoelectric focusing of labelled proteins with fluorescence whole column imaging detection based on a Teflon AF type I LCW. A CCD camera was positioned at a 90° angle to collect the fluorescence signal from the proteins that was transmitted through the Teflon AF walls. Reprinted and adapted with permission from [61] (Copyright 2003 American Chemical Society).

Raman spectroscopy has also shown to be an interesting application for these specific LCWs [62–70]. Upon irradiation of an analyte, approximately 1 in a million photons are scattered inelastically, i.e., as Raman photons. Therefore, measuring a Raman signal of low analyte concentrations can be challenging. The length of the LCW significantly

improves the Raman signal by the propagation of excitation light along the length of the waveguide, increasing the number of molecules that may emit Raman signals. In the case of fluorescence and Raman spectroscopy, interfering irradiation could be reduced by illuminating transversely, where the light source is placed at a 90° angle relative to the LCW tube (Fig. 3.3) [54,70–74]. Excitation light passes through the tubing walls and interacts with molecules inside the tube, resulting in fluorescence or Raman scattered photons in every direction. A part of these photons is guided along the length of the LCW towards the detector, while most of the excitation light exits through the tubing walls. In reality, some of the excitation light is also guided along the length of the LCW and a part of the emitted fluorescence/Raman will exit the LCW through the walls. Using this irradiation method, Holtz *et al.* [70] were able to collect Raman shifts close to 200 $cm^{-1}$ without the use of a holographic notch filter.

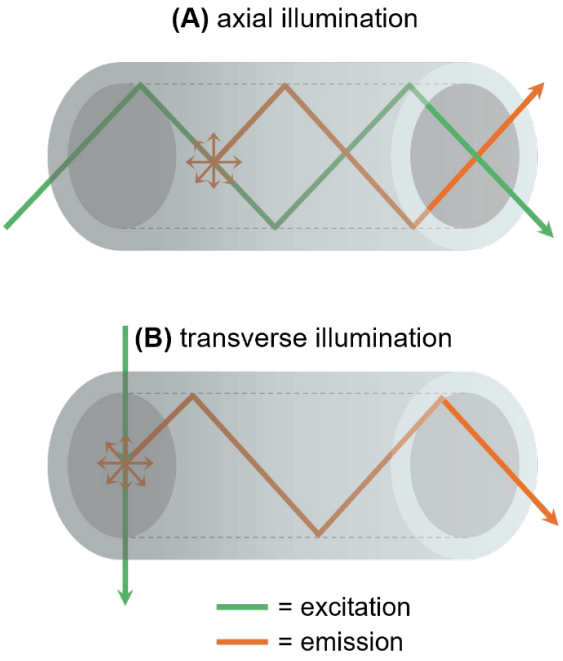


Figure 3.3. A simplified schematic description of the light path followed in the case of (A) an axially or (B) transversely irradiated type I LCW. In reality, a part of the excitation and emission light will exit the LCW through the capillary walls, and in the case of B, a small portion of the scattered excitation light will also be guided along the length of the LCW.

Type I LCWs have also been used as photoreactors, mostly in combination with a reactor gas, exploiting their gas permeability which allows for gas-liquid reactions. This is not possible with any other optical waveguides discussed in this review. Many have studied the use and performance of Teflon AF capillaries for gas-liquid reactions [75–81]. For

example, Polyzos et al. [82] developed a tube-in-tube reactor for continuous-flow synthesis of carboxylic acids using $CO_2$ and a combination of several Grignard reagents. The Teflon AF tube was placed inside a PTFE tubing, through which the $CO_2$ gas was delivered at a flow of 400 µL $min^{-1}$. They found that these experimental settings resulted in high conversions with a short residence time (42 s), meaning that diffusion through the Teflon AF wall occurred rapidly. However, none of the above-mentioned works used light to initiate photochemical reactions. Ponce and colleagues demonstrated an optical micro photoreactor of Teflon AF combining fast gas-liquid mass transfer in combination with in-situ absorbance spectroscopy [83]. The light was coupled into the Teflon AF LCW using a standard optical fiber. With a tube-in-tube configuration, such as the one described by Polyzos *et al.*, oxygen was introduced for the methylene blue catalyzed oxidation of D-glucose, which was studied in situ by absorbance spectroscopy. In this particular situation, the light source was not used for photo-activation, but the authors do mention that next to the above-mentioned redox reaction, photodegradation of methylene blue could take place. In earlier published work, we demonstrated the use of a type I LCW as a photoreactor for the photodegradation of the dyes crystal violet and eosin Y with real-time monitoring using absorbance spectroscopy [84]. Later, this fully automated system was coupled on-line with liquid chromatography to study the formed photodegradation products directly after irradiation [18]. Hence, the Teflon AF type I LCW shows promising features as a high-performing micro photoreactor.



### 3.2.3 Silica aerogels

A third, more recent approach to the construction of TIR-based LCW photoreactors is based on silica aerogels. Silica aerogels are nanostructured materials forming a solid structure with a large number of air-filled pores. The resulting high porosity leads to an RI close to that of air ($n$ = 1.00). Hollow channels can be made through the aerogels, which can be filled with a higher RI liquid so that light is guided along the length of this channel (Fig. 3.4). Light that can be used for waveguiding along the length of such a channel is limited to wavelengths higher than 300 nm, due to the absorbance of light of shorter wavelengths by the silica.

In recent studies, aerogels have been used quite successfully for waveguiding, although they may show significant losses of 150-1000 dB $m^{-1}$, which appears to be mostly caused by the faults made in the channel formation [85–91]. This is also why the lengths used for aerogel waveguides is limited to a few centimeters at most.

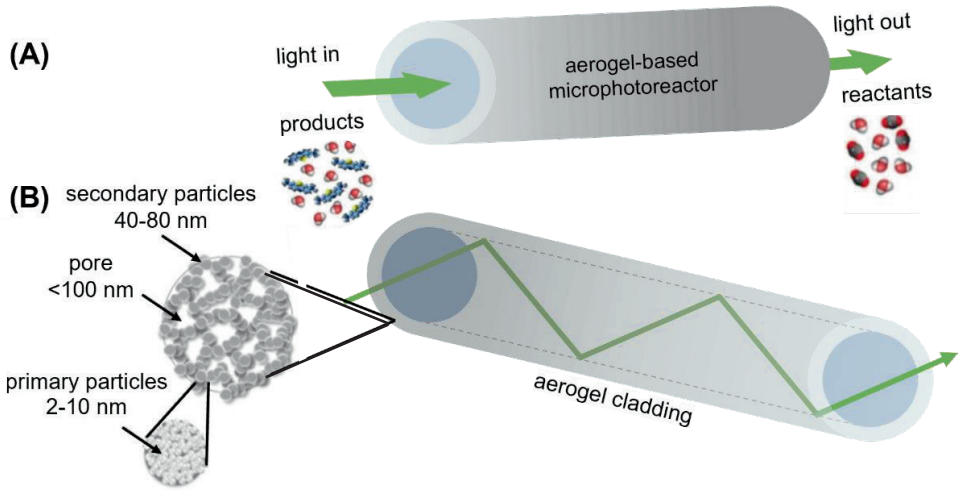


Figure 3.4. (A) Aerogel–based micro photoreactor with an integrated optofluidic waveguide, (B) cross–sectional view of the micro photoreactor/waveguide system illustrating light guiding in the liquid by TIR, by Özbakir et al.. Adapted with permission from [87] (Copyright 2018 the Royal Society).

Xiao et al. [89] were the first to report on LCWs consisting of water-filled microchannels in aerogels, which allowed the transmittance of laser light of 635 nm with relatively low intensity losses. Eris et al. [85] were able to produce both straight and U-shaped waveguides inside aerogels, opening up possibilities for the creation of complex three-dimensional networks. Later, Yalizay et al. [92] applied femtosecond-laser ablation as a more accurate alternative for the milling and cutting procedures for the creation of microchannels, which reduced light losses. Özbakir et al. showed that the aerogel LCWs could be used for applications including the detection or identification and quantification of particular chemical compounds by placing a power meter at the exit of the channel [86]. The aerogel LCW was used as a micro photoreactor for studying the photodegradation of methylene blue (MB) with an initial concentration of 37 μM using a laser with a wavelength of 388 nm. The sample was analyzed off-line by absorption spectroscopy after collection from the waveguide at different time intervals. Within 60 min, the concentration of MB decreased by 83% when exposed to an incident light power of 250 mW. They also found that the degradation rate was proportional to the light power [87]. Later, the same group embedded titanium particles in the walls of the aerogel microchannels to establish rapid photocatalytic transformation of MB; however, the readout was still performed off-line [88]. Most recently, the same authors showed an application of the titanium embedded aerogel waveguide for the photocatalytic degradation of an aqueous phenol mixture into $CO_2$ and water [93].

These results show that aerogel LCWs can be suitable as photoreactors, and provide flexibility for adapting the surface for catalytic reactions. Disadvantages of silica aerogels are their low transmittance of light below 300 nm, their high optical losses, and the high adsorptive behavior for organic molecules, although modifying the gels may be a solution to this problem.



## 3.3 Interference-based optical waveguides

Interference-based waveguiding presents an alternative for TIR-based LCWs. In interference-based waveguides, multiple layers of dielectric materials are used as a cladding material, as shown in Fig. 3.5. These layers create multiple reflections at each interface of the structured cladding material that can interfere constructively or destructively [29]. The key idea in the present context is that near-perfect reflections into the liquid medium can be achieved even if that medium has a lower RI than all of the cladding layer materials.

Based on the light guiding properties, the interference-based optical waveguides can be divided in two categories: (i) photonic crystal fibers (PCFs) and (ii) ARROWs [29,91,94].

### 3.3.1 Photonic crystal fibers (PCFs)

PCFs are optical fibers with a variety of cross-sectional structures as shown in Fig. 3.5. PCFs are generally produced by the so-called stack-and-draw method, where glass capillaries are stacked into a macroscopic version of the geometry desired in the fiber. This preform is then heated and drawn into a fiber with a final diameter of e.g., 125 μm. The cladding layer, therefore, consists of microscopic hollow capillaries along the length of the entire fiber [33]. The waveguiding principle is determined by the design of this cladding and the dimensions of the core. The light guiding of the discussed PCFs is based on TIR, but their efficiencies depend on the specific geometry and structural parameters of the PCF [95]. TIR will still occur when the RI of the core is higher than that of the cladding, which is generally the case for PCFs with a solid core or a fluid filled hollow core. Due to the tight light confinement and reduced sample volume that PCFs offer, they have been widely used as LCWs for chemical sensing, using absorbance [96,97], fluorescence [98,99], and Raman spectroscopy [100–103], but also for studying photochemistry.

Based on the design and the mode of light propagation of the PCFs, the following three subcategories can be discerned: (i) Bragg fibers, (ii) holey fibers, and (iii) Kagomé fibers (Fig. 3.5).

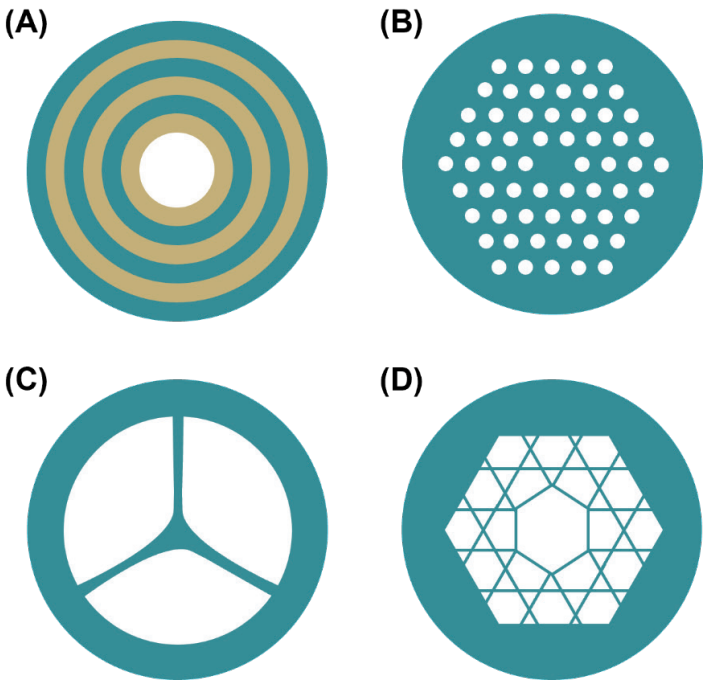


Figure 3.5. The four PCFs discussed in Section 3.3.1: (A) Bragg fiber, (B, C) holey fibers, and (D) Kagomé fiber.

### Bragg fibers

The Bragg fiber (Fig. 3.5A) is an interference-based waveguide, and is also known as the one- dimensional PCF. Bragg fibers contain multiple dielectric layers of low ($n_1$) and high ($n_2$) RI around a hollow core that are repeated periodically. An incident photon is guided along the length of the Bragg fiber when a) the Bragg frame is highly reflective, and b) the transverse component of the wave vector fulfills the same phase resonance condition as in the case of TIR. The partial reflections are equivalent to the Bragg reflections that are known from X-ray analysis of crystalline materials [94].

Temelkuran et al. [104] showed that these hollow-core fibers were perfectly suited for the efficient transmission of the light of a carbon dioxide laser, with transmission losses of less than 1 dB $m^{-1}$. Kuriki et al. [105] reported comparable transmission losses for the guiding of light in the mid-IR range measured with a Fourier-transform infrared (FTIR) spectrometer, using a lens to couple light into the fiber and an external detector. These examples, however, do not make use of a liquid-filled core.

A hollow-core Bragg fiber can be filled with a liquid or a gas, which changes the properties of the guided light and paves the way for new applications. This will result in shifts in the

detected band gaps peaks, which makes it an interesting tool to study the RI of solutions [95,106–109]. The fiber sensor operates using a resonant sensing principle, meaning that the fiber transmission spectrum changes in response to the RI of the core solution. Milenko *et al.* [95] used Bragg fibers for bio-sensing applications, where the core was filled with aqueous solutions to detect changes in their RI. In 2011, Qu et al. [109] similarly demonstrated a Bragg fiber with a liquid core as a sensor for liquid analyte RI detection. The Bragg fiber was 40 cm long and had a core diameter of 0.8 mm surrounded by alternating layers of polymethyl methacrylate and polystyrene. The core was filled with NaCl solutions with different weight concentrations, resulting in RIs ranging from $n = 1.33$ to 1.38. They were able to analyze the transmission spectra of these solutions with a spectrometer coupled on-line (Fig. 3.6).



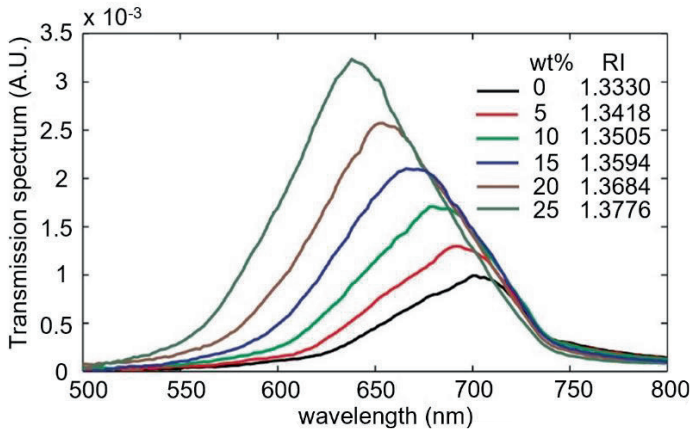


Figure 3.6. Experimental transmission spectra of Bragg fiber sensor filled with NaCl solutions of increasing RI in arbitrary units (A.U.). Reprinted and adapted with permission from [109] (Copyright 2011 AIP Publishing).

Despite the many publications that mention Bragg fibers as LCWs for the purpose of detection, as far as we are aware they have not been reported as photochemical microreactors yet. Most papers focus on the fabrication of Bragg fibers and its use as an air-filled, light-guiding tool. The limitation of Bragg fibers lies in the complex fabrication process, which involves multiple material deposition steps. This may result in imperfections that ultimately limit the transmission as well as the level of light confinement that can be achieved. Another reason why hollow Bragg fibers may not have been used for photochemical monitoring yet is due to the fact that these fibers offer a very narrow range for light transmittance [110], which means that only a small part of the light spectrum can be used. Despite or due to this reason, Bragg fibers have shown to be especially well suited for RI sensing, with low-refractive-index-contrast Bragg fibers in

particular. High-refractive-index-contrast Bragg fibers have shown to be most suitable for gas-core sensors. Although no reports were found on photochemical reactors based on Bragg fibers, if the very specific wavelength that is transmitted is applicable for photochemistry and translatable to a change in molecular structure, then this could also be detected using a Bragg fiber.

### Holey fibers

Contrary to Bragg fibers, holey fibers have a solid core (glass or flexible polymer) surrounded by a cladding that consists of many closely spaced air holes (Fig. 3.5B). Normally, the hollow channels are filled with air to reduce the effective RI of the cladding below that of the solid core, which causes the guidance of light through the solid core by TIR [33]. The holey fibers offer a large degree of freedom in the microstructure design, which allows for large mode areas, high nonlinearity, and remarkable control of dispersion. Advances in fabrication techniques have reduced transmission losses down to $18\times10^{-5}$ dB $m^{-1}$ at 1550 nm [111] and guiding of ultrabroad wavelength ranges of 400-2400 nm has been reported as well, which makes them suitable for broadband applications [112].

The hollow channels may be filled with a fluid or liquid sample with a RI lower than that of the solid core to benefit from the same TIR effect. When doing so, the light is again guided through the solid core and now interacts with the edge of the liquid sample via an evanescent wave that penetrates the liquid filled channels. The penetration depth of the evanescent field into the channels, however, is limited, and the light, therefore, does not affect the whole sample. Fortunately, this can be optimized by changing the core size, hole diameter and the distance between the hollow channels [113].

Examples where holey fibers were used for absorption, Raman and fluorescence spectroscopy include the detection of dyes [99,114], biomolecules [115–117], solvents [118] and gasses [119–121]. In the case of Raman or fluorescence, the emitted photons are also transported through the core. The microchannels, however, may result in large flow resistance, which is a limitation in optofluidics. To circumvent the issue of high flow resistance, a holey fiber with different geometry was designed where the solid core is held together by three relatively large nanowebs (Fig. 3.5C). Due to the size of the three cladding holes, the sample is easily pumped into the holey fiber and overlaps of 30% of the evanescent field with the liquid cores could be reached for relatively small cores [33]. Webb et al. [122] made several of these nanoweb holey fibers by drilling holes into a silica preform and drawing them into narrow fibers. The solid core size varied between 0.8 – 1.8 µm and the webs were around 8 µm in diameter. They concluded that the relatively high losses (0.29 dB $m^{-1}$ at 1550 nm) were mainly due to scattering losses because of

the rough surfaces followed by drilling. They found that these fibers have a lower flow resistance and the evanescent wave will have stronger interaction with the analytes inside the channels due to the penetration depth, but losses are higher compared to regular holey fibers.

Due to the evanescent wave mechanism, these fibers are ideal for the detection of surface-bound analytes [115,123]. In order to increase photochemical reaction rates, catalysts could be bound to the surface of a hollow channel and the photocatalytic reactions could be studied in situ. However, applications of holey fibers have not yet been reported for such studies. The reason may be the shallow penetration depth of the evanescent wave, which does not offer sufficient interaction with the solutes, resulting in long reaction times. In addition, we suspect that the evanescent wave is not as strong at the outer edges of the fiber as it is close to the core, meaning that in the design of Fig. 3.5B the channels may be irradiated heterogeneously. However, many improvements can be made in the design of the holey fibers, which may lead to the application for photochemical studies in the future.



### Kagomé fibers

Another type of hollow core PCF that is quite popular for photochemistry and chemical sensing is the Kagomé PCF, named after its particular lattice arrangement in the cladding structure (Fig. 3.5D) [33]. Kagomé fibers are generally made by the stack-and-draw method using silica or polymers such as PMMA. This type of PCF does not follow the guiding principles regularly observed for hollow core fibers, but through inhibited coupling (IC), resulting in losses up to 0.1 dB $m^{-1}$. IC is established by minimizing the spatial overlap between the fields of the core and cladding modes and by creating a strong mismatch between their spatial phases [124], which is why losses of Kagomé fibers are highly dependent on their structure. An advantage of Kagomé fibers is their large transmission window over a very broad wavelength range from UV to the NIR region, which is caused by the particular cladding structure.

Kagomé fibers have been widely applied as LCWs for broadband spectral detection and photochemical studies in solution. Cox et al. were the first to perform SERRS measurements inside a 20-cm long Kagomé fiber (ID=30 μm) filled with an aqueous solution of 0.21 μM Rhodamine 6G adsorbed to colloidal silver [125]. An Argon-ion laser was directed into the core of the fiber through a 20x microscope objective, which was also used to collect the back-scattered Raman signal. The researchers found that both the incoming Argon-ion laser beam and the scattered Raman signals originating from the analyte were guided along the fiber, which led to an enhanced signal compared to conventional Raman analysis. However, they also noticed that besides the core, the fiber

cladding also displayed weak Raman peaks, which indicated that the enhanced signal is partly a result of resonance reflection.

Williams et al. [126] performed long pathlength fluorescence measurements in solution and compared the results obtained with a Kagomé fiber with those of a holey fiber. The detection limit of the Kagomé fiber was at the attomolar level, whereas that of the holey fiber was at the nanomolar level. They also found that in the Kagomé fiber the excitation of the analyte is confined to the bulk solution, whereas in holey fibers exclusively molecules at the solution-cladding interface were excited. This is no surprise as the evanescent wave will penetrate the sample only close to the surface of the cladding. The use of Kagomé fibers for reaction chemistry is therefore preferred over holey fibers.

Williams *et al.* [127] used a Kagomé fiber for the photoisomerization of azobenzene. In 10 s the reaction process was completed, whereas using a cuvette, almost three orders of magnitude more power was needed to achieve the same result in a comparable reaction time. Cubillas et al. [128–130] used a Kagomé fiber to study complex multicomponent homogeneous and heterogeneous photocatalytic reactions. In one of their reports [130], they present the photolysis of $(HBPz'_3)Rh(CO)_2$ in toluene in a 35-cm long Kagomé fiber with a total volume of less than 175 nL. They irradiated the core solution with a 405 nm diode laser with excitation powers ranging between 5 and 30 μW, and the reaction was monitored by measuring the absorbance of the solution. At an excitation power of 15 μW, photolysis was complete within 60 min, whereas the same reaction studied in a cuvette took more than 8 hours. The optimized light–matter interaction in the fiber strongly enhanced the reaction rate.

Chen et al. [97] used a Kagomé LCW to study the photo-aquation of vitamin B12 (cyanocobalamin), and Unterkofler et al. [131] studied the same reaction in continuous flow in a 25 cm long Kagomé fiber and were able to measure the reaction products by on-line high-resolution MS. A total volume of 85 nL 5 μM vitamin B12 was irradiated with a laser of 488 nm. Due to the continuous flowrate of 27.7 nL $s^{-1}$ the irradiation time inside the fiber was only 20 s. A stunning 30% decrease in transmittance at 488 nm was observed at only 0.71 s, which indicated the photoconversion of vitamin B12. Later, the same set-up was coupled to ESI-MS to demonstrate its applicability for the efficient activation and analysis of photoactivatable drugs. A di-nuclear ruthenium complex was used as a model drug and was compared to standard irradiation techniques using the same 488 nm irradiation source [30]. They studied the reactions in the presence of small biomolecules, which were found to bind faster to the ruthenium complex when irradiated. The Kagomé fiber set-up drastically reduced the sample volumes and irradiation times

from hours to seconds and findings were in line with studies using cuvettes. Unfortunately, the reduced sample volume also resulted in a reduced MS signal intensity.

Overall, the Kagomé fiber shows good performance for chemical sensing and proves to be an efficient photoreactor due to its low attenuation and broad spectral transmittance. A limitation of Kagomé fibers is their small internal volumes, which could complicate measuring at low concentrations. In order to increase the volume, longer fibers should be used since their inner diameters are typically below 50 µm. However, an increased optical path length also means more absorption across the length of the fiber, meaning that the last few centimeters receive less light compared to the first centimeters: an effect undesirable in photochemistry.



### 3.3.2 Anti-resonant reflecting optical waveguides (ARROWs)

In ARROW fibers, the principle of thin-film interference is applied to guide light with low-intensity losses. Here, light waves are reflected by the upper and lower boundaries of a thin film, either enhancing or reducing the reflection of light (Fig. 3.7). The thickness of the film ($t_1$) is essential as it determines which effect will occur. When the thickness of the film is an odd quarter-wavelength (1/4 λ, 3/4 λ, 5/4 λ), the reflected waves interfere and cancel each other out. However, when the thickness of the film is half a wavelength different from that of the incident light wave (1/2 λ, λ, 3/2 λ), the reflected waves reinforce each other and increase the reflection [132]. In contrast to PCFs, the high- and low-index alternating layers ($n_1$ and $n_2$) in ARROW waveguides do not require high periodicity in the structure, which simplifies the manufacturing process.

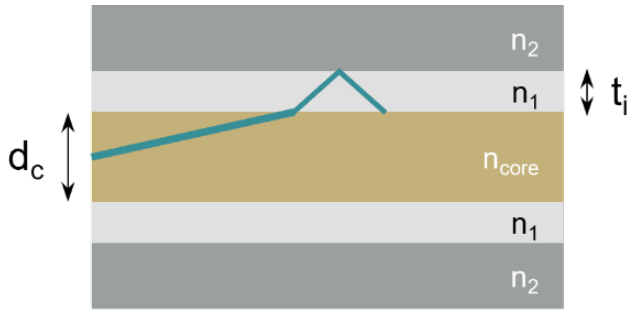


Figure 3.7. A schematic depiction of the reflections that occur between the refractive layers inside an ARROW. $d_c$ = core diameter, $t_i$ = layer thickness, $n_{core}$ = refractive index of the core, $n_1$ = refractive index of the first layer, $n_2$ = refractive index of the second layer.

With roughly 1000 dB $m^{-1}$, ARROWs result in the highest optical losses among the interference-based optical waveguides. Similar to Bragg fibers, ARROWs are complex to fabricate. The small inner diameters and short lengths result in very small volumes of the

core. This may be an issue for analytical techniques that require larger volumes than a few nano- or picolitres in order to analyze the sample. However, White *et al.* [133] demonstrated how they could actually make use of these high transmission losses. They used an ARROW to couple light into a liquid-core optical ring resonator (LCORR) via evanescent interaction at the points of contact. The LCORR contained immobilized analytes on the inner surface, which could interact with the evanescent field, resulting in a sensing signal.

Liquid-core (LC-)ARROWs have been used for several other detection applications, such as UV-Vis absorbance spectroscopy [134], transmission measurements [135], fluorescence spectroscopy [136–138] and Raman spectroscopy [29,139]. The work of Yin et al. [137] and Rahman et al. [140] describes how LC-ARROW can be used for single-molecule detection due to the pico- and nanoliter volumes.

Due to their small size, ARROWs are highly applicable for use in microfluidics or on-chip applications. Various optical elements have been added onto LC-ARROW chips in such a way [141–144]. For example, multimode interference (MMI) waveguides based on ARROWs have been used in on-chip optofluidic interferometers [145–149]. Several of such integrated optofluidic interferometric devices have been demonstrated in optofluidic ring resonators [150] and Mach–Zehnder interferometers [151,152] and other optofluidic devices [153,154]. Stambaugh et al. [155] presented an MMI-ARROW device with a fluorescence probe for the detection of single SARS-CoV-2 and influenza A antigens.

Bernini *et al.* [156] fabricated a liquid-core/liquid-cladding integrated ARROW device, which reduced optical losses in ARROWs. The design is different from the above-mentioned applications, where thin films are used, but makes use of the same guiding principle.

To our knowledge, until now no researchers have made an effort in using LC-ARROWs for the design of photo microreactors, despite their success in sensing applications. This may be because of the relatively high transmission losses, meaning that the waveguide must be made quite short and volumes may be too low to initiate and study photochemical reactions.

## 3.4 Conclusions

There are many different ways to use LCW-based photoreactors for in-situ detection. The low light losses and possibilities for coupling with analytical techniques are great assets

for the design of a photoreactor. Due to the direct irradiation within the core, optimum illumination of the whole sample can be reached, which can be difficult with other types of reactor cells. However, compared to microfluidic devices, the fabrication of interference-based optical waveguides can be quite tricky due to the thin-layered materials that are used and design flexibility is lacking, which may be considered as a disadvantage.



The waveguides discussed in this review each possess several unique advantages, but also disadvantages. The PCFs show low losses and small volumes compared to the polymer and aerogel LCWs, which may result in a higher reaction rate. Especially Kagomé fibers show very promising results for coupling to advanced analytical techniques. However, the small volumes of PCFs may also be a limitation for the detection of analytes at very low concentrations, which is likely to occur when photodegradation products are formed in low quantities. A unique advantage of the Teflon AF LCWs is their gas permeability, so photochemical processes can be studied under oxic vs anoxic conditions.

# References

[1] Z. Yuan, S. Das, R.A. Lazenby, R.J. White, Y.C. Park, Repetitive drug releases from light-activatable micron-sized liposomes, Colloids Surf A Physicochem Eng Asp. 625 (2021) 126778. https://doi.org/10.1016/j.colsurfa.2021.126778.

[2] A.C. Sun, D.J. Steyer, A.R. Allen, E.M. Payne, R.T. Kennedy, C.R.J. Stephenson, A droplet microfluidic platform for high-throughput photochemical reaction discovery, Nat Commun. 11 (2020) 1–6. https://doi.org/10.1038/s41467-020-19926-z.

[3] D.F. Earley, A. Guillou, D. van der Born, A.J. Poot, J.P. Holland, Microfluidic Preparation of 89Zr-Radiolabelled Proteins by Flow Photochemistry, Molecules. 26 (2021). https://doi.org/10.3390/MOLECULES26030764.

[4] D. Phillips, Light relief: photochemistry and medicine, Photochemical & Photobiological Sciences. 9 (2010) 1589–1596. https://doi.org/10.1039/C0PP00237B.

[5] W.L. Wang, Q.Y. Wu, N. Huang, Z. Bin Xu, M.Y. Lee, H.Y. Hu, Potential risks from UV/H2O2 oxidation and UV photocatalysis: A review of toxic, assimilable, and sensory-unpleasant transformation products, Water Res. 141 (2018) 109–125. https://doi.org/10.1016/j.watres.2018.05.005.

[6] N.M. Reis, G. Li Puma, A novel microfluidic approach for extremely fast and efficient photochemical transformations in fluoropolymer microcapillary films, Chemical Communications. 51 (2015) 8414–8417. https://doi.org/10.1039/C5CC01559F.

[7] I. Azzouz, Y.G. Habba, M. Capochichi-Gnambodoe, F. Marty, J. Vial, Y. Leprince-Wang, T. Bourouina, Zinc oxide nano-enabled microfluidic reactor for water purification and its applicability to volatile organic compounds, Microsystems & Nanoengineering 2. 4 (2018) 1–7. https://doi.org/10.1038/micronano.2017.93.

[8] J. Verduin, Photodegradation Products And Their Analysis In Food, Food Sci Nutr. 6 (2020) 1–16. https://doi.org/10.24966/FSN-1076/100067.

[9] S.A. Khayyat, L.S. Roselin, Recent progress in photochemical reaction on main components of some essential oils, Journal of Saudi Chemical Society. 22 (2018) 855–875. https://doi.org/10.1016/J.JSCS.2018.01.008.

[10] S.E. Duncan, H.H. Chang, Implications of Light Energy on Food Quality and Packaging Selection, Adv Food Nutr Res. 67 (2012) 25–73. https://doi.org/10.1016/B978-0-12-394598-3.00002-2.

[11] C. Miliani, L. Monico, M.J. Melo, S. Fantacci, E.M. Angelin, A. Romani, K. Janssens, Photochemistry of Artists Dyes and Pigments: Towards Better Understanding and Prevention of Colour Change in Works of Art, Angew. Chem. Int. Ed. 57 (2018) 7. https://doi.org/10.1002/ange.201802801.

[12] A. Chieli, C. Miliani, I. Degano, F. Sabatini, P. Tognotti, A. Romani, New insights into the fading mechanism of Geranium lake in painting matrix", Dyes and Pigments. 181 (2020) 108600. https://doi.org/10.1016/J.DYEPIG.2020.108600.

[13] B.W.J. Pirok, G. Moro, N. Meekel, S.V.J. Berbers, P.J. Schoenmakers, M.R. van Bommel, Mapping degradation pathways of natural and synthetic dyes with LC-MS: Influence of solvent on degradation mechanisms, J Cult Herit. 38 (2019) 29–36. https://doi.org/10.1016/J.CULHER.2019.01.003.

[14] X. Liu, M. Park, S.C. Beitel, C. Hoppe-Jones, X.Z. Meng, S.A. Snyder, Formation of nitrogenous disinfection byproducts in MP UV-based water treatments of natural organic matters: The role of nitrate, Water Res. 204 (2021) 117583. https://doi.org/10.1016/J.WATRES.2021.117583.

[15] G.S. Egerton, A.G. Morgan, The Photochemistry of Dyes II—Some Aspects of the Fading Process, Journal of the Society of Dyers and Colourists. 86 (1970) 242–249. https://doi.org/10.1111/j.1478-4408.1970.tb02954.x.

[16] C. Prüfert, R.D. Urban, T.G. Fischer, J. Villatoro, D. Riebe, T. Beitz, D. Belder, K. Zeitler, H.G. Löhmannsröben, In situ monitoring of photocatalyzed isomerization reactions on a microchip flow reactor by IR-MALDI ion mobility spectrometry, Anal Bioanal Chem. 412 (2020) 7899–7911. https://doi.org/10.1007/s00216-020-02923-y.

[17] L. Bliumkin, R. Dutta Majumdar, R. Soong, A. Adamo, J.P.D. Abbatt, R. Zhao, E. Reiner, A.J. Simpson, Development of an in Situ NMR Photoreactor To Study Environmental Photochemistry, Environ Sci Technol. 50 (2016) 5506–5516. https://doi.org/10.1021/acs.est.6b00361.

[18] I. Groeneveld, I. Bagdonaite, E. Beekwilder, F. Ariese, G.W. Somsen, M.R. van Bommel, Liquid Core Waveguide Cell with In Situ Absorbance Spectroscopy and Coupled to Liquid Chromatography for Studying Light-Induced Degradation, Anal Chem. 94 (2022) 7647–7654. https://doi.org/10.1021/acs.analchem.2c00886.

[19] M.J. den Uijl, Y.J.H.L. van der Wijst, I. Groeneveld, P.J. Schoenmakers, B.W.J. Pirok, M.R. van Bommel, Combining Photodegradation in a Liquid-Core-Waveguide Cell with Multiple-Heart-Cut Two-Dimensional Liquid Chromatography, Anal Chem. 94 (2022) 11055–11061. https://doi.org/10.1021/acs.analchem.2c01928.

[20] E.E. Coyle, M. Oelgemöller, Micro-photochemistry: Photochemistry in microstructured reactors. The new photochemistry of the future?, Photochemical and Photobiological Sciences. 7 (2008) 1313–1322. https://doi.org/10.1039/b808778d.

[21] H. Lu, M.A. Schmidt, K.F. Jensen, Photochemical reactions and on-line UV detection in microfabricated reactors, Lab Chip. 1 (2001) 22–28. https://doi.org/10.1039/b104037p.

[22] M. Khademalrasool, M. Farbod, M.D. Talebzadeh, The improvement of photocatalytic processes: Design of a photoreactor using high-power LEDs, Journal of Science: Advanced Materials and Devices. 1 (2016) 382–387. https://doi.org/10.1016/j.jsamd.2016.06.012.

[23] V.G. Bório, A.U. Fernandes, L. Silveira, Characterization of an ultraviolet irradiation chamber to monitor molecular photodegradation by Raman spectroscopy, Instrum Sci Technol. 44 (2016) 189–198. https://doi.org/10.1080/10739149.2015.1081936.

[24] R.W. Taylor, R.J. Coulston, F. Biedermann, S. Mahajan, J.J. Baumberg, O.A. Scherman, In Situ SERS Monitoring of Photochemistry within a Nanojunction Reactor, Nano Lett. 13 (2013) 5985–5990. https://doi.org/10.1021/nl403164c.

[25] D. Cambié, F. Zhao, V. Hessel, M.G. Debije, T. Noël, A Leaf-Inspired Luminescent Solar Concentrator for Energy-Efficient Continuous-Flow Photochemistry, Angewandte Chemie International Edition. 56 (2017) 1050–1054. https://doi.org/10.1002/ANIE.201611101.

[26] G.N. Ahn, M.J. Kim, S.J. Yim, B.M. Sharma, D.P. Kim, Chemical-Resistant Green Luminescent Concentrator-Based Photo-Microreactor via One-Touch Assembly of 3D-Printed Modules, ACS Sustain Chem Eng. 10 (2022) 3951–3959. https://doi.org/10.1021/ACSSUSCHEMENG.1C08240/SUPPL_FILE/SC1C08240_SI_002.MP4.

[27] C. Sambiagio, T. Noël, Flow Photochemistry: Shine Some Light on Those Tubes!, Trends Chem. 2 (2020) 92–106. https://doi.org/10.1016/j.trechm.2019.09.003.

[28] T. Dallas, P.K. Dasgupta, Light at the end of the tunnel: recent analytical applications of liquid-core waveguides, TrAC Trends in Analytical Chemistry. 23 (2004) 385–392. https://doi.org/10.1016/S0165-9936(04)00522-9.

[29] H. Schmidt, A.R. Hawkins, Optofluidic waveguides: I. Concepts and implementations, Microfluid Nanofluidics. 4 (2008) 3–16. https://doi.org/10.1007/s10404-007-0199-7.

[30] R.J. McQuitty, S. Unterkofler, T.G. Euser, P.St.J. Russell, P.J. Sadler, Rapid screening of photoactivatable metallodrugs: photonic crystal fibre microflow reactor coupled to ESI mass spectrometry, RSC Adv. 7 (2017) 37340–37348. https://doi.org/10.1039/C7RA06735F.

[31] P.K. Dasgupta, Z. Genfa, S.K. Poruthoor, S. Caldwell, S. Dong, S.-Y. Liu, High-Sensitivity Gas Sensors Based on Gas-Permeable Liquid Core Waveguides and Long-Path Absorbance Detection, (1998). https://doi.org/10.1021/ac980803t.

[32] X. Cheng, Z. Zhang, S. Tian, A novel long path length absorbance spectroscopy for the determination of ultra trace organophosphorus pesticides in vegetables and fruits, Spectrochim Acta A Mol Biomol Spectrosc. 67 (2007) 1270–1275. https://doi.org/10.1016/j.saa.2006.10.018.

[33] A.M. Cubillas, S. Unterkofler, T.G. Euser, B.J.M. Etzold, A.C. Jones, P.J. Sadler, P. Wasserscheid, P.S.J. Russell, Photonic crystal fibres for chemical sensing and photochemistry, Chem Soc Rev. 42 (2013) 8629–8648. https://doi.org/10.1039/c3cs60128e.

[34] H.S. Dutta, A.K. Goyal, V. Srivastava, S. Pal, Coupling light in photonic crystal waveguides: A review, Photonics Nanostruct. 20 (2016) 41–58. https://doi.org/10.1016/J.PHOTONICS.2016.04.001.

[35] F. Parandin, F. Heidari, Z. Rahimi, S. Olyaee, Two-Dimensional photonic crystal Biosensors: A review, Opt Laser Technol. 144 (2021) 107397. https://doi.org/10.1016/j.optlastec.2021.107397.

[36] S. Currivan, N. Upadhyay, B. Paull, Multi-channel capillaries and photonic crystal fibres for separation sciences, TrAC Trends in Analytical Chemistry. 102 (2018) 322–331. https://doi.org/10.1016/J.TRAC.2018.03.008.

[37] M. Kumar, A hollow waveguide Bragg reflector: A tunable platform for integrated photonics, Opt Laser Technol. 65 (2015) 5–13. https://doi.org/10.1016/J.OPTLASTEC.2014.06.009.

[38] G. Testa, C. Collini, L. Lorenzelli, R. Bernini, Planar silicon-polydimethylsiloxane optofluidic ring resonator sensors, IEEE Photonics Technology Letters. 28 (2016) 155–158. https://doi.org/10.1109/LPT.2015.2487680.

[39] R. Gupta, N.J. Goddard, Leaky waveguides (LWs) for chemical and biological sensing–A review and future perspective, Sens Actuators B Chem. 322 (2020) 128628. https://doi.org/10.1016/j.snb.2020.128628.

[40] P. Kozma, F. Kehl, E. Ehrentreich-Förster, C. Stamm, F.F. Bier, Integrated planar optical waveguide interferometer biosensors: A comparative review, Biosens Bioelectron. 58 (2014) 287–307. https://doi.org/10.1016/J.BIOS.2014.02.049.

[41] E. Benito-Peña, M.G. Valdés, B. Glahn-Martínez, M.C. Moreno-Bondi, Fluorescence based fiber optic and planar waveguide biosensors. A review, Anal Chim Acta. 943 (2016) 17. https://doi.org/10.1016/J.ACA.2016.08.049.

[42] R.N.M.J. Páscoa, I. v. Tóth, A.O.S.S. Rangel, Review on recent applications of the liquid waveguide capillary cell in flow based analysis techniques to enhance the sensitivity of spectroscopic detection methods, Anal Chim Acta. 739 (2012) 1–13. https://doi.org/10.1016/j.aca.2012.05.058.

[43] S.A. Pidenko, N.A. Burmistrova, A.A. Shuvalov, A.A. Chibrova, Y.S. Skibina, I.Y. Goryacheva, Microstructured optical fiber-based luminescent biosensing: Is there any light at the end of the tunnel? - A review, Anal Chim Acta. 1019 (2018) 14–24. https://doi.org/10.1016/j.aca.2017.12.010.

[44] T.H. Rehm, Reactor Technology Concepts for Flow Photochemistry, ChemPhotoChem. 4 (2019) 235–254. https://doi.org/10.1002/cptc.201900247.

[45] K. Hofstadler, R. Bauer, S. Novallc, G. Heisler, New Reactor Design for Photocatalytic Wastewater Treatment with TiO2 Immobilized on Fused-Silica Glass Fibers: Photomineralization of 4-Chlorophenol, Environ Sci Technol. 28 (1994) 670–674. https://doi.org/10.1021/es00053a021.

[46] R.H. Byrne, E. Kaltenbacher, Use of liquid core waveguides for long pathlength absorbance spectroscopy: Principles and practice, Limnol Oceanogr. 46 (2001) 740–742. https://doi.org/10.4319/lo.2001.46.3.0740.

[47] T. Rubles, D. Paige, C. Anastasio, Lens-coupled liquid core waveguide for ultraviolet-visible absorption spectroscopy, Review of Scientific Instruments. 77 (2006) 073103. https://doi.org/10.1063/1.2219973.

[48] P.K. Dasgupta, Multipath cells for extending dynamic range of optical absorbance measurements, Anal Chem. 56 (1984) 1401–1403. https://doi.org/10.1021/ac00272a044.

[49] J. Stone, Optical Transmission Loss in Liquid-Core Hollow Fibers, IEEE J Quantum Electron. 8 (1972) 386–388. https://doi.org/10.1109/JQE.1972.1076966.

[50] J.H. Lowry, Optical characteristics of Teflon AF fluoroplastic materials, Optical Engineering. 31 (2006) 1982. https://doi.org/10.1117/12.59910.

[51] M.K. Yang, Optical properties of Teflon® AF amorphous fluoropolymers, Journal of Micro/Nanolithography, MEMS, and MOEMS. 7 (2008) 033010. https://doi.org/10.1117/1.2965541.

[52] T. Rubles, D. Paige, C. Anastasio, Lens-coupled liquid core waveguide for ultraviolet-visible absorption spectroscopy, Review of Scientific Instruments. 77 (2006) 1–4. https://doi.org/10.1063/1.2219973.

[53] R. Altkorn, I. Koev, R.P. Van Duyne, M. Litorja, Low-loss liquid-core optical fiber for low-refractive-index liquids: fabrication, characterization, and application in Raman spectroscopy, Appl Opt. 36 (1997) 8992. https://doi.org/10.1364/ao.36.008992.

[54] P.K. Dasgupta, Z. Genfa, J. Li, C.B. Boring, S. Jambunathan, R. Al-Horr, Luminescence Detection with a Liquid Core Waveguide, Anal Chem. 71 (1999) 1400–1407. https://doi.org/10.1021/ac981260q.

[55] W.R. Melchert, F.R.P. Rocha, A greener and highly sensitive flow-based procedure for carbaryl determination exploiting long pathlength spectrophotometry and photochemical waste degradation, Talanta. 81 (2010) 327–333. https://doi.org/10.1016/J.TALANTA.2009.12.005.

[56] D.L. Rocha, F.R.P. Rocha, A multi-pumping flow system with on-line photochemical conversion and improved sensitivity for phosphorus fractionation in freshwaters, Int J Environ Anal Chem. 93 (2013) 1389–1401. https://doi.org/10.1080/03067319.2012.746324.

[57] J.Z. Zhang, C. Kelble, F.J. Millero, Gas-segmented continuous flow analysis of iron in water with a long liquid waveguide capillary flow cell, Anal Chim Acta. 438 (2001) 49–57. https://doi.org/10.1016/S0003-2670(01)01031-5.

[58] J.Z. Zhang, J. Chi, Automated analysis of nanomolar concentrations of phosphate in natural waters with liquid waveguide, Environ Sci Technol. 36 (2002) 1048–1053. https://doi.org/10.1021/es011094v.

[59] K. Fujiwara, S. Ito, Application of waveguiding in solutions for absorption and fluorescence spectrometry, TrAC Trends in Analytical Chemistry. 10 (1991) 184–190. https://doi.org/10.1016/0165-9936(91)85019-N.

[60] K. Fujiwara, I. Seiji, R.-E. Kojyo, H. Tsubota, R.L. Carter, Side-View Type of Waveguide Flow Cells for Fluorimetry as a Detector for Flow Injection Analysis of Lead, Appl Spectrosc. 46 (1992) 1032–1039. https://doi.org/10.1366/0003702924124286.

[61] Z. Liu, J. Pawliszyn, Capillary isoelectric focusing of proteins with liquid core waveguide laser-induced fluorescence whole column imaging detection, Anal Chem. 75 (2003) 4887–4894. https://doi.org/10.1021/ac034587m.

[62] T. Frosch, D. Yan, J. Popp, Ultrasensitive fiber enhanced UV resonance Raman sensing of drugs, Anal Chem. 85 (2013) 6264–6271. https://doi.org/10.1021/ac400365f.

[63] S. Tanikkul, J. Jakmunee, M. Rayanakorn, K. Grudpan, B.J. Marquardt, G.M. Gross, B.J. Prazen, L.W. Burgess, G.D. Christian, R.E. Synovec, Characterization and use of a Raman liquid-core waveguide

sensor using preconcentration principles, Talanta. 59 (2003) 809–816. https://doi.org/10.1016/S0039-9140(02)00623-9.

[64] R.J. Dijkstra, C.J. Slooten, A. Stortelder, J.B. Buijs, F. Ariese, U.A.Th. Brinkman, C. Gooijer, Liquid-core waveguide technology for coupling column liquid chromatography and Raman spectroscopy, J Chromatogr A. 918 (2001) 25–36. https://doi.org/10.1016/S0021-9673(01)00721-X.

[65] Y. Tian, L. Zhang, J. Zuo, Z. Li, S. Gao, G. Lu, Raman sensitivity enhancement for aqueous absorbing sample using Teflon-AF 2400 liquid core optical fibre cell, Anal Chim Acta. 581 (2007) 154–158. https://doi.org/10.1016/j.aca.2006.07.082.

[66] R.J. Dijkstra, A.N. Bader, G.P. Hoornweg, U.A.T. Brinkman, C. Gooijer, On-Line Coupling of Column Liquid Chromatography and Raman Spectroscopy Using a Liquid Core Waveguide, Anal Chem. 71 (1999) 4575–4579. https://doi.org/10.1021/ac9902648.

[67] R.J. Dijkstra, F. Ariese, C. Gooijer, U.A.T. Brinkman, Raman spectroscopy as a detection method for liquid-separation techniques, TrAC - Trends in Analytical Chemistry. 24 (2005) 304–323. https://doi.org/10.1016/j.trac.2004.11.022.

[68] R. Altkorn, M.D. Malinsky, R.P. Van Duyne, I. Koev, Intensity considerations in liquid core optical fiber Raman spectroscopy, Appl Spectrosc. 55 (2001) 373–381. https://doi.org/10.1366/0003702011951939.

[69] D. Yan, J. Popp, M.W. Pletz, T. Frosch, Fiber enhanced Raman sensing of levofloxacin by PCF bandgap-shifting into the visible range, Analytical Methods. 10 (2018) 586–592. https://doi.org/10.1039/c7ay02398g.

[70] M. Holtz, P.K. Dasgupta, G. Zhang, Small-volume Raman spectroscopy with a liquid core waveguide, Anal Chem. 71 (1999) 2934–2938. https://doi.org/10.1021/ac981261i.

[71] R. Manor, A. Datta, I. Ahmad, M. Holtz, S. Gangopadhyay, T. Dallas, Microfabrication and characterization of liquid core waveguide glass channels coated with teflon AF, IEEE Sens J. 3 (2003) 687–692. https://doi.org/10.1109/JSEN.2003.820342.

[72] D. Kottke, B.B. Burckhardt, J. Breitkreutz, B. Fischer, Application and validation of a coaxial liquid core waveguide fluorescence detector for the permeation analysis of desmopressin acetate, Talanta. 226 (2021). https://doi.org/10.1016/j.talanta.2021.122145.

[73] C. Lai, G. Chen, L. Chen, J. Li, Q. Liu, S. Fang, Integrated Surface-Enhanced Raman Spectroscopy (SERS) Chip Based on a Total Reflection Liquid Core Waveguide, Appl Spectrosc. 71 (2017) 2021–2025. https://doi.org/10.1177/0003702817711147.

[74] J. Li, P.K. Dasgupta, Z. Genfa, Transversely illuminated liquid core waveguide based fluorescence detection Fluorometric flow injection determination of aqueous ammonium/ammonia, 1999. https://ac.els-cdn.com/S0039914099001484/1-s2.0-S0039914099001484-main.pdf?_tid=d4080a4e-80f4-4c0b-a8fc-e5b644165bdc&acdnat=1546953996_7be9f2ebe2ae497508e3025851f36c1d (accessed January 8, 2019).

[75] M. Brzozowski, M. O'Brien, S. V Ley, A. Polyzos, Flow chemistry: Intelligent processing of gas-liquid transformations using a tube-in-tube reactor, Acc Chem Res. 48 (2015) 349–362. https://doi.org/10.1021/ar500359m.

[76] M. O'Brien, N. Taylor, A. Polyzos, I.R. Baxendale, S. V. Ley, Hydrogenation in flow: Homogeneous and heterogeneous catalysis using Teflon AF-2400 to effect gas-liquid contact at elevated pressure, Chem Sci. 2 (2011) 1250–1257. https://doi.org/10.1039/c1sc00055a.

[77] M. O'Brien, I. Baxendale, S. Ley, Flow Ozonolysis Using a Semipermeable Teflon AF-2400 Membrane, Synfacts. 2010 (2010) 1199–1199. https://doi.org/10.1055/s-0030-1258661.

[78] E.C. Aka, E. Wimmer, E. Barré, D. Cortés-Borda, T. Ekou, L. Ekou, M. Rodriguez-Zubiri, F.X. Felpin, Comparing Gas-Liquid Segmented and Tube-in-Tube Setups for the Aerobic Dimerization of Desmethoxycarpacine with an Automated Flow Platform, Org Process Res Dev. 24 (2020) 745–751. https://doi.org/10.1021/ACS.OPRD.9B00525/SUPPL_FILE/OP9B00525_SI_001.PDF.

[79] K. Skowerski, S.J. Czarnocki, P. Knapkiewicz, Tube-In-Tube Reactor as a Useful Tool for Homo- and Heterogeneous Olefin Metathesis under Continuous Flow Mode, ChemSusChem. 7 (2014) 536–542. https://doi.org/10.1002/CSSC.201300829.

[80] L. Yang, K.F. Jensen, Mass transport and reactions in the tube-in-tube reactor, Org Process Res Dev. 17 (2013) 927–933. https://doi.org/10.1021/op400085a.

[81] F. Mastronardi, B. Gutmann, C. Oliver Kappe, Continuous flow generation and reactions of anhydrous diazomethane using a teflon AF-2400 tube-in-tube reactor, Org Lett. 15 (2013) 5590–5593. https://doi.org/10.1021/ol4027914.

[82] A. Polyzos, M. O'Brien, T.P. Petersen, I.R. Baxendale, S. v. Ley, The Continuous-Flow Synthesis of Carboxylic Acids using CO2 in a Tube-In-Tube Gas Permeable Membrane Reactor, Angewandte Chemie - International Edition. 50 (2011) 1190–1193. https://doi.org/10.1002/anie.201006618.

[83] S. Ponce, H. Christians, A. Drochner, B.J.M. Etzold, An Optical Microreactor Enabling In Situ Spectroscopy Combined with Fast Gas-Liquid Mass Transfer, Chem Ing Tech. 90 (2018) 1855–1863. https://doi.org/10.1002/cite.201800061.

[84] I. Groeneveld, S.E. Schoemaker, G.W. Somsen, F. Ariese, M.R. van Bommel, Characterization of a liquid-core waveguide cell for studying the chemistry of light-induced degradation, Analyst. 146 (2021) 3197–3207. https://doi.org/10.1039/d1an00272d.

[85] G. Eris, D. Sanli, Z. Ulker, S.E. Bozbag, A. Jonás, A. Kiraz, C. Erkey, Three-dimensional optofluidic waveguides in hydrophobic silica aerogels via supercritical fluid processing, J Supercrit Fluids. 73 (2013) 28–33. https://doi.org/10.1016/j.supflu.2012.11.001.

[86] Y. Özbakır, A. Jonáš, A. Kiraz, C. Erkey, Total internal reflection-based optofluidic waveguides fabricated in aerogels, J Solgel Sci Technol. 84 (2017) 522–534. https://doi.org/10.1007/s10971-017-4426-8.

[87] Y. Özbakır, A. Jonáš, A. Kiraz, C. Erkey, A new type of microphotoreactor with integrated optofluidic waveguide based on solid-air nanoporous aerogels, R Soc Open Sci. 5 (2018). https://doi.org/10.1098/rsos.180802.

[88] Y. Özbakir, A. Jonáš, A. Kiraz, C. Erkey, Photocatalytic transformation in aerogel-based optofluidic microreactors, in: S.M. García-Blanco, P. Cheben (Eds.), Integrated Optics: Devices, Materials, and Technologies XXII, SPIE, 2018: p. 84. https://doi.org/10.1117/12.2292309.

[89] L. Xiao, T.A. Birks, Optofluidic microchannels in aerogel, Opt Lett. 36 (2011) 3275. https://doi.org/10.1364/ol.36.003275.

[90] B. Yalizay, Y. Morova, Y. Ozbakir, A. Jonas, C. Erkey, A. Kiraz, S. Akturk, Optofluidic waveguides written in hydrophobic silica aerogels with a femtosecond laser, in: J.-E. Broquin, G. Nunzi Conti (Eds.), Integrated Optics: Devices, Materials, and Technologies XIX, 2015: p. 936518. https://doi.org/10.1117/12.2077132.

[91] Y. Özbakir, A. Jonas, A. Kiraz, C. Erkey, Aerogels for optofluidic waveguides, Micromachines (Basel). 8 (2017). https://doi.org/10.3390/mi8040098.

[92] B. Yalizay, Y. Morova, K. Dincer, Y. Ozbakir, A. Jonas, C. Erkey, A. Kiraz, S. Akturk, Versatile liquid-core optofluidic waveguides fabricated in hydrophobic silica aerogels by femtosecond-laser ablation, Opt Mater (Amst). 47 (2015) 478–483. https://doi.org/10.1016/j.optmat.2015.06.024.

[93] Y. Özbakır, A. Jonáš, A. Kiraz, C. Erkey, An aerogel-based photocatalytic microreactor driven by light guiding for degradation of toxic pollutants, Chemical Engineering Journal. 409 (2021) 128108. https://doi.org/10.1016/J.CEJ.2020.128108.

[94] A.R. Hawkins, H. Schmidt, Optofluidic waveguides: II. Fabrication and structures, Microfluid Nanofluidics. 4 (2008) 17–32. https://doi.org/10.1007/s10404-007-0194-z.

[95] K. Mileńko, D.J.J. Hu, P.P. Shum, T.R. Woliński, Hollow-Core Bragg Fiber for Bio-Sensing Applications, Acta Phys Pol A. 118 (2010) 1205–1208. https://doi.org/10.12693/APhysPolA.118.1205.

[96] Y. Sun, X. Yu, T.N. Nam, P. Shum, C.K. Yien, Long path-length axial absorption detection in photonic crystal fiber, Anal Chem. 80 (2008) 4220–4224. https://doi.org/10.1021/ac800417n.

[97] J.S.Y. Chen, T.G. Euser, N.J. Farrer, P.J. Sadler, M. Scharrer, P.St.J. Russell, Photochemistry in Photonic Crystal Fiber Nanoreactors, Chemistry - A European Journal. 16 (2010) 5607–5612. https://doi.org/10.1002/chem.201000496.

[98] S.O. Konorov, A.M. Zheltikov, M. Scalora, Photonic-crystal fiber as a multifunctional optical sensor and sample collector, Opt Express. 13 (2005) 3454. https://doi.org/10.1364/opex.13.003454.

[99] G.O.S. Williams, T.G. Euser, P.S.J. Russell, A.C. Jones, Spectrofluorimetry with attomole sensitivity in photonic crystal fibres, Methods Appl Fluoresc. 1 (2013) 015003. https://doi.org/10.1088/2050-6120/1/1/015003.

[100] M. Azkune, T. Frosch, E. Arrospide, G. Aldabaldetreku, I. Bikandi, J. Zubia, J. Popp, T. Frosch, Liquid-Core Microstructured Polymer Optical Fiber as Fiber-Enhanced Raman Spectroscopy Probe for

Glucose Sensing, Journal of Lightwave Technology. 37 (2019) 2981–2988. https://doi.org/10.1109/JLT.2019.2908447.

[101] S. Wolf, T. Frosch, J. Popp, M.W. Pletz, T. Frosch, Highly Sensitive Detection of the Antibiotic Ciprofloxacin by Means of Fiber Enhanced Raman Spectroscopy, Molecules. 24 (2019) 4512. https://doi.org/10.3390/molecules24244512.

[102] D. Yan, T. Frosch, J. Kobelke, J. Bierlich, J. Popp, M.W. Pletz, T. Frosch, Fiber-Enhanced Raman Sensing of Cefuroxime in Human Urine, Anal Chem. 90 (2018) 13243–13248. https://doi.org/10.1021/acs.analchem.8b01355.

[103] A. V. Markin, N.E. Markina, I.Y. Goryacheva, Raman spectroscopy based analysis inside photonic-crystal fibers, TrAC Trends in Analytical Chemistry. 88 (2017) 185–197. https://doi.org/10.1016/j.trac.2017.01.003.

[104] B. Temelkuran, S.D. Hart, G. Benoit, J.D. Joannopoulos, Y. Fink, Wavelength-scalable hollow optical fibres with large photonic bandgaps for CO2 laser transmission, Nature. 420 (2002) 650–653. https://doi.org/10.1038/nature01275.

[105] K. Kuriki, O. Shapira, S.D. Hart, G. Benoit, Y. Kuriki, J.F. Viens, M. Bayindir, J.D. Joannopoulos, Y. Fink, Hollow multilayer photonic bandgap fibers for NIR applications, Opt Express. 12 (2004) 1510. https://doi.org/10.1364/OPEX.12.001510.

[106] L. Shang, S. Feng, Liquid-Filled Hollow Core Bragg Fiber Sensors Using Different Bandgaps for High-Refractive-Index Sensing, IEEE Photonics J. 11 (2019). https://doi.org/10.1109/JPHOT.2019.2928601.

[107] J. Li, H. Qu, M. Skorobogatiy, Simultaneous monitoring the real and imaginary parts of the analyte refractive index using liquid-core photonic bandgap Bragg fibers, Opt Express. 23 (2015) 22963. https://doi.org/10.1364/oe.23.022963.

[108] K.J. Rowland, S. Afshar, A. Stolyarov, Y. Fink, T.M. Monro, Bragg waveguides with low-index liquid cores, Opt Express. 20 (2012) 48. https://doi.org/10.1364/oe.20.000048.

[109] H. Qu, M. Skorobogatiy, Liquid-core low-refractive-index-contrast Bragg fiber sensor, Appl Phys Lett. 98 (2011) 201114. https://doi.org/10.1063/1.3592758.

[110] D.J.J. Hu, G. Alagappan, Y.-K. Yeo, P.P. Shum, P. Wu, Broadband transmission in hollow-core Bragg fibers with geometrically distributed multilayered cladding, Opt Express. 18 (2010) 18671. https://doi.org/10.1364/oe.18.018671.

[111] K. Kurokawa, K. Nakajima, K. Tsujikawa, T. Yamamoto, K. Tajima, Ultra-Wideband Transmission Over Low Loss PCF, Journal of Lightwave Technology. 27 (2009) 1653–1662. https://doi.org/10.1109/JLT.2009.2014174.

[112] J.M. Dudley, G. Genty, S. Coen, Supercontinuum generation in photonic crystal fiber, Rev Mod Phys. 78 (2006) 1135–1184. https://doi.org/10.1103/REVMODPHYS.78.1135/FIGURES/28/MEDIUM.

[113] T.M. Monro, W. Belardi, K. Furusawa, J.C. Baggett, N.G.R. Broderick, D.J. Richardson, Sensing with microstructured optical fibres, Meas Sci Technol. 12 (2001) 854. https://doi.org/10.1088/0957-0233/12/7/318.

[114] B. Wajnchold, A. Umińska, M. Grabka, D. Kotas, S. Pustelny, W. Gawlik, Suspended-core optical fibres for organic dye absorption spectroscopy, in: L.R. Jaroszewicz (Ed.), Fifth European Workshop on Optical Fibre Sensors, SPIE, 2013. https://doi.org/10.1117/12.2026019.

[115] J.B. Jensen, P.E. Hoiby, G. Emiliyanov, O. Bang, L.H. Pedersen, A. Bjarklev, A. van Eijkelenborg, M. Large, A. Argyros, J. Zagari, S. Manos, N. Issa, I. Bassett, S. Fleming, R. McPhedran, Cm. de Sterke, N. Nicorovici, J. Baker Jr, W. Wadsworth, G. Bouwmans, J. Knight, Ps. Russell, J. Jensen, L. Pedersen, P. Hoiby, L. Nielsen, T. Hansen, J. Folkenberg, J. Riishede, D. Noordegraaf, K. Nielsen, A. Carlsen, A. Bjarklev, Selective detection of antibodies in microstructured polymer optical fibers, Optics Express, Vol. 13, Issue 15, Pp. 5883-5889. 13 (2005) 5883–5889. https://doi.org/10.1364/OPEX.13.005883.

[116] C. Markos, W. Yuan, K. Vlachos, G.E. Town, O. Bang, Label-free biosensing with high sensitivity in dual-core microstructured polymer optical fibers, Opt Express. 19 (2011) 7790. https://doi.org/10.1364/OE.19.007790.

[117] M.T. Myaing, J.Y. Ye, T.B. Norris, T. Thomas, J.R. Baker, Jr., W.J. Wadsworth, G. Bouwmans, J.C. Knight, P.St.J. Russell, Enhanced two-photon biosensing with double-clad photonic crystal fibers, Opt Lett. 28 (2003) 1224. https://doi.org/10.1364/OL.28.001224.

[118] D. Pristinski, H. Du, Solid-core photonic crystal fiber as a Raman spectroscopy platform with a silica core as an internal reference, Opt Lett. 31 (2006) 3246. https://doi.org/10.1364/OL.31.003246.

[119] C. Strutynski, J. Picot-Clémente, F. Désévédavy, J.C. Jules, G. Gadret, B. Kibler, F. Smektala, Compact supercontinuum sources based on tellurite suspended core fibers for absorption spectroscopy beyond 2 μm, Laser Phys Lett. 13 (2016) 075402. https://doi.org/10.1088/1612-2011/13/7/075402.

[120] L. Liu, Z. Tang, C. He, S. Korposh, S. Lou, S.P. Morgan, Chemically Functionalised Suspended-Core Fibre for Ammonia Gas Detection, Journal of Lightwave Technology. 39 (2021) 5197–5205. https://doi.org/10.1109/JLT.2021.3083094.

[121] T.G. Euser, J.S.Y. Chen, M. Scharrer, P.S.J. Russell, N.J. Farrer, P.J. Sadler, Quantitative broadband chemical sensing in air-suspended solid-core fibers, J Appl Phys. 103 (2008). https://doi.org/10.1063/1.2924408.

[122] A.S. Webb, Suspended-core holey fiber for evanescent-field sensing, Optical Engineering. 46 (2007) 010503. https://doi.org/10.1117/1.2430505.

[123] W. Talataisong, R. Ismaeel, M. Beresna, G. Brambilla, Suspended-Core Microstructured Polymer Optical Fibers and Potential Applications in Sensing, Sensors. 19 (2019) 3449. https://doi.org/10.3390/s19163449.

[124] F. Couny, F. Benabid, P.J. Roberts, P.S. Light, M.G. Raymer, Generation and photonic guidance of multi-octave optical-frequency combs, Science (1979). 318 (2007) 1118–1121. https://doi.org/10.1126/SCIENCE.1149091/SUPPL_FILE/COUNY.SOM.PDF.

[125] F.M. Cox, A. Argyros, M.C.J. Large, S. Kalluri, Surface enhanced Raman scattering in a hollow core microstructured optical fiber, Opt Express. 15 (2007) 13675. https://doi.org/10.1364/OE.15.013675.

[126] G.O.S. Williams, T.G. Euser, P.S.J. Russell, A.C. Jones, Spectrofluorimetry with attomole sensitivity in photonic crystal fibres, Methods Appl Fluoresc. 1 (2013) 015003. https://doi.org/10.1088/2050-6120/1/1/015003.

[127] G.O.S. Williams, J.S.Y. Chen, T.G. Euser, P.St.J. Russell, A.C. Jones, Photonic crystal fibre as an optofluidic reactor for the measurement of photochemical kinetics with sub-picomole sensitivity, Lab Chip. 12 (2012) 3356. https://doi.org/10.1039/c2lc40062f.

[128] A.M. Cubillas, M. Schmidt, M. Scharrer, T.G. Euser, B.J.M. Etzold, N. Taccardi, P. Wasserscheid, P.S.J. Russell, Ultra-Low Concentration Monitoring of Catalytic Reactions in Photonic Crystal Fiber, Chemistry - A European Journal. 18 (2012) 1586–1590. https://doi.org/10.1002/chem.201102424.

[129] A.M. Cubillas, M. Schmidt, T.G. Euser, N. Taccardi, S. Unterkofler, P.S.J. Russell, P. Wasserscheid, B.J.M. Etzold, In Situ Heterogeneous Catalysis Monitoring in a Hollow-Core Photonic Crystal Fiber Microflow Reactor, Adv Mater Interfaces. 1 (2014) 1300093. https://doi.org/10.1002/admi.201300093.

[130] A.M. Cubillas, X. Jiang, T.G. Euser, N. Taccardi, B.J.M. Etzold, P. Wasserscheid, P.St.J. Russell, Photochemistry in a soft-glass single-ring hollow-core photonic crystal fibre, Analyst. 142 (2017) 925–929. https://doi.org/10.1039/C6AN02144A.

[131] S. Unterkofler, R.J. McQuitty, T.G. Euser, N.J. Farrer, P.J. Sadler, P.S.J. Russell, Microfluidic integration of photonic crystal fibers for online photochemical reaction analysis., Opt Lett. 37 (2012) 1952–4. https://doi.org/10.1364/OL.37.001952.

[132] H.A. MacLeod, Thin-Film Optical Filters, Tucson, Arizona, USA, 2001. https://doi.org/10.1201/9781420033236.

[133] I.M. White, H. Oveys, X. Fan, Integrated multiplexed biosensors based on liquid core optical ring resonators and antiresonant reflecting optical waveguides, Appl. Phys. Lett. 89 (2006) 191106. https://doi.org/10.1063/1.2387112.

[134] R. Bernini, E. De Nuccio, A. Minardo, L. Zeni, P.M. Sarro, Integrated silicon optical sensors based on hollow core waveguide, in: J.A. Kubby, G.T. Reed (Eds.), Silicon Photonics II, 2007: p. 647714. https://doi.org/10.1117/12.700410.

[135] S. Campopiano, R. Bernini, L. Zeni, P.M. Sarro, Microfluidic sensor based on integrated optical hollow waveguides, Opt Lett. 29 (2004) 1894. https://doi.org/10.1364/OL.29.001894.

[136] D. Yin, J.P. Barber, A.R. Hawkins, H. Schmidt, Highly efficient fluorescence detection in picoliter volume liquid-core waveguides, Appl Phys Lett. 87 (2005) 211111. https://doi.org/10.1063/1.2135378.

[137] D. Yin, D.W. Deamer, H. Schmidt, J.P. Barber, A.R. Hawkins, Single-molecule detection sensitivity using planar integrated optics on a chip, Opt Lett. 31 (2006) 2136. https://doi.org/10.1364/OL.31.002136.

[138] T. Wall, J. McMurray, G. Meena, V. Ganjalizadeh, H. Schmidt, A.R. Hawkins, Optofluidic Lab-on-a-Chip Fluorescence Sensor Using Integrated Buried ARROW (bARROW) Waveguides, Micromachines (Basel). 8 (2017). https://doi.org/10.3390/MI8080252.

[139] P. Measor, L. Seballos, D. Yin, J.P. Barber, A.R. Hawkins, J. Zang, H. Schmidt, Integrated ARROW Waveguide for Molecule Specific Surface-enhanced Raman Sensing, IEEE. (2006) 181–182.

[140] M. Rahman, M. Harrington, M.A. Stott, Y. Li, M.J.N. Sampad, T.D. Yuzvinsky, A.R. Hawkins, H. Schmidt, Optical trapping assisted detection rate enhancement of single molecules on a nanopore optofluidic chip, Optica. 6 (2019) 1130. https://doi.org/10.1364/OPTICA.6.001130.

[141] C. Grillet, P. Domachuk, V. Ta'Eed, E. Mägi, J.A. Bolger, B.J. Eggleton, Compact tunable microfluidic interferometer, Opt Express. 12 (2004) 5440–5447.

[142] A. Nitkowski, A. Baeumner, M. Lipson, On-chip spectrophotometry for bioanalysis using microring resonators, Biomed Opt Express. 2 (2011) 271. https://doi.org/10.1364/boe.2.000271.

[143] F. Prieto, B. Sepúlveda, A. Calle, A. Llobera, C. Domínguez, A. Abad, A. Montoya, L.M. Lechuga, An integrated optical interferometric nanodevice based on silicon technology for biosensor applications, Nanotechnology. 14 (2003) 907–912. https://doi.org/10.1088/0957-4484/14/8/312.

[144] G. Testa, G. Persichetti, R. Bernini, Liquid core ARROW waveguides: A promising photonic structure for integrated optofluidic microsensors, Micromachines (Basel). 7 (2016). https://doi.org/10.3390/mi7030047.

[145] L.K. Chin, A.Q. Liu, Y.C. Soh, C.S. Lim, C.L. Lin, A reconfigurable optofluidic Michelson interferometer using tunable droplet grating, Lab Chip. 10 (2010) 1072–1078. https://doi.org/10.1039/b920412a.

[146] P. Domachuk, C. Grillet, V. Ta'Eed, E. Mägi, J. Bolger, B.J. Eggleton, L.E. Rodd, J. Cooper-White, Microfluidic interferometer, Appl Phys Lett. 86 (2005). https://doi.org/10.1063/1.1849415.

[147] D. Ozcelik, J.W. Parks, T.A. Wall, M.A. Stott, H. Cai, J.W. Parks, A.R. Hawkins, H. Schmidt, Optofluidic wavelength division multiplexing for single-virus detection, Proc Natl Acad Sci U S A. 112 (2015) 12933–12937. https://doi.org/10.1073/pnas.1511921112.

[148] F. Yu, K. Yamamoto, X. Piao, S. Yokoyama, Multimode interference waveguide switch of electro-optic polymer with tapered access waveguides, Phys Procedia. 14 (2011) 25–28. https://doi.org/10.1016/j.phpro.2011.05.006.

[149] R. Bernini, G. Testa, L. Zeni, P.M. Sarro, A 2 × 2 optofluidic multimode interference coupler, in: IEEE Journal on Selected Topics in Quantum Electronics, 2009: pp. 1478–1484. https://doi.org/10.1109/JSTQE.2009.2020996.

[150] G. Testa, Y. Huang, P.M. Sarro, L. Zeni, R. Bernini, Integrated silicon optofluidic ring resonator, Appl Phys Lett. 97 (2010). https://doi.org/10.1063/1.3496027.

[151] R. Bernini, G. Testa, L. Zeni, P.M. Sarro, Integrated optofluidic Mach-Zehnder interferometer based on liquid core waveguides, Appl Phys Lett. 93 (2008) 1–4. https://doi.org/10.1063/1.2957031.

[152] G. Testa, Y. Huang, P.M. Sarro, L. Zeni, R. Bernini, High-visibility optofluidic Mach–Zehnder interferometer, Opt Lett. 35 (2010) 1584. https://doi.org/10.1364/ol.35.001584.

[153] E.S. Hamilton, V. Ganjalizadeh, J.G. Wright, H. Schmidt, A.R. Hawkins, 3D Hydrodynamic Focusing in Microscale Optofluidic Channels Formed with a Single Sacrificial Layer, Micromachines (Basel). 11 (2020). https://doi.org/10.3390/MI11040349.

[154] M.A. Stott, V. Ganjalizadeh, M. Olsen, M. Orfila, J. McMurray, H. Schmidt, A.R. Hawkins, Optimized ARROW-Based MMI Waveguides for High Fidelity Excitation Patterns for Optofluidic Multiplexing, IEEE J Quantum Electron. 54 (2018). https://doi.org/10.1109/JQE.2018.2816120.

[155] A. Stambaugh, J.W. Parks, M.A. Stott, G.G. Meena, A.R. Hawkins, H. Schmidt, Optofluidic multiplex detection of single SARS-CoV-2 and influenza A antigens using a novel bright fluorescent probe assay, Proc Natl Acad Sci U S A. 118 (2021). https://doi.org/10.1073/PNAS.2103480118.

[156] R. Bernini, E. De Nuccio, A. Minardo, L. Zeni, P.M. Sarro, Liquid-core/liquid-cladding integrated silicon ARROW waveguides, Opt Commun. 281 (2008) 2062–2066. https://doi.org/10.1016/j.optcom.2007.11.070.

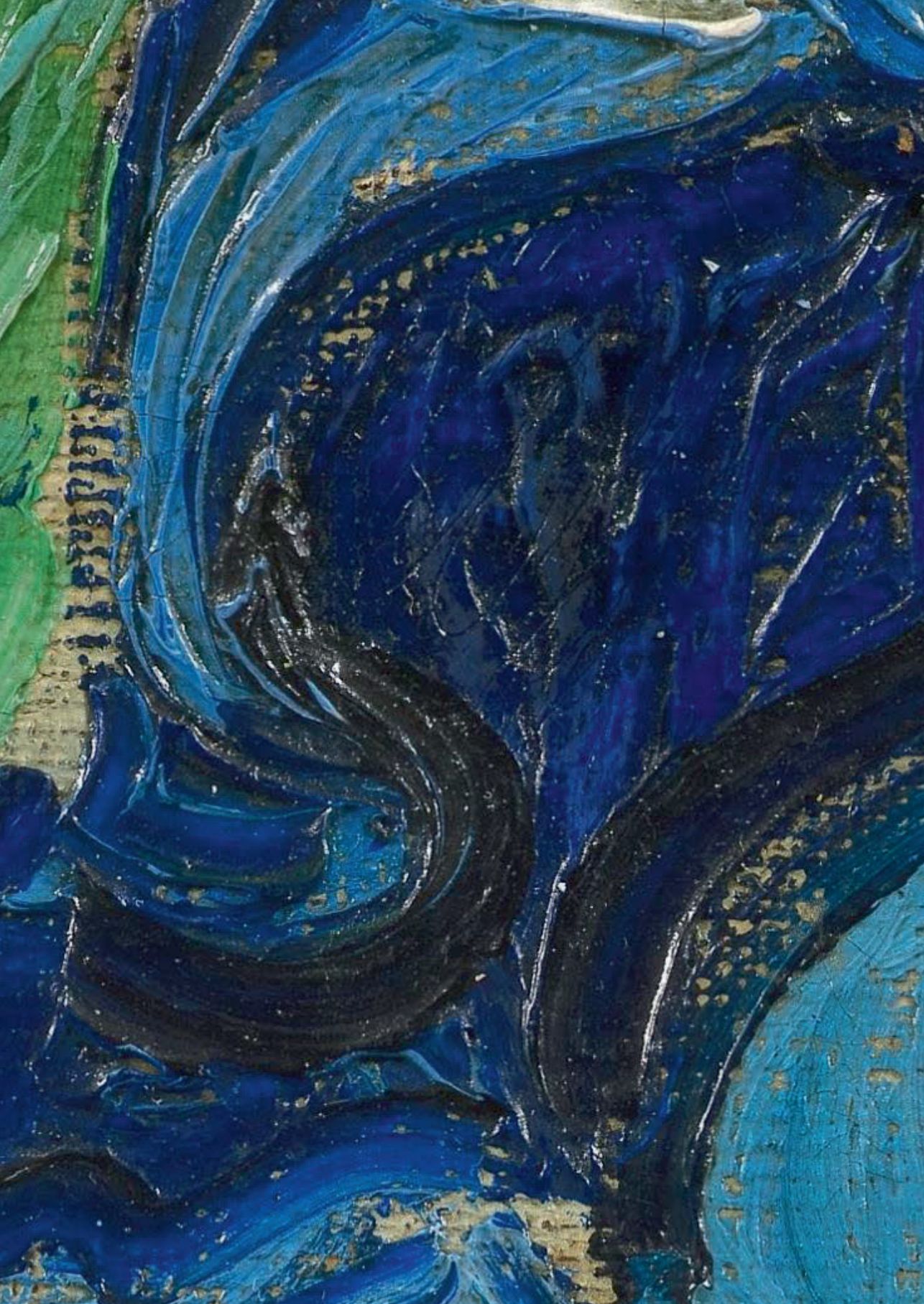

# CHAPTER 4

## The development of a generic analysis method for natural and synthetic dyes by LC-DAD and triethylamine as an ion-pairing agent

## Abstract

In cultural heritage the characterization of organic colorants is a challenging task. Currently, different chromatographic techniques are used to analyze natural and synthetic dyes separately, since the classes differ significantly in chemical properties and, therefore, chromatographic behavior. To save time, costs and sample material, we developed a method suitable for a wide variety of organic colorants using ultra-high-performance liquid chromatography coupled to a photo-diode-array detector. Gradient elution was performed with a mobile phase consisting of water and methanol with 5 mM triethylamine added as an ion-pairing agent at a pH of 3. Both linear and step gradients were optimized using the 'Program for Interpretive Optimization of Two-dimensional Resolution' (PIOTR) [1]. Two optimized linear gradients and two step gradients were evaluated experimentally. The method was applied on a complex dye mixture containing nearly 130 natural- and synthetic-dye reference compounds. More than 100 of these compounds could be identified in a single experiment. The feasibility of the method was demonstrated by analyzing samples of several precious objects that were found in the Texel shipwreck [2] and of two embroideries of Emile Bernard, the results of which are described in this paper.



**Publication**

The development of a generic analysis method for natural and synthetic dyes by ultra-high-pressure liquid chromatography with photo-diode-array detection and triethylamine as an ion-pairing agent

Iris Groeneveld, Bob W.J. Pirok, Stef R.A. Molenaar, Peter J. Schoenmakers, Maarten R. Van Bommel

*J. Chromatogr. A*, **2022**, *1673*, 463038, DOI: 10.1016/j.chroma.2022.463038

## 4.1 Introduction

Dyes and pigments have fascinated humankind ever since their discovery. Colorants have been used to enhance the aesthetics of paintings, textiles, furniture, and later also plastics. Dyeing itself is one of the most ancient arts, with history dating at least 5000 years back [3]. Until the mid-19th century all organic colorants were derived from natural sources, such as plants and animals. Hence, these are called 'natural dyes'. After the discovery of the first synthetic dye, mauveine, in 1856, brighter colors could be produced that were also cheaper to manufacture on a large scale. Within just a few decades natural dyes were replaced by their synthetic analogues, which led to a decline in the production of natural dyes [3]. Objects originating from this time period may contain natural or synthetic dyes or a mixture of both. Natural and synthetic dyes differ significantly in their chemical properties. Natural dyes are mostly neutral or slightly acidic compounds, while there is a huge range of neutral, acidic and basic synthetic dyes. Such compounds are typically analyzed using liquid chromatography (LC). Since the chromatographic behavior of these components varies significantly, different chromatographic methods are needed for an optimal separation of the dyestuffs in question. In order to select a suitable analysis method for cultural-heritage objects, information on the origin of the used dyestuffs is required. Unfortunately, in most cases information about the investigated object is insufficient to determine which method should be used. The typical solution to this problem is to apply multiple analytical methods on the sample to obtain sufficient chemical information, however, this is more time consuming. In addition, in cultural heritage sample material is limited as one must avoid jeopardizing the integrity of the object. Therefore, it is paramount that LC methods yield as much information as possible.



To illustrate the vast diversity and specificity of LC methods for dyestuffs in cultural heritage, we discuss several of them here. In 1985, Wouters and colleagues introduced an LC method using diode array detection (DAD) detection for red anthraquinone dyes [4]. The chromatographic method was based on a reversed-phase (RP) mechanism and employed gradient elution using water and methanol (MeOH) with 1% formic acid (FA). The sensitivity of this method allowed determining kermesic acid in both Polish and ordinary species of cochineal, insect species often used to dye red. In later research, the authors replaced FA by 0.5% phosphoric acid for the analysis of natural dyes, which could then also be applied to purple and blue indigoid dyes [5–7]. Another LC-DAD method for the analysis of natural dyes was presented in 1996 by Halpine et al., who used a water/acetonitrile gradient with 0.1% trifluoroacetic acid (TFA) to analyze fibers from furniture tapestries and lake pigments from a watercolor box [8]. The organic colorants that were analyzed ranged from indigo and Indian yellow to madder lakes. Subsequently,

in 2013, Serrano et al. described the performance and method development of a UHPLC system for the characterization of natural dyestuffs, including flavonoids, carotenoids, anthraquinones and indigoids [9]. Seven UHPLC columns were tested with different gradient-elution programs, different eluents, flow rates, temperatures, and run times. In addition, the differences in performance between 5% phosphoric acid and 1% FA were also evaluated. The final UHPLC method used a water/methanol gradient with 1% FA instead of phosphoric acid. The use of FA as an additive yielded better resolution and a larger peak capacity compared to phosphoric acid and allowed for hyphenation with mass spectrometry (MS), thanks to its volatility.

The analysis of synthetic dyes proved to require a different approach. Van Bommel et al. performed LC analyses on early synthetic dyes that were used in the period 1850 – 1900 [10]. The aim of their study was to investigate the performance of several analytical methods on a selection of 65 synthetic dyes, covering all dye classes from that period. They applied two gradient methods. The first was similar to the phosphoric acid method developed by Wouters, except that a different C18 column was used. Many of the synthetic acid dyes could be detected with this method. However, for most acid dyes broad and tailing peaks were observed. Therefore, a second method was investigated, using tetrabutylammonium (TBA) as an ion-pairing agent, which was based on earlier research on modern synthetic dyes, where TBA was introduced as a positively charged counter ion to neutralize sulfonic-acid groups [11–13]**.** Using the TBA method, good chromatographic behavior was observed for all acid and direct dyes. Direct dyes are bound to the substrate directly and are generally defined as anionic. Neutral and basic dyes, however, showed better peak shapes and higher peak capacities with the phosphoric-acid method. Both methods were successfully tested in practice by analyzing samples taken from two faded embroideries from Emile Bernard (ca. 1892 and 1904) [14]. As a result of this research, the phosphoric-acid and TBA methods were then accepted by the authors as the appropriate methods for natural and synthetic dyes, respectively. It should be stressed that each of the above mentioned methods either focuses on the analysis of natural or synthetic dyes, due to the vast molecular differences between the two dye classes. While each of the methods offered selective separation power, none provided a general approach.

Since then, there have been several reports that describe the successful analysis of both natural and synthetic dyes by reversed phase LC methods. However, most of these methods were limited to a small number of dyes or dye classes [15–17] and/or needed re-analysis for identification of synthetic dyes by a second system, mostly MS, using different gradient programs and solvents [18,19]. Chen et al. [20] reported on the identification of 42 synthetic and 17 natural dyes in fourteen silk samples by a single LC

method. They applied LC-DAD-ESI-MS using gradient elution with a mixture of water, acetonitrile and a constant amount of FA at 0.1%. Although successful, the authors stated that some synthetic dyes could be better analyzed using an ion-pair. They also shared their concern about the complexity of establishing a generic method for all dyes.

In an attempt to resolve this problem, Pirok et al. applied comprehensive two-dimensional LC (LC×LC) to analyze different types of synthetic dyes and their degradation products in one method [21]. In LC×LC fractions of the first-dimension eluents are subjected to a very different ('orthogonal') second-dimension separation to yield additional selectivity and separation power. One drawback of LC×LC is that method development is rather complex and time consuming. To reduce method-development time, the authors developed a computer-optimization tool called 'Program for Interpretive Optimization of Two-dimensional Resolution' (PIOTR) [1]. It was based on retention modelling and on efficient methods to obtain the unique retention parameters for each compound. The latter was used to derive method parameters that provided optimal separations considering various optimization criteria. Among the possible chromatographic parameters that must be selected in reversed-phase liquid chromatography (RPLC) experiments are the starting time of the gradient ($t_{\mathrm{init}}$), the duration of the gradient ($t_G$), the flow rate ($F$), and the initial ($\varphi_{\mathrm{init}}$) and final ($\varphi_{\mathrm{final}}$) fractions of the organic modifier. Other conditions such as column dimensions, the type of solvents and type of instrument are considered by the program to improve the accuracy of the prediction. Adjusting chromatographic parameters by means of a software program, instead of by trial-and-error experiments in the laboratory, saves a significant amount of work, time, and solvents. More information about the mathematics behind PIOTR is described in Appendix B-1. The authors used the program to develop a method for a mixture of 54 synthetic dyestuffs. Compounds were separated in the first LC dimension by ion-exchange chromatography (IEC), followed by ion-pair RPLC (IP-RPLC) in the second dimension, using 10 mM tetramethylammonium (TMA) or TBA at a pH of 3 (water/acetonitrile) with an Agilent ZORBAX Eclipse Plus C18 RRHD column [21].

Later, Pirok et al. optimized the LC×LC method for both natural and synthetic dyes, with TMA and TBA being replaced by 5 mM triethylamine (TEA) [22]. This method was successfully applied to extracts from cultural-heritage objects containing natural and synthetic dyes. While the method was widely applicable to all classes of dyes and allowed more unknown species to be detected, costs and detection sensitivity still favor a one-dimensional UHPLC method for routine analysis.

Therefore, we set out to develop a novel highly-optimized UHPLC method for the simultaneous analysis of acidic, basic and neutral dye components in a single

experiment. With the rather large number of dyes, baseline separation between all compounds within a reasonable analysis time is challenging. We therefore aim to the computer-optimization strategy (PIOTR) to optimize a gradient-elution method for a large number (nearly 130) natural and synthetic dye components. The final UHPLC method is applied on several artefacts to evaluate its performance and practicality for the analysis of historical objects, taking analysis time and resolution into consideration. The results will be compared with the results obtained with the previously discussed LC×LC method for natural and synthetic dyes [22]. Our final objective is to use the optimized method to create a compound library based on retention times and DAD spectra obtained from the most commonly applied dyestuffs in the field of cultural heritage.

## 4.2 Experimental

### 4.2.1 Chemicals

Aqueous solutions were prepared using ultrapure deionized water (Millipore Simplicity Simpak 2, R = 18.2 MΩ cm, U.S.A.). The mobile phases were prepared using methanol (LC-MS grade, ≥99.9%) and acetonitrile (LC-MS grade, ≥99.9%) obtained from Honeywell (Seelze, Germany), FA (99%) obtained from Acros Organics (Geel, Belgium), sodium hydroxide (NaOH) (≥97%) and TEA (98%) both obtained from Sigma-Aldrich (Steinheim, Germany). Dimethyl sulfoxide (DMSO) (99.9%) from Sigma-Aldrich was used for the preparation of reference solutions. In total, 100 natural and synthetic reference dyestuffs were obtained from the reference collection of the Cultural-Heritage Agency of the Netherlands (Amsterdam, The Netherlands).

### 4.2.2 Materials and instruments

All analyses were carried out on a Waters Acquity H-class UHPLC system (Waters, Nilford, MA, USA) equipped with a quaternary solvent-delivery system, a column oven, an autosampler and a DAD detector. The flow rate was set at 0.2 mL·min$^{-1}$ and the column oven was held at 40°C. The two chromatographic columns that were used for separation of analytes were a BEH Shield RP C18 column (150 × 2.1 mm i.d., 1.7 µm) from Waters (part number 186003977) and a ZORBAX Eclipse RRHD C18 column (150 × 2.1 mm i.d., 1.8 µm) from Agilent (part number 821725-901). Both columns were protected with guard columns (5 × 2.1 mm i.d.) containing the same C18 packing from the same manufacturer as the analytical column. DAD data were recorded from 200 to 800 nm with a resolution of 1.2 nm and a sampling frequency of 2 Hz. The equipment was controlled by Empower 2.0 Chromatography Data Software (Waters).

## 4.2.3 Methods

**Preparation and optimization of mobile phases**

For the preparation of the mobile phases, ultrapure water and methanol or acetonitrile were used. First, FA and NaOH were added to 1 L of ultrapure water at concentrations of 0.1 and 0.02 M, respectively, to obtain a pH of 3. The eluent was prepared by mixing buffered water and MeOH in ratios of 95/5 (by volume) for mobile phase A, and 5/95 for B, respectively. TEA was added as an ion-pairing agent to both A and B at a concentration of 1 or 5 mM, or was left out of mobile phase B entirely. In addition to MeOH, analyses were also executed with ACN as the organic modifier to compare the performance of the two modifiers.



**Reference dyestuffs**

Different mixtures containing reference dyestuffs were used throughout the process of method optimization. An overview of the composition of the used dye mixtures is presented in the Appendix B (Tables B-1 – B-3). It should be noted that many of these reference samples comprise original dye powders, which may originate from several decades ago. As a consequence, some dye powders may contain degradation products and/or impurities or side products formed during the synthesis, which would otherwise not be found in pure analogues. However, samples from cultural-heritage objects may feature these same components, which renders the references very useful for method development.

Stock solutions of each dyestuff were prepared at 1 mg/mL in DMSO. Using the stock solutions of the dyestuffs (henceforth referred to as 'dyes'), ten mixtures (henceforth referred to as 'dye mixtures') were created. The first two, mixtures A and B, were created for selection of the chromatographic column and the optimization of chromatographic parameters, such as the composition of the mobile phase (Appendix B, Tables B-1 and B-2). Both mixtures contained several natural and synthetic dyes covering different dye classes. Their molecular structures are presented in Fig. B-1 and B-2. The dyes were divided over mixtures A and B based on their retention times with the aim to prevent co-elution as much as possible for easy interpretation. Mix A was created by combining 100 µL of eight dyes into one vial with a final concentration of 125 µg/mL for each dye. The same procedure was followed for ten other dyes with a final concentration of 100 µg/mL for each dye to obtain mix B.

For the computer-aided optimization of the gradients, eight additional dye mixtures were created (Appendix B, Table B-3). The natural dyes were divided across mixtures 1-5 and

the synthetic dyes across mixtures 6-8 by transferring 100 µL of each dye in a new vial to obtain final concentrations ranging from 66.7 to 100 µg/mL for each dye.

Lastly, a dye mixture containing all dyes, hereafter called mix X, was prepared by combining 100 µL each of dye mixtures 1 through 8 in one sample vial, which was used to test the performance of the developed LC gradient methods. As a result, mix X contained 98 dyes, representing close to 130 dye components (including side products, impurities and degradation products).

**Sample preparation and analysis of historical objects**

To examine the suitability of the optimized LC-DAD method described in this paper, hereafter called the TEA method, samples from several historical objects of different age were analyzed. The samples were selected such that a wide range of natural and synthetic dyes were represented. The first group of samples originated from a unique archaeological find of textiles in a shipwreck near Texel [2], an Island in the north of The Netherlands. Sport divers discovered the wreck in 2009 and in 2015 several garments were discovered and brought to the surface. Among those were a complete 17$^{th}$ century gown, two kaftans, a large cape and several interior textiles, such as used for cushions (Fig. B-8 – B-11). The colors were surprisingly well preserved and, based on the dating, natural dyes were expected to be present. To complement the research, two late 19$^{th}$ century embroideries were investigated (Fig. B-12 and B-13), which were designed by Emile Bernard (1868-1941), who was known as a painter and a good friend of Vincent van Gogh. He designed a number of embroideries, several of which are now owned by the van-Gogh museum. Due to their date of origin, synthetic dyes were expected to be present. The same samples were also analyzed by the LC×LC method for natural and synthetic dyes recently developed by Pirok et al. [22]. Sample preparation was the same for both analytical methods, using the HCl method that was described in detail by Pirok [22].

## 4.3 Results and discussion

### 4.3.1 Chromatographic column

The first step towards optimization of the method was the comparison of the two types of stationary phases used by Serrano [9] and Pirok [21,22], a BEH Shield C18 and a ZORBAX Eclipse Plus C18 RRHD column, respectively. The BEH column contains trifunctional silica particles, with an additional hydrophilic carbamate group bonded to

C18 groups, and is endcapped. The ZORBAX column contains silica particles treated with a monolayer of C18 stationary phase and is doubly endcapped.

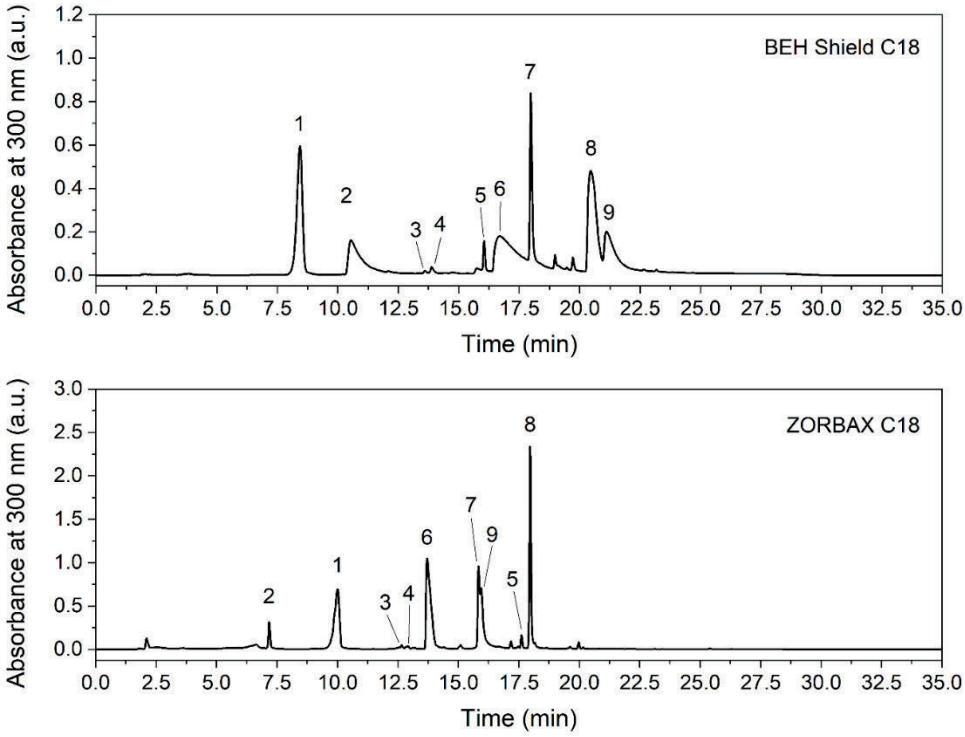


Figure 4.1. UHPLC–DAD chromatograms of dye mixture A analyzed with the BEH Shield C18 (top) and the ZORBAX C18 column (bottom) extracted at 300 nm; LC conditions as specified in Section 3.1; (1) isatin, (2) amaranth, (3/4) yellowish light green, (5) diamond green B, (6) crystal ponceau 6R, (7) quercetin, (8) martius yellow, and (9) congo red.

Fig. 4.1 and B-3 show the results of the analyses of mixtures A and B, respectively, on the two RP columns. The mobile phase was prepared as described in Section 2.3, containing MeOH and 5 mM TEA. A gradient was applied with mobile phase B increasing from 5% to 95% from 1.50 till 20.0 min, isocratic between 20.0 and 25.0 min, then again from 95% to 5% B within 2 minutes, and finally isocratic for 5 more minutes. The chromatogram obtained with the ZORBAX column shows narrower peaks and less tailing when compared to the BEH Shield column. This is especially observed for amaranth (A2), crystal ponceau 6R (A6), martius yellow (A8) and congo red (A9) in mixture A, as well as for tartrazine (B1), ponceau G (B6) and silk scarlet N (B9, B10) in mixture B. The broader peaks observed for the BEH Shield column may be explained by the additional hydrophilic carbamate groups of the stationary phase, which increase the affinity of very acidic compounds. Natural dyestuffs, in contrast to synthetic dyestuffs, contain mostly neutral

or slightly acidic compounds, which is why natural dyes show narrower peak shapes on the BEH column and also why this column has proven to work well for natural dyes before [9]. Most of the dyes that show peak broadening are indeed synthetic acid dyes, except for tartrazine which is a synthetic direct dye. The latter, however, shows chromatographic behavior more like that of an acid dye, due to the presence of two sulfonic acid groups.

Other compounds that showed poor peak shape on the BEH column contain either one or more sulfonic-acid groups that is charged at a pH of 3. These charged groups may undergo specific interaction with free amide groups on the surface of the stationary phase of the BEH column, resulting in increased band broadening [10]. This effect is not present with the ZORBAX C18 column as the stationary phase does not contain amide groups and free silanol groups that may cause additional band broadening are shielded off more effectively due to the double endcapping.

The challenging collection of compounds included in this study asks for an analytical column that facilitates sufficient retention for a wide range of analytes. As the stationary phase of the ZORBAX column yielded a more homogenous performance for this wide set of acidic, neutral and basic compounds, further experiments were conducted using this column.

### 4.3.2 Effect of organic modifier

The effect of the composition of the mobile phase on the chromatographic performance was studied by varying the concentration of the ion-pairing agent between 1 mM and 5 mM TEA in mobile phase A and B, and by omitting TEA from eluent B during analyses of mixtures A and B. In addition, the effects of MeOH or ACN as organic modifiers were studied. The same gradient as in Section 3.1 was applied. Increasing the concentration of TEA from 1 mM to 5 mM resulted in improved peak shapes and an increased peak capacity (Fig. 4.2 and B-4, for mixtures A and B, respectively). Improved peak symmetry was especially observed for compounds that possess multiple charged sites (crystal ponceau 6R, tartrazine, rhodamine B and silk scarlet N). More polar compounds (i.e., martius yellow and cochineal) eluted earlier using 5 mM compared to 1 mM TEA.

The decreased retention may be caused by competition between the dye and TEA for interaction with the stationary phase, or by ion pairing of TEA with remaining silanol groups on the stationary phase. Several compounds that elute later at a higher concentration of TEA are those that contain additional sulfonate and/or azo groups (amaranth, crystal ponceau 6R and tartrazine). Positively charged ion-pairing agents, such as TEA, are generally added to neutralize anionic fractions and to enhance retention of the ion pair based on hydrophobicity through alkyl chains on the ammonium ion [3].

The improved peak shapes and increased retention times for acid dyes with 5 mM TEA compared to 1 mM TEA can be assigned to an increased neutralizing effect of the ion-pairing agent, as there are more counterions present.

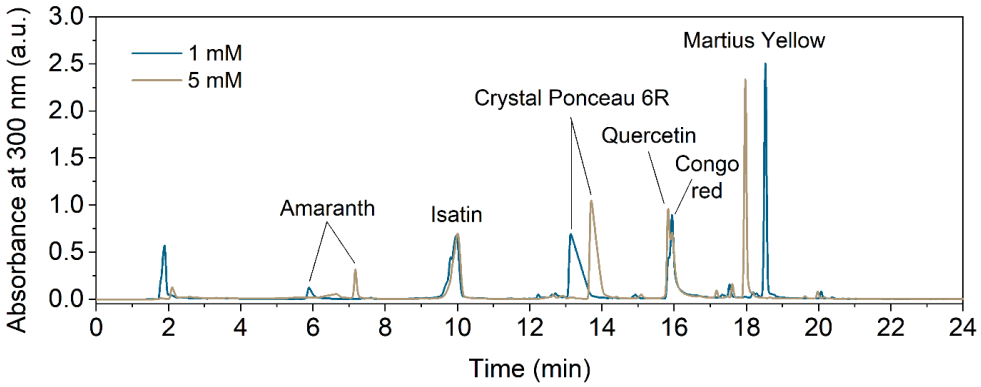


Figure 4.2. UHPLC–DAD chromatograms of dye mixture A extracted at 300 nm analyzed with 1 mM (blue) or 5 mM (beige) TEA in the mobile phase. The same gradient was applied as in Fig. 4.1.

When TEA was omitted from mobile phase B, a narrower retention window was observed, with poor peak shapes, especially for later eluting peaks (Fig. B-5). This starts to be noticeable after approximately 12 minutes, when the ratio of A and B is roughly 50/50%. If both mobile phases contain an equal amount of TEA, the ion-pair concentration will remain constant throughout the analysis. Therefore, TEA should be added to both A and B, as is generally done for IP-RPLC [9,23,24]. In some particular situations the ion-pair agent may be left out of the organic modifier, as Pirok et al. did to reduce the elution time in the second dimension in LC×LC [21].

The differences between MeOH and ACN as the organic modifier were assessed by analyzing dye mixtures 1-8 and importing the obtained retention times in PIOTR. Analyses with ACN resulted in significantly shorter retention times for all analytes, as shown for mixture 1 in Fig. B-6. Their respective peak widths, however, did not change, which led to more peak overlap and an overall decrease in peak capacity. Fig. 4.3 shows the retention plots for MeOH and ACN generated by PIOTR. The lines in these graphs represent all 127 dye components and show their retention characteristics ($ln\ k$) at any organic modifier fraction ($\varphi$). For MeOH the retention lines are distributed more evenly than for ACN, which implies that many of the compounds show different elution behavior. This phenomenon increases the possibility of computing a gradient method that results in the separation of as many compounds as possible. Based on these graphs, and because ACN is less environmental friendly and more expensive, further experiments were carried out with MeOH.

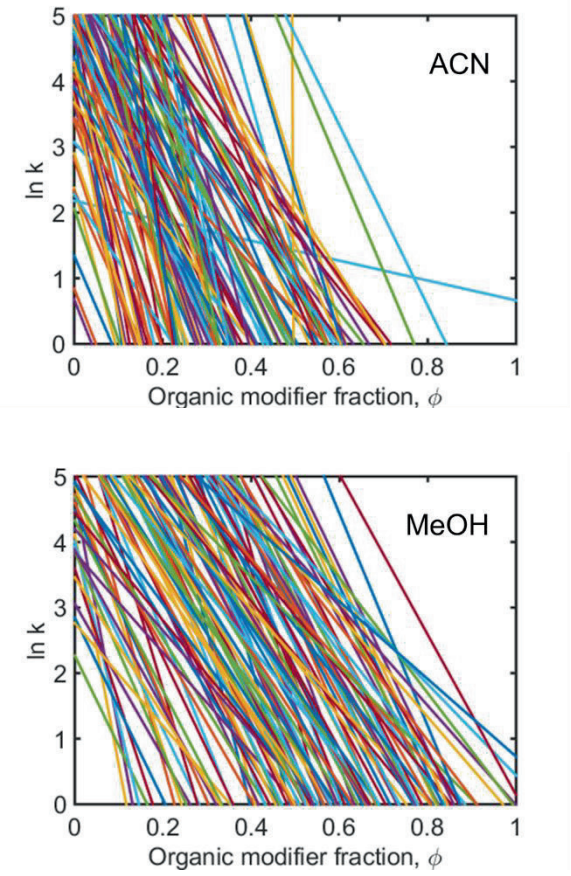


Figure 4.3. Retention plots for 127 analytes calculated by PIOTR after analyzing all components by UHPLC–DAD with 10–min and 30–min linear gradients from 5% to 95% ACN or MeOH.

### 4.3.3 Gradient optimization by PIOTR

The gradient-elution method was optimized using PIOTR and included the evaluation of both linear and step gradients. To optimize the LC gradient for a mixture of compounds based on a log-linear retention model, the retention parameters, i.e., the slope ($S$) and the intercept ($ln\ k_0$), of the retention lines must be known (Fig. 4.3) [25]. To obtain these, two or more experimental retention times are needed, which can most-conveniently be established from two gradient experiments, the effective slopes of which are substantially different. In general, more measurements lead to more accurate retention parameters. However, previous reports showed that robust findings could be obtained using just two scouting gradients [26,27]. Conventional wisdom prescribes a difference in slopes by at least a factor of three, but recent research has shown that smaller differences may suffice [26]. Nevertheless, two gradient experiments of 10 and 30 min duration ranging from 5% to 95% of B were performed for mixes 1 through 8. The

retention times of all dye components for both the short and the long gradient were entered in PIOTR. Next, the $ln\ k_0$ and $S$ values for each analyte were calculated (SI, Table B-4). These values were used for computational optimization of the gradient method.

Parameters that were optimized for both step gradients and linear gradients were the time before the gradient is programmed to start ($t_{init}$), the duration of the gradient ($t_G$), and the initial ($\varphi_{init}$) and final ($\varphi_{final}$) concentration of the organic modifier. The flow rate $F$ was fixed at 0.2 mL·min$^{-1}$. The maximum $t_G$ for linear and step gradients was set at 70 and 90 min, respectively. The concentration of the organic modifier was varied from at least 5% as initial condition up to 95% at the end of the gradient. For step gradients $t_{init}$, $t_G$ (in this case the time another gradient starts), $\varphi_{init}$ and $\varphi_{final}$ were varied for each individual step. This was done by a 'funneling approach', with broad settings being applied first and narrowing these down after observing their effects in the Pareto-optimization (PO) plots, the framework in which objectives such as the resolution, time of last eluting peak, or orthogonality are considered. In a PO plot every optimization criterion (e.g., analysis time, resolution score, detector sensitivity) is a dimension. PO-points are those for which no conditions exist that yield equal or better values for all optimization criteria simultaneously.

Eventually, a final optimization experiment was conducted for which the settings can be found in the Appendix B, Tables B-5 and B-6. Two linear (L1 and L2) and two step gradients (S1 and S2) were chosen from the PO plots. L1 and B-1 were chosen based on the optimum theoretical resolution score (Fig. 4.4). Gradients L2 and S2 are not PO-points, however, were chosen as sub-optimal references to compare to L1 and S1. The settings of the four gradients can be found in the Appendix B, Table B-7.

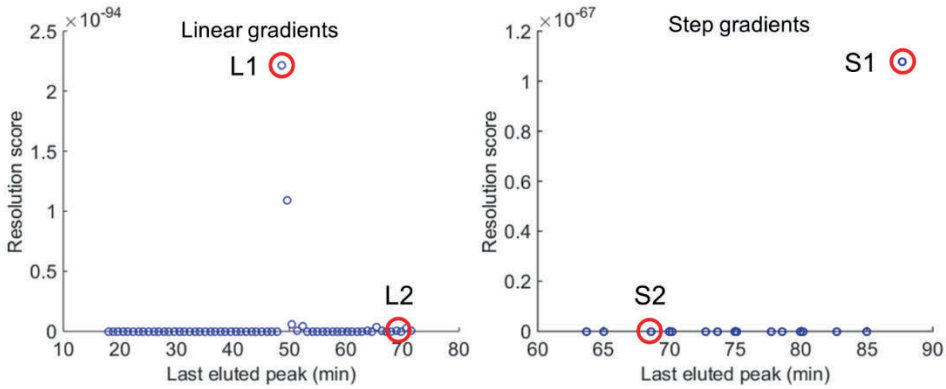


Figure 4.4. Pareto-plots presented as in PIOTR obtained after computing different experimental parameters for linear and step gradients. Two of both were chosen to be experimentally tested in the lab: L1, L2, S1, and S2.

The four gradients were first applied on dye mixtures 1-8 to obtain retention times of each analyte. Next, the mixture of all 98 dyes (mix X, Fig. 4.5) was analyzed. The retention times and absorption spectra retrieved from the analyses of mixes 1-8 were used to interpret the results obtained from the analysis of mix X. For several compounds that could not be assigned, we noted that the concentration was very low, which caused those peaks to be overshadowed by overlapping peaks of more-concentrated or more-absorbing compounds. These components were re-injected individually, several at higher concentrations, and all eluted at the expected retention times. It is good to note that most overlapping peaks showed very distinguishable DAD spectra, which would make it easier to identify both peaks when present at higher concentrations. This also brings forward the importance of the use of MS for identification of dyes in general, but especially in such complex mixtures. Fortunately, the ion pair in the optimized method is compatible with MS, however, implementation thereof was out of the scope of this work.

The performance of PIOTR to predict retention models was evaluated based on the accuracy of the prediction of the retention times for each compound in mix X. The error between the predicted and experimentally obtained retention times was very small for all four gradients and are presented as two overlays (Appendix B, Fig. B-7 and Table B-8). Prediction accuracies of 97.8% and 97.1% for gradients L1 and L2, and 96.4% and 97.2% for gradients S1 and S2 show that PIOTR can predict retention models accurately for both linear and step gradients.

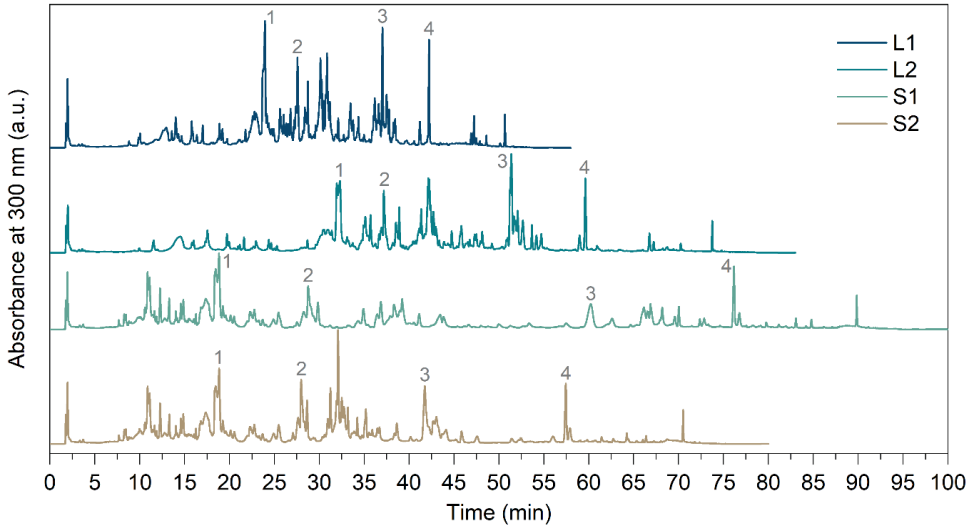


Figure 4.5. LC–DAD chromatograms of dye mixture X obtained after analysis using two linear (L1 and L2) and two step gradients (S1 and S2), which closely matched the retention predictions of PIOTR. Indicated peaks are (1) quercitrin, (2) martius yellow, (3) xantho-purpurin and (4) emodin.

The experimental results of the four gradients were evaluated in terms of chromatographic separation, the number of analytes that could be assigned, and the total analysis time. Due to the high complexity of the mixture, in contrast to what the PO plots may show, it is difficult to make a distinction between the four experimentally obtained chromatograms based on chromatographic separation. Furthermore, the percentage of compounds that could be assigned in mix X analyzed by each gradient method was very similar: 75% for gradients L1, S1 and S2, and 77% for gradient L2, the latter being the sub-optimal PO-point. This shows that the resolution score as a criterium for PO plots is not very meaningful for the optimization of such complex mixtures. The objective function of PIOTR was to maximize the product of corrected resolution scores, which means that two overlapping peaks will lower the resolution score towards zero. In PIOTR, the peak widths are estimated based on a standard plate number and a general Van Deemter model, meaning that peaks with higher retention times will be simulated broader than early eluting peaks. Nowadays, this may not be an accurate estimation anymore as UPLC methods with smaller particle columns are used more frequently, such as for the TEA method. With regards to the current work, the calculated resolution score was extremely low due to the use of nearly 130 compounds in the simulations. A better criterium for method optimization of complex samples may have been 'number of peaks', which unfortunately, was not an available option at the moment of optimization.



A choice for a method could not be made based solely on the number of identified peaks. The patterns and peak shapes obtained with gradients L1, L2 and S2 are quite similar. Method S1 results in slightly broader peaks due to the small gradient step from 60/40 to 50/50 A/B in 20 min, the relatively long isocratic step of 15 min, followed by the slow gradient (30 min) to 5/95 A/B (Table B-7). Step gradient S1 shows good peak shapes early in the chromatogram. However, the space between 40 and 80 min is relatively empty and this space could be used more efficiently. The overall analysis time is one of the criteria in the PO optimization. A shorter analysis time is generally preferred. Since the better resolution score seen in Fig. 4.4 for method L1 is barely reflected in the chromatogram of the very complex mixture, both linear methods (L1 and L2) are thought to perform equally well. Therefore, the shortest method (L1) was selected as the decrease in analysis time weighed heavier than the marginal improvement in resolution score. Using the results obtained with this gradient on mixture X, a compound database was created, which included the retention times and absorption spectra of each analyte.

### 4.3.4 Repeatability

The final method, using gradient L1, was validated for within-day and inter-day repeatability. This was done by analyzing several natural and synthetic compounds

(listed in Table 4.1) in triplicate during five successive days (a technical error on the 5th day caused the exclusion of data for a few compounds). The data were interpreted manually using the new compound database and the within-day and inter-day repeatability were calculated from the variation in retention times.

The repeatability is calculated as the RSD% of the retention times between triplicates within each day. The obtained RSDs ranged from 0.00% to 0.39%, indicating a good repeatability. An overview of the RSDs of each compound is shown in Table 4.1 in order of elution time. The inter-day repeatability of the method from day to day was calculated by applying a one way ANOVA on the complete data set. A P-value of 0.999 was obtained, indicating a good inter-day repeatability.

Table 4.1. Overview of the selected natural and synthetic dyes that were used to assess the within-day and inter-day repeatability. The RSDs were calculated based on the differences between triplicates on each day.

| Compound name | $t_R$ (min) | RSD% | | | | |
|---|---|---|---|---|---|---|
| | | Day 1 | Day 2 | Day 3 | Day 4 | Day 5 |
| Tartrazine | 8.81 | 0.30% | 0.39% | 0.17% | 0.06% | 0.11% |
| Catechin hydrate | 10.33 | 0.06% | 0.09% | 0.11% | 0.00% | |
| Amido naphthol red G | 18.88 | 0.05% | 0.15% | 0.08% | 0.06% | 0.08% |
| Fuchsine, component 1 | 21.05 | 0.07% | 0.12% | 0.12% | 0.09% | 0.10% |
| Chrysoidine | 21.82 | 0.07% | 0.12% | 0.14% | 0.09% | 0.09% |
| Methylene blue | 22.97 | 0.07% | 0.09% | 0.11% | 0.02% | 0.09% |
| Munjistin | 22.97 | 0.03% | 0.07% | 0.05% | 0.02% | |
| Fuchsine, component 2 | 23.53 | 0.06% | 0.09% | 0.13% | 0.08% | 0.09% |
| Quercitrin | 23.96 | 0.02% | 0.06% | 0.02% | 0.02% | |
| Fast red B | 25.64 | 0.02% | 0.06% | 0.10% | 0.04% | 0.06% |
| Rhamnetin | 27.22 | 0.04% | 0.06% | 0.00% | 0.04% | |
| Luteolin | 28.42 | 0.04% | 0.05% | 0.00% | 0.04% | |
| Uranine A | 29.63 | 0.02% | 0.13% | 0.09% | 0.05% | 0.04% |
| Diamond green B | 32.30 | 0.03% | 0.14% | 0.08% | 0.06% | 0.06% |
| Alizarin | 33.53 | 0.00% | 0.06% | 0.02% | 0.03% | |
| Purpurin | 37.52 | 0.02% | 0.04% | 0.02% | 0.02% | |
| Victoria blue B | 40.39 | 0.01% | 0.08% | 0.07% | 0.04% | 0.03% |
| Wool scarlet | 41.19 | 0.01% | 0.06% | 0.03% | 0.01% | 0.01% |
| Flavazine L | 43.69 | 0.01% | 0.05% | 0.03% | 0.01% | 0.03% |

### 4.3.5 Analysis of historical objects

To assess the performance and applicability of the TEA method for the characterization of historical artefacts containing natural and synthetic dyes, several samples taken from the objects described in paragraph 2.5 were analyzed. The same samples were also analyzed by the LC×LC method described by Pirok [22] since this method was

successfully applied for both natural and synthetic dyes and can be used as a benchmark for comparison. Table 4.2 presents the results obtained by both methods. A more extensive overview of the obtained results are given in Appendix B-7, together with the obtained LC-DAD data and measured masses in Appendix B-8.

Table 4.2. Results of the analysis of the historical samples T038.1, T044.1, T087.5, T095.1, V111-11, V111-13, V111-21, V113-3, V113-11, V113-18 analyzed by both the TEA method and the LC×LC method described by Pirok [22]. Some components were present at low concentrations. As a result the identification is not conclusive and these components are labelled 'possibly'. Components with spectra resembling known reference materials but eluting at different retention times are labelled 'equivalent'. Unidentified compounds in the second dimension of the LC×LC method are suspected to be degradation products (DP), thus are labelled 'DP'.

| Sample | Compound detected | TEA method | LC×LC method |
|---|---|---|---|
| T038.1 | Carminic acid | X | X |
| | Possibly DP of carminic acid | | X |
| | dcIV | X | |
| | Ellagic acid | X | |
| | dcVII | X | |
| | Possibly kermesic acid | X | |
| | Alizarin | X | |
| | Purpurin | X | |
| | Possibly Pseudo-purpurin | X | |
| T044.14 | Carminic acid | X | X |
| | Possibly DP of carminic acid | | X |
| | Type C component | X | |
| | Ellagic acid | X | |
| | Fisetin | X | |
| | Possibly Kermesic acid | X | |
| | Carminic acid equivalent | X | |
| T087.5 | Carminic acid | X | X |
| | Possibly DP of carminic acid | | X |
| | Possibly dcIV/dcVII | X | |
| | Purpurin equivalent | X | |
| | Alizarin | X | X |
| | Possibly DP of alizarin | X | X |
| | Purpurin | X | X |
| | Possibly Pseudo-purpurin | X | |
| T095.1 | Carminic acid | X | X |
| | Possibly DP of carminic acid | | X |
| | dcIV | X | |
| | Ellagic acid | X | |
| | Possibly dcVII | X | |
| | Possibly dcVII equivalent | X | |
| | Possibly Kermesic acid | X | |
| V111-11 (green) | Napthol yellow equivalent | X | X |
| | Ellagic acid | X | X |
| | Quinoline yellow, component 1 | X | X |
| | Quinoline yellow, component 2 | X | X |

| Sample | Compound detected | TEA method | LC×LC method |
|---|---|---|---|
| | Diamond green B equivalent | X | X |
| | Quinoline yellow equivalent | X | X |
| V111-13 (turquoise) | Picric acid | X | X |
| | Unknown yellow(s) | X | |
| | Diamond green equivalent 1 | X | |
| | Diamond green equivalent 2 | X | |
| | Victoria blue equivalent(s) | X | X |
| | Victoria blue B | X | X |
| | Diamond green B | X | |
| | Diamond green equivalent(s) 3-8 | X | |
| V111-21 (beige) | Methyl violet equivalent(s) | X | X |
| | Methyl violet, trimethylated | X | X |
| | Methyl violet, tetramethylated | X | X |
| | Methyl violet, pentamethylated | X | X |
| | Crystal violet | X | X |
| V113-3 (carmine) | Azo fuchsine 6B | X | |
| | Amido naphthol red G | X | X |
| | Rhodamine B equivalent | X | X |
| | Orange II | X | X |
| | Rhodamine B equivalent | X | X |
| | Eosin equivalent | X | |
| | Rhodamine B equivalent | X | X |
| | Rhodamine B | X | X |
| | Fast acid magenta B | X | |
| V113-11 (yellow) | Naphthol yellow S | X | X |
| | Picric acid | X | X |
| | Orange II | X | X |
| | Orange IV | X | X |
| | Diamond green B equivalent | X | X |
| | Diamond green B equivalent | X | X |
| | Diamond green G equivalent | X | X |
| V113-18 (blue - cobalt) | Patent blue V equivalent(s) | X | |
| | Crystal violet equivalent | X | X |
| | Victoria blue R equivalent(s) | X | X |
| | Victoria blue R | X | X |

The results described in Table 4.2 and Appendix B show that, like the LC×LC method, the TEA method is perfectly capable of analyzing a wide range of natural and synthetic organic colorants used in historical objects from different periods. Therefore, even with little knowledge about the historical background of a sample, this method may be successfully applied, saving time and precious sample material.

In comparison with the LC×LC method, the TEA method was able to detect more compounds especially in the samples from the Texel shipwreck. This may be due to dilution of the sample in the second dimension in LC×LC, causing analytes that are already in low abundance to be non-detectable. However, the LC×LC method also

showed non-identified analytes in the second dimension, which could be isomers, side-products or degradation products, which were not separated by the 1D TEA method.

Overall, both methods are comparatively strong, but may be used for different purposes. The LC×LC method provides more in-depth information about the presence of possible isomers, side-products and degradation products, but data processing requires more time. In situations where the additional information is not required, the TEA method may serve as a robust routine analysis method providing high throughput and good sensitivity.



## 4.4 Conclusions

A UHPLC-DAD analysis method for natural and synthetic dyes was developed and a compound library for nearly 130 dyestuff compounds was created. It is important to note that dyes are a very diverse group of small molecules with vastly ranging chemical properties (e.g., charge and hydrophobicity) which renders them representative of other chemical classes. Consequently, this work and the method-development strategy will be of use to the development of methods for other classes of small molecules.

The method included the use of a ZORBAX Eclipse Plus C18 RRHD column and a linear gradient elution with a mobile phase consisting of water and methanol with 5 mM TEA at a pH of 3. PIOTR proved to be an extremely useful tool to build retention models and to predict the outcomes of linear and step gradients for RPLC. However, the resolution score used in this study proved of limited use for the separation of such a complex chromatogram. Thus, more research is required into the development of suitable chromatographic response functions (i.e., objective function or optimization criteria). Fortunately, a more advanced version of PIOTR, called MOREPEAKS [28], is being developed which does include this feature.

The TEA method described in this paper was successfully applied for the characterization of historical artefacts containing synthetic and natural dyes. Comparison with the LC×LC method for natural and synthetic dyes proved that this method is equally capable of analyzing a broad range of acidic, basic and neutral dye components in a single run, which circumvents the need of having to perform different methods on the same sample, saving precious sample material and time in the lab. The TEA method requires less data processing and specialized knowledge than the LC×LC method and, therefore, provides a good alternative for high-throughput routine analysis.

# References

[1] B.W.J. Pirok, S. Pous-Torres, C. Ortiz-Bolsico, G. Vivó-Truyols, P.J. Schoenmakers, Program for the interpretive optimization of two-dimensional resolution, J Chromatogr A. 1450 (2016) 29–37. https://doi.org/10.1016/j.chroma.2016.04.061.

[2] A.D. Vos, B. van den Hoven, I. Toussaint, Wereldvondsten uit een Hollands schip. Basisrapportage BZN17/Palmhoutwrak, Haarlem, 2019.

[3] V.A. Popoola, The Chemistry of Colours in Dyes and Pigments, Wits Publishing Ltd., 2015.

[4] J. Wouters, High Performance Liquid Chromatography of Anthraquinones: Analysis of Plant and Insect Extracts and Dyed Textiles, Studies in Conservation. 30 (1985) 119. https://doi.org/10.2307/1505927.

[5] J. Wouters, A. Verhecken, High-performance liquid chromatography of blue and purple indigoid natural dyes, Journal of the Society of Dyers and Colourists. 107 (1991) 266–269. https://doi.org/10.1111/j.1478-4408.1991.tb01351.x.

[6] J. Wouters, A. Verhecken, A. Verhecken, The Coccid Insect Dyes: HPLC and Computerized Diode-Array Analysis of Dyed Yarns, Studies in Conservation. 34 (1989) 189. https://doi.org/10.2307/1506286.

[7] J. Wouters, A. Verhecken, The chemical nature of flavokermesic acid, Tetrahedron Lett. 28 (1987) 1199–1202. https://doi.org/10.1016/S0040-4039(00)95325-5.

[8] S.M. Halpine, An Improved Dye and Lake Pigment Analysis Method for High-Performance Liquid Chromatography and Diode-Array Detector, Studies in Conservation. 41 (1996) 76. https://doi.org/10.2307/1506519.

[9] A. Serrano, M. Van Bommel, J. Hallett, Evaluation between ultrahigh pressure liquid chromatography and high-performance liquid chromatography analytical methods for characterizing natural dyestuffs, J Chromatogr A. 1318 (2013) 102–111. https://doi.org/10.1016/j.chroma.2013.09.062.

[10] M.R. van Bommel, I. Vanden Berghe, A.M. Wallert, R. Boitelle, J. Wouters, High-performance liquid chromatography and non-destructive three-dimensional fluorescence analysis of early synthetic dyes, J Chromatogr A. 1157 (2007) 260–272. https://doi.org/10.1016/j.chroma.2007.05.017.

[11] J.W. Wegener, J.C. Klamer, H. Govers, U.A.T. Brinkman, Determination of organic colorants in cosmetic products by high-performance liquid chromatography, Chromatographia. 24 (1987) 865–875. https://doi.org/10.1007/BF02688601.

[12] M. Holčapek, P. Jandera, P. Zderadička, High performance liquid chromatography-mass spectrometric analysis of sulphonated dyes and intermediates, in: J Chromatogr A, 2001: pp. 175–186. https://doi.org/10.1016/S0021-9673(01)00933-5.

[13] D. Ansorgová, M. Holčapek, P. Jandera, Ion-pairing high-performance liquid chromatography-mass spectrometry of impurities and reduction products of sulphonated azodyes, J Sep Sci. 26 (2003) 1017–1027. https://doi.org/10.1002/jssc.200301489.

[14] J. Barnett, Analysis of synthetic dyes in an embroidery of Emile Bernard ( circa 1892 ) I Vanden Berghe and J Wouters, Journal of the American Institute for Conservation. (2004) 969–977.

[15] S. Mathiyalagan, B.K. Mandal, Y.C. Ling, Determination of synthetic and natural colorants in selected green colored foodstuffs through reverse phase-high performance liquid chromatography, Food Chem. 278 (2019) 381–387. https://doi.org/10.1016/J.FOODCHEM.2018.11.077.

[16] B.K. Mandal, S. Mathiyalagan, R. Dalavai, Y.C. Ling, Simultaneous identification of synthetic and natural dyes in different food samples by UPLC-MS, IOP Conf Ser Mater Sci Eng. 263 (2017) 022011. https://doi.org/10.1088/1757-899X/263/2/022011.

[17] N. Yoshioka, K. Ichihashi, Determination of 40 synthetic food colors in drinks and candies by high-performance liquid chromatography using a short column with photodiode array detection, Talanta. 74 (2008) 1408–1413. https://doi.org/10.1016/J.TALANTA.2007.09.015.

[18] D. Tamburini, E. Breitung, C. Mori, T. Kotajima, M.L. Clarke, B. McCarthy, Exploring the transition from natural to synthetic dyes in the production of 19th-century Central Asian ikat textiles, Herit Sci. 8 (2020) 1–27. https://doi.org/10.1186/A-40494-020-00441-9/FIGURES/8.

[19] D. Mantzouris, I. Karapanagiotis, L. Valianou, C. Panayiotou, HPLC-DAD-MS analysis of dyes identified in textiles from Mount Athos, Anal Bioanal Chem. 399 (2011) 3065–3079. https://doi.org/10.1007/S00216-011-4665-4/FIGURES/6.

[20] V.J. Chen, G.D. Smith, A. Holden, N. Paydar, K. Kiefer, Chemical analysis of dyes on an Uzbek ceremonial coat: Objective evidence for artifact dating and the chemistry of early synthetic dyes, Dyes and Pigments. 131 (2016) 320–332. https://doi.org/10.1016/J.DYEPIG.2016.04.019.

[21] B.W.J. Pirok, J. Knip, M.R. van Bommel, P.J. Schoenmakers, Characterization of synthetic dyes by comprehensive two-dimensional liquid chromatography combining ion-exchange chromatography and fast ion-pair reversed-phase chromatography, J Chromatogr A. 1436 (2016) 141–146. https://doi.org/10.1016/j.chroma.2016.01.070.

[22] B.W.J. Pirok, M.J. den Uijl, G. Moro, S.V.J. Berbers, C.J.M. Croes, M.R. van Bommel, P.J. Schoenmakers, Characterization of Dye Extracts from Historical Cultural-Heritage Objects Using State-of-the-Art Comprehensive Two-Dimensional Liquid Chromatography and Mass Spectrometry with Active Modulation and Optimized Shifting Gradients, Anal Chem. 91 (2019) 3062–3069. https://doi.org/10.1021/acs.analchem.8b05469.

[23] M. Holčapek, P. Jandera, P. Zderadička, High performance liquid chromatography-mass spectrometric analysis of sulphonated dyes and intermediates, in: J Chromatogr A, 2001: pp. 175–186. https://doi.org/10.1016/S0021-9673(01)00933-5.

[24] D. Ansorgová, M. Holčapek, P. Jandera, Ion-pairing high-performance liquid chromatography-mass spectrometry of impurities and reduction products of sulphonated azodyes, J Sep Sci. 26 (2003) 1017–1027. https://doi.org/10.1002/jssc.200301489.

[25] L.R. Snyder, J.W. Dolan, J.R. Gant, Gradient elution in high-performance liquid chromatography. I. Theoretical basis for reversed-phase systems, J Chromatogr A. 165 (1979) 3–30. https://doi.org/10.1016/S0021-9673(00)85726-X.

[26] M.J. den Uijl, P.J. Schoenmakers, G.K. Schulte, D.R. Stoll, M.R. van Bommel, B.W.J. Pirok, Measuring and using scanning-gradient data for use in method optimization for liquid chromatography, J Chromatogr A. 1636 (2021) 461780. https://doi.org/10.1016/j.chroma.2020.461780.

[27] B.W.J. Pirok, S.R.A. Molenaar, R.E. van Outersterp, P.J. Schoenmakers, Applicability of retention modelling in hydrophilic-interaction liquid chromatography for algorithmic optimization programs with gradient-scanning techniques, J Chromatogr A. 1530 (2017) 104–111. https://doi.org/10.1016/J.CHROMA.2017.11.017.

[28] S.R.A. Molenaar, P.J. Schoenmakers, B.W.J. Pirok, MOREPEAKS, (2021). https://doi.org/10.5281/ZENODO.5710443.

# CHAPTER 5

## Characterization of a liquid-core waveguide cell for studying the chemistry of light-induced degradation

## Abstract

Many organic compounds undergo changes under the influence of light. This might be beneficial in, for example, water purification, but undesirable when cultural-heritage objects fade or when food ingredients (e.g., vitamins) degrade. It is often challenging to establish a strong link between photodegradation products and their parent molecules due to the complexity of the sample. To allow effective study of light-induced degradation (LID), a low-volume exposure cell was created in which solutes are efficiently illuminated (especially at low concentrations) while simultaneously analyzed by absorbance spectroscopy. The new LID cell encompasses a gas-permeable liquid-core waveguide (LCW) connected to a spectrograph allowing collection of spectral data in real-time. The aim of the current study was to evaluate the overall performance of the LID cell by assessing its transmission characteristics, the absolute photon flux achieved in the LCW, and its capacity to study solute degradation in presence of oxygen. The potential of the LID set-up for light-exposure studies was successfully demonstrated by monitoring the degradation of the dyes eosin Y and crystal violet.



**Publication**

Characterization of a liquid-core waveguide cell for studying the chemistry of light-induced degradation

Iris Groeneveld, Suzan E. Schoemaker, Govert W. Somsen, Freek Ariese, Maarten R. van Bommel

*Analyst*, **2021**, 146, 3197, DOI: 10.1039/d1an00272d

## 5.1 Introduction

Light-induced degradation (LID) or photodegradation takes place almost everywhere light reaches. After absorbing light, a molecule is prone to react with other molecules to form new products or degrade, losing particular structural properties. This can be a beneficial process, for instance for production of drinking water when photodegradation is used for the removal of unwanted chemicals by applying ultra-violet (UV) radiation to surface water. However, in some cases, this might lead to the formation of unknown compounds which may be toxic or affect the environment. In addition, chemical degradation after light exposure is unwanted in, for example, cultural heritage or the food industry where properties such as color and structure or smell and taste should remain stable as long as possible.



A straight-forward method for studying photodegradation is irradiation of a solution of the sample in a vial or cell for a fixed time, followed by analysis of solution aliquots by e.g., liquid chromatography (LC). Using such an approach, for example, Confortin studied the degradation of the dye crystal violet (CV), Toohey investigated the effect of iron in presence of UV light on the sweetener rebaudioside A, and Hora examined the degradation of pharmaceutical compounds in wastewater [1–3]. Similar approaches have been applied to e.g., pharmaceuticals [4–9], pesticides [10,11], foodstuffs [12], and polymers [13,14].

These approaches mostly work well if a single, fairly pure compound is studied and a limited number of degradation products is formed. However, if the sample is a (complex) mixture and potentially contains unknown components, interpretation of the results becomes very difficult. This complexity increases when multiple types of molecules degrade and/or start to react with other sample components or formed fragments. A major challenge in such photodegradation studies is, therefore, to distinguish which degradation products arise from which (parent) molecule.

A way to decrease sample complexities that are met in LID studies, might be to carry out a separation of the sample components prior to light exposure. This preferably would be done in an on-line fashion where a separation technique like LC is coupled to a low-volume irradiation cell in which isolated components can be exposed to light. Ideally, such a cell would also allow real-time spectroscopic monitoring of the content. After exposure, the cell content could be transferred on-line to another LC system for separation and analysis of the degradation products. On-line post-column photoreactors have been reported for reaction detection of target compounds [15–18], however, these reactors are less suited for on-line LID studies. The continuous flow reactors have

relatively large volumes, the actual illumination of the sample is hard to control, and they do not allow in-situ monitoring of photochemical reactions.

Liquid core waveguides (LCWs) are tubes of small internal diameter that are based on the principle of total internal reflection (TIR) and are typically made of low refractive index (RI) materials, which behave as an optical fiber once filled with a liquid of higher RI. They might offer a solution to the abovementioned challenges faced in on-line coupling of photoreactors. The possibility of coupling LCWs with LC has already been proven to be possible in earlier work where the LCW was used as a post-column (chemically-active) detection cell [19–21]. Therefore, we anticipate that on-line coupling of an LCW as an LID cell to LC in a pre- or post-column fashion will be feasible. LCWs facilitate axial illumination of its entire content and the possibility to detect the transmitted light, making the optical path length of an LCW quite significant (up to 1 m), which is an advantage when concentrations of exposed components are low. Furthermore, since the light source is focused inside the capillary, the light dose can be easily controlled. Because of these properties, Teflon AF capillaries or coatings have been used for sensitive UV-Vis absorbance [22,23], fluorescence [24,25], mid-IR [26], and Raman spectroscopic detection [27–31].

LCWs are typically made of Teflon AF, which is an amorphous and translucent polymer of tetrafluoroethylene (TFE) and 2,2-bis(trifluoromethyl)-4,5-difluoro-1,3-dioxole (PDD) with an RI of 1.29 – 1.31. This makes it suitable as an LCW when using core solvents such as water (RI≈1.33), methanol (RI≈1.333) and acetonitrile (RI≈1.34), which all are frequently used in LC eluents. There are currently two types of LCWs that are fabricated using Teflon AF. Type I is a tube entirely made of such a polymer, whereas type II is a silica capillary coated externally with Teflon AF [32]. For a type II LCW, TIR occurs both at the core/silica and the silica/polymer interface, making it less suited as LID cell because a significant fraction of the light will travel through the capillary wall rather than through the liquid core where the sample will be located. For type I LCWs, TIR occurs at the core/polymer interface, providing optimal light-exposure of the total content in the LCW. An additional benefit of the use of type I LCWs made of Teflon AF is their permeability to gases, allowing diffusion of e.g., oxygen into the cell required for photooxidation processes [33,34].

This study investigates the potential of a Teflon AF2400 LCW as an LID cell coupled to a spectrograph allowing efficient illumination together with collection of real-time transmission and absorption spectra of the cell content. The light transmission characteristics of LCWs of different length were studied as a function of wavelength. The effects of filling procedures and stability throughout the measurements were evaluated,

and the diffusion of oxygen gas through the cell walls was verified using methylene blue as indicator. The absolute photon flux in the cell was determined by actinometry. The basic performance of the new LID cell was evaluated by monitoring the degradation of eosin Y (EY) and crystal violet (CV) in the LCW and subsequent analysis of the content of the LID by LC. To the best of our knowledge, the use of an LCW cell for studying photodegradation has not been reported before.

## 5.2 Experimental

### 5.2.1 Chemicals

For the preparation of LC eluents, Ultrapure Milli-Q water (MQ), methanol (MeOH) (Biosolve, UPLC/MS grade), formic acid (FA) (Sigma-Aldrich), sodium hydroxide (NaOH) (Sigma-Aldrich) and triethylamine (TEA) (Sigma-Aldrich) were used. Actinometry experiments were performed using 1,2-Bis(2,4-dimethyl-5-phenyl-3-thienyl)-3,3,4,4,5,5-hexafluoro-1-cyclopentene (DAE) obtained from TCI Chemicals (Tokyo, Japan) dissolved in hexane (Sigma-Aldrich). In order to assess gas diffusion, methylene blue hydrate (Sigma-Aldrich, ≥ 97% purity), NaOH and glucose (Sigma) were used. Degradation experiments were executed using solutions of eosin Y (Sigma-Aldrich, ≥ 99% purity) and crystal violet (Sigma-Aldrich, ≥ 90% purity) dissolved in MQ.



### 5.2.2 Methods

**LID cell set-up and detection system**

A schematic overview of the LID set-up is shown in Fig. 5.1. Illumination was performed with a Xenon lamp purchased from Hamamatsu. When only a specific part of the spectrum of the Xenon lamp was required, bandpass filters were placed inside the lamp housing. The light from the lamp was guided through an optical fiber (core diameter, 1500 µm) into the LID cell via a coupling piece (Fig. C-1, Appendix C). An identical coupling piece was used at the end of the LID cell to measure the transmitted light. The coupling pieces were made of PEEK and designed with three threaded inlets: one in the axial face for fitting the LID cell, and two side inlets at a 45° angle. The back of the pieces were sealed with a quartz window to allow introduction or collection of light. The two side inlets at the first coupling piece can be used for introduction of the sample and (if necessary) another solvent or reagent e.g., a catalyst or inhibitor; details of sample introduction are provided in Section 2.3. The side inlets of the coupling piece at the end of the LCW were used for waste or for sample collection.

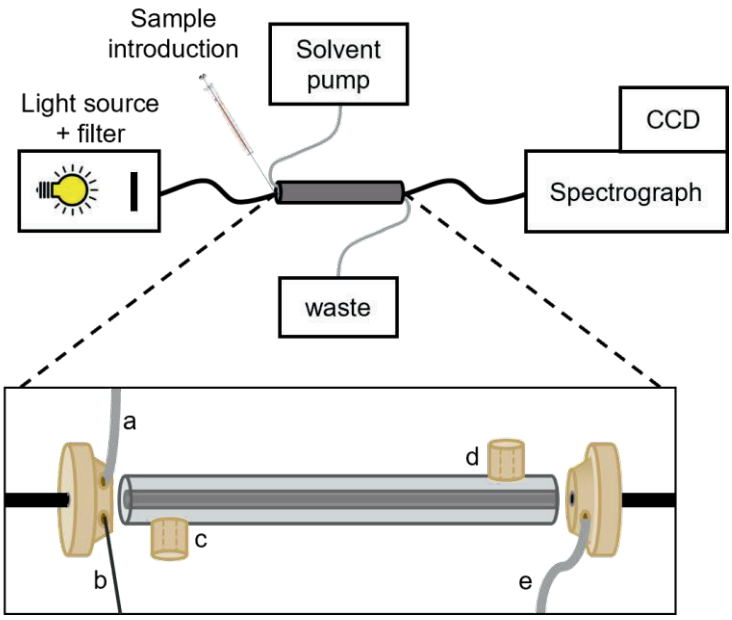


Figure 5.1. Schematic overview of the design of the LID cell. From left to right: (a) connection with solvent pump, (b) sample delivery by syringe, (c) gas inlet, (d) gas outlet, (e) waste channel.

The LID cell consisted of a type I LCW made of Teflon AF2400 (ID, 800 µm; OD, 1000 µm), obtained from Cambridge Reactor Design (Cottenham, United Kingdom), which was placed inside an outer tubing made of high-density polyethylene (HDPE), creating a tube-in-tube design. T-pieces made of PEEK were glued into the outer tubing to permit addition of gases, such as nitrogen or oxygen (see Fig. 5.1). Both ends of the LID cell were glued into standard chromatographic finger-tight fittings with Valco thread facilitating the connection of the LID cell to the coupling pieces. To study the effect of gas permeability of the type I LCW, type II LCWs were also used which are not gas permeable. These were made of fused-silica, coated externally with ±15 µm Teflon AF2400 (ID, 100 µm; OD, 363 µm), obtained from CM Scientific Ltd (Silsden, United Kingdom). The type II LCW was fitted with two chromatographic finger-tight fittings using micro sleeves to prevent leaking.

Transmitted light was collected by use of an optical fiber at the other end of the cell that was connected to an SR-163 spectrograph equipped with a DV420A CCD camera, both from Andor Technologies (Belfast, UK). The distance of the optical fiber from the cell could be varied to either increase or decrease the intensity of the measured signal. Generally, a 1% transmission filter was placed in between the end of the LID cell and the optical fiber to reduce the signal and to avoid overloading the detector response. The spectrograph was equipped with a grating of 600 lines/mm blazed at 300 nm, a light

entrance slit with adjustable width, and a back illuminated CCD chip of 256x1024 pixels with a pixel size of 26 $\mu m^2$ for detection of the dispersed transmitted light. The spectral range covered by the CCD camera in non-scanning mode was about 263 nm and was calibrated using a Hg calibration lamp. The CCD chip was cooled at -60 °C. Unless stated differently, detection settings used for transmission measurements were: slit width, 10 µm; exposure time, 0.1 s; vertical shift speed, 8.25 µs; horizontal read-out, 33 kHz at 16-bit. Acquired spectra were collected using the Full Vertical Binning mode and were background corrected in the case of absorption measurements. Data acquisition was performed using Solis software from Andor Technologies.

### Injection/filling

The LID cells were filled and flushed with solvent by means of a K-500 solvent pump (Knauer, Berlin, Germany) at a flow rate of 200 µL/min. The pump was connected to one of the side inlets of the first coupling piece, unless specified otherwise. Samples of EY and CV were directly introduced using a syringe, which was connected to the second inlet, while the solvent pump was turned off. The cell was cleaned in between samples by flushing with 300 µL of MeOH followed by 300 µL of MQ using the solvent pump.



### LC system

In order to prepare the LC eluent, a buffer was made by adding FA and NaOH to 1 L of MQ at a final concentration of 0.1 M and 0.02 M respectively, to obtain a pH of 3. The eluent was prepared by mixing buffer and MeOH volumes in ratios of 95/5 respectively for mobile phase A, and 5/95 for B. TEA was added as an ion pairing agent to both A and B at a final concentration of 5 mM. All analyses were carried out on an Agilent 1100 series LC system equipped with a quaternary solvent delivery system, a column oven, an autosampler and a diode array detector (DAD). A ZORBAX Eclipse RRHD C18 column (2.1 x 150 mm; particle size, 1.8 µm) and a security guard column (2.1 x 5 mm) containing the same C18 packing were both obtained from Agilent. Gradient elution was performed going linearly from 5% to 95% B in 10 min. After 5 min at 95% B, the mobile phase changed back to 5% B with a total analysis time of 30 min, including 15 min equilibration time. The flow rate was set at 150 µL/min and the column oven was set at 40 °C. Spectral data were recorded from 250 to 800 nm with a resolution of 1.0 nm, a sampling rate of 144 Hz, and analysis monitoring was set at detection wavelengths of 254, 400, 515, 550, and 595 nm. The equipment was controlled by ChemStation Chromatography Data Software from Agilent.

## 5.3 Results and discussion

The performance of the LCW is first characterized with respect to parameters affecting its transmittance. We then evaluate the photon flux and gas permeability of the Teflon AF2400 LCW. Finally, we demonstrate the applicability of the LCW in a proof-of-concept experiment studying the LID of EY and CV.

### 5.3.1 LCW transmittance

The light transmittance of the LCW inside the LID cell is a critical property: it determines both the photodegradation rate as well as the detection limit when used in combination with spectroscopy. Preferably, light losses should be minimized to achieve a consistent illumination of the entire solution. Transmittance of the LCW can be dependent on or influenced by several parameters, such as length of the LCW, concentration and molar absorption coefficient of the sample components, scattering losses inside the LCW, pressure applied on the LCW, and temperature. Furthermore, it has recently been reported that when transmittance is sufficient, small internal LCW diameters (< 1 mm) allow higher and a more homogeneous irradiance resulting in shorter reaction times of photochemical reactions [35]. For this study we used LCWs with an ID of 800 µm and the effects of the above-mentioned parameters were studied.

**Length of LCW**

The use of an LCW as LID cell allows exposure of the entire sample and the increased optical path length results in a higher overall absorbance, enhancing photodegradation efficiency [31]. However, the length of the LCW should be chosen carefully, as light transmittance is expected to decrease exponentially with the optical path length when an absorbing compound is present. Overall absorbance should not be too high, as light should still reach the detector to obtain spectral information and molecules at the end of the LCW should still be exposed sufficiently. The influence of the cell length was tested by fabricating four LID cells using type I LCWs of 12 cm (cell volume ~60 µL), 20 cm (~100 µL), 40 cm (~200 µL) and 60 cm (~300 µL) long. These were filled with water and the intensity of the transmitted light was measured for each cell at different wavelengths using specific bandpass filters. The intensities followed from power measurements in triplicate (each time after realignment, RSD < 9%), where the sensor of the power meter was positioned at the excitation fiber outlet or at the exit of the LCW filled with MQ. The light transmittance was calculated by comparing the intensity at the end of the LCW ($I$) with the intensity at the exit of the excitation fiber ($I_0$). Fig. 5.2 shows the average (n=3) transmittance of the four LCWs at different wavelengths, normalized to the highest transmittance value measured for the 12 cm LCW at 630 nm.

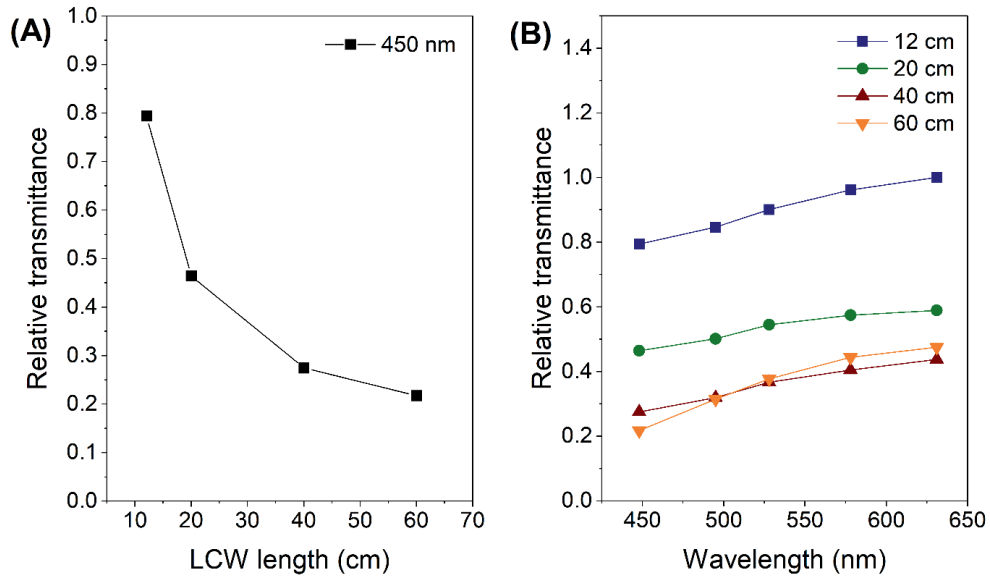


Figure 5.2. (A) The relative transmittance for light of 450 nm as function of LCW length calculated by comparing the transmitted (I) with the input power ($I_0$); (B) the relative transmittance for light of different wavelengths using LCW lengths of 12, 20, 40 and 60 cm.

Fig. 5.2A shows that the transmittance decreases significantly with increasing length. Light losses are most probably due to reflection losses caused by pores and imperfections in the Teflon capillary surface, as also indicated by Altkorn et al. [31]. The number of reflections increases with the length of the capillary, causing more light to be lost. Apparently, this effect is strongest in the first part of the LCW; the difference between LCWs of 40 and 60 cm was found to be negligible in our experiment.

The light absorbance by a compound inside the cell is a point of consideration. Increased analytical sensitivity due to a long optical path length might be beneficial, however, from the viewpoint of analyte degradation, the formation of a strong light-intensity gradient inside the LID cell is not favored. Therefore, for LID studies of samples showing significant light absorbance at the applied wavelength, medium-length LCWs are preferred over very long ones. Another reason to limit the length of the LCWs, is to increase compatibility with LC. LCW volumes larger than LC peak volumes would cause loss of LC resolution when using the cell in a post-column setup.

### Wavelength of light

The LID cell should ideally provide adequate light transmittance over a broad wavelength range. Its wavelength dependency was tested by measuring the light transmittance of an LCW filled with MQ using bandpass filters of 450, 500, 532, 580 and 633 nm (nominal

values) (Fig. 5.2B). The LCW can be used over this entire range, but the transmittance increases with increasing wavelength. The porosity and imperfections of the polymer surface might cause light losses by scattering, which will be stronger for photons of shorter wavelength. The observed wavelength dependencies of the light transmittance, although not very large, should be considered when using polychromatic light sources for photodegradation.

### Variation due to filling procedure

The performance of Teflon AF2400 cells, e.g., for absorbance spectroscopy, might be sensitive to changes in liquid pressure caused by solvent injection or filling of the cell [36]. Therefore, the light throughput of the LID cell was measured after filling a type I LCW in triplicate using an HPLC pump at flow rates of 50, 100, 150, 200 and 250 µL/min. The average transmitted light intensities with corresponding spread (standard error) are shown in Fig. C-2 (left) in the Appendix. The average measured intensities at the applied flow rates did not differ significantly. The standard error, however, decreased going from 50 up to 200 µL/min, but increased again at 250 µL/min. It is hypothesized that flow rate and pressure may affect to what extent the liquid penetrates air-filled pores in the Teflon material and this would affect the TIR properties of the LCW [37]. We also observed that filling the LCW manually by syringe results in variability of the transmittance, which is most likely caused by irregularities in the applied pressure. When the same experiment was performed using a type II LCW, the effect of different flow rates on transmittance and spread was negligible (Fig. C-2, right). Therefore, we conclude that the porous Teflon AF wall is more susceptible to pressure fluctuations and that it is important to choose a well-reproducible filling or injection method using a stable pump that transfers the sample from the autosampler to the LID cell.

### Signal stability

During a typical photodegradation experiment, the LID cell is irradiated for a prolonged period of time, while simultaneously spectral data are collected. To test the cell stability, repetitive light throughput measurements of 1 min each over a period of 90 min were performed in triplicate with a type I and a type II LCW, both filled with MQ. Fig. 5.3 shows the measured intensities over time for the LCWs. The graph for the type I LCW shows a quick rise of the intensity after filling of the cell and a more or less constant signal after 5 min. For the type II, however, it takes (much) longer for the signal to stabilize and the variation between measurements is larger. A reason for this difference may be found in the external silica coating of the type II modified Teflon. Teflon AF2400, like other polymers, is susceptible to temperature changes, as Dlubek et al. [37] described. Increased temperature results in an increased hole-free volume, which lowers the RI of

the LCW and may affect transmittance. We hypothesize that due to the silica coating in the type II LCW, heat may not be exchanged efficiently and a slow increase in transmittance is observed. For the type I LCW, the thin wall and/or the permeability may contribute to better heat dissipation, providing stable signals after 5 min and allowing spectral data to be measured in a repeatable manner.

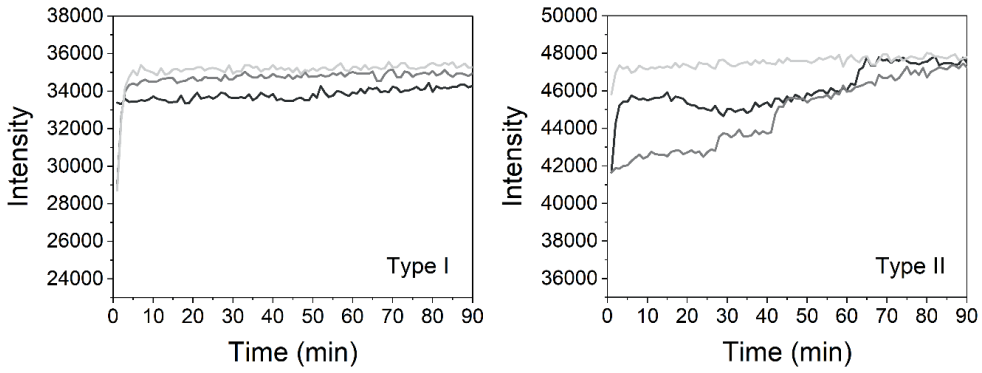


Figure 5.3. The intensity of the transmitted light measured in triplicate at 462 nm every minute for 90 min for a type I LCW and a type II LCW filled with MQ.

## 5.3.2 Light absorption in LCW

**Absorbance as a function of analyte concentration**

The LCW can be used as an absorbance cell allowing sensitive, in-situ monitoring of photodegradation. The performance of the LCW for absorption detection was determined by measuring the absorbance of an aqueous dilution series of CV. The absorbance at 585 nm of the solutions was plotted against the CV concentration (Fig. 5.4).

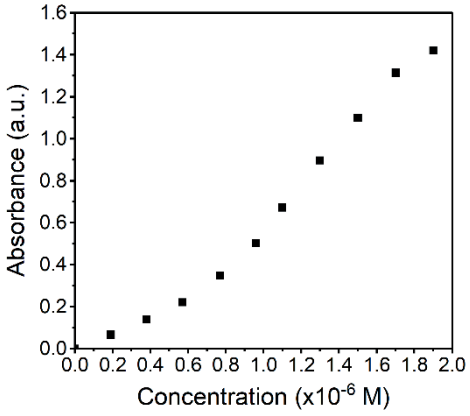


Figure 5.4. Measured absorbance as a function of the concentration of CV measured in a 12-cm long LCW.

The 12-cm LCW shows a clearly increasing absorbance over a relevant concentration range. Although not perfectly linear, the observed relation will enable us to correlate absorbance changes to changes in molecular composition of the sample due to photodegradation. Notably, the design of the LCW LID cell is very suitable for measuring low concentrations, for instance after sample pre-separation with LC, where the concentration of minor components can be rather low.

**Photon flux in LCW determined by actinometry**

In order to assess photodegradation processes, the photon flux (photons/sec) inside the LID cell should be known. This was determined using a chemical actinometer: a compound that undergoes a light-induced reaction for which the quantum yield (Q) is known. The actinometer of choice was DAE, a diarylethene derivate known for its photoisomerization reaction. The color change of DAE between violet and colorless is a result of a ring-closing and -opening reaction, which takes place upon irradiation with either UV or Vis light and is reversible up to 3000 times (Fig. C-3) [38–40]. This compound is especially suitable as an actinometer in closed systems, such as the LID cell, as the change in the absorption spectrum can be measured in real-time, so that sampling of the solution is not required. Furthermore, in contrast to e.g., ferrioxalate actinometers, DEA remains in solution throughout the reaction, making it compatible in combination with microchannels, such as the LCW.

A 20-cm LCW was filled with a solution of DAE in hexane and was irradiated with the Xenon lamp. Since this is a polychromatic light source, an equilibrium between the open and closed form will be reached after a certain period of time. Therefore, a UV shortpass filter (<350 nm) was used to turn DAE into the violet closed form (DAE-c), and a bandpass filter of (nominal value) 580 nm was used to allow DAE to turn into the colorless open form (DAE-o). This wavelength was chosen because it is close to the absorption maximum of DAE-c. The actual maximum transmitted wavelength of the bandpass filter was determined to be 578 nm and was taken into account. Calculations and technical aspects regarding the measured photon flux are further elaborated in the Appendix.

Fig. 5.5 shows the decrease in absorbance in real-time for the reaction from DAE-c to DAE-o at 578 nm. The linear part of the decrease in absorption was plotted and used to calculate the average rate of the conversion. From this, the photon flux at 578 nm was calculated. This was compared to the flux calculated from power measurements, obtained by placing the power meter behind the end of the LID cell filled with water. Using actinometry, a photon flux of $10.3 \cdot 10^{12}$ photons/s was calculated, compared to $9.49 \cdot 10^{12}$ photons/s obtained from power measurements. The similar results obtained with both methods indicate that the power measurements are a good estimate of the photon flux

passing the LCW. However, the power meter measures the number of photons reaching the end of the LID cell, whereas the actinometer measures the effective intensity inside the LCW. Therefore, we presume that the DAE actinometer gives a better representation of the real photon flux inside the LID cell.

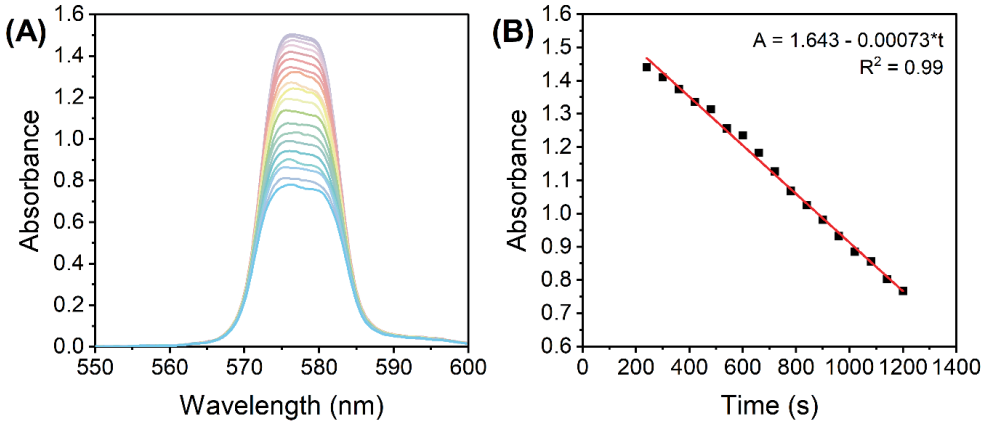


Figure 5.5. Actinometry of the LCW. (A) Measured change in absorbance in real-time during the isomerization reaction of DAE-c to DAE-o at 578 nm inside a 20-cm long LID cell. (B) Linear part of the of the decrease in absorbance is plotted; slope was used to determine the photon flux (Appendix C).

### 5.3.3 Gas diffusion through LCW wall

Oxygen gas plays an important role in many photodegradation reactions. The Teflon AF LCW comprises a gas permeable wall, which offers the possibility to influence the photodegradation process by adding or removing oxygen gas to or from the exposed solution. Oxygen diffusion was tested by using methylene blue (MB) as an indicator for oxygen. The LID cell was filled with an aqueous solution of MB, glucose and sodium hydroxide. In the presence of oxygen, MB is oxidized and the solution will turn blue, resulting in absorption of visible light by MB. When oxygen is removed or consumed, MB will be reduced by the sodium hydroxide and the solution turns colorless, resulting in a reduced visible absorbance. The decolorization reaction of MB by oxygen was recorded in real-time by measuring the transmitted light intensity of the LCW at the absorption maximum of MB (668 nm). Fig. 5.6 shows the LCW light transmittance in real-time (green curve) while the outer tubing of the LID cell, which initially contained air, was flushed with nitrogen gas. During the flushing, part of the LID cell was filmed using a camera and fragments of this footage are shown at the corresponding time points.

After about 50 s, the nitrogen flow was turned on, and from 65 s onwards the transmitted light intensity increased, indicating decolorization, and thus reduction of MB caused by oxygen depletion in the LCW. After about 200 s the nitrogen flow was turned off, and

subsequently a reduction of the transmittance was observed, implying oxidation of MB due to presence of oxygen in the LCW. The latter means that spontaneous diffusion of oxygen occurs from air back into the solution. Since the solution inside the LCW is not stirred, we assume an oxygen gradient will exist from the wall to the middle of the LCW. As expected, the video recording of the color changes showed no sign of inhomogeneity along the length dimension of the LCW. This experiment showed that the Teflon AF wall is gas permeable even at ambient pressure, which is in line with previous findings [41]. The experiment also demonstrated that oxygen levels in the LCW can be controlled using the tube-in-tube design, and that the reaction process can be followed in real-time by absorbance spectroscopy. This is a clear advantage of the type I LCW over the type II, as it allows the study of photodegradation under oxygen-saturated conditions and evaluation of the effect of oxygen on degradation, providing more detailed mechanistic insight.

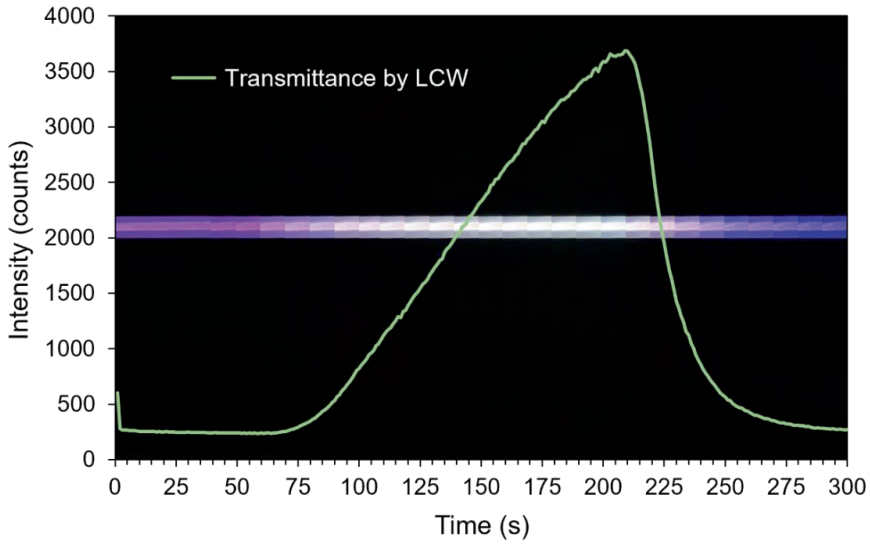


Figure 5.6. Monitoring of oxygen in the LCW. The LID cell was filled with a solution of MB, glucose and NaOH which was used as reagents to observe the presence of dissolved oxygen in the LCW. The green curve shows the measured transmittance of the LCW at 668 nm. The blue/purple trace shows the actual color of the LCW at the corresponding time points. When the oxygen concentration decreases by flushing nitrogen gas through the outer tubing (50–200 sec), MB is reduced and turns colorless.

### 5.3.4 Monitoring the LID of EY and CV

Two proof-of-concept experiments were performed by monitoring the photodegradation of the dyes EY (Fig. C-4) and CV (Fig. C-5). The photodegradation processes of these dyes are well known, allowing thorough evaluation of the results obtained with the LCW setup and LC analyses. A 12-cm LCW was filled with a $5 \cdot 10^{-7}$ M solution of EY (ε at 517

nm, 95,000 $cm^{-1}M^{-1}$), and subsequently exposed to light from the Xenon lamp for 3 hrs while recording absorption spectra in real time every 10 min. An aliquot of the starting (unexposed) EY solution was also analyzed by LC with DAD detection. After 3 hrs the exposed EY solution was collected off-line by flushing the LID cell with 60 µL of MeOH. The collected sample was immediately analyzed by LC-DAD in order to measure potential degradation products. The same procedure was followed for a $2.5 \cdot 10^{-6}$ M solution of CV (ε at 590 nm, 87,000 $cm^{-1}M^{-1}$), but then using a 5-hr light exposure time.

**Eosin Y**

According to Alvarez-Martin et al., the degradation of EY in the presence of oxygen follows an oxidative process resulting in breakdown of the chromophore and consequently full discoloration [42]. Under anoxic conditions, debromination of EY takes place while its chromophore remains intact. Fig. 5.7A shows the in-situ absorption spectra recorded during the 3-hr irradiation of EY. A clear and steady decrease of the absorbance in time over the whole visible EY spectrum was observed, indicating a loss of the chromophoric moiety by light degradation of the EY present in the LCW. During 3-hr light exposure, the absorbance intensity of EY at 515 nm reduced with 97%. The LC chromatograms recorded at 515 nm obtained before and after light exposure of the EY solution are shown in Fig. 5.7B with EY eluting at 18.4 min. The peak area obtained for EY in the light-exposed solution is only 4% from the EY peak area of the solution before irradiation, which correlates nicely with the reduction in absorbance observed in the LCW measurements.



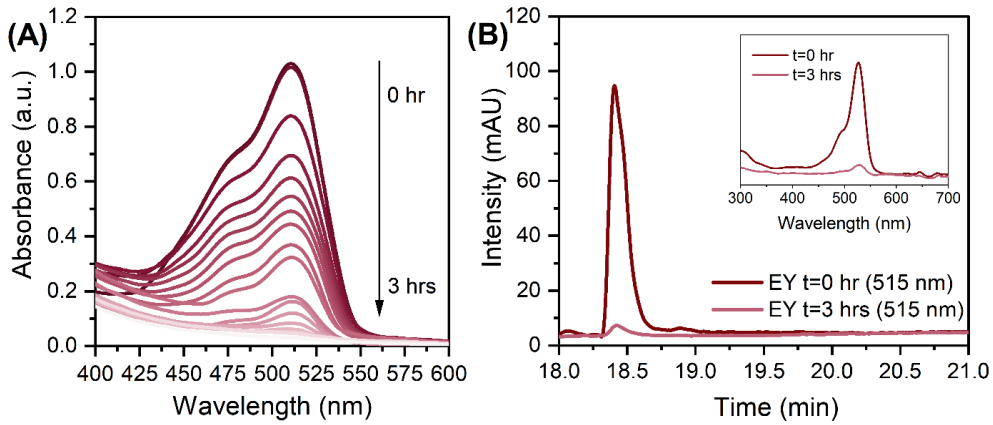


Figure 5.7. (A) Real-time absorption spectra of a solution of EY (5·10-7 M in water) present in the LID-cell during light irradiation for 3 hrs; (B) LC chromatograms of the EY solution before (at t=0 hr) and after exposure (at t=3 hr) in the LID cell. The insert shows the DAD spectra obtained during LC analysis at t=0 hr and t=3 hr for the peak at a retention time of 18.48 min.

For EY, debromination will take place in the first phase of degradation. Since the UV/Vis absorption spectra of partly debrominated EY are similar to that of EY [43], no shift in absorption is observed in the LCW. The final degradation products only absorb in the UV region, as a result a decrease in response of the signal of EY is observed in the LCW, whereas EY degraded for 3 hours mainly shows UV-absorbing components in the chromatogram (Fig. C-6). The change in absorbance during irradiation as provided by the LCW setup can directly be correlated to the degree of photodegradation.

### Crystal violet

LID of CV revealed a more complicated degradation pathway than observed for EY, exhibiting both colorless as well as visible-light absorbing degradation products. The real-time absorption spectra obtained during light exposure of CV in the LCW over a 5-hr period (Fig. 5.8) show a 32% decrease in the absorbance of the sample, accompanied by a slight blueshift of the absorption maximum.

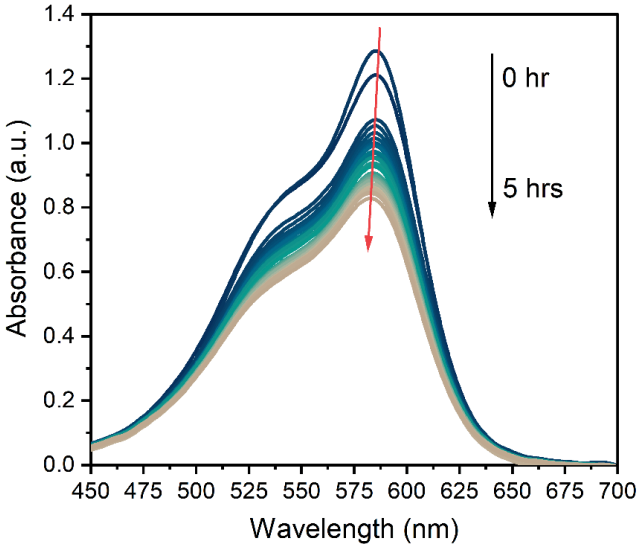


Figure 5.8. Real-time absorption spectra of a solution of CV ($2.5 \cdot 10^{-6}$ M) in water present in the LID cell during light irradiation for 5 hrs.

This implies that the chemical composition of the sample is changing due to photodegradation. The absorbance measured in the LCW is the sum of the absorbance of all Vis-absorbing compounds (CV + degradation products). The absorption coefficients of the degradation products may differ from CV and are generally unknown. A decrease of 32% in absorbance suggests that apart from demethylation products (of which the chromophore is largely unaffected) a significant percentage of CV may have degraded into colorless products, such as dimethylaminobenzophenone (Michler's

ketone) and dimethylaminophenol, also reported by Confortin and Kuramoto (Fig. C-7) [1,44]. LC-DAD analysis of the 5-hr degraded CV sample showed several peaks (11, 12 and 14) that exhibit absorption in the UV region. Of course, based on the absorption spectra only, the compounds could not be identified and additional MS analysis should be performed.

A slight shift towards shorter wavelength of the absorption maximum was observed for the whole sample during the in-situ absorption measurements in Fig. 5.8. Evaluating the absorption spectra of the degradation products measured by the LC-DAD (Fig. C-8), a similar blueshift was noticed for each degradation product, which was also observed in degradation research studies of CV by Confortin et al., and others [1,45,46]. This is most likely a consequence of the demethylation process of CV resulting in a 5 nm shift of the absorption maximum for each newly formed product. Demethylation also results in a decreased retention time, caused by an increased polarity of the degradation products, which can be seen in Fig. 5.9.



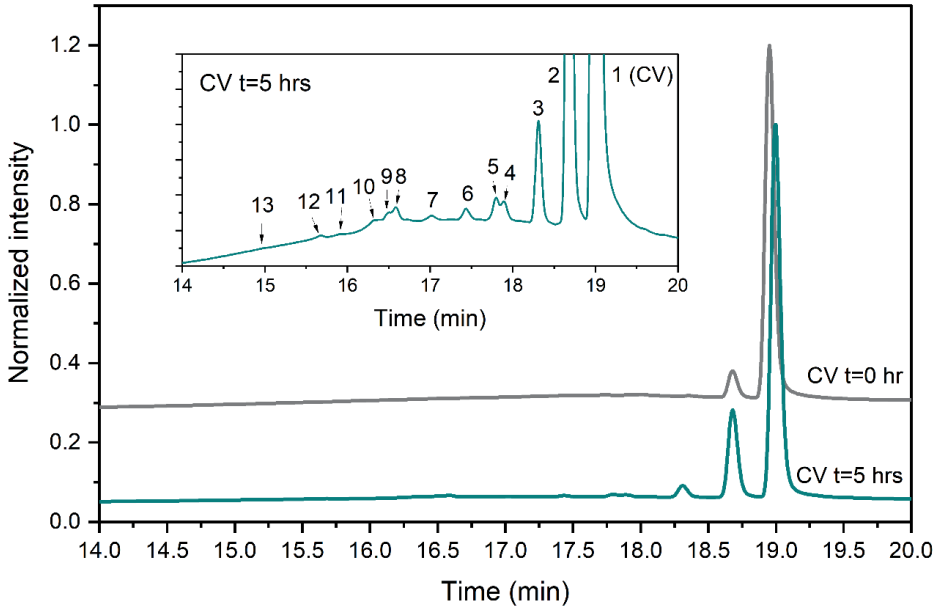


Figure 5.9. Normalized LC-DAD chromatograms (at 595 nm) of the CV solution before (at t=0 hr) and after exposure (at t=5 hrs) in the LID cell. The insert shows a zoom of the chromatogram obtained at t=5 hrs revealing the peaks of degradation products (2–13).

An overview of the detected analytes and tentative assignments is given in Table C-1. When comparing the obtained results with those by Confortin et al. peaks 2, 3, and 4 are most likely mono-, di-, and tri-demethylated CV, respectively. Peak 5 may be an isomer of tri-demethylated CV, and peaks 6 and 7 show similar absorption spectra as tetra-, and

penta-demethylated CV. Three more peaks (8 – 10) were found of which peaks 8 and 9 show similar absorption maxima as that of diamond green B (Fig. C-9). However, as Confortin also explains, these may also be assigned to N-oxide derivatives of CV. Peaks 11, 12 and 14 show absorbance in the UV, but remain unidentified as the concentration was too low to obtain well defined absorption spectra and are therefore not shown. Peak 13, however, showed an absorption maximum of 546 nm, which is similar to that of pararosaniline, which is completely demethylated CV. This was later confirmed by the analysis of a pararosaniline standard. The relative peak areas (derived from the LC-DAD signals) of CV and its degradation products, before and after irradiation, are shown in Fig. 5.10.

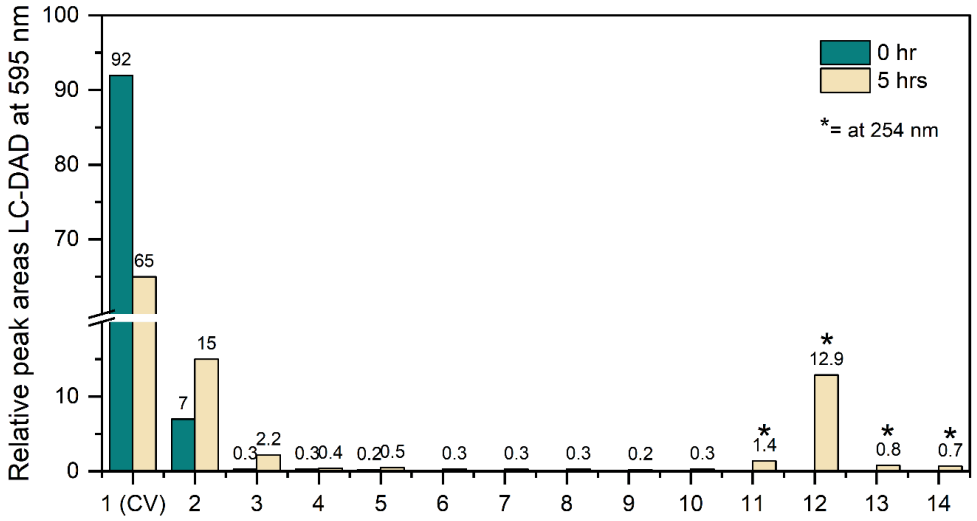


Figure 5.10. Relative peak areas of CV and degradation products obtained by LC-DAD before (0 hr) and after (5 hrs) exposure in the LID-cell. Peak areas are extracted at 595 or 254 nm (*) if absorbance was in the UV.

To make final conclusions about the identity of the abovementioned peaks, additional MS analyses should be performed. However, the most important result shown here is that a >30% reduction of the main component CV was obtained after 5 hrs of degradation. Weyermann and Confortin, who performed off-line degradation of CV in solution, reported near complete degradation after 25 and 115 hours, respectively [1,45]. For simple degradation processes, such as for EY, the decrease in absorbance is a straightforward measure for the degradation rate. For compounds like CV, however, for which the degradation products also absorb in the same wavelength range as the parent compound, it is slightly more complicated to use the absorbance for this purpose.

## 5.4 Conclusions

This study has shown that it is possible to initiate photodegradation of EY and CV while collecting real-time spectral data using an LID cell based on an LCW made of Teflon AF2400. The LCW is an efficient tool for illumination of the whole sample and is able to guide the light towards a detector. The results from the degradation experiments showed that real-time absorbance spectroscopy is useful for acquiring information on the stage of degradation. Changes in the shape of the absorption spectrum as well as the absorbance intensity are indicative for the extent of degradation. The results of the photodegradation of EY and CV are in line with previous studies, and the high photodegradation rate compared to conventional 'in-beaker' degradations looks promising [1,42,45,46]. Clearly, the potential for on-line coupling of the cell to LC for further characterization of the degradants, comes as an advantage here.



There is also room for improvement. The speed of photodegradation could be enhanced by improving the efficiency of light coupling into the cell, and automation of the injection system may result in more reproducible spectral data as variation in applied pressure is reduced. The long path length of the LCW is beneficial for (diluted) samples with low absorbances. The transmittance by the LCW, however, decreases with the length of the capillary, caused by pores and imperfections in the material. As a result, the intensity of the light inside the LCW also decreases with length. Therefore, for LID studies, medium-length LCW are preferred over very long ones to prevent the formation of a strong light-intensity gradient inside the LID cell.

# References

[1] D. Confortin, H. Neevel, M. Brustolon, L. Franco, A.J. Kettelarij, R.M. Williams, M.R. van Bommel, Crystal violet: Study of the photo-fading of an early synthetic dye in aqueous solution and on paper with HPLC-PDA, LC-MS and FORS, J Phys Conf Ser. 231 (2010) 012011. https://doi.org/10.1088/1742-6596/231/1/012011.

[2] M.J. Toohey, L.N. Bell, Food chemical stability as affected by iron and ultraviolet light exposure: Rebaudioside A degradation as a case study, J Food Process Preserv. 43 (2019) 1–5. https://doi.org/10.1111/jfpp.14201.

[3] P.I. Hora, P.J. Novak, W.A. Arnold, Photodegradation of pharmaceutical compounds in partially nitritated wastewater during UV irradiation, Environ Sci (Camb). 5 (2019) 897–909. https://doi.org/10.1039/c8ew00714d.

[4] M. Shamsipur, B. Hemmateenejad, N.J. Jahani, K.M. Majd, Liquid chromatographic-mass spectrometric monitoring of photodegradation of diphenylamine using experimental design methodology, Journal of Photochemistry and Photobiology A: Chemistry. 299 (2015) 62–68. https://doi.org/10.1016/j.jphotochem.2014.12.002.

[5] V.G. Bório, A.U. Fernandes, L. Silveira, Characterization of an ultraviolet irradiation chamber to monitor molecular photodegradation by Raman spectroscopy, Instrum Sci Technol. 44 (2016) 189–198. https://doi.org/10.1080/10739149.2015.1081936.

[6] R. Salgado, V.J. Pereira, G. Carvalho, R. Soeiro, V. Gaffney, C. Almeida, V.V. Cardoso, E. Ferreira, M.J. Benoliel, T.A. Ternes, A. Oehmen, M.A.M. Reis, J.P. Noronha, Photodegradation kinetics and transformation products of ketoprofen, diclofenac and atenolol in pure water and treated wastewater, Journal of Hazardous Materials. 244–245 (2013) 516–527. https://doi.org/10.1016/j.jhazmat.2012.10.039.

[7] A.Y.C. Lin, M. Reinhard, Photodegradation of common environmental pharmaceuticals and estrogens in river water, Environmental Toxicology and Chemistry. 24 (2005) 1303–1309. https://doi.org/10.1897/04-236R.1.

[8] A.Y.C. Lin, X.H. Wang, W.N. Lee, Phototransformation determines the fate of 5-fluorouracil and cyclophosphamide in natural surface waters, Environmental Science and Technology. 47 (2013) 4104–4112. https://doi.org/10.1021/es304976q.

[9] F. Gosetti, M. Bottaro, V. Gianotti, E. Mazzucco, P. Frascarolo, D. Zampieri, C. Oliveri, A. Viarengo, M.C. Gennaro, Sun light degradation of 4-chloroaniline in waters and its effect on toxicity. A high performance liquid chromatography - Diode array - Tandem mass spectrometry study, Environmental Pollution. 158 (2010) 592–598. https://doi.org/10.1016/j.envpol.2009.08.012.

[10] A. Kiss, S. Rapi, C. Csutorás, GC/MS studies on revealing products and reaction mechanism of photodegradation of pesticides, Microchemical Journal. 85 (2007) 13–20. https://doi.org/10.1016/j.microc.2006.06.017.

[11] K. Sivagami, R.R. Krishna, T. Swaminathan, Photo catalytic degradation of pesticides in immobilized bead photo reactor under solar irradiation, Solar Energy. 103 (2014) 488–493. https://doi.org/10.1016/j.solener.2014.02.001.

[12] V. Thu Trang, Y. Kurogi, S. Katsuno, T. Shimamura, H. Ukeda, Protective effect of aminoreductone on photo-degradation of riboflavin, International Dairy Journal. 18 (2008) 344–348. https://doi.org/10.1016/j.idairyj.2007.10.001.

[13] G.J.M. Fechine, P.A. Christensen, T.A. Egerton, J.R. White, Evaluation of poly(ethylene terephthalate) photostabilisation using FTIR spectrometry of evolved carbon dioxide, Polymer Degradation and Stability. 94 (2009) 234–239. https://doi.org/10.1016/j.polymdegradstab.2008.10.025.

[14] E. Yousif, N. Salih, J. Salimon, Improvement of the photostabilization of PVC films in the presence of 2N-salicylidene-5-(substituted)-1,3, 4-thiadiazole, Journal of Applied Polymer Science. 120 (2011) 2207–2214. https://doi.org/10.1002/app.33463.

[15] D.A. Volmer, Investigation of photochemical behavior of pesticides in a photolysis reactor coupled on-line with a liquid chromatography-electrospray ionization tandem mass spectrometry system, Journal of Chromatography A. 794 (1998) 129–146. https://doi.org/10.1016/S0021-9673(97)00587-6.

[16] P.J. Harman, G.L. Blackman, G. Phillipou, High-performance liquid chromatographic determination of clomiphene using post-column on-line photolysis and fluorescence detection, Journal of Chromatography B: Biomedical Sciences and Applications. 225 (1981) 131–138. https://doi.org/10.1016/S0378-4347(00)80252-2.

[17] S.X. Peng, S.M. Dansereau, Ion-exchange liquid chromatographic analysis of bisphosphonates by on-line post-column photochemical reaction and spectrophotometric detection, Journal of Chromatography A. 914 (2001) 105–110. https://doi.org/10.1016/S0021-9673(00)01118-3.

[18] T. Pérez-Ruiz, C. Martínez-Lozano, M.D. García-Martínez, Simultaneous determination of thiamine and its phosphate esters by a liquid chromatographic method based on post-column photolysis and chemiluminescence detection, Journal of Pharmaceutical and Biomedical Analysis. 50 (2009) 315–319. https://doi.org/10.1016/j.jpba.2009.04.035.

[19] A.F. Kadjo, P.K. Dasgupta, C.P. Shelor, Optimum Cell Pathlength or Volume for Absorbance Detection in Liquid Chromatography: Transforming Longer Cell Results to Virtual Shorter Cells, Analytical Chemistry. 92 (2020) 6391–6400. https://doi.org/10.1021/acs.analchem.9b05464.

[20] L. Ganranoo, S.K. Mishra, A.K. Azad, A. Shigihara, P.K. Dasgupta, Z.S. Breitbach, D.W. Armstrong, K. Grudpan, B. Rappenglueck, Measurement of nitrophenols in rain and air by two-dimensional liquid chromatography-chemically active liquid core waveguide spectrometry, Analytical Chemistry. 82 (2010) 5838–5843. https://doi.org/10.1021/ac101015y.

[21] D. Kottke, B.B. Burckhardt, J. Breitkreutz, B. Fischer, Application and validation of a coaxial liquid core waveguide fluorescence detector for the permeation analysis of desmopressin acetate, Talanta. 226 (2021). https://doi.org/10.1016/j.talanta.2021.122145.

[22] K. Bescherer, J.A. Barnes, H.P. Loock, Absorption measurements in liquid core waveguides using cavity ring-down spectroscopy, Analytical Chemistry. 85 (2013) 4328–4334. https://doi.org/10.1021/ac4007073.

[23] T. Rubles, D. Paige, C. Anastasio, Lens-coupled liquid core waveguide for ultraviolet-visible absorption spectroscopy, Review of Scientific Instruments. 77 (2006) 1–4. https://doi.org/10.1063/1.2219973.

[24] Z. Liu, J. Pawliszyn, Capillary isoelectric focusing of proteins with liquid core waveguide laser-induced fluorescence whole column imaging detection, Anal Chem. 75 (2003) 4887–4894. https://doi.org/10.1021/ac034587m.

[25] A. Datta, I.Y. Eom, A. Dhar, P. Kuban, R. Manor, I. Ahmad, S. Gangopadhyay, T. Dallas, M. Holtz, H. Temkin, P.K. Dasgupta, Microfabrication and characterization of Teflon AF-coated liquid core waveguide channels in silicon, IEEE Sensors Journal. 3 (2003) 788–795. https://doi.org/10.1109/JSEN.2003.820343.

[26] K. Flavin, H. Hughes, P. McLoughlin, The development of a novel smart mid-infrared sensing methodology for residual solvents, International Journal of Environmental Analytical Chemistry. 87 (2007) 29–42. https://doi.org/10.1080/03067310600833443.

[27] B.J. Marquardt, P.G. Vahey, R.E. Synovec, L.W. Urgess, A Raman Waveguide Detector for Liquid Chromatography, Analytical Chemistry. 71 (1999) 4808–4814. https://doi.org/10.1021/ac9907336.

[28] S. Tanikkul, J. Jakmunee, M. Rayanakorn, K. Grudpan, B.J. Marquardt, G.M. Gross, B.J. Prazen, L.W. Burgess, G.D. Christian, R.E. Synovec, Characterization and use of a Raman liquid-core waveguide sensor using preconcentration principles, Talanta. 59 (2003) 809–816. https://doi.org/10.1016/S0039-9140(02)00623-9.

[29] R.J. Dijkstra, A.N. Bader, G.P. Hoornweg, U.A.T. Brinkman, C. Gooijer, On-Line Coupling of Column Liquid Chromatography and Raman Spectroscopy Using a Liquid Core Waveguide, Anal Chem. 71 (1999) 4575–4579. https://doi.org/10.1021/ac9902648.

[30] Y. Tian, L. Zhang, J. Zuo, Z. Li, S. Gao, G. Lu, Raman sensitivity enhancement for aqueous absorbing sample using Teflon-AF 2400 liquid core optical fiber cell, Anal Chim Acta. 581 (2007) 154–158. https://doi.org/10.1016/j.aca.2006.07.082.

[31] R. Altkorn, I. Koev, M.J. Pelletier, Raman performance characteristics of Teflon-AF 2400 liquid-core optical-fiber sample cells, Applied Spectroscopy. 53 (1999) 1169–1176. https://doi.org/10.1366/0003702991945560.

[32] R. Altkorn, I. Koev, R.P. Van Duyne, M. Litorja, Low-loss liquid core optical fiber for low-refractive-index liquids: fabrication, characterization, and application in Raman spectroscopy, Applied Optics. 36 (1997) 8992–8998. https://doi.org/10.1364/AO.36.008992.

[33] M. Brzozowski, M. O'Brien, S. V Ley, A. Polyzos, Flow chemistry: Intelligent processing of gas-liquid transformations using a tube-in-tube reactor, Acc Chem Res. 48 (2015) 349–362. https://doi.org/10.1021/ar500359m.

[34] S. Ponce, H. Christians, A. Drochner, B.J.M. Etzold, An Optical Microreactor Enabling In Situ Spectroscopy Combined with Fast Gas-Liquid Mass Transfer, Chemie Ingenieur Technik. 90 (2018) 1855–1863. https://doi.org/10.1002/cite.201800061.

[35] C. Sambiagio, T. Noël, Flow Photochemistry: Shine Some Light on Those Tubes!, Trends Chem. 2 (2020) 92–106. https://doi.org/10.1016/j.trechm.2019.09.003.

[36] WPI, 4000 Series Liquid Waveguide Capillary Cell, Instruction Manual, 2014.

[37] G. Dlubek, J. Pionteck, K. Rätzke, J. Kruse, F. Faupel, Temperature dependence of the free volume in amorphous teflon AF1600 and AF2400: A pressure-volume-temperature and positron lifetime study, Macromolecules. 41 (2008) 6125–6133. https://doi.org/10.1021/ma800748a.

[38] A. Roibu, S. Fransen, M.E. Leblebici, G. Meir, T. Van Gerven, S. Kuhn, An accessible visible-light actinometer for the determination of photon flux and optical pathlength in flow photo microreactors, Scientific Reports. 8 (2018) 1–10. https://doi.org/10.1038/s41598-018-23735-2.

[39] M. Irie, K. Sakemura, M. Okinaka, K. Uchida, Photochromism of Dithienylethenes with Electron-Donating Substituents, Journal of Organic Chemistry. 60 (1995) 8305–8309. https://doi.org/10.1021/jo00130a035.

[40] T. Sumi, Y. Takagi, A. Yagi, M. Morimoto, M. Irie, Photoirradiation wavelength dependence of cycloreversion quantum yields of diarylethenes, Chemical Communications. 50 (2014) 3928–3930. https://doi.org/10.1039/c4cc00396a.

[41] M. O'Brien, I. Baxendale, S. Ley, Flow Ozonolysis Using a Semipermeable Teflon AF-2400 Membrane, Synfacts. 2010 (2010) 1199–1199. https://doi.org/10.1055/s-0030-1258661.

[42] A. Alvarez-Martin, S. Trashin, M. Cuykx, A. Covaci, K. De Wael, K. Janssens, Photodegradation mechanisms and kinetics of Eosin-Y in oxic and anoxic conditions, Dyes and Pigments. 145 (2017) 376–384. https://doi.org/10.1016/j.dyepig.2017.06.031.

[43] B.W.J. Pirok, G. Moro, N. Meekel, S.V.J. Berbers, P.J. Schoenmakers, M.R. van Bommel, Mapping degradation pathways of natural and synthetic dyes with LC-MS: Influence of solvent on degradation mechanisms, Journal of Cultural Heritage. 38 (2019) 29–36. https://doi.org/10.1016/j.culher.2019.01.003.

[44] N. Kuramoto, T. Kitao, The contribution of singlet oxygen to the photofading of triphenylmethane and related dyes, Dyes and Pigments. 3 (1982) 49–58. https://doi.org/10.1016/0143-7208(82)80012-0.

[45] C. Weyermann, D. Kirsch, C. Costa Vera, B. Spengler, Evaluation of the Photodegradation of Crystal Violet upon Light Exposure by Mass Spectrometric and Spectroscopic Methods, J Forensic Sci. 54 (2009) 339–345. https://doi.org/10.1111/j.1556-4029.2008.00975.x.

[46] G. Favaro, D. Confortin, P. Pastore, M. Brustolon, Application of LC-MS and LC-MS-MS to the analysis of photo-decomposed crystal violet in the investigation of cultural heritage materials aging, Journal of Mass Spectrometry. 47 (2012) 1660–1670. https://doi.org/10.1002/jms.3110.

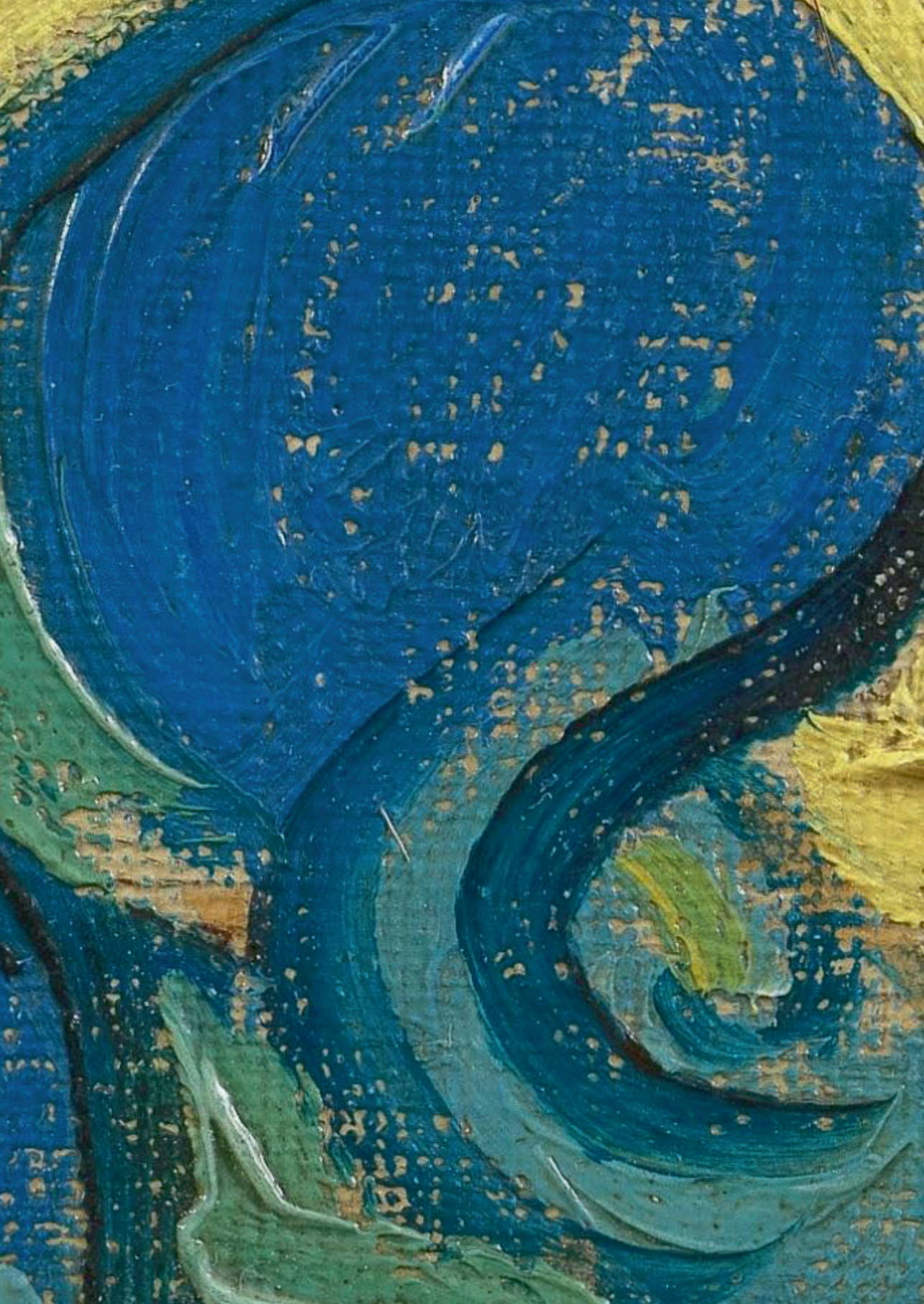

# CHAPTER 6

## Liquid-core waveguide cell with in-situ absorbance spectroscopy and coupled to liquid chromatography for studying light-induced degradation

## Abstract

In many areas, studying photostability or the mechanism of photodegradation is of high importance. Conventional methods to do so can be rather time consuming, laborious, and prone to experimental errors. In this paper, we evaluate an integrated and fully automated system for the study of light-induced degradation, comprising a liquid handler, an irradiation source and exposure cell with dedicated optics and spectrograph, and a liquid chromatography (LC) system. A liquid core waveguide (LCW) was used as exposure cell, allowing efficient illumination of the sample over a 12-cm path length. This cell was coupled to a spectrograph allowing in-situ absorbance monitoring of the exposed sample during irradiation. The LCW is gas permeable permitting diffusion of air into the cell during light exposure. This unit was coupled online to LC with diode array detection for immediate and automated analysis of the composition of the light-exposed samples. The analytical performance of the new system was established by assessing linearity, limit of detection and repeatability of the in-cell detection, sample recovery and carryover, and overall repeatability of light-induced degradation monitoring, using riboflavin as test compound. The applicability of the system was demonstrated by recording a photodegradation time profile of riboflavin.



**Publication**

Liquid-core waveguide cell with in-situ absorbance spectroscopy and coupled to liquid chromatography for studying light-induced degradation

Iris Groeneveld, Ingrida Bagdonaite, Edwin Beekwilder, Freek Ariese, Govert W. Somsen, Maarten R. Van Bommel

*Anal. Chem.,* **2022**, 94, 21, 7647–7654, DOI: 10.1021/acs.analchem.2c00886

## 6.1 Introduction

Photodegradation or light-induced degradation (LID) is the process where molecules degrade under the influence of light. There are applications where light is deliberately used to destroy molecules, for instance for the removal of chemicals in waste water. There are also areas where photodegradation should be prevented as much as possible, for example in art conservation, in the food and pharmaceutical industry [1], and for every-day products, such as wall paints, car coatings or textile dyes. Whether it is to prevent or to actually initiate photodegradation, these processes have to be studied in a controllable and semi-quantitative manner in order to achieve effective application or prevention.

Studying these photochemical processes, however, is complicated and laborious. Photodegradation is significantly influenced by a number of factors, such as the light dose, the applied wavelength, the solution pH and the presence of other compounds or gases, such as oxygen. These parameters may affect the kinetics as well as the degradation products formed. To add to the complexity related to the many physical parameters, there is also a challenge in studying the influence that different analytes may have on each other when studying mixtures. With commonly used methods it is often difficult to find a strong link between the parent molecule and the degradation product(s). An example of such a method is where solutions are degraded in a beaker placed under a light source [2–11]. These experiments can take rather long as the irradiation (power per area) is often low; i.e., Confortin et al. [6] irradiated a solution of crystal violet for at least 100 hrs and Weyermann et al. [7] required 54 hrs. Besides, errors are easily introduced since samples are taken manually, and solvents may evaporate during irradiation [7], resulting in irreproducible results. Hence, efficient tools are needed to study photodegradation in a simple and repeatable manner, while including the most important parameters affecting photodegradation.



In a previous report, we demonstrated the use of a liquid core waveguide (LCW) with a low refractive index (n=1.29) as an LID cell with in-situ absorbance detection to study photodegradation in aqueous solution (n=1.33) in an efficient way [12]. The gas permeable LCW allows for continuous supply of air to the photoreaction to create an environment similar to reality. In the same paper we suggested how a post-separation in on-line fashion could deal with the sample complexities that are met in LID studies [12], something that was not yet done with other photoreactors based on an LCW [13,14]. Den Uijl et al. [15] demonstrated that the LCW-based LID cell allows for more-rapid photodegradation of crystal violet and eosin Y as compared to standard in-solution photodegradation approaches. Within the TooCOLD project (Toolbox for studying the Chemistry Of Light-induced Degradation) we have now developed the TooCOLD box,

which includes the aforementioned LID cell and established coupling with liquid chromatography (LC) for analysis of the product mixture after the degradation process.

Here, we report on the analytical performance and use of this new tool using riboflavin as a model compound. Riboflavin, also known as vitamin B2, has been widely studied for its limited photostability and degradation in aqueous and organic solvents. The vitamin, which has also been applied as a textile dye [16], degrades rapidly under the influence of light, losing its health benefits and colour characteristics. Typical degradation products include formylmethylflavin, lumichrome, lumiflavin and carboxymethylflavin [17–21]. Due to its very poor lightfastness, however, it has also been used as an efficient photosensitizer in order to study the photodegradation of other compounds [22]. In short, the photodegradation of riboflavin is well known under different circumstances, hence why it was chosen as a model compound for this study.

In this paper, we report on the linearity and linear range, limit of detection (LOD) and repeatability of the in-cell detection with and without addition of airflow. We determined the recovery of the analyte from the LID cell for LC analysis, and the repeatability of degradation experiments. To demonstrate the applicability of the system for studying photodegradation, a time profile of the degradation of riboflavin was measured fully automatically.

## 6.2 Experimental

### 6.2.1 Chemicals

For LC analysis we used ultrapure Milli-Q water (MQ), methanol (MeOH) (Biosolve, UPLC/MS grade), formic acid (FA) (Sigma-Aldrich), sodium hydroxide (NaOH) (Sigma-Aldrich) and triethylamine (TEA) (Sigma-Aldrich). All experiments were performed using solutions of riboflavin (RF) (Sigma-Aldrich, pharmaceutical secondary standard) in MQ.

### 6.2.2 Materials and methods

**TooCOLD set-up**

The TooCOLD system consists of five main parts: (i) a liquid handler, (ii) the TooCOLD box, (iii) an irradiation source, (iv) a CCD spectrometer and (v) an LC-diode array detector (DAD) system. The complete set-up is shown in Fig. D-1 in Appendix D, with details of the irradiation light path in Fig. D-2. See also Figs. 12.1-12.6 for more detailed pictures of the set-up.

*Liquid handler*

The liquid handler is a Multipurpose Sampler (MPS) from GERSTEL and is controlled by MAESTRO software (GERSTEL). The MPS was configured to inject samples via the injection port of the TooCOLD box (see Fig. 6.1, a), to perform washing cycles of the LID cell, and to transfer the sample from the LID cell to the LC. It was also used to trigger the CCD detector to record real-time spectra at regular intervals and the LC system to start the analysis. The methods for each experiment were designed in the MAESTRO software (see Fig. D-3). Injections were done with the MPS into the TooCOLD system, unless stated otherwise. In order to prevent the formation of air bubbles inside the LCW after injection, samples were always injected at a flow rate of 10 µL·s$^{-1}$.

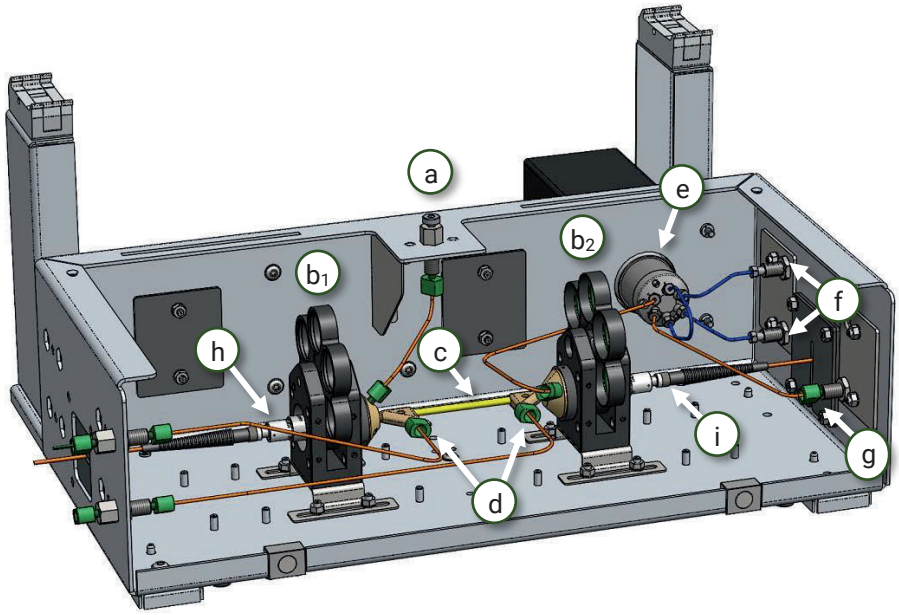


Figure 6.1. Drawing of TooCOLD box (without lid) depicting all its components: (a) injection port, ($b_{1,2}$) filter wheels with lenses before and after the LID cell, (c) LID cell, (d) gas in- and outlet, (e) 6-port valve with 20 µL sample loop, (f) connection to LC pump and column, (g) waste channel, (h) excitation fibre with collimator, (i) detection fibre with collimator.

*TooCOLD box*

The TooCOLD box was engineered by DaVinci Laboratory Solutions based on research dedicated to the characteristics of an LCW-based LID cell which was published previously [12]. The LID cells were fabricated by the Precision Mechanics and Engineering Group of the Vrije Universiteit Amsterdam. A schematic overview of the TooCOLD box is presented in Fig. 6.1. The box consists of (a) an injection port, (b) two filter wheels, (c) the LID cell, which contains the LCW (Teflon AF2400, i.d., 800 µm; wall

thickness, 100 µm; physical path length, 12 cm; volume, 60 µL), (d) connections for air supply (in- and outlets) to study photo-oxidation processes, (e) a 6-port valve with a 20 µL sample loop, which is connected to (f) the LC system and (g) a waste channel. The filter wheels can be used to implement optical filters to e.g., study the effect of selected wavelengths of the light spectrum or to decrease the exposure light intensity to check whether the product ratio is intensity dependent (for future experiments, not used in this study). The filter wheel holders also align the excitation fibre (h) with the LID cell, and the LID cell with the detection fibre (i).

*Irradiation source*

A 75 W Xenon short-arc fibre-coupled light source from Thorlabs (SLS205) was used for the illumination of the LID cell. The solarization-resistant excitation fibre (M112L01; i.d., 200 µm; NA=0.22) was connected to a UV/Vis collimator from Avantes (COL-UV/VIS), which was attached to a plano-convex lens (Thorlabs, LA4052-ML) with a focal length of 35 mm by means of a lens tube. The collimated beam is guided through the lens tube to reach the lens, so that the light was focused into the opening of the LID cell (Fig. D-2).

*Spectrometer*

A spectrometer from Thorlabs (CCS100/M) was used for real-time, in-situ monitoring of the irradiated sample inside the LCW. It was fibre-coupled to the back-end of the LID cell with the same lens and collimator as the excitation fibre. The spectrometer has a spectral range of 350-700 nm, with a spectral accuracy of 0.5 nm at 435 nm (FWHM), and a signal/noise ratio of ≤2000:1 (maximum signal/noise ratio per pixel). For light detection a 3648 pixel CCD line array was used, with signal integration times between 5 and 15 ms.

*LC–DAD*

All LC analyses were carried out on an Agilent 1100 series LC system equipped with a quaternary solvent delivery system, a column oven, an autosampler and a diode array detector (DAD). A ZORBAX Eclipse RRHD C18 column (2.1 x 150 mm; particle size, 1.8 µm) and a security guard column (2.1 x 5 mm) containing the same C18 phase were both obtained from Agilent Technologies. The LC method applied gradient elution with mobile phase A consisting of 95/5 (by volume), and B of 5/95 buffered MQ (0.1 M FA, 0.02 M NaOH, pH=3) and MeOH, respectively, both with 5 mM TEA as an ion pairing agent. A gradient was applied at a flow rate of 120 µL·min$^{-1}$ with first 5% mobile phase B for 1.5 min, then increasing from 5% to 95% in 15 min, and then isocratic for 5 min. Then, the mobile phase was brought back to 5% B within 2 min, and the column is equilibrated for 5 min to be ready for the next analysis.

### Operation of the TooCOLD system

A typical method for a 30-min degradation experiment can be found in Fig. D-3. In short, for each degradation experiment the MPS injected 70 µL MQ, which served as a blank sample after which it triggered the CCD spectrometer to record a reference signal ($I_0$). Then, 70 µL of sample was injected. After this, the syringe of the liquid handler was washed with 300 µL of 75% MeOH in MQ, followed by the same volume of MQ. After washing of the needle, a transmission spectrum was recorded at t=0 min for control. Then, a delay time was programmed, corresponding to the total irradiation time for the specific degradation experiment. Trigger signals to record transmission spectra were programmed at certain intervals, e.g., every 10 min, to monitor the overall content of the LCW. Absorbance spectra were later calculated by the software of the CCD spectrometer. Next, the sample was transferred to the sample loop of the 6-port valve. Unless stated otherwise, this was done by injecting 50 µL of 75% MeOH in MQ to transfer the middle part of the LID cell's content to the loop. Then, the LC was triggered by the MPS to start the analysis of the irradiated sample. Directly after the pulse was given, the 6-port valve was automatically switched from the 'load' into the 'inject' position, so that the sample loop was flushed with the mobile phase of the LC system. Finally, the valve was switched to the load position again and the LID cell was cleaned with 300 µL of 75% MeOH in MQ and then with pure MQ.



### Analytical performance

The performance of the TooCOLD set-up was evaluated with regards to the in-situ UV/Vis spectroscopy, and repeatability of the degradation experiments. The LC method validation is presented in another report [23]. In order to test significance, F-tests and t-tests were performed on the corresponding datasets.

The linearity, linear range and LOD of the in-cell absorbance measurements (optical pathlength, 12 cm) were determined in five-fold. A dilution series of RF was prepared in MQ with concentrations from $1 \cdot 10^{-6}$ to $13 \cdot 10^{-6}$ M. Prior to each sample, a blank sample (MQ) was injected and the intensity was recorded as $I_0$ signal at a wavelength of 450 nm.

The repeatability and stability of the in-situ UV/Vis detection were determined in two ways: (i) the in-cell stability by injecting a solution of RF ($5 \cdot 10^{-6}$ M) while measuring every 15 min for 3 hrs, and (ii) possible fluctuations caused by the injector by injecting the same RF solution every 15 min for 3 hrs and measuring the absorbance.

The TooCOLD system was also tested for recovery from the LID cell by injecting a sample of RF without subsequent irradiation and analysing the sample by LC. The recovery was calculated by comparing the measured peak area of the RF main peak with that of a

reference sample measured directly by LC-DAD while circumventing the TooCOLD box. As mentioned in Section 2.3, the transfer of the sample to the loop was accomplished by addition of a so called 'transfer volume', consisting of 75% MeOH in MQ. The tested volumes were 50, 70, or 110 µL. These volumes were chosen for specific reasons, as depicted in Fig. D-4: 50 µL was the physical minimum required by the MPS and allows the middle of the content of the LCW to be transferred to the sample loop; 70 µL should transfer the part of the sample present closer to the entrance of the LCW; 110 µL was chosen to determine whether the 'tail' of the flushing solvent would contain significant amounts of RF. Another factor affecting the recovery was the sample loop flushing time, i.e., the period of the LC mobile phase travelling through the sample loop. This flushing time was 12, 18, or 24 s, which is equivalent to 24, 36 and 48 µL when using a flow rate of 120 $\mu L \cdot min^{-1}$ for LC analysis.

The repeatability of the degradation experiments was assessed in two ways: according to the standard deviation (SD) of the decrease in absorbance of a solution of RF measured in the LCW, and the decrease in peak area of RF measured by LC after degradation.

**Degradation time profile of Riboflavin**

A time profile of the degradation of a solution of $5 \cdot 10^{-6}$ M RF in MQ was performed in triplicate in order to test the potential of the TooCOLD system. In total, 9 time points were taken: at 0 min (control, no irradiation), 30, 60, 90, 120, 150, 180, 210 and 240 min. In-situ absorbance measurements of the content of the LCW were taken every 10 min. For the control measurements, a sample was injected and after 10 min without irradiation, the sample was analysed by LC-DAD. For all other time points, a fresh sample was injected and irradiated for the designated time, followed by LC analysis. The whole experiment lasted for 54 hrs and was fully automated.

## 6.3 Results and discussion

### 6.3.1 Analytical performance

This section describes and discusses the analytical performance of the system, including the linearity, linear range and stability of the in-cell detection with and without an active airflow surrounding the LCW. The recovery from the LID cell for LC analysis, and the repeatability of the degradation experiments were determined.

### Linearity and linear range

In Fig. 6.2 the average absorbances measured for different concentrations (1-13·10$^{-6}$ M) of RF using the LCW are plotted, including the resulting linear trend line fitted through the averages. The correlation coefficient R was 0.984 and the relative standard deviation (RSD) ranged between 0.07 and 0.13 for the RF solutions between 3.0·10$^{-6}$ and 12·10$^{-6}$ M. Higher RSDs of 0.38 and 0.32 were observed for 1.0·10$^{-6}$ and 2.0·10$^{-6}$ M, respectively. High RSD values are to be expected for low absorbance levels since in an absorption experiment the absolute SD does not decrease for lower concentrations. The LOD for RF was calculated using the linear trend line in Fig. 6.2 and was determined to be 1.74·10$^{-7}$ M (calculation method is described in more detail in Appendix D-6). At 13·10$^{-6}$ M, all measured absorbances fall outside the 95% CI of the linear fit of the absorbance-concentration relation, indicating the upper limit of the linear range (1-12·10$^{-6}$ M) is reached at a measured absorbance of approximately 1.5.

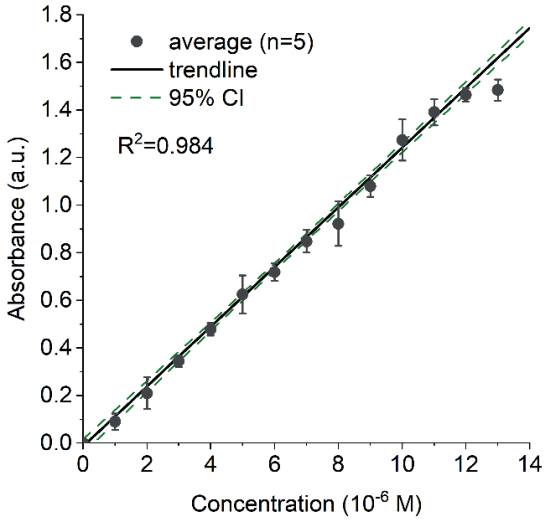


Figure 6.2. Average absorbance values with error bars of a dilution series of RF (1.0 – 13·10$^{-6}$ M) measured in five-fold using the LCW. A linear trendline (–) was fitted through all points and a 95% CI for the trend line was calculated (– – –).

Therefore, for compounds absorbing in the visible range, concentrations that result in an absorbance of up to about 1.5 can be measured using this particular spectrograph. However, in order to assure a pseudo-uniform analyte illumination across the whole length of the cell when studying photodegradation, the concentration of the solution and its corresponding absorbance should be considered carefully. A too high concentration may result in too strongly decreasing light intensities across the length of the cell, resulting in different degradation rates depending on the concentration and the position

in the cell. This assumption was tested by irradiating solutions with different concentrations of RF for 30 min (n=3) followed by LC-DAD analysis (results presented in Fig. D-5). As expected, higher concentrations resulted in slower degradation rates, but this effect was found to be negligible below concentrations of 6.5 µM. Therefore, we continued our study with a concentration of 5 µM, corresponding to an absorbance below 0.6 over a 12-cm long LCW, and thus lower than 0.3 for the distance to the central part of the LCW.

### System repeatability and stability

The repeatability and stability of the system are important features during in-situ monitoring, especially because the photodegradation experiment may take up to several hours. With our set-up, diffusion of air or nitrogen through the permeable LCW wall has been proven to be fairly simple to control, as demonstrated in a previous publication [12], and is of high interest for studying photo-oxidation reactions. The effect of applying an active airflow surrounding the LCW on the repeatability and stability was therefore evaluated.

The measurement system's repeatability and stability were assessed in two ways: (i) injecting a single sample solution of RF ($5 \cdot 10^{-6}$ M) and monitoring its absorbance measurement in the LID cell over time and (ii) repeated injections and measurement of the same fresh sample solution to check for any fluctuations related to the injection system, with and without a continuous airflow around the LCW. The experiments were done without inducing LID, i.e., the light source was switched on exclusively for taking a measurement every 15 min.

Table D-2 shows the measured absorbances of a solution of RF in the cell over time for the four conditions. The result at 120 min for repeated injection with airflow was found to be an outlier (Grubb's test, Table D-2) and, thus, was excluded from further calculations. A relatively stable signal over a period of 3 hrs was observed for all conditions. The repeatability and stability were characterized by the RSD of the measurements, which for all conditions was relatively low, ranging between 0.012 and 0.024 (Table D-3). To add to this, the variances were not significantly different from one another (confidence level=95%, Table D-1), proving that repeated injections and the application of a continuous airflow around the LCW do not affect the in-situ absorption measurements. For further degradation experiments, a continuous airflow was applied at all times.

**Recovery**

Coupling the TooCOLD box with LC may come with sample losses due to transferring the content of the LCW to LC, which should be prevented as much as possible. The transfer volume required to transfer the irradiated sample from the LCW to the sample loop was optimized (see scheme in Fig. D-4), together with the sample loop flushing time, i.e., the time the sample loop was in the inject position. Fig. D-6A shows the recovery of different LCW transfer volumes, while maintaining a loop flushing time of 12 s. In Fig. D-6B, the results are presented when the LCW transfer volume remained constant at 50 µL, while the sample loop flushing time was 12, 18 and 24 s, respectively. The results of significance testing of the repeatability by F-tests can be found in Table D-1.

It can be concluded that increasing the transfer volume from 50 to 70 µL results in a small, but significant, increase of recovery of only 3%. The error obtained for the 5 replicates is very low (RSD ≤ 0.003), showing that the transfer from LID cell to LC is highly repeatable. For all further degradation experiments, we applied a 50 µL volume to transfer the central part of the LCW content for LC analysis, because the first few cm of the LCW may not experience a uniform light intensity over the cross section of the LCW tube. The 'tail' of the transfer solvent, obtained by using 110 µL, contained only 4% of RF, meaning that RF was efficiently removed from the LID cell. The blank runs, which were run in between each replicate of RF analysis, showed that there was no detectable carryover.



A stronger effect was observed for increasing the sample loop flushing time. A significant improvement in recovery from 73% to 87% was observed for an increase in flushing time from 12 to 18 s. With a flushing time of 24 s, the recovery further increased to 89% (Fig. D-6B). A flushing time of 12 s proved to be too short to completely empty the sample loop, and the lowest RSD (0.008) was obtained for a sample loop flushing time of 24 s. Based on these results, and considering the volume of the LCW (60 µL), a transfer volume of 50 µL (corresponding to the middle of the content of the LCW) and a sample loop flushing time of 24 s were used. These parameters, however, depend on the length of the tubing between the injection port, the LID cell and the 6-port valve, and the flow rate of the LC system. The transfer volume and the flushing time should, therefore, be optimized after any change to these parameters. It should also be noted that the recovery may be different for other analytes, due to the well-known 'stickiness' of Teflon AF. This may be circumvented by dissolving compounds, that are otherwise easily adsorbed to Teflon, in partly organic solvent, e.g., 50% methanol in water [12].

**Degradation repeatability**

The repeatability of the analytical system can be affected by several factors and was determined for both the in-situ spectroscopic detection as well as for the degradation experiments. For a $5 \cdot 10^{-6}$ M test solution of RF, which was irradiated for 4 hrs, Fig. 6.3A shows the decreases of both the in-situ absorbance and the peak area of RF measured with LC-DAD with error bars indicating the SD (n=5). The RSDs of the peak areas of RF and degradation products are presented in Table D-4 and an example of a resulting LC chromatogram can be found in Fig. 6.5. Low RSDs of 0.038 and 0.010 were observed for in-situ absorbance and peak area decreases of RF, respectively, which indicates that the TooCOLD system can monitor photodegradation in a highly repeatable manner.

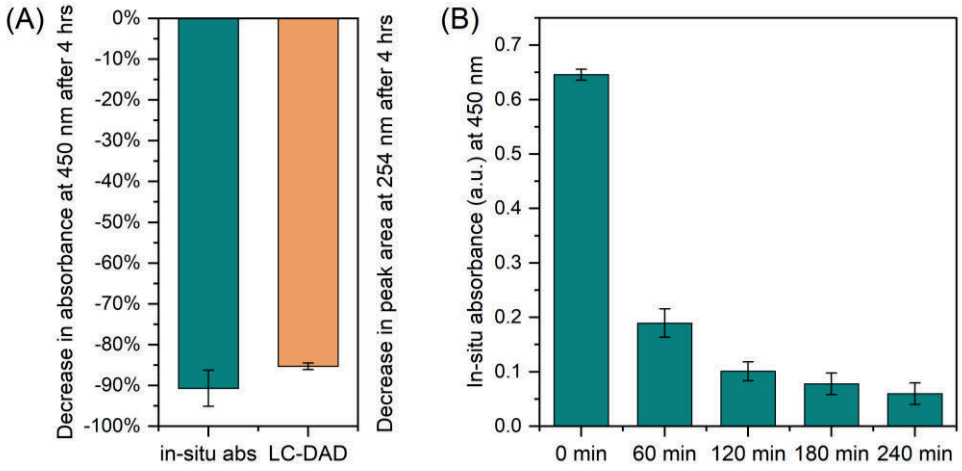


Figure 6.3. The relative decrease (%) in absorbance of RF at 450 nm after 4 hrs of irradiation measured in-situ (blue), and in peak area of RF measured by LC-DAD at 254 nm (orange). B: absorbances measured in-situ at 60-min time intervals during the same 4-hr degradation experiments of RF. Error bars indicate SD (n=5).

The decrease in in-situ absorbance (-91%) was somewhat, but significantly, larger than the decrease (-85%) observed using LC-DAD. This is rather unexpected, since the in-situ measurements show the cumulative absorbance spectrum of RF and its degradation products, of which some also show absorption at 450 nm. A factor potentially contributing to the observed difference is the connecting volume between the LID cell and the 6-port valve, which is about 10 µL. This may contain non-degraded RF, influencing LC analysis in case of a slight memory effect.

During the 4-hr degradations the absorbance was recorded every 10 min, which is shown in Fig. 6.3B with intervals of 60 min for legibility. With a decrease in absorbance over time, the SDs first increase, then after one hour of irradiation remain relatively stable, as

also shown in Table D-5. This increase could be the result of variation introduced by the degradation process combined with the increased uncertainty associated with measuring low absorbances. Nevertheless, it was concluded that the on-line absorbance measurements can be used as a convenient tool to estimate the decrease of the main compound, and to monitor the extent of the photodegradation process inside the LCW in real-time.

### 6.3.2 Degradation time profile of riboflavin

A time profile of the photodegradation of RF was measured to show the applicability of the TooCOLD system. RF was irradiated in the LCW for 0 min (control, no irradiation), 30, 60, 90, 120, 150, 180, 210 and 240 minutes in triplicate, with a continuous airflow around the LCW, followed by LC analysis of the LCW content. The system was operated in a fully automated fashion, that is, the 2.5-day sequence was carried out unattended requiring no manual action.

The results of the RF degradation measurements in time are presented in Figs. 6.4, 6.5 and 6.6. Fig. 6.4 shows the changes observed in relative peak areas measured by LC-DAD in the irradiated sample at different time points. Fig. 6.5 shows a chromatogram of the RF solution after a 3-hr degradation. The corresponding absorbance spectra recorded by the DAD are shown in Fig. D-7 and the analyte retention times in Table D-6. Fig. 6.6 shows the in-situ absorbance spectra taken every 30 min during a 4-hr degradation.



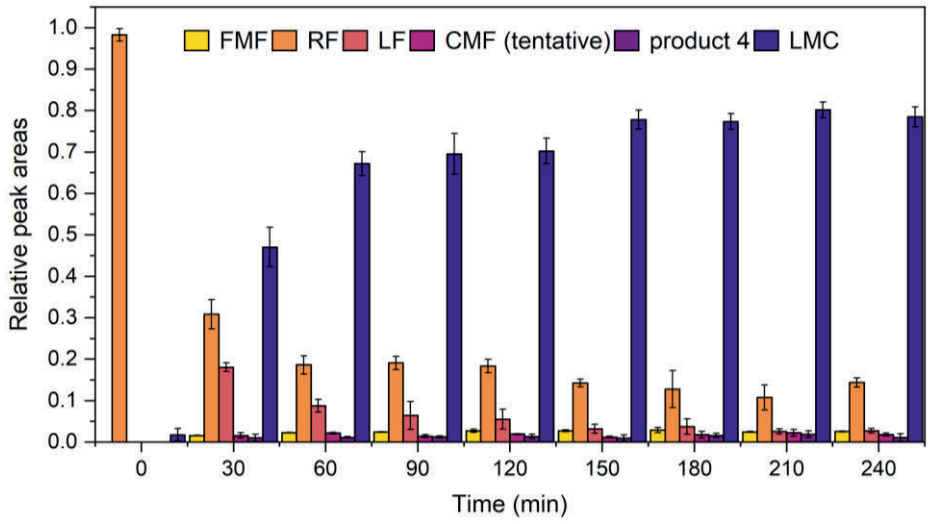


Figure 6.4. The relative peak areas of RF and five formed products measured by LC after degradation in the LCW for the indicated time; error bars indicate SDs (n=3). RF was degraded for 0 min (control, no irradiation), 30, 60, 90, 120, 150, 180, 210 and 240 min. Note that the LC-DAD peak areas (measured at

254 nm) will not reflect the actual relative molar concentrations, since for most products the absorption coefficients are not known and may vary.

Fig. 6.4 shows that the parent compound RF degraded rapidly between 0 and 30 min. After roughly 150 min, the degradation of RF seems to level off. According to literature, the major degradation products that are formed after photolysis of RF include formylmethylflavin (FMF), lumichrome (LMC) and lumiflavin (LF), and also cyclodehydroriboflavin (CDRF) after a photoaddition pathway [17,20,24,25]. Other minor degradation products that may be found are carboxymethylflavin (CMF) after oxidation (when oxygen is present), β-keto acid and flavo-violet (ring-cleavage products), and 2,3-butanedione [18]. Six distinctive peaks were found for the degraded samples when analyzed by LC (Fig. 6.5). Five peaks that could be identified based on their retention times and absorbance spectra were FMF, RF, LF, LMC and possibly also CMF. The sixth (product 4) had an absorbance spectrum similar to RF, but could not be identified. A few very small additional peaks were observed at 450 nm (Fig. D-8), but these could also not be identified based on their weak absorbance spectra. Identification of the degradation products would require coupling of the TooCOLD system to mass spectrometry, however, this was beyond the scope of the present study.

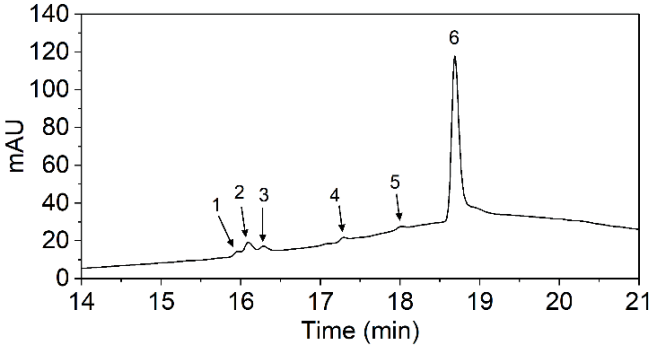


Figure 6.5. LC–DAD chromatogram recorded at 254 nm obtained after a 3-hr degradation of RF. Peaks were (tentatively) identified as FMF (1), RF (2), LF (3), CMF (4), product 4 (5) and LMC (6).

Besides the observed changes in the LC chromatograms, the changes in the in-situ absorbance spectra during a 4-hr degradation are shown in Fig. 6.6. From the first measurement on, a clear change in the ratio of the absorption maxima at 350 and 450 nm (i.e., the absorption maxima of RF) can be observed. This indicates a change in composition of the sample inside the LCW, which was confirmed by LC analysis. With time, the absorption spectrum transforms into a spectrum close to that of LMC, the main degradation product. These spectra clearly show the usefulness of a spectroscopic monitoring tool coupled to the LID cell. Following the real-time change in the overall

absorption spectrum may help to decide when the time has come to transfer the content of the LCW to the LC-DAD for analysis of the degradation products.

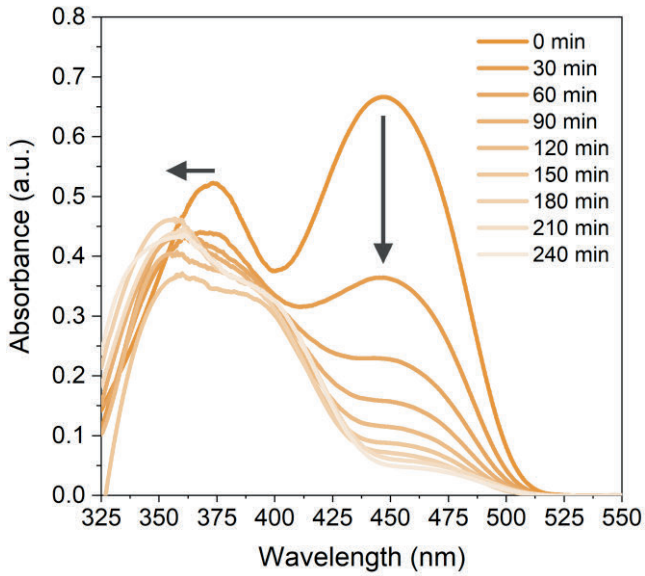


Figure 6.6. In-situ absorbance spectra measured every 30 min during a 4-hr degradation of RF. The vertical arrow signifies an over-time reduction in absorbance at 450 nm, and the horizontal arrow an over-time blue-shift from 375 to 350 nm, indicating a gradual change in the LCW content.

## 6.4 Conclusions

An integrated LCW-based LID system encompassing automated liquid handling, irradiation source and spectrograph was coupled successfully to LC-DAD and tested for its analytical performance. As demonstrated for RF, the total system allowed for quantitative unattended photodegradation experiments over longer periods of time in a highly repeatable fashion with RSDs for peak areas below 0.033. The in-situ absorbance monitoring of the content of the LCW during photodegradation also showed good repeatability (RSDs of absorbance signals below 0.044). The in-situ recorded absorption spectrum is the resultant of contributions from the remaining parent compound and formed degradation products. Since the spectra and absorption coefficients of the latter are often not known, the total absorbance signal should not be used for quantitative analysis. Still, it is highly useful for monitoring the progress of the degradation process in real-time. The light intensity inside the LCW can be determined using actinometry (as we demonstrated earlier [12]), but can also be approximated with a power meter behind

the LCW exit. Coupling to the LC-DAD system permits separation and relative quantification of the formed degradation products based on their UV/Vis response. Unambiguous identification of (unknown) degradation products and potential elucidation of reaction pathways requires the current system to be coupled to mass spectrometry, which is the objective of a follow-up study in our lab. In a future project we will study differences in photodegradation mechanisms or kinetics under aerobic vs. anaerobic conditions, and how results obtained in solution can help to elucidate photodegradation in solid materials where different irradiation conditions and diffusion processes play a role.

The LOD of the in-situ absorbance detection is relatively low due to the optical path length of 12 cm. This characteristic comes in especially useful when degrading low analyte concentrations. Notably, at lower concentrations the LCW also ensures that the whole sample will be irradiated very efficiently and almost uniformly, resulting in faster overall photodegradation. At high analyte concentrations a large part of the incoming light may be absorbed within the first section of the LCW, and the analyte molecules in the subsequent part of the LCW will experience lower light intensities and therefore lower degradation rates.

Overall, this study demonstrates that with the TooCOLD box coupled to LC, reliable photodegradation studies can be simplified and very well automated, shortening the operator's time spent in the lab significantly. The suitability of the system for studying relatively low analyte concentrations seems especially relevant when only very small samples are available or when an LC separation of a sample mixture is performed prior to LID. Currently, we are studying the feasibility and usefulness of a multidimensional LC-TooCOLD box-LC-DAD set-up. The first outcomes of this study are very promising and we believe that integration of the LCW-based approach can transform the way photodegradation studies are performed for a wide variety of analytes.

# References

[1] International Council for Harmonisation, Q1B Photostability Testing of New Drug Substances and Products, 1998. http://www.emea.eu.int.

[2] A. Kolkman, B.J. Martijn, D. Vughs, K.A. Baken, A.P. van Wezel, Tracing nitrogenous disinfection byproducts after medium pressure UV water treatment by stable isotope labeling and high resolution mass spectrometry, Environ Sci Technol. 49 (2015) 4458–4465. https://doi.org/10.1021/es506063h.

[3] R. Ameta, P. Bala Punjabi, S.C. Ameta, Photodegradation of Naphthol green B in the presence of semiconducting antimony trisulphide, J. Serb. Chem. Soc. 76 (2011) 1049–1055. https://doi.org/10.2298/JSC100425082A.

[4] Jisi Li, Xianhui Wen, Qiujing Zhang, Shijie Ren, Adsorption and visible-light photodegradation of organic dyes with TiO 2 /conjugated microporous polymer composites, RSC Adv. 8 (2018) 34560–34565. https://doi.org/10.1039/C8RA06491A.

[5] A. Kundu, A. Mondal, Photodegradation of methylene blue under direct sunbeams by synthesized anatase titania nanoparticles, SN Applied Sciences 2019 1:3. 1 (2019) 1–17. https://doi.org/10.1007/S42452-019-0280-3.

[6] D. Confortin, H. Neevel, M. Brustolon, L. Franco, A.J. Kettelarij, R.M. Williams, M.R. van Bommel, Crystal violet: Study of the photo-fading of an early synthetic dye in aqueous solution and on paper with HPLC-PDA, LC-MS and FORS, J Phys Conf Ser. 231 (2010) 012011. https://doi.org/10.1088/1742-6596/231/1/012011.

[7] C. Weyermann, D. Kirsch, C. Costa Vera, B. Spengler, Evaluation of the Photodegradation of Crystal Violet upon Light Exposure by Mass Spectrometric and Spectroscopic Methods, J Forensic Sci. 54 (2009) 339–345. https://doi.org/10.1111/j.1556-4029.2008.00975.x.

[8] M.S. Islam, A. Patras, B. Pokharel, Y. Wu, M.J. Vergne, L. Shade, H. Xiao, M. Sasges, UV-C irradiation as an alternative disinfection technique: Study of its effect on polyphenols and antioxidant activity of apple juice, Innovative Food Science and Emerging Technologies. 34 (2016) 344–351. https://doi.org/10.1016/j.ifset.2016.02.009.

[9] M.J. Toohey, L.N. Bell, Food chemical stability as affected by iron and ultraviolet light exposure: Rebaudioside A degradation as a case study, J Food Process Preserv. 43 (2019) 1–5. https://doi.org/10.1111/jfpp.14201.

[10] P.I. Hora, P.J. Novak, W.A. Arnold, Photodegradation of pharmaceutical compounds in partially nitritated wastewater during UV irradiation, Environ Sci (Camb). 5 (2019) 897–909. https://doi.org/10.1039/c8ew00714d.

[11] F. Sabatini, I. Degano, M. van Bommel, Investigating the in-solution photodegradation pathway of Diamond Green G by chromatography and mass spectrometry, Coloration Technology. 137 (2021) 456–467. https://doi.org/10.1111/COTE.12538.

[12] I. Groeneveld, S.E. Schoemaker, G.W. Somsen, F. Ariese, M.R. van Bommel, Characterization of a liquid-core waveguide cell for studying the chemistry of light-induced degradation, Analyst. 146 (2021) 3197–3207. https://doi.org/10.1039/d1an00272d.

[13] S. Ponce, H. Christians, A. Drochner, B.J.M. Etzold, An Optical Microreactor Enabling In Situ Spectroscopy Combined with Fast Gas-Liquid Mass Transfer, Chem Ing Tech. 90 (2018) 1855–1863. https://doi.org/10.1002/cite.201800061.

[14] S. Ponce, M. Trabold, A. Drochner, J. Albert, B.J.M. Etzold, Insights into the redox kinetics of vanadium substituted heteropoly acids through liquid core waveguide membrane microreactor studies, Chemical Engineering Journal. 369 (2019) 443–450. https://doi.org/10.1016/j.cej.2019.03.103.

[15] M.J. den Uijl, A. Lokker, B. van Dooren, P.J. Schoenmakers, B.W.J. Pirok, M.R. van Bommel, Comparing different light-degradation approaches for the degradation of crystal violet and eosin Y, Dyes and Pigments. 197 (2022) 109882. https://doi.org/10.1016/J.DYEPIG.2021.109882.

[16] S.N. Iyer, N. Behary, V. Nierstrasz, J. Guan, G. Chen, Study of photoluminescence property on cellulosic fabric using multifunctional biomaterials riboflavin and its derivative Flavin mononucleotide, Scientific Reports 2019 9:1. 9 (2019) 1–16. https://doi.org/10.1038/s41598-019-45021-5.

[17] R. Huang, J.K. Hyun, D.B. Min, Photosensitizing Effect of Riboflavin, Lumiflavin, and Lumichrome on the Generation of Volatiles in Soy Milk, J Agric Food Chem. 54 (2006) 2359–2364. https://doi.org/10.1021/JF052448V.

[18] M.A. Sheraz, S.H. Kazi, S. Ahmed, Z. Anwar, I. Ahmad, Photo, thermal and chemical degradation of riboflavin, Beilstein Journal of Organic Chemistry 10:208. 10 (2014) 1999–2012. https://doi.org/10.3762/BJOC.10.208.

[19] M. Insińska-Rak, D. Prukała, A. Golczak, E. Fornal, M. Sikorski, Riboflavin degradation products; combined photochemical and mass spectrometry approach, J Photochem Photobiol A Chem. 403 (2020) 112837. https://doi.org/10.1016/j.jphotochem.2020.112837.

[20] I. Ahmad, Q. Fasihullah, F.H.M. Vaid, Effect of phosphate buffer on photodegradation reactions of riboflavin in aqueous solution, J Photochem Photobiol B. 78 (2005) 229–234. https://doi.org/10.1016/j.jphotobiol.2004.11.010.

[21] I. Ahmad, Q. Fasihullah, F.H.M. Vaid, Effect of light intensity and wavelengths on photodegradation reactions of riboflavin in aqueous solution, J Photochem Photobiol B. 82 (2006) 21–27. https://doi.org/10.1016/J.JPHOTOBIOL.2005.08.004.

[22] C. Gambetta, A. Reynoso, J. Natera, M.I. Sancho, P. Montaña, W.A. Massad, Riboflavin sensitized photodegradation of Furaneol in a β-cyclodextrin complex, J Photochem Photobiol A Chem. 411 (2021) 113188. https://doi.org/10.1016/J.JPHOTOCHEM.2021.113188.

[23] I. Groeneveld, B.W.J. Pirok, S.R.A. Molenaar, P.J. Schoenmakers, M.R. van Bommel, The development of a generic analysis method for natural and synthetic dyes by ultra-high-pressure

liquid chromatography with photo-diode-array detection and triethylamine as an ion-pairing agent, J Chromatogr A. 1673 (2022) 463038. https://doi.org/10.1016/J.CHROMA.2022.463038.

[24] M.A. Sheraz, S.H. Kazi, S. Ahmed, K. Qadeer, M.F. Khan, I. Ahmad, Multicomponent spectrometric analysis of riboflavin and photoproducts and their kinetic applications, Central European Journal of Chemistry. 12 (2014) 635–642. https://doi.org/10.2478/S11532-014-0527-1.

[25] F.H.M. Vaid, W. Gul, A. Faiyaz, Z. Anwar, M.A. Ejaz, S. Zahid, I. Ahmad, Divalent anion catalyzed photodegradation of riboflavin: A kinetic study, J Photochem Photobiol A Chem. 371 (2019) 59–66. https://doi.org/10.1016/J.JPHOTOCHEM.2018.10.048.

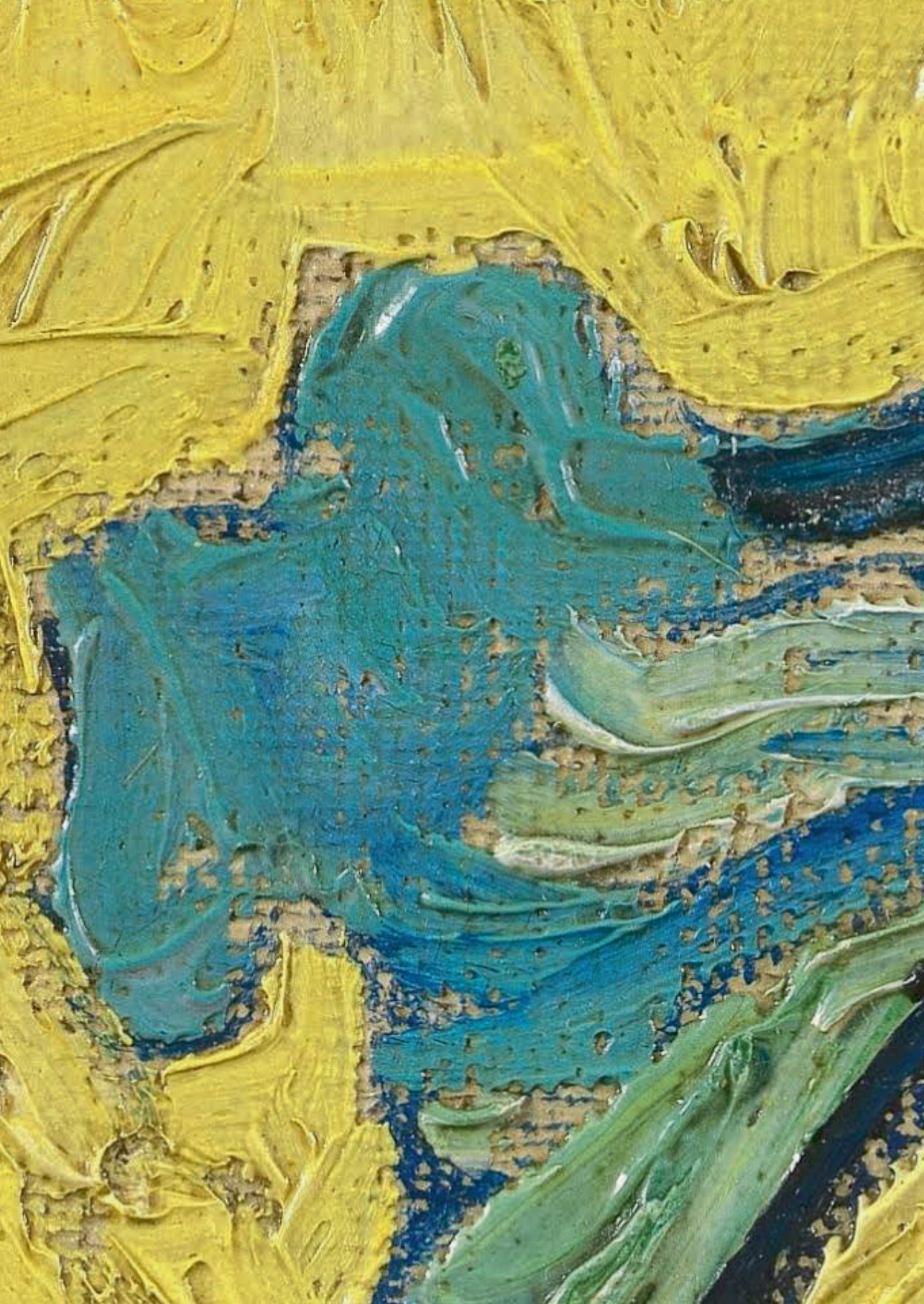

# CHAPTER 7

## Gas-permeable liquid-core waveguide coupled to LC-MS for studying the influence of oxygen on photodegradation processes

## Abstract

Light-induced degradation (LID) strongly depends on experimental conditions, among which the presence of oxygen is a major parameter. Elucidating LID processes is of high concern to many areas of interest, e.g., for the conservation of cultural heritage, safety and shelf life of food, and UV-disinfection methods for water purification. Recently, we presented a new, fully automated tool to study molecular photodegradation in solution. The tool employs a gas-permeable liquid-core waveguide (LCW) as a light-exposure cell with in-situ absorption spectroscopy for real-time monitoring, coupled on-line to liquid chromatography (LC) with diode-array (DAD) and mass spectrometry (MS) for characterization of the photodegradation products. The current work reports on the assessment of the potential of the LCW in a tube-in-tube geometry for studying the role of oxygen in photodegradation processes, using Riboflavin and Eosin Y as model compounds. The LID results obtained for Riboflavin and Eosin Y using the LCW set-up were in line with reported data obtained with conventional approaches. On-line LC-MS analysis allowed semi-quantitative monitoring of LID differences under oxic and anoxic circumstances. An increase in degradation by 9% and 30% for Riboflavin and Eosin Y, respectively, was observed after 10 min under anoxic conditions. Moreover, for the first time, the fully debrominated species of Eosin Y (i.e. fluorescein), was identified as a photodegradation product in solution. The presented set-up can be highly useful for the investigation of photodegradation mechanisms and kinetics in solution, including the role of oxygen while increasing analytical efficiency and reducing time spent in the lab.



**Publication**

Gas-permeable liquid-core waveguide coupled to LC-MS for studying the influence of oxygen on photodegradation processes

Iris Groeneveld, Freek Ariese, Govert W. Somsen, Maarten R. van Bommel

*J. Photochem. Photobiol. A,* **2023**, 441, 114685, DOI: 10.1016/j.jphotochem.2023.114685

## 7.1 Introduction

The interaction between light and matter is essential to life as we know it. Unfortunately, these interactions may not always be beneficial. In many cases, they lead to the loss of physical and/or structural properties of molecules. These degradations must be revealed to understand and avoid adverse effects on products and processes. Elucidation of photodegradation mechanisms can be challenging as it may involve many parameters, such as the applied wavelength range, light dose, solution pH, and the presence of oxygen [1]. Especially the latter plays a significant role in photodegradation mechanisms. Dissolved oxygen enhances the photodegradation of many compounds and, for example, is important for the production of superoxide in heterogenous catalysis [1–5]. On the other hand, for some compounds, the triplet excited state is quenched by oxygen, so that it returns to the ground state before reacting [6,7]. For such compounds, the photodegradation rate actually decreases when oxygen is present, as many photodegradation reactions involve the relatively long-lived triplet excited state.

Clearly, oxygen is an important parameter to include when studying photodegradation. The effect of oxygen is generally studied by irradiating aerated and deaerated sample solutions in a beaker or cuvette for a specific amount of time and comparing the resulting compositions after analysis by, e.g., liquid chromatography coupled to mass spectrometry (LC-MS) [8–11]. Although straightforward, this approach can be quite tedious and also prone to error as it often requires manual subsampling and degassing the set-up to perform kinetic studies.



This paper presents an alternative approach for studying the influence of oxygen on light-induced degradation (LID) processes using a recently developed platform [8,9]. The fully automated set-up employs a gas-permeable liquid-core waveguide (LCW) as a light exposure cell with in-situ absorbance spectroscopy for real-time monitoring of the photodegradation reactions during irradiation. The LCW is coupled on-line to LC with diode-array detection and quadrupole time-of-flight MS (LC-DAD-QTOFMS) allowing characterization and selective detection of degradation products. The analytical performance of the LID set-up was assessed and demonstrated in previous studies [12,13]. Here, we evaluate the suitability of the gas-permeable LCW for both oxic and anoxic LID studies, using two colored test compounds (Riboflavin and Eosin Y) of which the photodegradation is well documented.

Riboflavin (RF; Fig. 7.1), known as the water-soluble vitamin B2, present in a wide variety of foods and also used as a food dye (E101), has been widely studied for its limited photostability and degradation in aqueous and organic solvents [14–20]. It participates in important biological processes, such as the metabolism of carbohydrates, proteins,

and fats, hemoglobin synthesis, and the functioning of the eye [21]. Many factors influence the photodegradation of RF, among which oxygen is an important parameter [15,20,22].

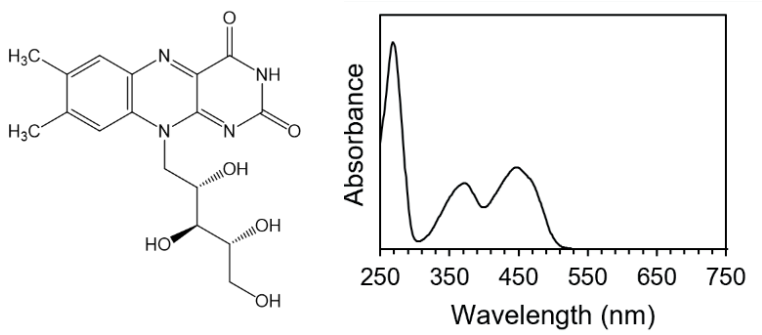


Figure 7.1. Molecular structure of riboflavin and its absorption spectrum measured by LC–DAD.

Fig. E-1 (Appendix E) presents a simplified scheme for the proposed photodegradation mechanisms of RF. The reported photodegradation products formed upon irradiation of RF by UV and visible light are cyclodehydroriboflavin (CDRF), formylmethylflavin (FMF), lumiflavin (LF), lumichrome (LMC), and carboxymethylflavin (CMF) [23–25]. In addition, the quinoxaline derivatives 1,2-dihydro-1-methyl-2-keto-3-quinoxaline carboxylic acid (KA) and 1,2,3,4-tetrahydro-1-methyl-2,3-dioxo-quinoxaline (DQ), have been described as a result from ring cleavage of FMF in alkaline solutions [18,26,27]. Sheraz et al. [17] proposed a general scheme for the photodegradation of RF, indicating that LMC is formed through the singlet excited state of RF (1RF), as well as through photolysis of FMF, which is an intermediate formed via the triplet excited state (3RF). FMF is further degraded into LF and photo-oxidized to CMF. According to several studies [17,22], oxygen decreases the photodegradation rate of RF by quenching 3RF to generate singlet oxygen ($^1O_2$). Anoxic conditions induce enhanced photodegradation of RF along a different degradation route as the photooxidation product CMF cannot be formed. The absorption spectra of the aforementioned degradation products, except for LMC, are virtually identical to that of RF. Therefore, MS is indispensable for the identification of these products.

Eosin Y (EY) is a synthetic red dye (Fig. 7.2) that has been studied widely due to its low light fastness [8,28–33]. EY was used by famous artists, such as Vincent van Gogh, who was aware of its low light stability and therefore had “all the more reason boldly to use them too raw, time will only soften them too much”, as he wrote in a letter to his brother Theo [34]. EY has not only been applied as a pigment in art objects but is also used as a staining agent for biomedical microscopy [35] or as a metal-free photocatalyst [36].

Photodegradation studies with EY have been performed in, e.g., alkaline methanolic solutions [28,29], in water [8] and DMSO [31], on textiles [37], and in paints or paints simulations [30,32,33]. The photodegradation of EY in solution follows consecutive bromine losses (EY-Br, EY-2Br, etc.), similar to those reported on substrates. Fig. E-2 presents a simplified scheme for the proposed photodegradation mechanisms of EY.

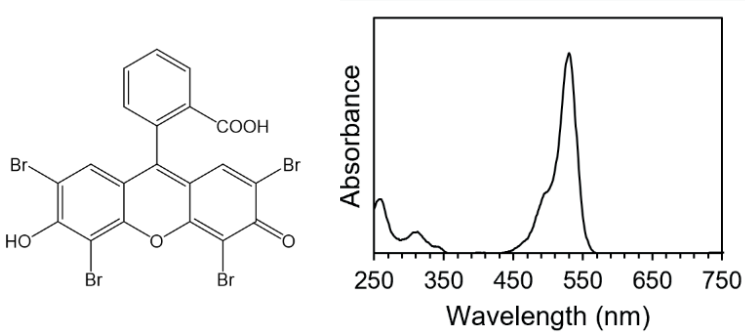


Figure 7.2. Molecular structure of Eosin Y and its absorption spectrum measured by LC–DAD.

Alvarez-Martin et al. [8] found that under oxic conditions the degradation rate of EY is lower, but that discoloration occurs faster as compared to anoxic conditions. They proposed two different degradation mechanisms: (i) in the presence of oxygen, the degradation mechanism is an oxidative process where the breakdown of the chromophore of the first debromination product (EY-Br) causes total discoloration; (ii) in the absence of oxygen, debromination takes place while the chromophore remains essentially intact. Ultimately, the fully debrominated product, fluorescein, is expected to be formed [8,29], however, it has never been identified as a photodegradation product. Pirok et al. [31] detected fluorescein in EY samples by LC-MS but assigned it to a sample impurity (i.e. byproduct in the synthesis of EY) which was already present before irradiation.

In this study, we evaluate the usefulness of a LID cell based on a gas-permeable LCW as a potential tool to efficiently study the effect of oxygen on photodegradation rates and processes. First, we assess the rate of oxygen diffusion into the LCW using the well-known methylene blue (MB) reaction. Subsequently, using the LCW we present a new approach for on-line deaeration of the irradiated sample, reducing the number of required manual steps. To investigate the applicability of the system, we conducted LID experiments for RF and EY under oxic and anoxic conditions and measured degradation time profiles by in-situ absorbance monitoring of the irradiated sample in the LCW and LC-MS analysis of the photodegradation products.

## 7.2 Experimental

### 7.2.1 Chemicals

Aqueous solutions were prepared using ultrapure deionized water (MQ; R = 18.2 MΩcm) (Millipore Simplicity Simpak 2, USA.). Methanol (MeOH) and acetonitrile (ACN) were both UPLC/MS grade and purchased from Biosolve (Valkenswaard, The Netherlands). Formic acid (FA; ≥99%) was purchased from VWR Chemicals (Darmstadt, Germany). Ethanol (EtOH) (99.8%), ammonium formate (97%), potassium hydroxide (KOH; 90%), D-glucose (99.5%), methylene blue (MB; ≥97%), riboflavin (RF; pharmaceutical secondary standard), and Eosin Y (EY; 99%) were purchased from Sigma-Aldrich (Steinheim, Germany).

### 7.2.2 Materials and instruments

**Light exposure cell set–up**

The set-up used for all photodegradation experiments is shown in Fig. E-3 and was described in great detail in a previous publication [13]. Briefly, the 12-cm long LID cell consists of a tube-in-tube design (Fig. E-4) of which the inner tube is a gas-permeable Teflon AF2400 LCW (Cambridge Reactor Design, UK; i.d., 800 µm; o.d., 1000 µm; volume, 60 µL). The outer tubing made of polytetrafluoroethylene (PTFE or Teflon), has an inlet and outlet for the supply of a continuous flow of gas that surrounds the LCW. In this study, air (≈170 mL $min^{-1}$) or nitrogen (≈300 mL $min^{-1}$) was used. The gases can reach the liquid core by diffusion through nanopores in the LCW wall without the formation of bubbles. The LID cell is attached to two PEEK connection pieces that contain a quartz optical window that allows in-coupling of light from the Xenon short-arc fiber-coupled irradiation source (Thorlabs SLS205, Newton, NJ, USA; 240-1200 nm), and out-coupling of the transmitted light at the distal end of the LCW. The transmitted light, which was converted into absorbance spectra, was measured in real-time by a fiber-coupled CCD spectrometer from Thorlabs with a spectral range of 350-700 nm (CCS100/M). The PEEK combination pieces were both attached to a filter wheel for the potential addition of optical filters to study the effect of selected wavelengths; these were not used in the current study. The combination pieces contain fluid connections for sample introduction by a Multi-Purpose Sampler (MPS) from Gerstel (Mülheim an der Ruhr, Germany), and for transfer of the LCWs content to a 6-port valve (VICI, Houston, TX, USA) with a 20 µL sample loop, connected to an LC system (Agilent 1100 series, Waldbronn, Germany). Transfer of the irradiated sample was performed by adding 50 µL of 'flushing solvent' (75% MeOH in MQ) to the LID cell, which 'pushed' the middle section of the LID cell's content to the sample loop. The LC system was coupled to a DAD (Agilent) and Agilent 6520 Q-TOF mass spectrometer and was triggered by the MPS to start the analysis after the sample loop was filled. After starting the LC-DAD-MS analysis, the LID cell was

automatically cleaned by flushing with 300 µL of 75% MeOH in MQ, followed by 300 µL of MQ to be prepared for the next experiment.

**LC-DAD-QTOFMS**

The LC system was comprised of a quaternary solvent pump, a reversed-phase ZORBAX Eclipse RRHD C18 column (2.1 x 150 mm; particle size, 1.8 µm) of Agilent, and a security guard column (2.1 x 5 mm) with the same C18 phase, a column oven set at 40 °C, and a DAD providing UV/Vis absorbance spectra (250-800 nm) of the column effluent with a spectral resolution of 1 nm at a sampling rate of 1 Hz. Different from Chapter 5, the mobile phases A and B consisted of 95-2.5-2.5 (v/v/v) and 5-47.5-47.5 (v/v/v) MQ-MeOH-ACN, respectively. Both A and B contained 0.1% FA and 20 mM ammonium formate. This was chosen over triethylamine to prevent ion suppression in the source. The LC gradient ran at a flow rate of 120 µL $min^{-1}$ starting at 5% B for 1.5 min, increasing from 5% to 95% in 15 min, followed by an isocratic step at 95% B for 5 min, then decreasing to 5% B within 2 min, to finally equilibrate the column for 5 min at 5% B to be ready for the next LC analysis. MS data were recorded using electrospray ionization (ESI) in the positive ion mode in the 150-2000 m/z range at a data sampling rate of 1 Hz. The settings of the ESI source were: gas temperature, 300 °C; drying gas, 5 L $min^{-1}$; nebulizer gas pressure, 35 psi; capillary voltage, 3500 V. The QTOF settings for the analysis of RF were: fragmentor, 100 V; skimmer, 75 V; octupole 1 RF Vpp, 200 V. For the analysis of EY, the fragmentor was 200 V, and the octupole 1 RF Vpp was 300 V. All MS data were processed with MassHunter software.



## 7.2.3 Methods

**Determination of gas-diffusion rate into the LCW**

A solution of 1 g $L^{-1}$ MB in EtOH was prepared, and 1.6 g KOH and 2 g glucose were added to 60 mL of MQ. Then, 1 mL of the MB solution was added to the KOH/glucose solution. The latter was diluted with MQ to give a solution that exhibited an absorbance of about 1.5 AU when measured in the LID cell; this solution was then used for the experiments. Prior to sample introduction, the system and MB solution were deaerated by purging with nitrogen for 30 min. Then, 70 µL of MB solution was injected into the LCW while the nitrogen flow surrounding the LCW was still on to keep the system free of oxygen. After injection (t=0 s), the absorbance was measured every second. At t=40 s the nitrogen flow was substituted by a flow of air. Between t=105 and 115 s the nitrogen flow was turned on again. When the absorbance stabilized again, the measurement was stopped. The LID system was cleaned and a fresh MB solution was injected. This process was carried out in five-fold.

**Removal of oxygen from samples and solvents**

To study photodegradation under anoxic conditions, oxygen must be removed from all samples and solvents. This was first done conventionally ('external purging') by bubbling a flow of nitrogen gas through the samples in an LC vial for 5 min. Solvents that were used for cleaning the LID cell were also purged for 30 min before use. With our new approach ('in-situ purging'), the sample was introduced in the LID cell and then purged with nitrogen via the LCW wall, while the light source was turned off. To compare the effectiveness of the in-situ and external purging methods, aqueous solutions of RF (2 mg $L^{-1}$) were purged inside the LID cell for 1, 2, 3, 4, 5, 7.5, and 10 min in triplicate. Then, the purged samples were irradiated for 10 min with a continuous flow of nitrogen inside the outer tubing of the LID cell, followed by their LC-DAD analysis.

**Photodegradation of Riboflavin and Eosin Y**

For photodegradation experiments using the LCW set-up, solutions of 10 mg $L^{-1}$ (2.7 µM) RF and 1 mg $L^{-1}$ (0.15 µM) EY were prepared in MQ. The method of in-situ purging of the samples with nitrogen was applied to create anoxic conditions before irradiation. RF was irradiated for 10 min under oxic and anoxic conditions, i.e., with a continuous air or nitrogen flow, respectively, through the outer tubing. This was done in triplicate (n=3). For EY, a photodegradation time profile was created by irradiating solutions for 5, 10, 15, 20, and 30 min under oxic and anoxic conditions, which was performed in duplicate (n=2). In-situ absorption spectra were recorded every 2 min throughout all experiments. After irradiation, the samples were online transferred to and analyzed by LC-DAD-QTOFMS. Extracted-ion chromatograms (EICs) for the m/z's of the compound ions of interest (±0.01 m/z) were constructed and peak areas were established and used for quantitative interpretation.

## 7.3 Results and discussion

### 7.3.1 Gas–diffusion rate into LCW

It is important to know how fast gas diffuses through the LCW capillary wall into the liquid core of the LID cell to prevent oxygen depletion during irradiation and to effectively introduce or remove oxygen from the sample inside the LCW. Similarly to what we presented in an earlier study [12], the redox reaction of MB involving glucose and oxygen was employed to study the diffusion rate through a color change. Under anoxic conditions, the reduced form of MB (colorless) will be present, which is transformed to the oxidized form (dark blue) when oxygen is introduced into the solution. The color change was monitored by absorbance measurements at 668 nm in real-time. The

absorbance increase is an indication of the rate at which oxygen diffuses through the 100-µm thick LCW wall into the liquid core.

The experiment was started under anoxic conditions. A nitrogen-purged MB solution was injected at t=0 s into the LCW while nitrogen gas was flushed through the outer tube so that MB was mainly present in its reduced, i.e. colorless, form ($MB_{red}$). Subsequently at t=40 s, air was introduced to the outer tube, and immediately a strong rise in absorbance at 688 nm was observed, indicating the formation of oxidized MB ($MB_{ox}$) in the LCW. Under these oxygen-rich conditions, a maximum absorbance (1.4 AU) was reached in only 20 s (at t=60 s). When nitrogen was flushed through the outer tube again, the absorbance decreased within 60 s to the starting level, showing $MB_{ox}$ is reconverted to $MB_{red}$. This experiment convincingly shows that oxygen can be rapidly introduced to and removed from the solution in the core of the LCW. In line with previous observations [8], the full removal of oxygen seems to take more time than introducing it. This might be due to the lower diffusion rate of nitrogen through the pores [38,39], while the fact that only a little oxygen is needed to induce a significant color change, might also play a significant role here. Although the experiment does not quantitatively determine the concentration of dissolved oxygen inside the LCW, it adequately indicates the rate at which oxygen can be added or removed, exhibiting a valuable merit of the LID set-up.



### 7.3.2 In-situ vs. external purging with nitrogen

The LCW-LC-DAD-QTOFMS set-up represents a fully automated system to study photodegradation in solution. To investigate compounds under anoxic conditions, oxygen should be removed before exposure to light, which is conventionally done by bubbling samples with nitrogen ('external purging'), requiring additional manual steps and related equipment. This would have to be done or repeated right before the start of every new experiment to prevent oxygen from diffusing back into the sample, which is rather laborious. Considering the LCW wall is permeable for nitrogen gas, oxygen can be removed from a sample by purging with nitrogen via the outer tube after it has been introduced to the LCW ('in-situ purging'). This approach of oxygen removal was tested and compared to conventional external deoxygenation employing the photodegradation of RF. Oxygen decreases the LID rate of RF (see also below). Therefore, a higher percentage of native RF will remain if oxygen is not properly removed from the system. The extent of LID of RF in samples deoxygenated by conventional external purging with nitrogen for 5 min was compared with samples deoxygenated by in-situ purging with nitrogen for 1-10 min. After purging, both types of deoxygenated samples were irradiated by light from the Xenon source for 10 min while maintaining a continuous stream of nitrogen through the outer tube to sustain an anoxic environment. To further assess the

effectiveness of in-situ deoxygenation, also samples that were not pre-purged with nitrogen and irradiated while having a continuous stream of air in the outer tube, were analyzed. The overall results of these experiments are shown in Fig. 7.3.

On the left in the figure, the remaining percentages of intact RF (as determined by LC-DAD) are presented for the samples irradiated under oxic conditions (i.e. without prior purging; blue bar) and under anoxic conditions after external purging with nitrogen (green bar). On the right, the remaining percentages of intact RF are shown for samples irradiated during in-situ purging with nitrogen for different time intervals (orange bars). Already after 1 min of in-situ purging with nitrogen, a significant difference in RF percentage as compared to the sample irradiated under oxic conditions is observed, indicating fast removal of oxygen from the core of the LCW. Furthermore, in-situ deoxygenation results in similar RF percentages as obtained after external purging of samples, with a slight overall decrease in RF percentage with increasing in-situ purging time (up to 10 min). In addition, standard deviations seem to decrease with longer in-situ purging times. Considering that in-situ obtained RF percentages are not significantly different from the RF percentage obtained with the external method, we conclude that deoxygenation in the core of the LCW before irradiation is just as effective as conventional nitrogen purging by sample bubbling. The new approach, however, is much more straightforward requiring fewer manual interventions, and, therefore, was applied to all further experiments.

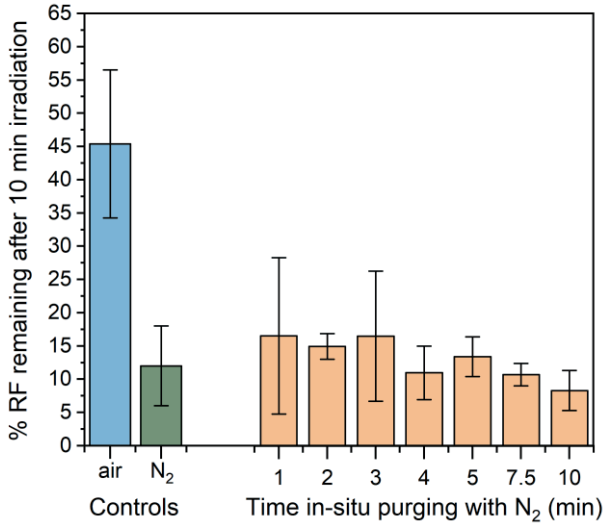


Figure 7.3. Effectiveness of deoxygenation methods. The percentages of intact riboflavin remaining after 10 min irradiation inside the LID cell under oxic conditions without pre-purging (blue), and under anoxic conditions with 5 min of conventional external purging (green), and in-situ purging (orange) with nitrogen for different periods (n=3). Error bars indicate standard deviations of repeated experiments.

### 7.3.3 Photodegradation studies under oxic and anoxic conditions

It is well known that oxygen has a significant effect on the photodegradation kinetics as well as the formed products of RF and EY [8,15,20,22]. Both the photodegradation mechanisms as well as the kinetics and k-values have been studied extensively for RF and EY [8,25,26,40]. These compounds were therefore chosen to assess the potential of the gas-permeable LCW for studying photodegradation processes in the presence and absence of oxygen. The assessment is based on the in-situ absorbance spectra measured during irradiation of the RF and EY solutions, and on the UV/Vis spectra and peak areas derived from EICs obtained during LC-DAD-MS analysis of the irradiated samples (Figs. E-9, E-10, E-16, and E-17). Assignment of the photodegradation products was based on matching measured m/z values with molecular masses of degradation products of RF and EY reported in the literature (Tables 7.1 and 7.2).

**Photodegradation of Riboflavin**

Aqueous solutions of 10 mg $L^{-1}$ RF were irradiated (Xenon source, 240-1200 nm) for 10 min (n=3) in the LCW under oxic and anoxic conditions while monitoring their absorbance. Subsequently, the irradiated samples were analyzed by LC-DAD-QTOFMS. The in-situ absorbance spectra measured in real-time (Figs. 7.4A and 7.4B) already indicate differences in irradiated sample composition, and thus the photodegradation process, when applying oxic or anoxic conditions. In Fig. 7.4B the faster decrease of absorbance at 450 nm (i.e. the absorption maximum of RF; Fig. 7.1) can be assigned to the higher degradation rate of RF under anoxic conditions. Under oxic conditions (Fig. 7.4A), the absorption at 450 nm also decreases due to the light-induced conversion of RF, however, the absorbance between 350-400 nm hardly decreases. This may be related to the formation of relatively large quantities of LMC (absorbance spectrum in Fig. E-8) in those samples.

The results obtained by LC-DAD-QTOFMS nicely confirm the observations made from the in-situ absorption measurements. LC-DAD chromatograms of RF before and after irradiation under oxic and anoxic conditions are reported in Appendix E (Figs. E-5 to E-7). Quantitative interpretation of the results was done by establishing and comparing the peak areas in the EICs for the parent and degradation products obtained under oxic and anoxic conditions, as shown in Table 7.1 and Fig. 7.4C.

The remaining amount of RF (m/z 377.142; Fig. E-11A) after irradiation is higher in the oxic samples, again indicating that the photodegradation rate of RF is decreased in the presence of oxygen, which is in line with the literature [22]. The slower photodegradation of RF under oxic conditions is a result of $^3$RF being quenched by oxygen, leading to the return to the ground state of RF and the formation of $^1O_2$. This mechanism has been well

documented in the literature [41–43]; no attempt was made to detect singlet oxygen inside the LCW. This also contributes to the differences in sample composition between the oxic and anoxic irradiated samples. The photooxidation product CMF (m/z 301.087; Fig. E-11B) was only observed in aerated samples. According to the proposed degradation scheme by Sheraz et al. [17], FMF is formed only through $^3$RF, meaning that higher concentrations of this intermediate can be expected in the anoxic samples.

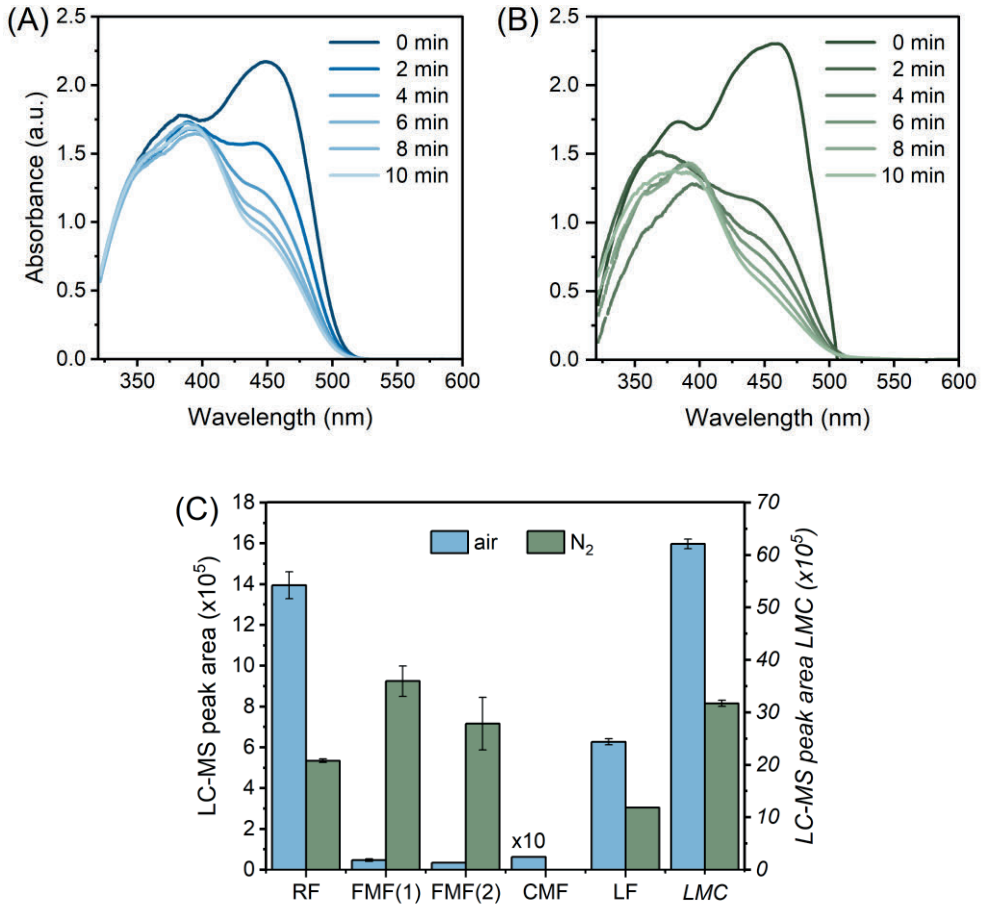


Figure 7.4. In-situ absorbance spectra of 10 mg L$^{-1}$ RF samples measured every 2 min during irradiation under (A) oxic and (B) anoxic conditions. (C) Peak areas for RF and identified degradation products derived from EICs obtained during LC-MS of RF solutions irradiated for 10 min under oxic (air, blue) and anoxic (N$_2$, green) conditions (n=3). Note that for the sake of readability, the values for CMF are scaled by a factor 10 with respect to the left y axis, and the values for LMC are scaled against the right y axis.

LC-MS analysis showed a split peak for FMF (EIC m/z 285.093; Fig. E-11C) of which the relative peak areas also differed between oxic and anoxic conditions. These peaks were

therefore indicated as FMF(1) and FMF(2). According to Ahmad et al. [18], FMF undergoes cyclization before forming CMF, LF, and LMC. An explanation for the split peaks may be that a part of the FMF present in the samples has undergone this cyclization, resulting in two compounds with the same mass, but slightly different LC retention. From Fig. 7.4A, it can be deduced that FMF is present in higher abundance in anoxic samples, while final degradation products LF (m/z 257.098; Fig. E-11D) and LMC (m/z 243.084; Fig. E-11E) are present in lower concentrations compared to oxic conditions. Indeed, under oxic conditions, the concentration of LMC is expected to be higher as this product can be formed through both $^1$RF and $^3$RF. However, it was not expected that LF would be formed in higher abundance under oxic conditions as it is reported that FMF is more light-sensitive than RF [15,20]. From our results, it appears that FMF is less efficiently transformed into LF and LMC when oxygen is removed, which may indicate that the degradation of FMF is accelerated by oxygen or by other reactive species formed through the reaction of singlet oxygen with water, e.g., $H_2O_2$ or $OH^-$ [18]. Several other degradation products reported in the literature, such as CDRF, KA, and DQ, were not detected in any of the irradiated samples. This may be because their concentrations were below the detection limits and/or because in the other studies, alkaline conditions were used during light exposure [18,26,27]. However, two other compounds were formed ('unknown 1' and 'unknown 2'), but we were unable to identify these based on the observed m/z because of their low abundance.



Table 7.1. Overview of the compounds detected during LC-DAD-MS of RF solutions exposed to light in the LCW under oxic and anoxic conditions with observed m/z (for $[M+H]^+$) and maximum absorption wavelength ($\lambda_{max}$). Assignment based on degradation products as reported in the literature (reference indicated). Compounds that were not detected in our study are indicated by 'nd'.

| RT (min) | ID | Molecular formula | Exact mass (Da) | Observed m/z | Observed $\lambda_{max}$ (nm) | Oxic | Anoxic | Also reported by |
|---|---|---|---|---|---|---|---|---|
| 11.47 | RF | $C_{17}H_{20}N_4O_6$ | 376.138 | 377.142 | 371; 447 | ✓ | ✓ | |
| - | CDRF | $C_{17}H_{20}N_4O_6$ | 376.138 | - | - | nd | nd | Ahmad et al. [14] |
| 11.13 | CMF | $C_{14}H_{12}N_4O_4$ | 300.086 | 301.087 | 368; 448 | ✓ | ✓ | Ahmad et al. [15,16] |
| 11.79<br>12.87 | FMF(1)<br>FMF(2) | $C_{14}H_{12}N_4O_3$ | 284.091 | 285.093 | 375; 440<br>371; 447 | ✓ | ✓ | Smith et al. [20]<br>Ahmad et al. [14–16] |
| 12.67 | LF | $C_{13}H_{12}N_4O_2$ | 256.096 | 257.098 | 377; 447 | ✓ | ✓ | Ahmad et al. [14–16] |
| 13.26 | unknown 1 | - | - | - | 369; 444 | ✓ | ✓ | - |
| 13.76 | unknown 2 | - | - | - | 371; 448 | ✓ | ✓ | - |
| 14.13 | LMC | $C_{12}H_{10}N_4O_2$ | 242.080 | 243.084 | 352; 388 | ✓ | ✓ | Smith et al. [20]<br>Ahmad et al. [14–16]<br>Sheraz et al. [17] |
| - | KA | $C_{12}H_{12}N_2O_3$ | 232.085 | | - | nd | nd | Ahmad et al. [18,26,27] |
| - | DQ | $C_{11}H_{12}N_2O_2$ | 204.090 | | - | nd | nd | Ahmad et al. [18,26,27] |

**Photodegradation of Eosin Y**

Aqueous solutions of 1 mg $L^{-1}$ EY were irradiated in the LCW for 0, 5, 10, 15, 20, and 30 min (n=2) under oxic and anoxic conditions while monitoring their absorbance (Figs 5 A and 5C), and subsequently subjected to LC-DAD-QTOFMS analysis. LC-DAD chromatograms of EY before and after irradiation under oxic and anoxic conditions can be found in Appendix E (Figs. E-12 to E-14). Table 7.2 presents the assignment of EY and degradation products based on their measured m/z values and bromine isotope patterns in the corresponding mass spectra (Figs. E-16 to E-18). The quantitative interpretation was done by establishing and comparing the LC-MS peak areas in the EICs for the parent and degradation products obtained under oxic and anoxic conditions (Figs. 7.5B and 7.5D, respectively).

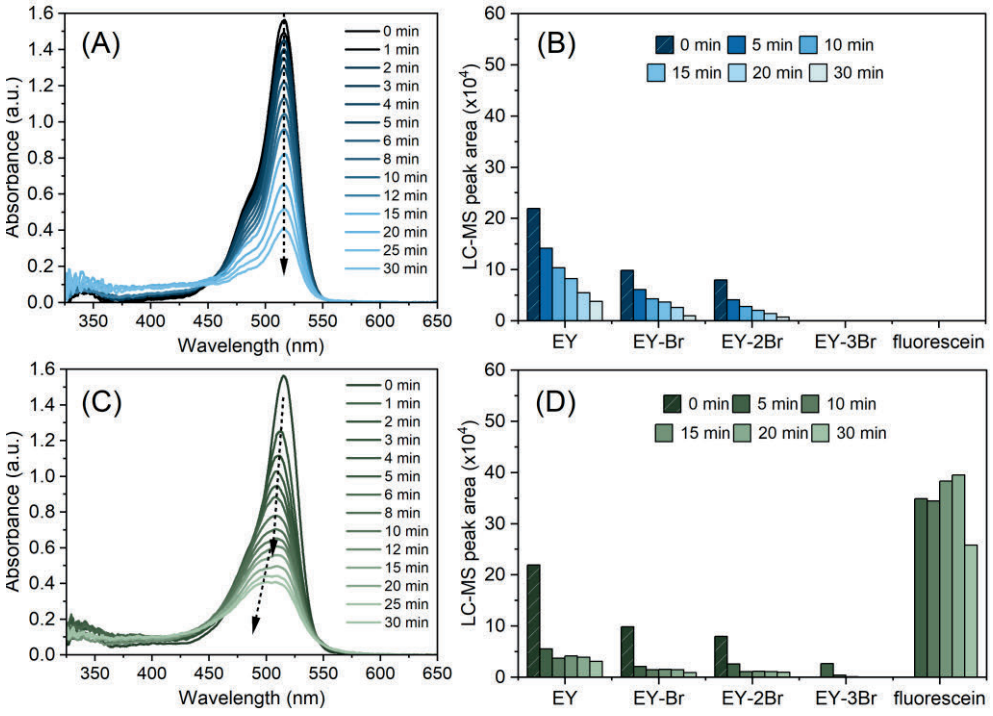


Figure 7.5. In-situ absorbance spectra measured of 1 mg L-1 EY samples over time under (A) oxic and (C) anoxic conditions. Peak areas of EY and its degradation products derived from EICs obtained during LC-MS analysis of 1 mg L-1 EY samples after 0, 5, 10, 15, 20, and 30 min of irradiation under (B) oxic and (D) anoxic conditions (n=2).

Under oxic and anoxic conditions, a rapid decrease in absorbance is observed for EY within 30 min of irradiation. The LC-MS results confirm these observations showing a decrease in the peak area of EY (m/z 648.716; Fig. E-18A; Figs. 7.5B and 7.5D). The LC-MS data also show that EY-Br (m/z 568.806; Fig. E-18B) and EY-2Br (m/z 490.895; Fig. E-

18C) were already present in the non-irradiated EY samples (t=0 min) and that their levels seem significant. However, the LC-DAD chromatograms show much lower relative peak areas for EY-Br and EY-2Br (Fig. E-12). Since it is expected that the absorption coefficients of the debrominated species do not differ greatly from that of EY (Fig. E-15), we conclude that these products were present in rather low amounts in the original EY sample. Possibly, the ionization efficiency of the debrominated products is higher than that of EY, resulting in relatively high relative peak areas for EY-Br and EY-2Br in the LC-MS chromatograms. Nevertheless, as the ionization efficiency per product is constant, it was still possible to monitor the change in the concentration of each degradation product over different irradiation times based on the obtained MS peak areas.

EY degraded much slower under oxic conditions, as follows from the comparison of the results obtained for aerated and deaerated samples, and also has been described in the literature [8]. The slower degradation under oxic conditions most likely results from the quenching of the triplet excited state of EY by oxygen to form $^1O_2$. This mechanism has been well documented in the literature [8,44,45]; no attempt was made to detect singlet oxygen inside the LCW. The LC-MS results indicate a gradual decrease in the concentration of EY, EY-Br, and EY-2Br over time in the presence of oxygen. The rate at which EY-2Br decreases (49%) during the first 5 min is higher than for EY (35%) and EY-Br (38%). This may indicate that EY first loses a single bromine, followed by chromophore breakdown. If EY-2Br would have been formed through EY-Br, a slower decrease of the former compound should have been observed. The triply and fully debrominated products (EY-3Br and fluorescein, respectively) were not detected in any of the aerated samples. This result is in line with the mechanism under oxic conditions (i.e. breakdown of the chromophore) as proposed by Alvarez-Martin et al. [8]. Unfortunately, no EY fragments related to the breakdown of the structure by photooxidation could be found in the obtained LC-MS data. This may be due to their low concentrations and potentially low ionization efficiencies. However, the in-situ absorbance spectra (Fig. 7.5A) do support the chromophore breakdown indicated by a decrease in absorbance at the maximum absorbance wavelength of EY. Similar to Alvarez-Martin's reports, the aerated samples' absorbance spectra do not show obvious shape changes, indicating that no significant levels of differently absorbing compounds are being formed.

A different trend is observed in the absorbance spectra measured under anoxic conditions (Fig. 7.5C). In addition to a decrease in absorbance intensity, a gradual shift in the absorbance maximum is observed over time. The recorded absorption spectra are very similar to the spectra of debrominated EY species reported by Kimura et al., who studied the photodegradation of EY in deaerated samples [28]. After about 8 min of irradiation of EY, the absorption spectrum gets a broader shape and shifts to that of

fluorescein ($\lambda_{max}$≈490 nm). This observation can be directly correlated to the composition of the photodegraded samples as determined by LC-MS (Fig. 7.5D). Already after 5 min of irradiation under anoxic conditions, fluorescein (m/z 333.078; Fig. E-18E) is formed in relatively high abundance. Next to fluorescein, also the formation of EY-3Br was observed after 5 min of irradiation in the absence of oxygen, indicating a different photodegradation mechanism as observed under oxic conditions. Between t=0 and t=5 min, a concentration decrease of 75% is observed for EY, 79% for EY-Br, and 68% for EY-2Br. The somewhat lower decrease of EY-2Br in the first minutes under anoxic conditions indicates that this compound may be formed through EY-Br losing another bromine, followed by the loss of a third bromine to form EY-3Br (m/z 410.987; Fig. E-18D). The concentration of EY-3Br rapidly decreases after 5 min of irradiation, while the presence of fluorescein increases further. This process of consecutive bromine losses leading to fluorescein would support the mechanism proposed by Alvarez-Martin et al. [8] and Pirok et al. [31]. To obtain more information about the first stages of the photodegradation of EY, experiments with irradiation times below 5 min should be conducted. After 30 min of irradiation a decrease in fluorescein concentration is observed, indicating that eventually, this 'final' photodegradation product decomposes even further. No products related to the degradation of fluorescein were found, which again might be due to the low concentrations at which these products are formed and/or their low ionization efficiency.

The results presented here, as well as for Riboflavin, are broadly in line with reports from the literature, which affirms that the set-up is a valuable addition to the existing methods for studying photodegradation under oxic and anoxic conditions.

Table 7.2. Overview of the compounds detected during LC–DAD–MS of EY solutions exposed to light in the LCW under oxic and anoxic conditions with observed m/z (for $[M+H]^+$) and maximum absorption wavelength ($\lambda_{max}$). Assignment based on degradation products as reported in the literature (reference indicated). Compounds that were not detected are indicated by 'nd'. The concentrations of EY-3Br and fluorescein were too low to reliably determine the $\lambda_{max}$ by DAD.

| RT (min) | ID | Molecular formula | Exact mass (Da) | Observed m/z | Observed $\lambda_{max}$ (nm) | Oxic | Anoxic | Also reported by |
|---|---|---|---|---|---|---|---|---|
| 20.01 | EY | $C_{20}H_8Br_4O_5$ | 647.706 | 648.716 | 531 | ✓ | ✓ | |
| 19.58 | EY-Br* | $C_{20}H_9Br_3O_5$ | 567.798 | 568.806 | 524 | ✓ | ✓ | Alvarez-Martin et al. [8,30] Pirok et al. [31] |
| 18.62 | EY-2Br* | $C_{20}H_{10}Br_2O_5$ | 489.835 | 490.895 | 519 | ✓ | ✓ | Alvarez-Martin et al. [8,30] Pirok et al. [31] |
| 17.74 | EY-3Br | $C_{20}H_{11}Br_1O_5$ | 409.979 | 410.987 | nd | nd | ✓ | Pirok et al. [31] |
| 17.05 | Fluorescein | $C_{20}H_{12}O_5$ | 332.068 | 333.078 | nd | nd | ✓ | - |

## 7.4 Conclusions

This study shows the potential of a gas-permeable LCW for studying LID processes under both oxic and anoxic conditions. The tube-in-tube design provides sufficiently high diffusion rates for oxygen and nitrogen to purge the samples under study. In-situ deaeration of samples in the LCW shows to be as effective as conventional oxygen removal by bubbling with nitrogen. This offers a convenient and straightforward means of deoxygenation, reducing the number of manual interventions and associated error sources. The feature of in-situ absorbance spectroscopy as provided by the used LID set-up has shown to be helpful. In general, it allows real-time monitoring of the irradiated sample and, more specifically, it supported the hypothesis of the chromophoric breakdown of EY under oxic conditions. The decrease and change in the absorption spectra during irradiation also correlated nicely with the sample compositions as determined by LC-DAD-MS. Interestingly, fluorescein was identified for the first time as a degradation product in irradiated samples of EY. Importantly, the results of the photodegradation experiments obtained with LCW, essentially follow the results reported in the literature, meaning that the current LID cell set-up can be applied to study the effect of oxygen on photodegradation processes. Although not utilized in this study, the set-up also offers the option to employ optical filters to investigate the wavelength dependency of photodegradation. We expect that the system will be useful for a wide audience covering many application areas. For example, in the food industry, knowledge about the influence of oxygen may impact the type of packaging material to increase shelf life. In museums, the obtained information will help to decide how vulnerable items should be stored and protected. Even in the pharmaceutical industry, tests have to be employed where the influence of, e.g., light and oxygen on drugs are studied. We believe that, with the automated system presented here, this can be done in a fast and straightforward manner, while providing high repeatability.

# References

[1] I. Groeneveld, M. Kanelli, F. Ariese, M.R. van Bommel, Parameters that affect the photodegradation of dyes and pigments in solution and on substrate – An overview, Dyes and Pigments. 210 (2023) 110999. https://doi.org/10.1016/J.DYEPIG.2022.110999.

[2] W. Xue, J. Chen, Q. Xie, Direct and dissolved oxygen involved photodegradation of MeO-PBDEs in water, J Hazard Mater. 307 (2016) 344–349. https://doi.org/10.1016/J.JHAZMAT.2016.01.016.

[3] A.L. Boreen, B.L. Edhlund, J.B. Cotner, K. McNeill, Indirect photodegradation of dissolved free amino acids: the contribution of singlet oxygen and the differential reactivity of DOM from various sources., Environ Sci Technol. 42 (2008) 5492–8. https://doi.org/10.1021/es800185d.

[4] J.C. Védrine, Heterogeneous Catalysis on Metal Oxides, Catalysts. 7 (2017) 341. https://doi.org/10.3390/CATAL7110341.

[5] S. Karuppusamy, F. Marken, M.A. Kulandainathan, Role of dissolved oxygen in nitroarene reduction by a heterogeneous silver textile catalyst in water, New Journal of Chemistry. 44 (2020) 17780–17790. https://doi.org/10.1039/D0NJ03713C.

[6] K. Kawaoka, A.U. Khan, D.R. Kearns, Role of Singlet Excited States of Molecular Oxygen in the Quenching of Organic Triplet States, J Chem Phys. 46 (1967) 1842. https://doi.org/10.1063/1.1840943.

[7] F. Wilkinson, A.A. Abdel-Shafi, Mechanism of quenching of triplet states by oxygen: Biphenyl derivatives in acetonitrile, Journal of Physical Chemistry A. 101 (1997) 5509–5516. https://doi.org/10.1021/jp970706o.

[8] A. Alvarez-Martin, S. Trashin, M. Cuykx, A. Covaci, K. de Wael, K. Janssens, Photodegradation mechanisms and kinetics of Eosin-Y in oxic and anoxic conditions, Dyes and Pigments. 145 (2017) 376–384. https://doi.org/10.1016/j.dyepig.2017.06.031.

[9] X. Zhang, Z. Liu, Q. Kong, G. Liu, W. Lv, F. Li, X. Lin, Aquatic photodegradation of clofibric acid under simulated sunlight irradiation: kinetics and mechanism analysis, RSC Adv. 8 (2018) 27796–27804. https://doi.org/10.1039/C8RA03140A.

[10] L. Wang, J. Ali, Z. Wang, N.A. Oladoja, R. Cheng, C. Zhang, G. Mailhot, G. Pan, Oxygen nanobubbles enhanced photodegradation of oxytetracycline under visible light: Synergistic effect and mechanism, Chemical Engineering Journal. 388 (2020) 124227. https://doi.org/10.1016/J.CEJ.2020.124227.

[11] J. Zhang, D.S. Kalonia, The effect of neighboring amino acid residues and solution environment on the oxidative stability of tyrosine in small peptides, AAPS PharmSciTech 2007 8:4. 8 (2007) 176–183. https://doi.org/10.1208/PT0804102.

[12] I. Groeneveld, S.E. Schoemaker, G.W. Somsen, F. Ariese, M.R. van Bommel, Characterization of a liquid-core waveguide cell for studying the chemistry of light-induced degradation, Analyst. 146 (2021) 3197–3207. https://doi.org/10.1039/d1an00272d.

[13] I. Groeneveld, I. Bagdonaite, E. Beekwilder, F. Ariese, G.W. Somsen, M.R. van Bommel, Liquid Core Waveguide Cell with In Situ Absorbance Spectroscopy and Coupled to Liquid Chromatography for Studying Light-Induced Degradation, Anal Chem. 94 (2022) 7647–7654. https://doi.org/10.1021/acs.analchem.2c00886.

[14] I. Ahmad, Q. Fasihullah, F.H.M. Vaid, A study of simultaneous photolysis and photoaddition reactions of riboflavin in aqueous solution, J Photochem Photobiol B. 75 (2004) 13–20. https://doi.org/10.1016/j.jphotobiol.2004.04.001.

[15] I. Ahmad, Q. Fasihullah, F.H.M. Vaid, Photolysis of formylmethylflavin in aqueous and organic solvents, Photochemical & Photobiological Sciences. 5 (2006) 680–685. https://doi.org/10.1039/B602917E.

[16] I. Ahmad, Q. Fasihullah, F.H.M. Vaid, Effect of light intensity and wavelengths on photodegradation reactions of riboflavin in aqueous solution, J Photochem Photobiol B. 82 (2006) 21–27. https://doi.org/10.1016/J.JPHOTOBIOL.2005.08.004.

[17] M.A. Sheraz, S.H. Kazi, S. Ahmed, Z. Anwar, I. Ahmad, Photo, thermal and chemical degradation of riboflavin, Beilstein Journal of Organic Chemistry 10:208. 10 (2014) 1999–2012. https://doi.org/10.3762/BJOC.10.208.

[18] I. Ahmad, T. Mirza, Z. Anwar, S. Ahmed, M.A. Sheraz, M.A. Ejaz, S.H. Kazi, Photodegradation of formylmethylflavin by side–chain and isoalloxazine ring cleavage in alkaline solution: A kinetic study, J Photochem Photobiol A Chem. 374 (2019) 106–114. https://doi.org/10.1016/j.jphotochem.2019.01.028.

[19] M. Schuman Jorns, G. Schollnhammer, P. Hemmerich, Intramolecular Addition of the Riboflavin Side Chain. Anion-Catalyzed Neutral Photochemistry, Eur J Biochem. 57 (1975) 35–48. https://doi.org/10.1111/j.1432-1033.1975.tb02274.x.

[20] E.C. Smith, D.E. Metzler, The Photochemical Degradation of Riboflavin, J Am Chem Soc. 85 (1963) 3285–3288. https://doi.org/https://doi.org/10.1021/ja00903a051.

[21] A. Nezamzadeh-Ejhieh, P. Pouladsaz, Voltammetric determination of riboflavin based on electrocatalytic oxidation at zeolite-modified carbon paste electrodes, Journal of Industrial and Engineering Chemistry. 20 (2014) 2146–2152. https://doi.org/10.1016/J.JIEC.2013.09.044.

[22] A. de la Rochette, E. Silva, I. Birlouez-Aragon, M. Mancini, A.-M. Edwards, P. Morlière, Riboflavin Photodegradation and Photosensitizing Effects are Highly Dependent on Oxygen and Ascorbate Concentrations¶, Photochem Photobiol. 72 (2000) 815. https://doi.org/10.1562/0031-8655(2000)072%3C0815:RPAPEA%3E2.0.CO;2.

[23] I. Ahmad, S. Ahmed, M.A. Sheraz, F.H.M. Vaid, I.A. Ansari, Effect of divalent anions on photodegradation kinetics and pathways of riboflavin in aqueous solution, Int J Pharm. 390 (2010) 174–182. https://doi.org/10.1016/J.IJPHARM.2010.01.042.

[24] I. Ahmad, Q. Fasihullah, F.H.M. Vaid, Effect of phosphate buffer on photodegradation reactions of riboflavin in aqueous solution, J Photochem Photobiol B. 78 (2005) 229–234. https://doi.org/10.1016/j.jphotobiol.2004.11.010.

[25] F.H.M. Vaid, W. Gul, A. Faiyaz, Z. Anwar, M.A. Ejaz, S. Zahid, I. Ahmad, Divalent anion catalyzed photodegradation of riboflavin: A kinetic study, J Photochem Photobiol A Chem. 371 (2019) 59–66. https://doi.org/10.1016/J.JPHOTOCHEM.2018.10.048.

[26] I. Ahmad, Q. Fasihullah, A. Noor, I.A. Ansari, Q.N.M. Ali, Photolysis of riboflavin in aqueous solution: a kinetic study, Int J Pharm. 280 (2004) 199–208. https://doi.org/10.1016/J.IJPHARM.2004.05.020.

[27] I. Ahmad, T. Mirza, Z. Anwar, M.A. Ejaz, M.A. Sheraz, S. Ahmed, Multicomponent spectrofluorimetric method for the assay of formylmethylflavin and its hydrolytic products: Kinetic applications, Spectrochim Acta A Mol Biomol Spectrosc. 205 (2018) 540–550. https://doi.org/10.1016/J.SAA.2018.07.066.

[28] K. Kimura, T. Miwa, M. Imamura, Photochemical debromination of eosin in basic methanolic solution, Chemical Communications (London). (1968) 1619. https://doi.org/10.1039/c19680001619.

[29] K. Kimura, T. Miwa, M. Imamura, The Radiolysis and Photolysis of Methanolic Solutions of Eosin. II. The Photo-Debromination of Eosin in an Alkaline Solution, Bull Chem Soc Jpn. 43 (1970) 1337–1342. https://doi.org/10.1246/BCSJ.43.1337.

[30] A. Alvarez-Martin, T.P. Cleland, G.M. Kavich, K. Janssens, G.A. Newsome, Rapid Evaluation of the Debromination Mechanism of Eosin in Oil Paint by Direct Analysis in Real Time and Direct Infusion-Electrospray Ionization Mass Spectrometry, Anal Chem. 91 (2019) 10856–10863. https://doi.org/10.1021/acs.analchem.9b02568.

[31] B.W.J. Pirok, G. Moro, N. Meekel, S.V.J. Berbers, P.J. Schoenmakers, M.R. van Bommel, Mapping degradation pathways of natural and synthetic dyes with LC-MS: Influence of solvent on degradation mechanisms, J Cult Herit. 38 (2019) 29–36. https://doi.org/10.1016/J.CULHER.2019.01.003.

[32] F. Sabatini, E. Eis, I. Degano, M. Thoury, I. Bonaduce, A. Lluveras-Tenorio, The issue of eosin fading: A combined spectroscopic and mass spectrometric approach applied to historical lakes, Dyes and Pigments. 180 (2020) 108436. https://doi.org/10.1016/J.DYEPIG.2020.108436.

[33] A. Chieli, C. Miliani, I. Degano, F. Sabatini, P. Tognotti, A. Romani, New insights into the fading mechanism of Geranium lake in painting matrix", Dyes and Pigments. 181 (2020) 108600. https://doi.org/10.1016/J.DYEPIG.2020.108600.

[34] Van Gogh, Vincent. Letter to Theo van Gogh. 11 April 1888, Arles. Letter 595 in collection from Van Gogh Museum, Amsterdam, The Netherlands.

[35] A. Ozawa, M. Sakaue, New decolorization method produces more information from tissue sections stained with hematoxylin and eosin stain and masson-trichrome stain, Annals of Anatomy. 227 (2020). https://doi.org/10.1016/J.AANAT.2019.151431.

[36] N.C. Taylor, J.F. Mcgouran, Organic & Biomolecular Chemistry Investigating eosin Y as a photocatalyst for the radical-dependent activity-based probing of deubiquitinating enzymes †, Org. Biomol. Chem. 19 (2021) 2177. https://doi.org/10.1039/d1ob00253h.

[37] M.J. den Uijl, A. Lokker, B. van Dooren, P.J. Schoenmakers, B.W.J. Pirok, M.R. van Bommel, Comparing different light-degradation approaches for the degradation of crystal violet and eosin Y, Dyes and Pigments. 197 (2022) 109882. https://doi.org/10.1016/J.DYEPIG.2021.109882.

[38] I. Pinnau, L.G. Toy, Gas and vapor transport properties of amorphous perfluorinated copolymer membranes based on 2,2-bistrifluoromethyl-4,5-difluoro-l,3-dioxole/tetrafluoroethylene, J Memb Sci. 109 (1996) 125–133. https://doi.org/10.1016/0376-7388(95)00193-X.

[39] A.Y. Alentiev, V.P. Shantarovich, T.C. Merkel, V.I. Bondar, B.D. Freeman, Y.P. Yampolskii, Gas and vapor sorption, permeation, and diffusion in glassy amorphous teflon AF1600, Macromolecules. 35 (2002) 9513–9522. https://doi.org/10.1021/ma020494f.

[40] M.K. Hossain, M.M. Hossain, S. Akhtar, Photodegradation and reaction kinetics for eosin yellow using ZnO nanoparticles as catalysts, Reaction Kinetics, Mechanisms and Catalysis. 135 (2022) 2247–2263. https://doi.org/10.1007/S11144-022-02244-4/FIGURES/10.

[41] R. Huang, E. Choe, D.B. Min, Kinetics for Singlet Oxygen Formation by Riboflavin Photosensitization and the Reaction between Riboflavin and Singlet Oxygen, J Food Sci. 69 (2004) C726–C732. https://doi.org/10.1111/J.1365-2621.2004.TB09924.X.

[42] A. Wolnicka-Glubisz, A. Pawlak, M. Insinska-Rak, A. Zadlo, Analysis of photoreactivity and phototoxicity of riboflavin's analogue 3MeTARF, J Photochem Photobiol B. 205 (2020) 111820. https://doi.org/10.1016/J.JPHOTOBIOL.2020.111820.

[43] R. Huang, J.K. Hyun, D.B. Min, Photosensitizing Effect of Riboflavin, Lumiflavin, and Lumichrome on the Generation of Volatiles in Soy Milk, J Agric Food Chem. 54 (2006) 2359–2364. https://doi.org/10.1021/JF052448V.

[44] L.S. Herculano, L.C. Malacarne, V.S. Zanuto, G.V.B. Lukasievicz, O.A. Capeloto, N.G.C. Astrath, Investigation of the photobleaching process of eosin y in aqueous solution by thermal lens spectroscopy, Journal of Physical Chemistry B. 117 (2013) 1932–1937. https://doi.org/10.1021/jp3119296.

[45] F. Amat-Guerri, M.M.C. López-González, R. Martínez-Utrilla, R. Sastre, Singlet oxygen photogeneration by ionized and un-ionized derivatives of Rose Bengal and Eosin Y in diluted solutions, J Photochem Photobiol A Chem. 53 (1990) 199–210. https://doi.org/10.1016/1010-6030(90)87124-T.

# CHAPTER 8

## Exploring the feasibility of Raman spectroscopy for in-situ monitoring of photodegradation processes

# Abstract

Raman scattering (RS) or surface-enhanced Raman scattering (SERS) provides more specific information on molecular structures than absorption spectroscopy, and therefore, might be an alternative technique for the in-situ monitoring of photodegradation. The feasibility of RS and SERS for studying structural changes in irradiated molecules was explored during several preliminary experiments. Crystal Violet (CV) was irradiated inside the liquid-core waveguide (LCW) and the photodegradation products were isolated by LC. These were subsequently analyzed by SERS after mixing with a silver colloid, yielding distinctive Raman spectra for each degradation product. In-situ SERS monitoring during photodegradation was explored using leaning-pillar chips as SERS substrates. Firstly, several aspects of the leaning pillar chips were assessed, such as signal enhancement obtained with silver and gold coatings, excitation laser wavelength (532 and 785 nm) lasers, repeatability, substrate cleaning procedures, and memory effect. The on-chip SERS spectra showed similarities with the changes observed for SERS spectra of the photodegradation products separated by LC. LC-DAD-QTOFMS analysis confirmed the presence of the same degradation products, however, the presence of a gold-coated chip seems to influence the photodegradation process. Finally, silver and gold-coated carbon paper was used as a potential gas-permeable SERS substrate for implementation in a microfluidic device that allows studying the influence of oxygen on the photodegradation process.

## 8.1 Introduction

In the previous chapters, the development, optimization, and successful application of an LCW-based cell for the study of photodegradation were described. The developed system allowed the in-situ monitoring of the irradiated sample in real-time by means of absorption spectroscopy. Next to full UV/Vis spectra, the absorbance detection provided useful information about, e.g., the potential presence of air bubbles in the LCW and whether the sample was correctly injected. The absorbance measurement was relatively easy to implement, but intrinsically the amount of structural information it can provide is limited. As the absorption spectra are broad and dominated by the chromophore, small changes to the molecular structure can be hard to observe or are not reflected in the spectrum. This is especially true when the absorption spectrum is recorded from a mixture, as is the case for in-situ monitoring of photodegradation, where degradation products are often present at low concentration and show strong similarities to the parent compound. An alternative spectroscopic technique that can provide more specific information on the molecular structure is Raman scattering (RS) or surface-enhanced Raman scattering (SERS). The aim of this chapter is to describe the results of several preliminary experiments that were conducted to assess the feasibility of RS and SERS for the monitoring of photodegradation processes in real time. The obtained results provide interesting and useful starting points for future research.

### Basics of Raman spectroscopy



RS is based on the measurement of inelastically scattered photons, known as Raman scattering. A beam of light, usually from a laser in the visible, near IR, or UV range, interacts with molecular vibrations of the sample molecules. Due to this interaction, the energy of a small part of the scattered photons may be shifted down or up relative to the laser's photon energy, known as the Stokes or anti-Stokes shift, respectively. This energy shift is characteristic of a specific molecular vibrational mode and, therefore, gives information about the molecular structure(s) of the system. In contrast to ordinary UV/Vis absorption spectroscopy, Raman spectroscopy is even able to differentiate between structural isomers [1–3].

Typical instrumentation for Raman spectroscopy comprises, besides a laser, a spectrometer with a CCD camera in order to translate the received signals into a spectrum. A Raman microscope uses an objective to focus the laser into a small spot size to increase the spatial resolution of the instrument. In addition to a laser and spectrometer, the microscope setup consists of a mirror to reflect the laser into the direction of the sample, a microscope objective to focus the light onto the sample, a beam splitter that transmits the laser light to the sample, and collects the reflected,

scattered signal from the sample, a focusing lens, and a notch filter or edge filter to remove residual light originating from the laser (Fig. 8.1).

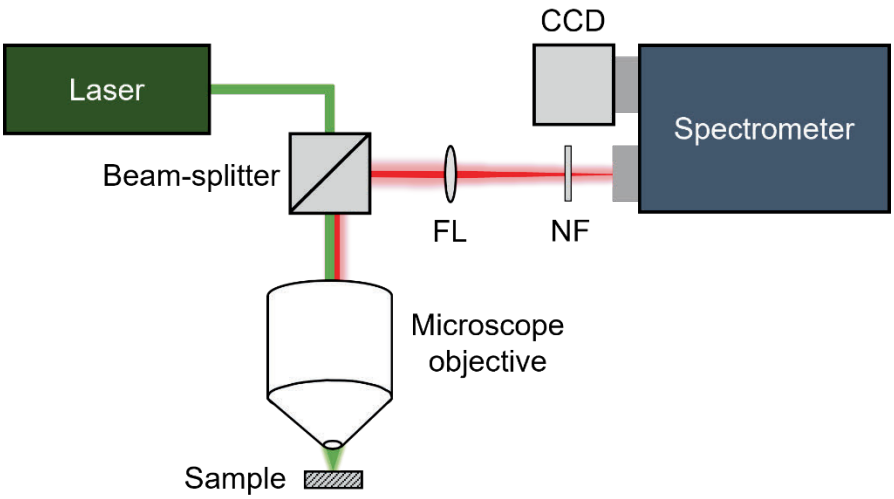


Figure 8.1. Schematic diagram of a typical Raman microscope setup. FL=focusing lens, NF=notch filter, CCD=charge-coupled device. Red beam is back-scattered light from sample. Adapted with permission from [4].

### Surface enhanced Raman spectroscopy (SERS)

Unfortunately, Raman scattering is relatively rare compared to other scattering phenomena; approximately 1 in 1 million scattered photons is scattered inelastically. Next to that, the absorption of laser photons may lead to emission by fluorescence. In contrast to Raman scattering, absorption and fluorescence are the result of 'real' molecular electronic transitions, which can occur if the laser photons have matching energy. The fluorescence signal can completely obscure the Raman signal, as shown in Fig. 8.2, and constitutes a real challenge in RS. Therefore, the use of low excitation-energy lasers, such as in the near-infrared region, is often preferred in RS over lasers in the Vis region. Lastly, deep UV lasers may also be used to circumvent the adverse effect of auto-fluorescence as that is often limited to wavelengths above 270 nm and then will not interfere with the Raman signals below 270 nm.

A solution for weak Raman signals has been found in SERS, where molecules adsorbed to certain colloidal metal particles or roughened metal surfaces, such as silver or gold, show an enhanced Raman signal by a factor of up to $10^{10}$ [6]. The enhancement can be explained by two possible contributions: (i) an electromagnetic, and (ii) a chemical enhancement mechanism [4].

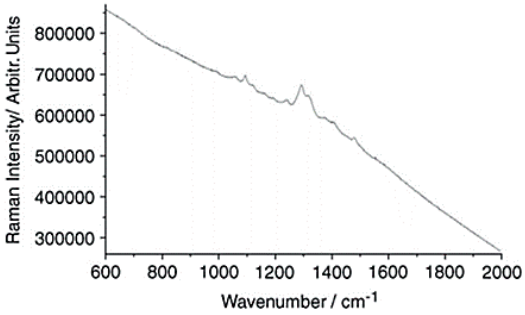


Figure 8.2. Raman spectrum of a pink pigment without fluorescence background subtraction. Excitation wavelength, 785 nm. Reproduced with permission from [5].

The intensity of Raman scattering is directly proportional to the Raman polarizability (α), and the magnitude of the incident electromagnetic field ($E^2$). According to (i), $E$ is enhanced when the localized surface plasmon resonance (LSPR) (Fig. 8.3A) of a nanostructured or nanoparticle metal surface is excited. The emitted Raman intensity is then enhanced further by an additional factor $E^2$ on the way out due to the formation of so-called 'hotspots' where molecules are positioned. Researchers found this contribution to be the largest [4,7]. The chemical contribution to the enhancement factor arises from the excitation of adsorbate localized electronic resonances or metal-to-adsorbate charge-transfer resonances (e.g., resonance Raman scattering) [4]. The large enhancement factors make SERS much more sensitive than regular RS and, due to quenching effects by the metal substrate, make it possible to also use high-energy lasers in the UV/Vis region without fluorescence background causing serious problems, as shown in Fig. 8.3B.



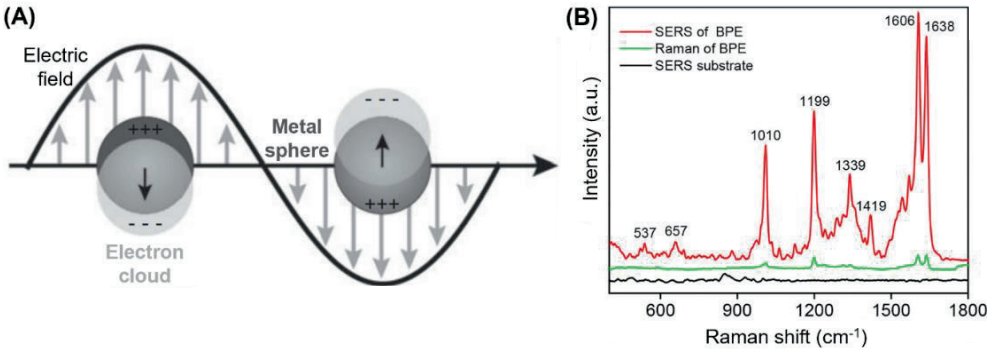


Figure 8.3. (A) Illustration of the localized surface plasmon resonance effect. Reproduced and adjusted with permission from [4]. (B) Comparison of Raman and SERS spectra of 10 mM and 1 μM 1,2-bis-(4-pyridyl) ethylene (BPE), respectively. Excitation wavelength, 785 nm. Note that the concentration of BPE used for Raman is $10^5$ times higher than that used for SERS. Reproduced and adjusted with permission from [8].

**SERS as in-situ detection technique**

The high specificity of Raman spectra and the increased sensitivity that SERS offers, makes it an attractive method for monitoring changes made to the molecular structure during photodegradation. Preferably, this should be done in situ as to avoid manipulation of the sample. It was shown by Dijkstra et al. that it is possible to perform 'regular' RS inside an LCW [9,10]. Raman spectra of adenosine, guanosine, and uridine 5'-monophosphate were obtained inside a 50-cm long LCW. However, the total measuring times (exposure time and the number of accumulations) to obtain a spectrum were relatively long (≈10 min) for solutions of 1-2 mg $mL^{-1}$ [10]. Much lower concentrations of products may be encountered in the photodegradation process and, therefore, much longer measuring times are expected. This, however, may affect the photodegradation process, which should be avoided to not interpret the results wrongly. SERS may provide a solution to the low concentrations present during photodegradation studies. For the past 10-20 years, the demonstration of SERS as an in-situ detection technique for microfluidic devices is growing and applications vary from the detection of trace molecules in water to the sensing of virus DNA in biological samples [11–17]. In general, the SERS substrate is embedded in the microfluidic device, as freely moving colloidal particles can clog or irreversibly adsorb and contaminate the microfluidic channels. Analysis is mostly done by Raman microscopy, where the microfluidic device is simply placed underneath the microscope for focusing of the laser on the substrate [11–13,17]. Most literature, describing the analysis of a broad array of analytes, mentions the use of bare, unmodified metal nanoparticles (NPs) [12–14], but these can also be functionalized with, e.g., DNA or antibodies to create a highly specific probe for suspect screening [11,15–17]. The shape and size of the NPs have proven to be important factors for enhancing sensitivity and analyte capture [12–14,18]. For example, Jeon et al. found that the rough surfaces of branched gold particles, such as nanoflowers, resulted in enhanced electromagnetic hot spots as compared to non-branched gold particles, such as nanospheres [13]. Stamplecoskie et al. [18] found that the optimal size of silver NPs for obtaining a maximum SERS intensity was 50-60 nm. Detection limits down to 0.01 ppb have been reported [17].

The reported work shows SERS to be promising for in-situ monitoring, however, some challenges still have to be overcome, as others have also stated in extensive review articles [19–21]. One of these challenges is the memory effect of SERS substrates, as analytes are usually adsorbed to the substrate. This may hinder the use of these substrates for repeated measurements and reduces repeatability.

The current chapter presents the results of several exploratory studies, aimed at developing an on-chip SERS detection method for the monitoring of photodegradation.

First, in section 8.2 the separation and subsequent analysis of photodegradation products of crystal violet (CV) by SERS is described. This is followed by the assessment of commercially available SERS substrates with silver and gold coating in Section 8.3. The studied parameters were the optimal excitation wavelength, substrate metal, a cleaning procedure to reduce carry-over (i.e., memory effect), and repeatability. Section 8.4 describes the potential use of SERS to monitor the photodegradation of CV in a microfluidic device using the optimized detection method with leaning pillar chips as substrate. The obtained SERS spectra were compared to those obtained for the isolated photodegradation products. Then, in Section 8.5, carbon paper is assessed as a gas-permeable SERS substrate that can potentially be used as an oxygen-diffusive layer in a microfluidic device. Finally, in Section 8.6, several conclusions are drawn from the results discussed in this chapter.

## 8.2 SERS analysis of photodegradation products of crystal violet after separation by LC

### 8.2.1 Introduction

As a starting point for the monitoring of photodegradation by means of SERS, CV was chosen as a model compound. The photodegradation of CV has been assessed by SERS before on a paper surface by Cesaratto et al. [22]. One of the degradation pathways of CV follows consecutive demethylation of the three amine groups, as shown in Fig. 8.4, ultimately forming the fully demethylated form of CV (CV-6Me), also known as pararosaniline.

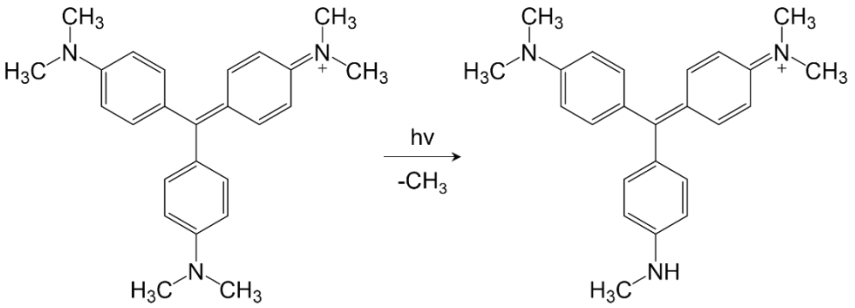


Figure 8.4. Crystal violet (CV) and the main pathway during photodegradation: the first step of consecutive demethylation of the amine groups, ultimately leading to pararosaniline after the removal of all methyl groups.

Cesaratto et al. exposed samples of CV on paper for 54 days to light above 400 nm using a light fading unit. Different light doses were simulated by covering parts of the paper with transmission step wedges, indicated by steps 1-4 in Fig. 8.5, with step 1 being the lowest dose. The SERS procedure included the deposition of silver colloids on a small paper sample and the addition of 0.5 M $KNO_3$ solution to induce colloid aggregation. SERS spectra as shown in Fig. 8.5 were acquired using a 488-nm laser. The authors were able to track changes occurring to CV on the paper after exposure to different light doses, and obtained spectra that showed high similarities to the SERS spectra of CV-6Me or pararosaniline (R/P ref. in Fig. 8.5). The most pronounced spectral changes were observed for the peaks around 1580 and 1620 $cm^{-1}$, which possibly indicates asymmetry in the molecules as occurs after demethylation of CV. Another important change was observed at 3218 and 3348 $cm^{-1}$, which could correspond to the formation of N-H groups after the loss of methyl.

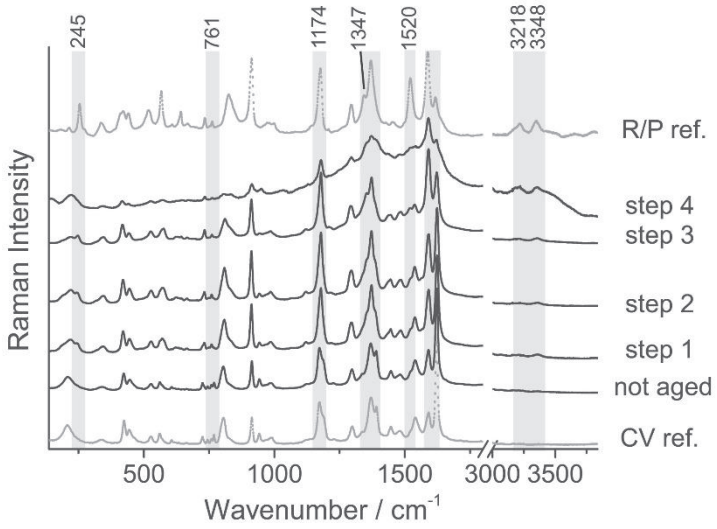


Figure 8.5. SERS spectra obtained after five different aging steps of CV on paper. The spectra of CV (CV ref.) and rosaniline/pararosaniline references (R/P ref.) are added for comparison. Reproduced with permission from [22].

In our lab, the photodegradation products of CV were established using the LCW-based LID cell and analyzed by LC-DAD as presented in Chapter 5. Baseline separation of the demethylation products of CV was achieved (Fig. 5.9), which indicates that it is possible to fractionate the LC column effluent and analyze the products separately by means of SERS. The work presented here describes the fractionation of a sample of CV that was irradiated for 48 hrs inside the LCW-based LID cell, in order to isolate the formed degradation products and allow their SERS measurement by means of silver colloids. The work by Cesaratto et al. was used for comparison with the work presented here.



## 8.2.2 Experimental

### Chemicals

Aqueous solutions were prepared using ultrapure deionized water (MQ) (Millipore Simplicity Simpak 2, R = 18.2 MΩ cm, U.S.A.). Methanol (MeOH) (>99%) was purchased from Biosolve (Valkenswaard, The Netherlands). Crystal violet (CV) (>90%), nitric acid ($HNO_3$) (70%), silver nitrate ($AgNO_3$) (>99%), and sodium citrate ($Na_3C_6H_5O_7$) (>99%) were purchased from Sigma-Aldrich (Steinheim, Germany).

### Materials and instruments

*Raman spectrometer*

The Renishaw Raman microscope employed for the SERS measurements was of the type inVia, equipped with a 532 nm and 785 nm laser. The spectrometer was calibrated using

a silicone reference prior to each new measurement series. The grating selected for the 532 nm laser was 1800 L $mm^{-1}$ and 1200 L $mm^{-1}$ for the 785 nm laser. All data were recorded using WiRE software. The settings used for the measurements with silver colloid were as follows: objective, 5x; laser, 532 nm; laser power, 1%; exposure time, 1 s; accumulations, 4.

*LC–DAD*

The LC system consisted of a quaternary solvent pump, a reversed-phase ZORBAX Eclipse RRHD C18 column (2.1 x 150 mm; particle size, 1.8 µm; Agilent), and a security guard column (2.1 x 5 mm) with the same C18 phase, and a column oven set to 40°C. DAD detection provided UV/Vis spectra from 250-800 nm with a spectral resolution of 1 nm. The developed LC method described in Chapter 4 was applied for the analysis of the irradiated samples.

**Methods**

*Preparation of silver colloids*

Silver colloids were prepared according to the Lee-Meisel method [23]. All glassware was cleaned with concentrated nitric acid and washed with MQ before use. 45 mg of silver nitrate was added to 250 mL of MQ in a conical flask, which was heated until boiling under reflux conditions. Upon boiling, 5 mL of 1% aqueous sodium citrate was added and was left to boil for 1 hr. After the suspension had cooled down to room temperature, 1 mL aliquots were transferred to Eppendorf tubes and centrifuged for 30 min at 10,000 rpm. Lastly, 950 µL of the supernatant was removed, leaving roughly 50 µL of colloid suspension per tube.

*Photodegradation of CV and SERS analysis of photodegradation products*

A 10 mg $L^{-1}$ aqueous solution of CV was irradiated inside a 20-cm long LCW for 48 hrs. The LCW cell set-up was similar to the schematic presented in Fig. 5.1. The sample was collected manually and analyzed by LC-DAD. LC fractions were collected every 15 s during the elution window (15-20 min) of CV and the main degradation products. These fractions were then analyzed by SERS using the prepared silver colloids. Equal volumes (3 µL) of sample and colloid were mixed on a glass slide and left to dry, followed by SERS analysis using the Renishaw microscope. Spectra were recorded on five different spots for each sample and then averaged.

## 8.2.3 Results and discussion

The aim of the experiment was to measure SERS spectra of isolated photodegradation products of CV and to compare these to the spectrum of the parent compound. Product

isolation was achieved by LC fractionation of a photodegraded solution of CV collected from a 20-cm long LCW. The experiment was conducted at an early stage of the TooCOLD project, meaning that the photodegradation was not performed in the LID cell as described in chapters 6 and 7, but in a prototype similar to that presented in Fig. 5.1. The obtained chromatogram, the fractions taken and corresponding absorbance spectra are shown in Fig. 8.6.

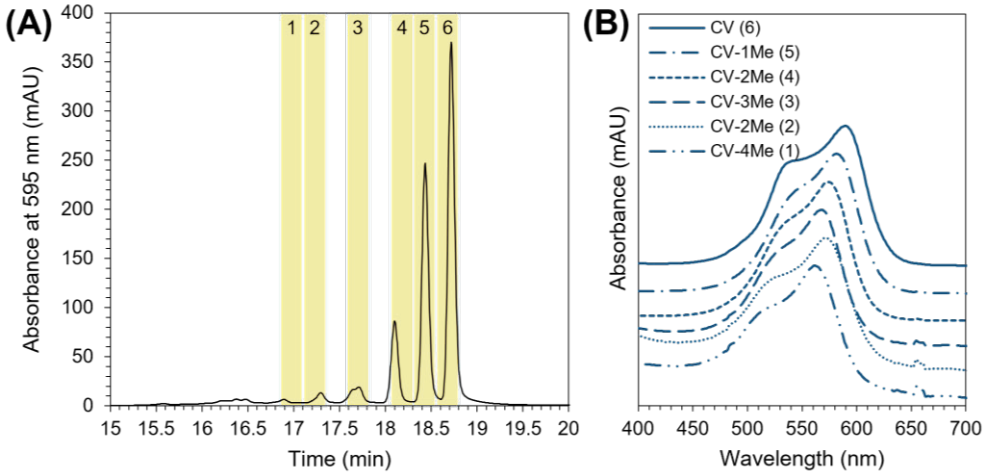


Figure 8.6. (A) LC–DAD of photodegraded CV and (B) corresponding UV–Vis spectra of isolated degradation products. The numbers 1–6 correspond to the fraction number.



The degradation pathway for CV was studied previously in Chapter 5, and photodegradation of CV in the LCW mainly showed consecutive demethylation of the amine groups of the parent compound (Fig. 5.9). Degradation along a similar pathway was found for the 48-hr irradiated sample, as can be concluded from Fig. 8.6. The SERS spectra of the collected LC fractions are shown in Fig. 8.7. The most pronounced change in the spectra of the degradation products when compared to CV (top) is the change in the ratio of the peaks at 1580 (non-totally symmetric benzene mode) and 1620 $cm^{-1}$ (totally symmetric benzene mode) that may indicate the loss of one or more methyl groups. Other major changes in the spectra of the degradation products are observed for 1540 $cm^{-1}$ (C-N stretching), 1350-1386 $cm^{-1}$ (phenyl-N-stretching), 1176 $cm^{-1}$ (indicating asymmetric benzene mode, asymmetric stretching of the central C-C-C), 808 $cm^{-1}$ (asymmetric benzene mode), and 573 $cm^{-1}$ (in-plane ring deformation) [22].

Although this was the first time isolated photodegradation products of CV were analyzed by SERS, it is instructive to compare with the spectra obtained by Cesaratto et al. [22] who tracked the photofading of several triarylmethane dyes (basic fuchsine, methyl violet, and CV) on paper by SERS. As described in the Introduction, they observed

changes in the SERS spectra over time that eventually resembled that of pararosaniline, indicating the complete demethylation of CV. These findings are in line with the results presented in the current work.

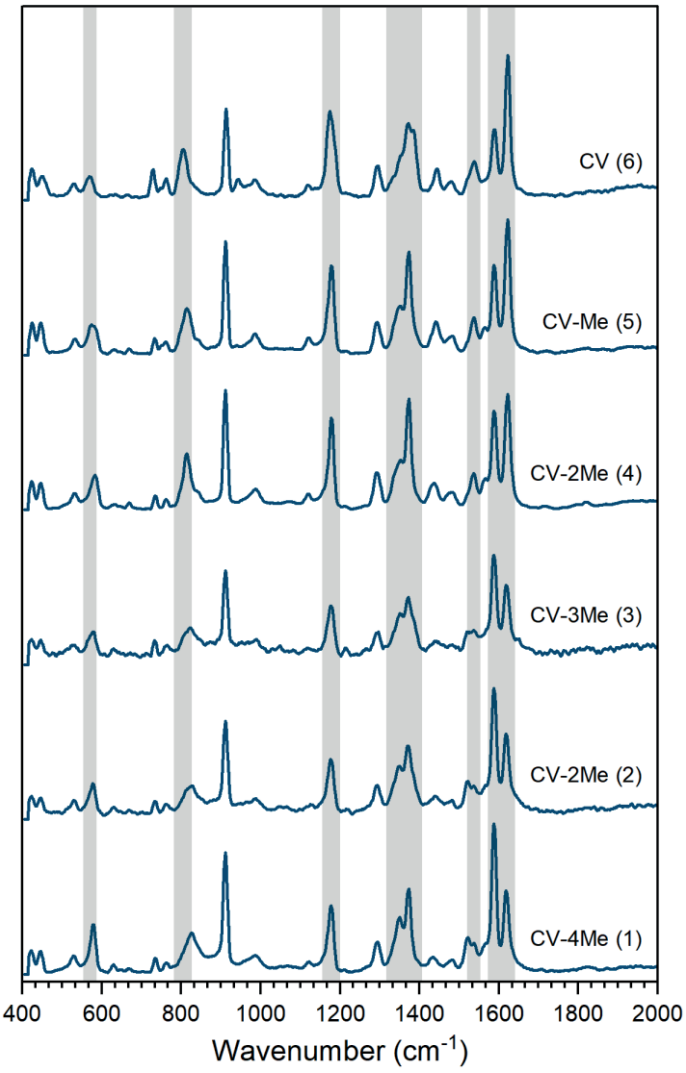


Figure 8.7. SERS spectra of the collected LC fractions 1–6. The process of consecutive demethylation of CV is indicated by CV–xMe. The grey bands indicate peaks showing significant change relative to the spectrum of CV. Spectra are normalized based on the highest peak.

This proof-of-principle experiment shows that, for CV, differences between SERS spectra of its photodegradation products can be detected. Peaks 2 and 4 in Fig. 8.6 are isomers of bis-demethylated CV, which have lost two methyl groups either on the same or two different amine groups. They elute at different times, and their structures differ enough

to result in two very different SERS spectra. The loss of two methyl groups from one amine will result in a higher polarity, as described by Chen et al. [24]. Therefore, we suspect that this particular isomer can be assigned to peak 2 in Fig 8.6 and 8.7.

The next question is whether it would be possible to monitor these spectral changes in an irradiated mixture where the structurally highly similar parent and degradation compounds are not separated and concentrations are generally low. As mentioned in Section 8.1, it was shown that it is possible to perform RS inside an LCW, however, it requires long measuring times for the relatively low concentrations generally present during photodegradation studies. Prolonged exposure by the excitation laser may also affect the photodegradation process, thus, must be avoided. SERS may be performed inside an LCW by means of metal colloids, however, they may block or be flushed out of the system in between experiments, or adsorb to the walls and, therefore, contaminate the LCW. To overcome the challenges that come with the use of free metal colloids, a microfluidic device may be used where an immobilized SERS substrate can be embedded. Therefore, the feasibility of leaning pillar chips for monitoring photodegradation inside a microfluidic device has been explored (section 8.3).

## 8.3 Potential of leaning pillar chips for in-situ SERS measurements

### 8.3.1 Introduction

The character of SERS substrates varies widely with respect to size, shape, and type of metal. The most popular approach to perform SERS is by the use of silver or gold colloids, as mentioned before. Due to the challenges they bring for implementation with microfluidic devices, we looked into the feasibility of immobilized SERS substrates. Most of the research papers in the literature present self-created SERS substrates, whereas others use commercially available substrates. An example of commercially available substrates is leaning pillar chips. The manufacturing process and performance of these chips were described by Schmidt et al. [25]. In brief, the silicon nanopillars of these chips lean together when a solution evaporates, hence, trapping the analyte and forming hotspots that enhance the SERS signal. According to Ochoa-Vazquez et al. [26], these substrates are complicated to produce compared to other substrates but show great stability and reproducibility. An example of the implementation of nanopillar substrates is shown by Durucan et al. [27,28]. Gold-coated silicon nanopillar chips were placed in a microfluidic 'disk' for the analysis of several compounds in different matrices. Using centrifugation, the sample migrated to the nanopillar chips and was then left to dry before SERS analysis was performed. The development and performance of nanogap leaning pillars for SERS analysis in solution were shown by Lao et al. [29], showing that leaning pillars are a potentially suitable substrate for microfluidic SERS devices.

The continuous and repeated monitoring of the sample inside a microfluidic device requires the same SERS substrate to be used in a repeatable manner. However, the adsorption of molecules onto the substrate is a common source of error in real-time SERS, also called the 'SERS memory effect' [30]. Several authors have claimed that the memory effect can be overcome by cleaning the substrates with solvents [31,32], by applying electricity [33,34], or by UV light-induced photodegradation [35].

This section describes the characterization of commercially available leaning pillar chips for future applicability inside a microfluidic device. The experiments described here, however, were performed outside of such a device for simplicity reasons. The tested parameters include the signal enhancement by the silver and gold coatings in combination with lasers of 532 or 785 nm, repeatability, and we looked into a cleaning procedure to reduce the memory effect.

## 8.3.2 Experimental

### Chemicals

Aqueous solutions were prepared using ultrapure deionized water (MQ) (Millipore Simplicity Simpak 2, R = 18.2 MΩ cm, U.S.A.). Methanol (MeOH) (>99%) and ethanol (EtOH) (LC-MS purity) were purchased from Biosolve (Valkenswaard, The Netherlands). Acetone (>99.9%), hydrochloric acid (HCl) (37%), and Rhodamine B (RhB) (>97%) were purchased from Sigma-Aldrich (Steinheim, Germany).

### Materials and instruments

*SERS substrates*

On-chip SERS analysis and the optimization thereof were performed with silver- and gold-coated leaning pillar chips (Silmeco, Copenhagen, Denmark). These chips are fabricated of silicon and sputtered with a silver or gold coating.

*Raman spectrometer*

The Raman microscope described in Section 8.2.2 was used for the experiments described in this section. The settings were as follows: objective, 20x; laser, 532 or 785 nm; laser power, 10%; exposure time, 0.5 s; accumulations, 40.

### Methods

*Preparation of solutions*

A dilution series was prepared from an RhB stock solution of 1 g $L^{-1}$ in MeOH by diluting with MQ to a final concentration of $10^{-5}$ M.

*Characterization of SERS chips*

The repeatability was tested by determining the spread in the measurement signals recorded on different days. The memory effect was assessed by applying and measuring a $10^{-5}$ M aqueous solution of RhB, after which the chip was cleaned according to an optimized procedure, and was then used again for measurement. The cleaning procedure was tested and optimized by flushing with different solvents, always followed by flushing with an equal volume of MQ. For each sample or measurement, the spectra of five different spots on the substrate were recorded and averaged. Data processing was executed in MATLAB R2020b using the background correction code by Mazet (version 1.4.0.0) published on MATLAB Central File Exchange34.

## 8.3.3 Results and discussion

### Dry vs. in-solution measurements

Leaning pillar chips are meant to be used for dried samples to make the pillar lean towards each other to create so-called hotspots. Therefore, we tested whether leaning pillar chips provide good enhancement for wet (i.e., in-solution) measurements as well. Dry and in-solution Raman measurements of $10^{-5}$ M RhB on a gold chip were carried out and the results were compared (Fig. 8.8). For that, first a droplet of RhB was applied and measured, and after letting it dry to the air, the measurement was repeated on the dry spot. From Figure 8.8, it can be seen that the dried spot overall resulted in a slightly more intense spectrum, with some exceptions for the peaks around 1125, 1600, and 1700 $cm^{-1}$. It is expected that the drying of the droplet resulted in more hot spots due to the leaning of the pillars. However, the difference observed was surprisingly small and shows rather convincingly that the leaning pillar chips can be used for the Raman measurement of solutions, possibly also in a microfluidic device. Considering the intensity of the SERS signals obtained for $10^{-5}$ M RhB, we estimate the LOD to be in the $10^{-7}$ M range.

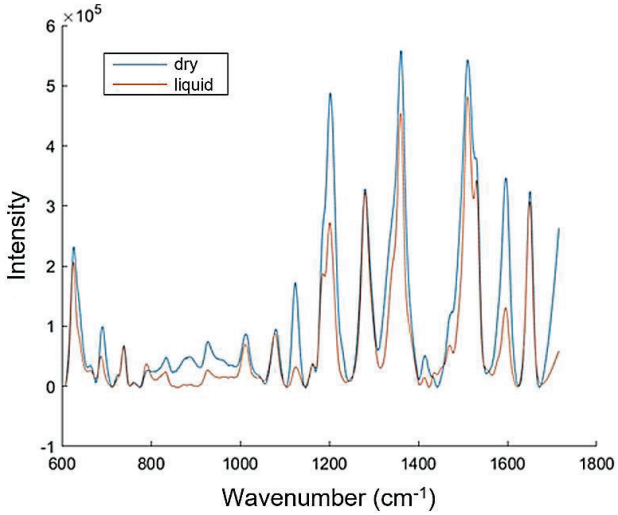


Figure 8.8. SERS spectra of RhB on a gold leaning pillar chip measured before (liquid) and after drying of the sample droplet. Spectra shown are the average of five different spots.

### Enhancement on silver and gold substrates

It was found that excitation using the 785 nm laser was favorable (results not shown), as this laser caused much less fluorescence background. With the 532 nm laser, fluorescence dominated the SERS spectrum, which is due to the overlap of the laser wavelength with the absorption spectrum of RhB. In addition, we suspect that the

relatively large fluorescence background is caused RhB molecules free in solution. Only a fraction of the RhB molecules may be adsorbed to the silver substrate so that the fluorescence quenching effect of silver may is limited in this case.

The enhancement provided by the silver and gold substrates was compared by measuring a $10^{-5}$ M RhB solution with the 785-nm excitation laser (Fig. 8.9). The gold substrate resulted in significantly higher SERS signals for RhB as compared to the silver substrate. This can be explained by the fact that the plasmon absorption band of gold shows a more favorable overlap with 785 nm [36] than with 532 nm, which would be more feasible for silver substrates [37]. Still, at this point, the silver substrates remained included for further exploration as the results for RhB may be compound specific.

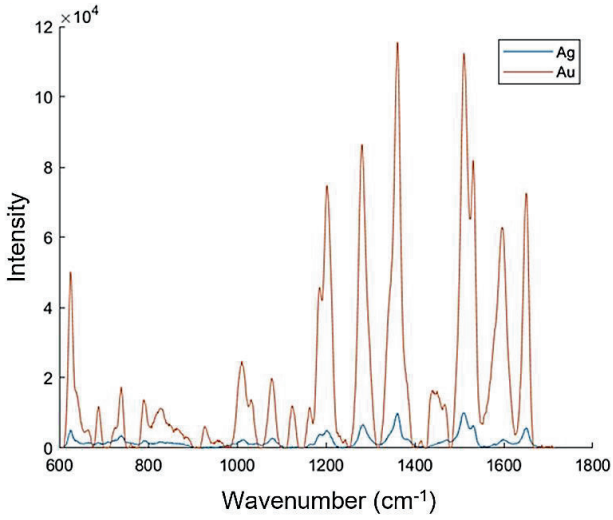


Figure 8.9. SERS spectra of RhB on a silver (Ag) and gold (Au) leaning pillar chip; Excitation wavelength, 785 nm. Spectra shown are the average of five different spots.

### Cleaning procedures and memory effect

In order to allow repeated use of solid substrates for SERS, the potential removal of analytes is essential to prevent a 'memory effect'. Cleaning of the substrate surface between experiments might be difficult, because (i) the substrates often are fragile, and (ii) compounds may be strongly adsorbed. The latter leads to carry-over affecting the reliability of the next measurement. The leaning pillar producer Silmeco provided a cleaning procedure with their substrates that consisted of washing with 1.5% HCl in MeOH. Here, several solvents were tested for cleaning the chips: 1.5% HCl in either MeOH, EtOH, or acetone. Fig. 8.10 shows the corresponding SERS spectra using acidified acetone (A, B), EtOH (C, D), and MeOH (E, F).

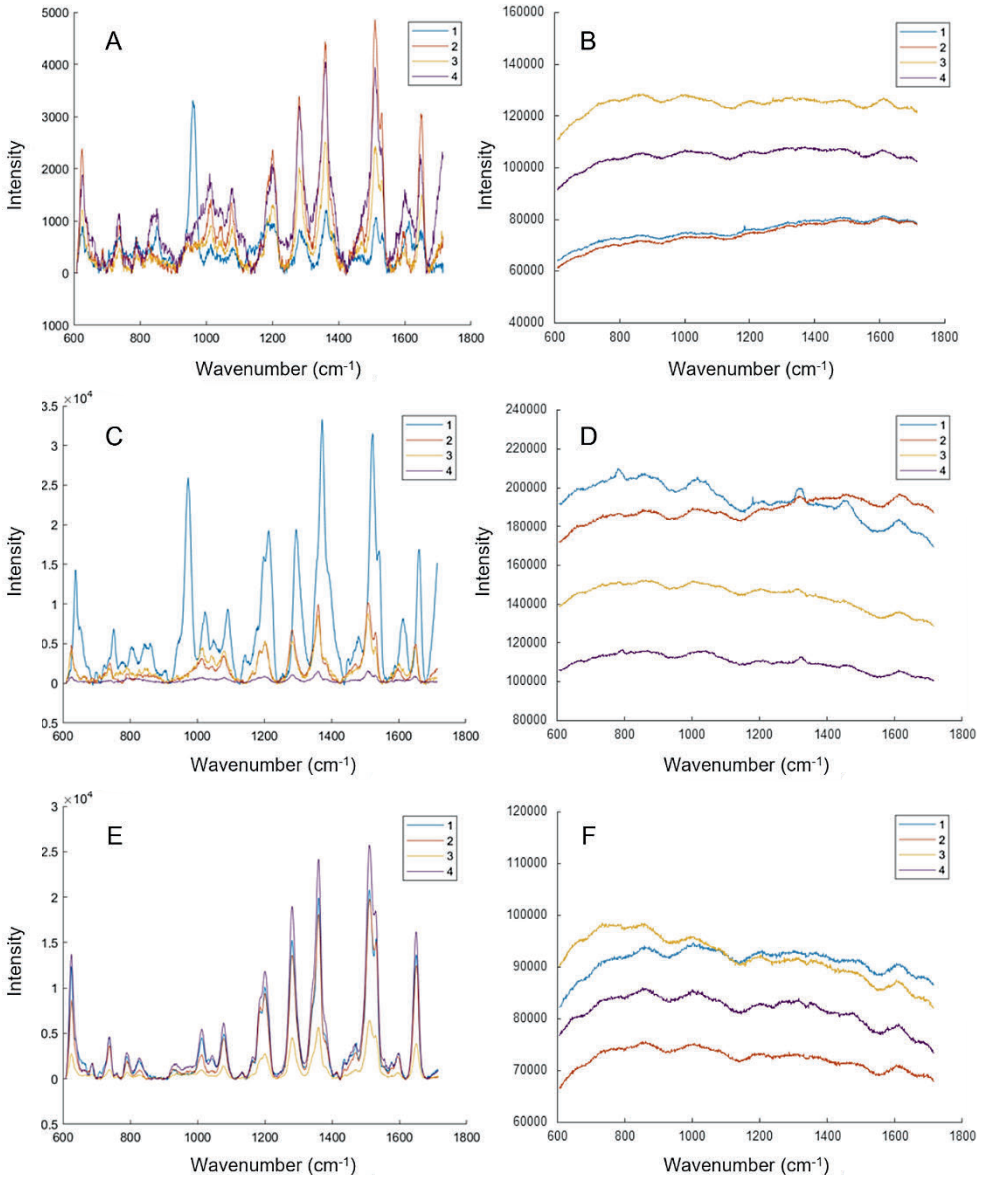


Figure 8.10. SERS spectra of $10^{-5}$ M RhB on the silver substrate before (left) and after (right) every cleaning cycle with 1.5% HCl in acetone (A, B), EtOH (C, D), and MeOH (E, F). Cleaning cycles were performed four times, and the spectrum corresponding to each cycle is numbered 1–4. Each spectrum is the average of five different spots; excitation wavelength, 785 nm.

The cleaning procedure was performed in four cycles, which consisted of two steps: (1) a measurement of $10^{-5}$ M RhB (shown in Fig. 8.10A, C, and E), and (2) a measurement after flushing with the indicated cleaning solvent (shown in Fig. 8.10B, D, and F). This

was repeated four times (cycles 1 to 4). The spectra from step 1 represent a reference point, including the effect of the solvent on the performance of the SERS substrate, while the spectra from step 2 indicate the efficiency of the corresponding solvent for removing RhB from the substrate.

Looking at the results for washing with 1.5% HCl in acetone, the intensity of the spectra of RhB after its application (Fig. 8.10A) vary in absolute intensity, but without a specific trend with the washing cycle order. For washing with 1.5% HCl in EtOH a consecutive decrease in the intensity of the SERS signal was observed after each washing cycle (Fig. 8.10C). Using 1.5% HCl in MeOH, the signal of RhB remained relatively constant, showing the highest repeatability in the measured SERS intensity after each cycle (Fig. 8.10E).

The SERS spectra, measured after cleaning, showed that all three solvents showed similar efficiency for removing RhB from the substrates (concluding from Fig. 8.10B, D, and F), although some background signal remains. The SERS spectra of the chips obtained after cleaning (shown without background subtraction) are similar to a blank measurement and do not show the typical narrow Raman peaks observed for RhB. Since the shape of the RhB spectra obtained after each cleaning cycle was very similar among the different solvents, we concluded that the solvents were equally efficient at removing RhB. As indicated, 1.5% HCl in MeOH showed higher repeatability throughout the four cycles, thus it was decided to continue with acidified MeOH as the washing solvent.

The cleaning procedure using 1.5% HCl in MeOH was also applied on gold substrates (Fig. 8.11A and B). The variation in signal intensities observed in the obtained SERS spectra did not follow a trend that correlated with the order of the washing cycles, which may indicate that the cleaning solvent also does not affect the gold substrate. However, the spectra in Fig. 8.11B show weak but significant signals from RhB, indicating the cleaning efficiency is not 100%. Gold provides better enhancement at the used wavelength, as a result, an increased RhB response is observed after cleaning compared to silver. In addition, it has been shown that the adsorption of molecules with respect to orientation to binding sites can be different for gold and silver [38–40] and thus may contribute to different enhancement and/or differences in the removal of adsorbed analytes. Fig. 8.11D shows that the cleaning efficiency of 1.5% HCl in MQ is very poor. Clear SERS signals of RhB were observed after aqueous cleaning. We assume analyte protonation only is not sufficient for removing analytes from the substrate, but a polar organic solvent is needed as well.

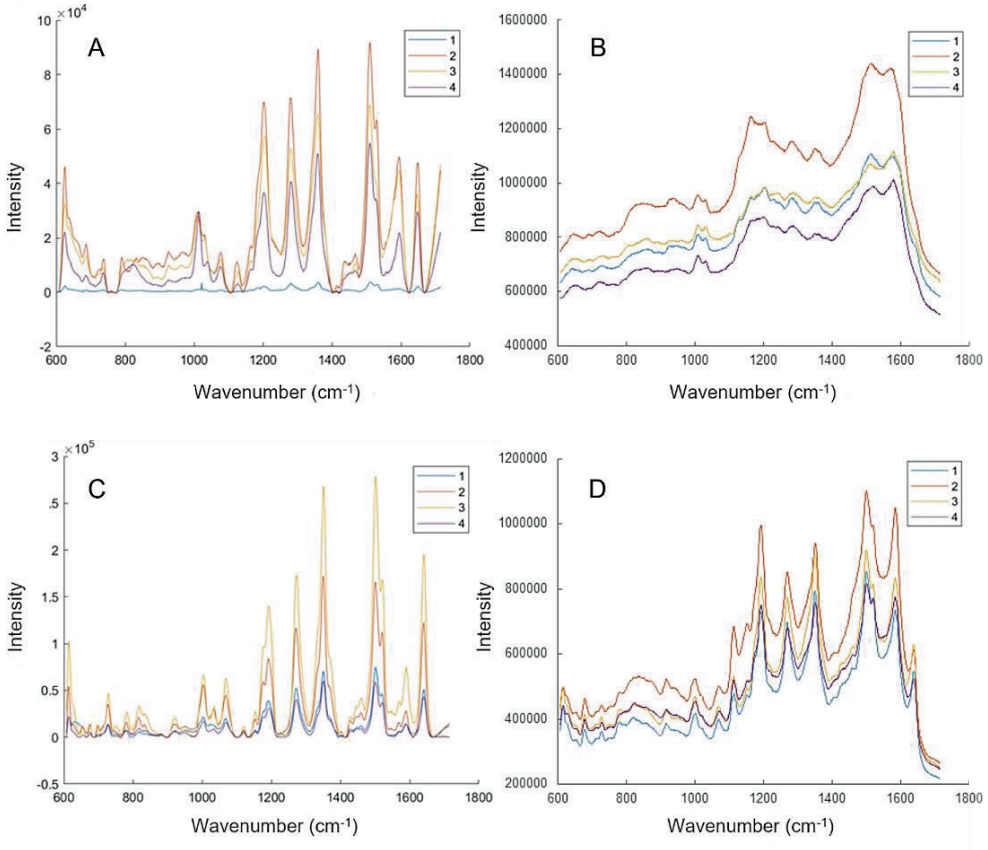


Figure 8.11. SERS spectra of $10^{-5}$ M RhB on the gold substrate before (left) and after (right) every cleaning cycle with 1.5% HCl in MeOH (A, B), and MQ (C, D). Cleaning cycles were performed four times, and the spectrum corresponding to each cycle is numbered 1–4. Each spectrum is the average of five different spots; excitation wavelength, 785 nm.

## 8.4 On-chip SERS monitoring of photodegradation of crystal violet

### 8.4.1 Introduction

Following the characterization and optimization of the leaning pillar chips for the SERS analysis of solutes, a proof-of-principle experiment was conducted where the photodegradation of CV was measured in situ during irradiation. Although the silver substrates were less affected by carry-over (i.e., the memory effect), gold substrates from Silmeco (Copenhagen, Denmark) were used for the purpose of on-chip monitoring of the photodegradation of CV, because gold showed a higher enhancement. For the purpose of monitoring the photodegradation of CV, the golden substrates were used only once in order to prevent cleaning procedures from affecting the results.

### 8.4.2 Experimental

#### Chemicals

Aqueous solutions were prepared using ultrapure deionized water (MQ) (Millipore Simplicity Simpak 2, R = 18.2 MΩ cm, U.S.A.). Methanol (MeOH) (>99%) was purchased from Biosolve (Valkenswaard, The Netherlands). Hydrochloric acid (HCl) (37%) and crystal violet (CV) (>90%) were purchased from Sigma-Aldrich (Steinheim, Germany).

#### Materials and instruments

*SERS substrates*

On-chip SERS analysis and gold-coated leaning pillar chips (Silmeco, Copenhagen, Denmark).

*Microfluidic device*

The microfluidic device (called the 'PI cell') that was used for these photodegradation experiments was developed at the University of Amsterdam. A scheme and cross-section of the device is depicted in Fig. 8.13. It contains a microfluidic channel (7) with a volume of 100 µL, with fluidic in- and outlets (8). The channel contains a rectangular notch (4) where the SERS chip can be inserted to decrease height differences to avoid fluid resistance inside the channel as much as possible. The device is sealed by a circular quartz window (2) and a retainer ring (3) that is wide enough to accommodate a 5x, 20x, or 63x objective for Raman analysis. The 63x objective has a working distance of 5 mm, therefore, the thickness of the quartz window was kept below a maximum of 3 mm to allow ample space for focusing on the SERS chip. For the sealing and protection of the quartz window, two rubber rings were added (5 and 6). For more details on the PI cell, we

refer to Chapter 8 of the thesis of Mimi J. Den Uijl *"Under the Influence of Light – New Chromatographic Tools for Elucidating Photodegradation Mechanisms"*.

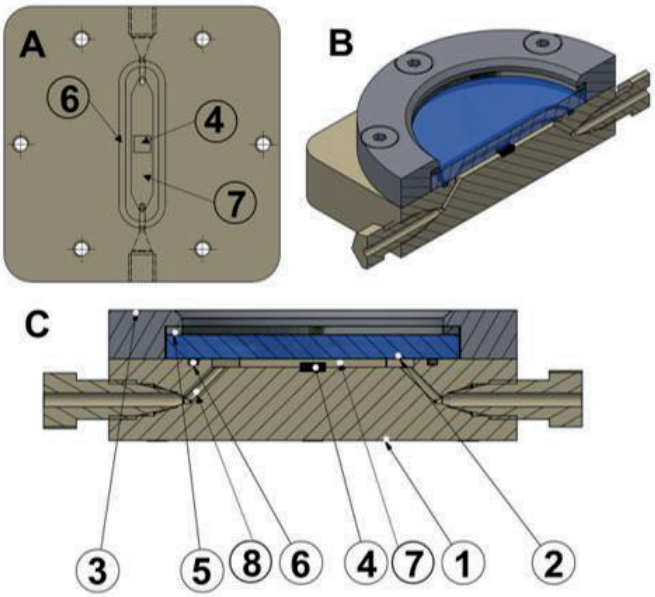


Figure 8.13. Bottom part (A) and cross-sections (B and C) of the PI cell used for photodegradation of CV solutions with in-situ SERS. Components: 1, PEEK bottom part including the microfluidic channel; 2, quartz optical window; 3, retainer ring; 4, SERS substrate; 5 and 6, rubber ring; 7, microfluidic channel of 100 µL; 8, fluidic in- or outlet.

### *Light source photodegradation*

The light source used for the in-cell photodegradation of CV solutions was a high-energy white LED from Thorlabs (MCWHLP1) with a broad emission spectrum between 400-700 nm, and a typical output of 2.35 W.

### *Raman spectrometer*

The Raman microscope described in Section 8.2.2 was used for the acquisition of the results described in this section. The settings for on-chip photodegradation measurements with leaning pillar chips were as follows: objective, 20x; laser, 532 nm; laser power, 10%; exposure time, 0.5 s; accumulations, 40.

### *LC-DAD-QTOFMS*

The LC-DAD system described in Section 8.2.2 was coupled to a QTOFMS instrument (Agilent 6520) for the analysis of irradiated samples. The LC-QTOFMS method for Riboflavin described in Chapter 7 was applied for the analysis of CV and its photodegradation products. The settings of the ESI source were as follows: gas

temperature, 300 °C; drying gas, 5 L $min^{-1}$; nebulizer gas, 35 psig; capillary voltage, 3500 V. The Q-TOF settings for the analysis of RF were as follows: fragmentor, 100 V; skimmer, 75 V; octupole 1 RF Vpp, 200 V.

**Methods**

*On–chip SERS monitoring of photodegradation crystal violet*

Similarly to the degradation experiment performed inside the LCW-based light cell, a 10-mg $L^{-1}$ aqueous solution of CV was irradiated inside the PI cell containing a gold-coated leaning pillar chip. The LED light source was fixed above the device using mounts and a lab stand. The sample was irradiated for 2 and 48 hrs and in-situ SERS measurements were performed at every 0.5 to 1 hr. To assess whether the SERS substrate influences the photodegradation process, the experiment was repeated without a SERS chip in the device. This was done by off-line measuring a droplet of sample on a leaning pillar chip before irradiation, and after 2 hrs of irradiation the sample was reclaimed from the PI cell and measured in the same way. For each sample or measurement, the spectra of five different spots were recorded and averaged. Data processing was done in MATLAB R2020b using the background correction method by Mazet. For identification of the photodegradation products the irradiated samples were analyzed by LC-DAD-QTOFMS.

## 8.4.3 Results and discussion

**Photodegradation of crystal violet**

The irradiation of CV inside the microfluidic device was conducted for 2 and 48 hrs, while measuring the SERS spectrum every 30 min (Fig. 8.14). Afterward, the samples were measured by LC-DAD-QTOFMS, of which the results are presented in Fig. 8.15. LC-DAD chromatograms are shown in Appendix F as Fig. F-1 and identified compounds by LC-MS are shown in Table F-1.

The SERS spectra measured during irradiation for both 2 and 48 hrs show a decrease in intensity and a change in the relative peak ratios, indicating that photodegradation of CV takes place and molecular changes occur. The spectral changes are in line with those observed for the SERS spectra measured of the isolated photodegradation products of CV (Fig. 8.7). As can be expected, the changes in relative peak intensities are less pronounced, since the in-situ measured spectra originate from a mixture of compounds representing the convoluted spectra of all components. From the SERS spectra, it seems that the change in the ratio between the peaks around 1580 and 1620 $cm^{-1}$ is much smaller, which would indicate that CV is still the predominant component. Analysis by LC-DAD-QTOFMS revealed that this was indeed true for the 2-hr irradiated sample, and

that from the parent compound CV, only about 8% was left and that it was virtually diminished from the 48-hr irradiated sample.

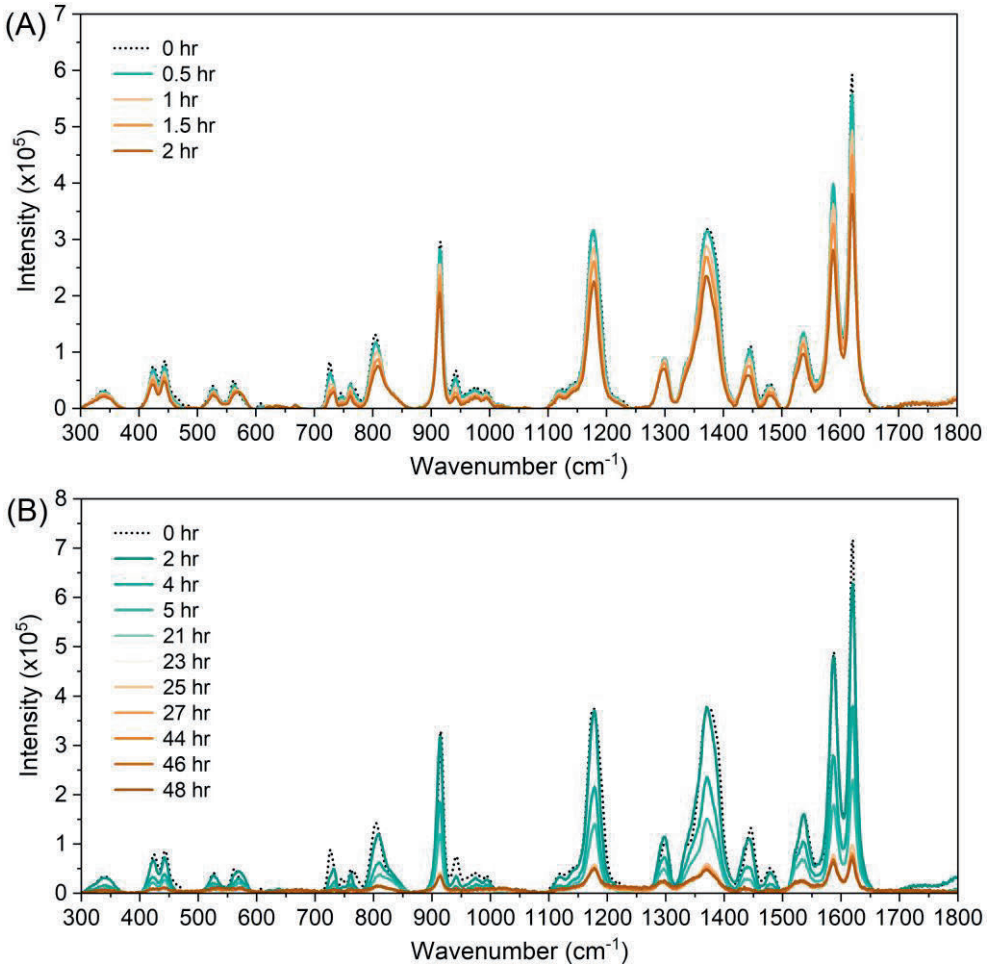


Figure 8.14. SERS spectra measured of CV samples during irradiation for (A) 2 and (B) 48 hrs inside the microfluidic device (PI cell). For each condition, five SERS spectra were recorded at different spots and averaged.

We believe that the small changes in the shape of the SERS spectra can be attributed to the fact that the overall sample composition does not change much in the first 2 hrs, as each product degrades further at comparable rates. The fact that the 48-hr irradiated sample still shows a spectrum that is very similar to that of CV may be because of the formation of high concentrations of colorless compounds that, at the same time, are less efficient Raman scatterers. Next to demethylated CV products, Michler's ketone (MK) and demethylated MK (MK-1Me) were found in the samples, which both absorb in the UV

region and, therefore, are colorless. Also, an unknown product with m/z 187.127 and absorbance below 280 nm was found at significant abundance in both samples, being most prominent in the 48-hrs irradiated sample. The absorbance spectrum as measured by LC-DAD is included in Appendix F (Fig. F-2). A photodegradation product of CV with this specific mass has not been reported in the literature, so for now we can only speculate about its identity and if the PI cell material played a role in its formation.

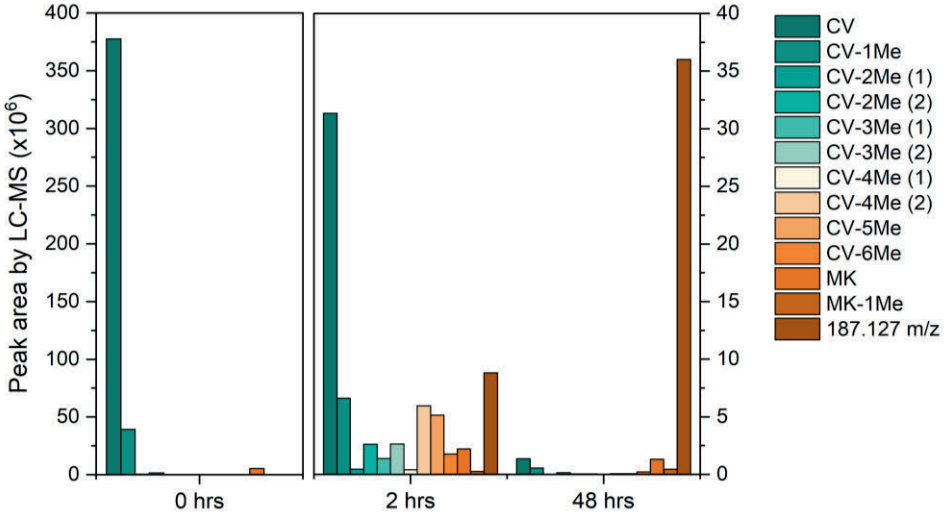


Figure 8.15. LC–MS peak areas obtained for the CV sample irradiated before (0 hrs) and after 2 and 48 hrs of irradiation in the microfluidic device (PI cell).



There are potentially other explanations for the small changes observed in the Raman shifts after irradiation. The formed degradation products may not adsorb as well to the SERS substrate as the parent compound. This idea would be in line with the observed decrease in SERS signal intensity as the concentration of CV decreased while photodegradation products increased over time. Furthermore, it may be that the lifetime of the excited state of adsorbed compounds is quenched by the gold layer, resulting in a decreased occurrence of chemical reactions. This would lead to a decreased photodegradation for those compounds, therefore, leading to smaller changes in the SERS spectrum, while compounds that are not adsorbed degrade faster, hence the low concentrations of CV determined by LC-MS after irradiation. To determine whether these statements are true, a comparison should be made with photodegradation in the absence of the substrate.

### Effect of gold SERS substrate on photodegradation

The gold layer on the leaning pillar chips may potentially influence the photodegradation or the way the analyte is effectively irradiated. The photodegradation of CV was, therefore, also performed inside the microfluidic device without the leaning pillar chip present (Fig 8.16C and D). In the absence of the substrate inside the PI cell, SERS spectra were recorded off-line using a chip before irradiation, and after irradiation by reclaiming the sample from the PI cell after 2 hrs (Fig. 8.17). Afterward, the samples were analyzed by LC-DAD-QTOFMS (Fig. 8.18) of which the LC-DAD chromatogram is shown in Fig. F-3.

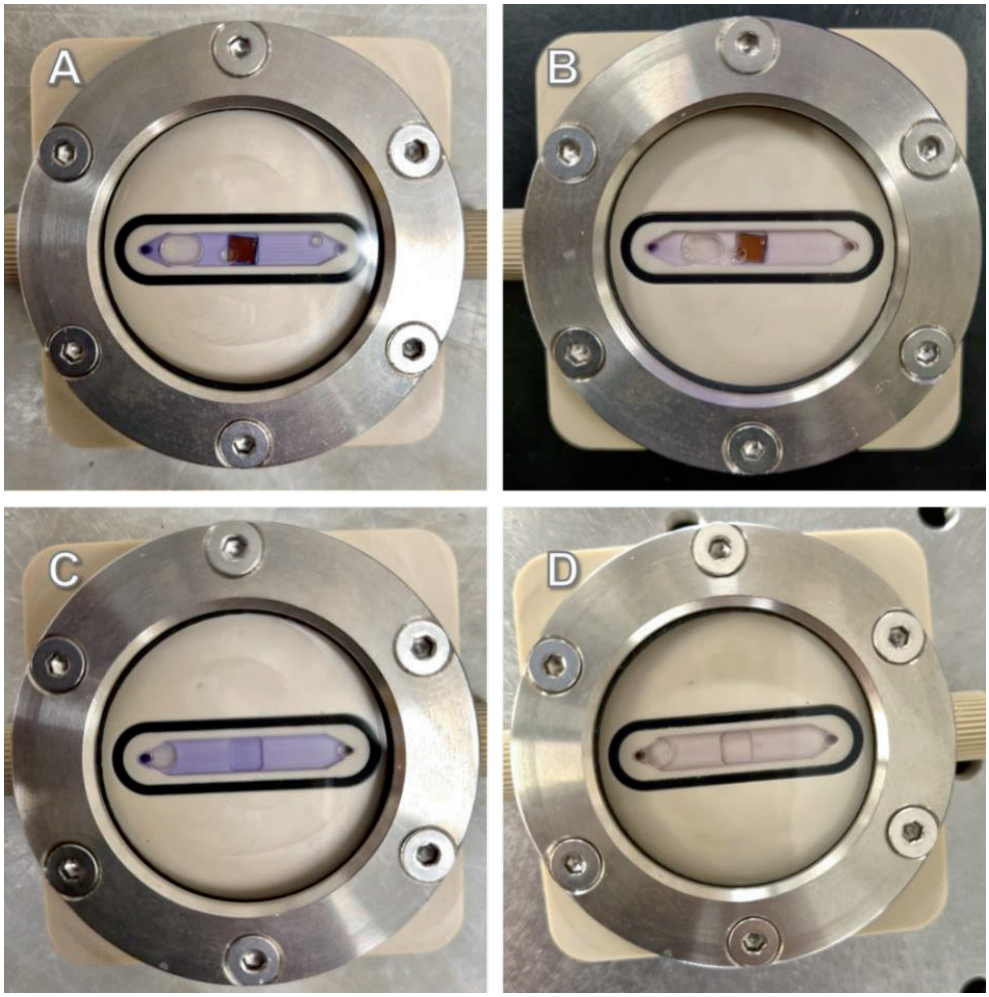


Figure 8.16. Solutions of CV in the microfluidic device (A) before and (B) after irradiation of 2 hrs with a leaning pillar chip installed, and (C) before and (D) after irradiation without a leaning pillar chip installed.

The SERS spectra (Fig. 8.17) obtained for the samples with and without the chip present in the PI cell during irradiation look very similar. For reference, the spectrum of CV is added. While the purple color has almost completely vanished after 2 hrs of irradiation (Fig. 8.16), only a small difference can be observed between the peak ratios of 1580 and 1620 $cm^{-1}$. LC-MS analysis showed that, although the concentration of CV decreased rapidly after 2 hrs, it was still the predominant compound in both samples (Fig. 8.18), and the spectrum of the mixture, therefore, shows high similarity to that of CV.

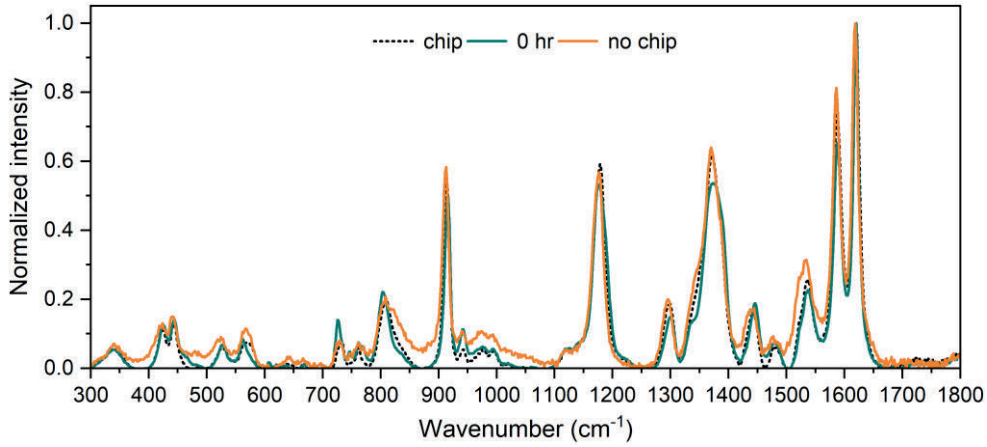


Figure 8.17. Normalized SERS spectra of CV measured after 2 hrs of irradiation with and without the presence of a gold leaning pillar chip.



The change in the ratio between the peaks at 1580 and 1620 $cm^{-1}$ is slightly larger for the sample without the chip, probably indicating a slightly faster degradation. The peak ratios as determined by LC-MS in Fig. 8.18 show differences that possibly confirm an increased degradation of the main compound in absence of the chip. The peak ratios of the degradation products CV-3Me, CV-4Me, CV-5Me, and CV-6Me are all higher in absence of the chip. In addition to the possible effects that the SERS substrate may have on the measured spectra, it may also affect the photodegradation rate in other ways. Besides the earlier-mentioned effect of quenching by the gold coating, the dark SERS substrate may absorb a part of the light that then cannot be absorbed by the dye molecules, decreasing the photodegradation rate. Also, molecules may be 'less accessible' to absorb photons when they are trapped in between the leaning pillars.

The area of the chip covers roughly 13% of the total area of the microfluidic channel. Considering that the observed differences are caused by a relatively small area, it must be considered that the SERS substrate may have a bigger influence on the photodegradation than initially expected. Since no duplicates were performed, we are unable to determine whether these deviations may be within the standard error of the

overall photodegradation experiment and measurements. Therefore, further research is needed.

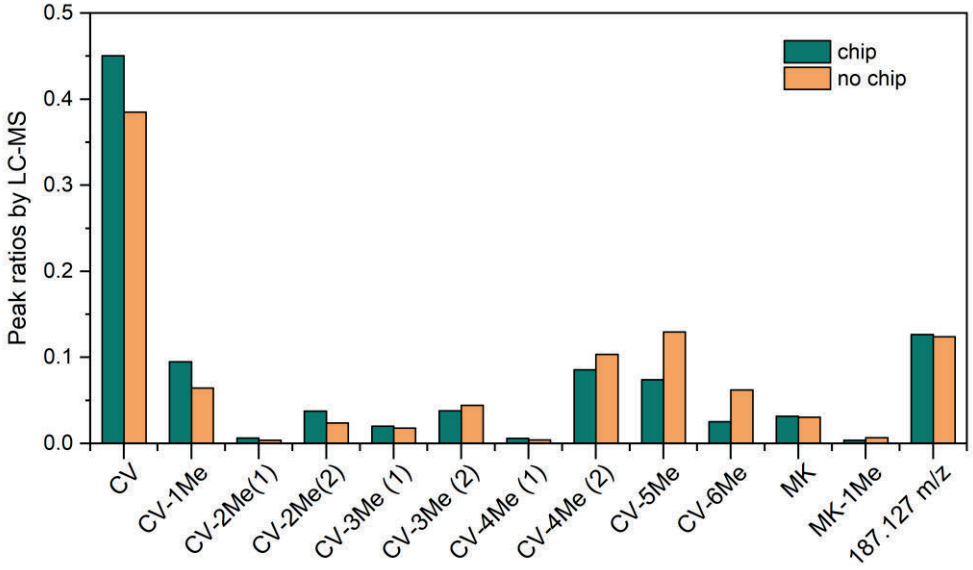


Figure 8.18. LC-MS peak ratios of CV photodegraded for 2 hrs with and without gold leaning pillar chip in the microfluidic device (n=1).

## 8.5 Carbon paper as a gas-permeable SERS substrate

### 8.5.1 Introduction

The effect of oxygen on photodegradation is known to be important, as also illustrated in Chapters 2 and 7. Using the LCW-based LID cell, it is possible to introduce and remove oxygen from the sample to efficiently study this effect. The results in Section 8.4 have shown that the PI cell shows potential for in-situ SERS analysis. However, it is not yet possible to effectively add or remove gases from the PI cell. The introduction of gases, such as oxygen or nitrogen, in a microfluidic device in principle could be established by adding a diffusive layer to the design, which creates a barrier between the microfluidic channel on one side and a compartment for gas on the other. The first steps for creating such a barrier were taken using carbon paper (CP) coated with a hydrophobic PTFE layer. CP is a flat and porous material made of pressed carbon fibers and is used as a gas-diffusive layer (GDL) in, e.g., proton exchange membrane (PEM) fuel cells [38–41]. A scanning electron microscopy (SEM) image of CP coated with PTFE is given in Fig. 8.19, clearly showing the porosity of the material.

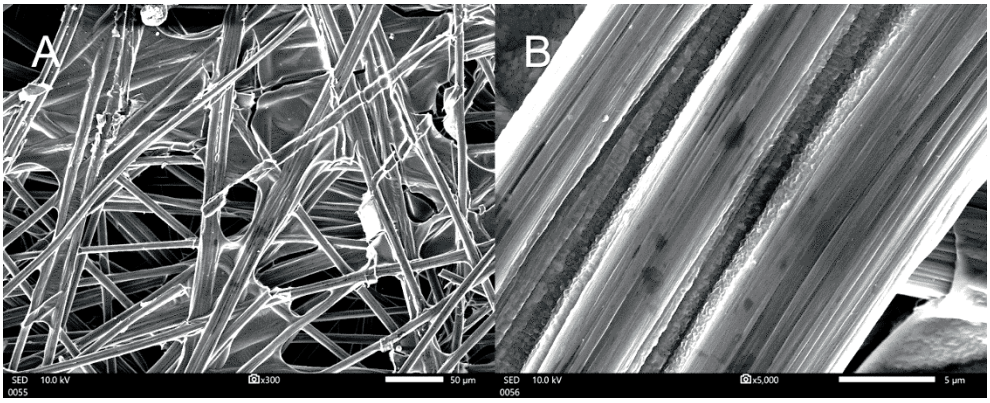


Figure 8.19. SEM images of carbon paper with a hydrophobic layer of PTFE. (A) 300x magnification shows the porous structure of the carbon paper. (B) 5,000x magnification shows the structure of three carbon fibers. Scale bars: left 50 µm; right 5 µm. Credit: Ineke Joosten, Cultural Heritage Agency of The Netherlands.

In PEM fuel cells, the GDL is embedded between the catalyst layer and the gas flow channel and functions as a gas diffuser, a current collector, and physical support between the water and gas channels [41]. CP is widely used due to its high gas permeability and electronic conductivity. The porous characteristic is especially of interest for implementation as a GDL in the developed microfluidic device. Additionally, the CP could be used as a substrate for SERS active NPs, as CP is known to be a suitable

support for coating with metal nanoparticles (NPs) and has even been used for the production of SERS substrates [42–45].

Several applications have been presented where CP or carbon cloth was used to fabricate SERS substrates. Examples of such applications include the analysis of pesticides in droplets [45] and on vegetables or fruit [46], and for virus detection [47]. Lu et al. [45] prepared SERS substrates by depositing silver nanodendrites (NDs) on carbon cloth by electrochemical deposition. They reached a detection limit of $10^{-10}$ M for CV and demonstrated the use of the substrate for the detection of several pesticides in lake water. They found that the cylinder shape of the carbon fiber provides a three-dimensional structure for the silver NDs, which increases the hot-spot effect. Tran et al. [47] presented a SERS-active substrate based on porous carbon films with silver NPs and were able to reach an even lower detection limit for CV: $10^{-14}$ M. The SERS substrate was then used for the label-free detection of animal viruses.

Electrochemical deposition of silver on CP can be achieved in a two-electrode system where the CP substrate is attached to the cathode and a carbon rod is attached to the anode [45]. This is placed in a solution containing silver ions and the applied voltage results in the precipitation of silver particles which are deposited on the cathode. A second deposition method can be found in the silver mirror reaction (SMR) [48,49]. The SMR is a redox reaction, which results in the formation of a silver layer on a substrate after silver ions in an ammonia solution (Tollen's reagent) are reduced by glucose. Using this reaction, Verma et al. [50] were able to deposit silver NPs on paper filters and use these as low-cost SERS sensors for the detection of food adulteration.

VSPARTICLE (Delft, the Netherlands) is a company that specializes in the production of instruments for the generation of metallic NPs. The VSP-P1 NanoPrinter is one of their latest developments for the production of nanoporous thin films and layers with a high surface-to-volume ratio. This is important for a good-performing SERS substrate as a high surface-to-volume ratio will increase the chance of inducing and measuring a SERS signal. 3D printing is established by guiding NPs with a stream of inert gas through a nozzle (Fig. 8.20), which can move in X-Y-Z directions to create layers of nanoporous materials on a substrate.

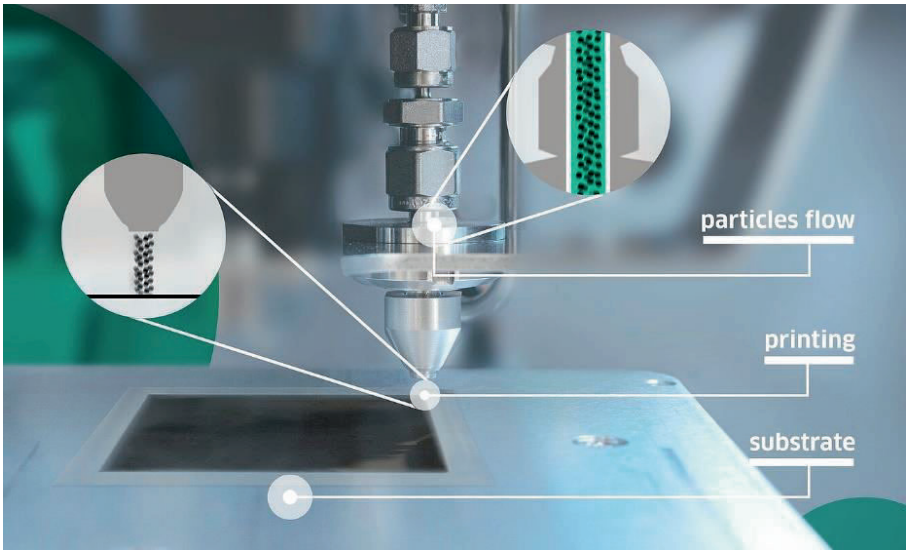


Figure 8.20. The 3D printing nozzle of the VSP-P1 NanoPrinter used for printing a porous material on a substrate [51].

## 8.5.2 Experimental

### Chemicals

Aqueous solutions were prepared using ultrapure deionized water (MQ) (Millipore Simplicity Simpak 2, R = 18.2 MΩ cm, U.S.A.). Methanol (MeOH, >99%) was purchased from Biosolve (Valkenswaard, The Netherlands). Rhodamine B (>97%), sodium hydroxide (NaOH, >98%), silver nitrate ($AgNO_3$, 99.9%), and glucose (99.5%) were purchased from Sigma-Aldrich (Steinheim, Germany).

### Materials and instruments

*Carbon paper*

Carbon paper coated with a layer of hydrophobic Teflon (TGP-H-060) was purchased from Toray (Tokyo, Japan). A 55°C and ice water bath were used for temperature control.

*Scanning Electron Microscope (SEM)*

SEM analyses were run on a JEOL JSM-IT700HR scanning electron microscope with a JED-2300-Fully integrated JEOL EDS system (100 $mm^2$ SDD). The SEM was operated in low vacuum mode at a chamber pressure of 30 Pa, with an operating voltage of 20 kV, and a working distance of 10 mm. The cross-section was not coated prior to analysis. The applied accelerating voltage was 10 kV. SEM analyses were conducted for both the SMR and 3D printing treatment to obtain information about the density of silver and gold NPs on the substrate.

*Raman spectrometer*

SERS analyses were performed on the inVia Renishaw Raman microscope as described in Section 8.2.2. SERS spectra were measured at 785 nm excitation, using the 20x objective; conditions: laser power, 100%; exposure time, 10 s; 3 accumulations. Aqueous solutions of 50 mg $L^{-1}$ RhB were used as test samples.

**Methods**

*Silver Mirror Reaction*

The procedure was performed according to Cheng et al. [48,49]. First, a small CP sheet was cleaned with MeOH, followed by MQ. Tollen's reagent was prepared in a beaker placed in an ice water bath. In the beaker, 50 µL of 1 M NaOH and 5 mL of 50 mM $AgNO_3$ were combined, and several droplets of 300 mM ammonia were added to obtain a clear solution. The CP sheet was immersed in the reagent and after 5 min 1.5 mL of the reducing agent (500 mM glucose) was added under continuous stirring (Fig. 8.20A). Then, the beaker was moved to a 55°C water bath. After 10 min, the treated CP was cleaned thoroughly with MQ and MeOH consecutively and left to air-dry afterward.

*3D–printing*

Gold NPs were 3D printed on a CP sheet by VSPARTICLE. This was performed on-site printing a 5x5-mm square of 1 µm and 2 µm thickness of gold NPs on CP (Fig. 8.20B).

## 8.5.3 Results and discussion

Coating of CP with silver was attempted through the SMR (Fig. 8.21A), and with gold by 3D printing of NPs by VSPARTICLE (Fig. 8.21B).

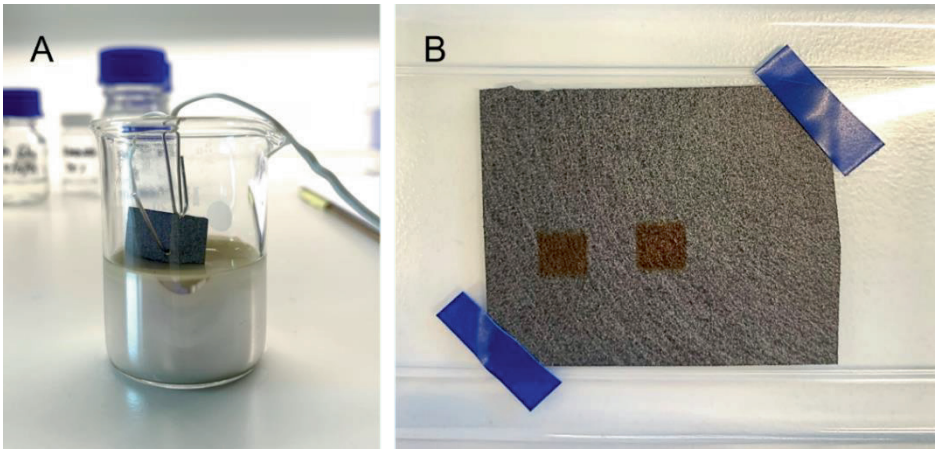


Figure 8.21. (A) Carbon paper undergoing the silver mirror reaction, (B) 1–µm (left) and 2–µm (right) layers of gold NPs 3D printed by VSPARTICLE on carbon paper.

### SEM analysis

SEM images were made of the SMR and 3D-printing coated CP, as shown in Fig. 8.22 and 8.23, respectively. When comparing these figures it is clear that, although successful in coating, the SMR was much less efficient compared to 3D printing. The SMR resulted in fewer particles on the CP fibers, and the particle size was also highly irregular and relatively large when compared to the 3D printing method. As the size and shape of silver NPs are related to the SERS intensity of adsorbates [18] it is important to be able to generate NPs of equal shape and size to increase sensitivity and repeatability. The 3D printing approach appeared more efficient in this respect. However, the 3D-printed gold NP microlayer was observed to crack and release at several places (Fig. 8.23B and C). This most likely happened as a result of substrate handling. It suggests that the layer is fragile and the CP may need a pre-treatment before printing of NPs.

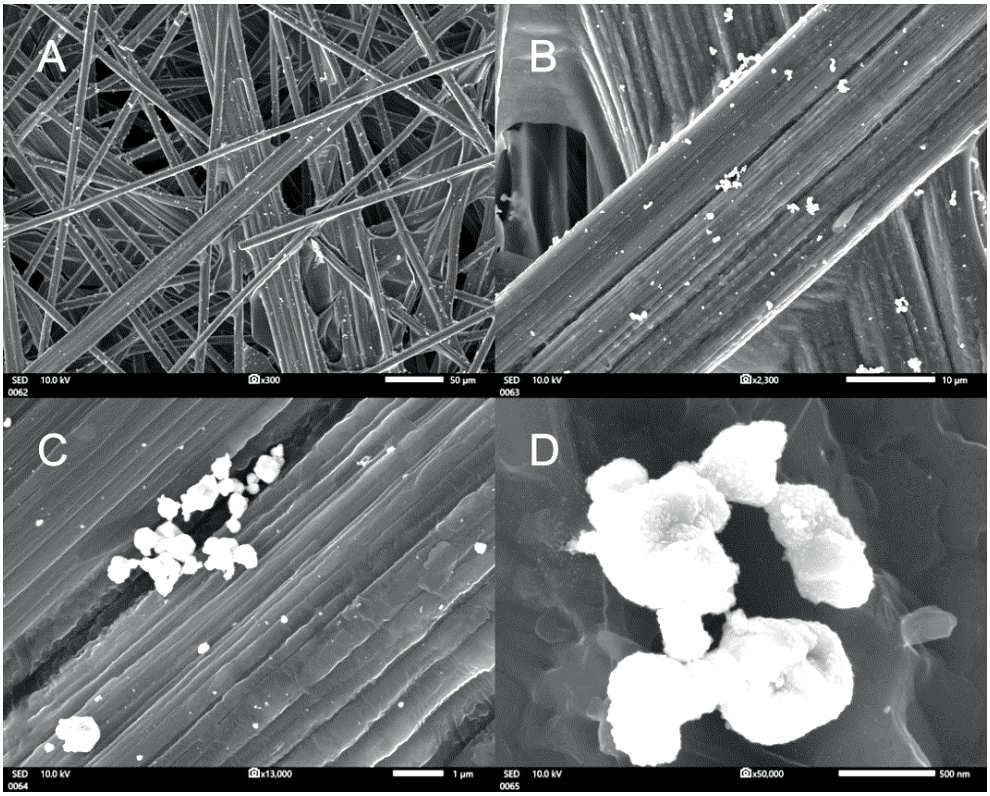


Figure 8.22. SEM pictures of carbon paper treated with the silver mirror reaction. Magnification: (A) 300x, (B) 2,300x, (C) 13,000x, (D) 50,000x. Scale bars: 50 µm, 10 µm, 1 µm, 500 nm, respectively. Credit: Ineke Joosten, Cultural Heritage Agency of The Netherlands.

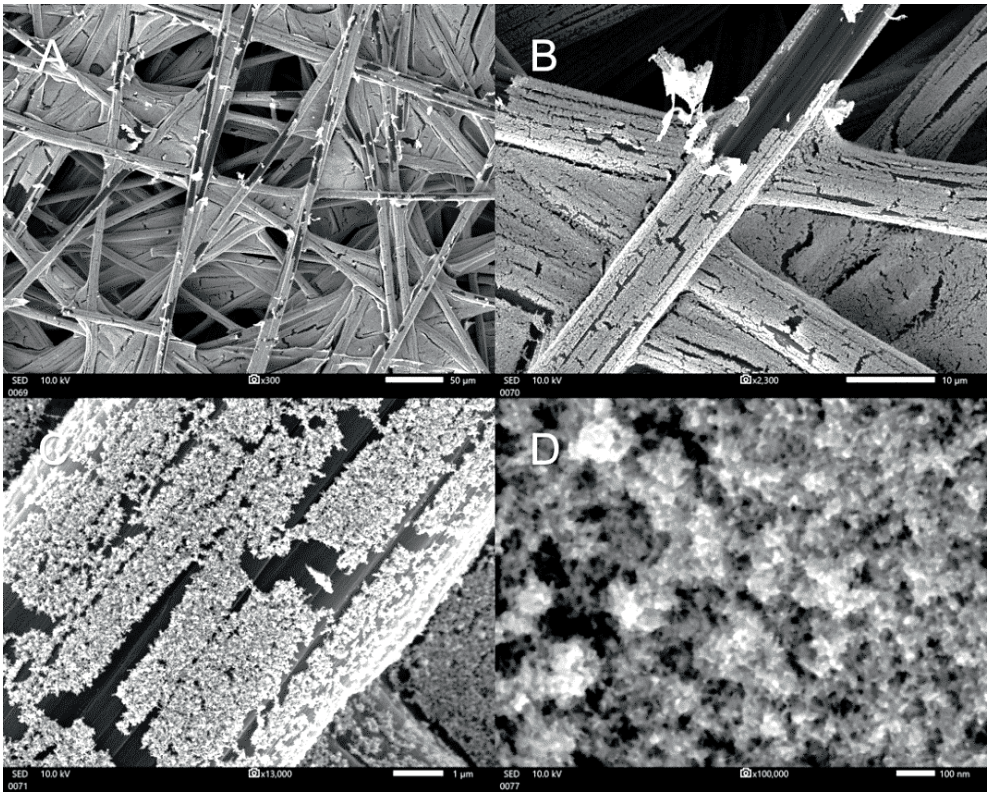


Figure 8.23. SEM pictures of carbon paper with a 1 µm layer of 3D-printed gold NPs. Magnification: (A) 300x, (B) 2,300x, (C) 13,000x, (D) 100,000x. Scale bars: 50 µm, 10 µm, 1 µm, 100 nm, respectively. Credit: Ineke Joosten, Cultural Heritage Agency of The Netherlands.

### SERS analysis

Attempts were made to record SERS spectra using the coated CP sheets. Only on the substrates prepared with 3D printing, SERS spectra were obtained under the conditions used. On the SMR-coated CP surface, only a broad emission band was observed (data not shown). Probably, the coating density and silver particles' size and shape on the SMR-coated surface are insufficient (Fig 8.22).

The samples were measured before drying, as to simulate the situation as it would be inside the microfluidic device, and after drying. A background correction was not conducted to show the performance of the substrates without manipulation of the data. Interestingly, for the 3D-printed substrates, the SERS spectrum is slightly more intense and better resolved when the sample is measured as a liquid droplet. Similar to what was observed for the leaning pillar chips in Fig. 8.8, the spectrum of the dried sample represents a more intense peak at 1122 $cm^{-1}$ and lacks a peak at 1655 $cm^{-1}$. Since these differences occur for both the leaning pillar as well as for the 3D-printed substrates, it is

suspected that the peaks occur due to the influence of the solvent. Compared to the 1-µm layer, the 2-µm layer presents a slightly increased signal intensity, which could be attributed to a higher density of gold NPs. However, this may be non-significant as no duplicates were prepared.

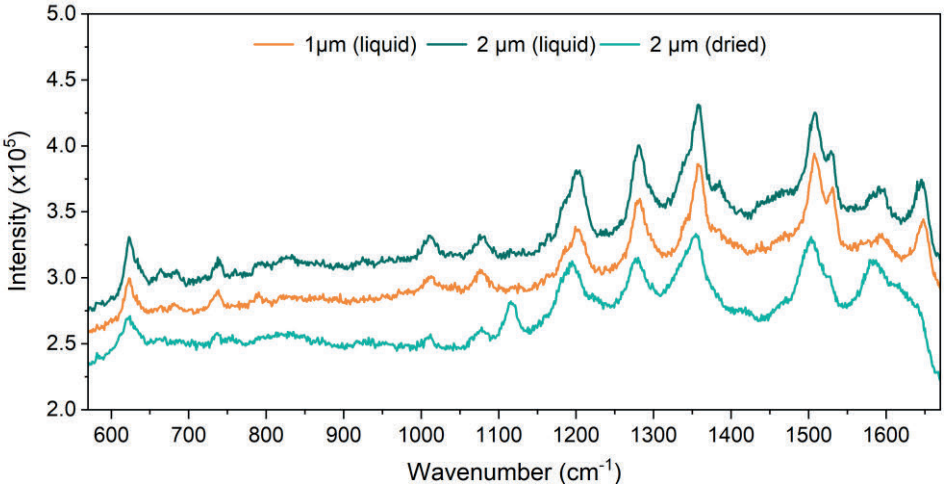


Figure 8.24. SERS spectra of 50 mg $L^{-1}$ RhB measured on CP with 3D printed gold NPs on a layer thickness of 1 µm (yellow) and 2 µm (red) before drying, and 2 µm (purple) after drying.

## 8.6 Conclusions

This chapter provided the results from a collection of exploratory experiments to study the feasibility of RS and SERS for monitoring photodegradation in situ in real-time to provide information on structural chemical changes during irradiation.

Good-quality SERS spectra of isolated photodegradation products from CV after LC-DAD analysis with silver colloids could be obtained. Different SERS spectra for CV and each of its degradation products were observed, even for the two isomers of bis-demethylated CV. As discussed in Section 8.3, leaning pillar chips were characterized as a solution for in-situ and real-time monitoring of photodegradation processes. It was shown that the SERS spectra obtained from RhB in solution were not much different from dried sample spots of RhB, indicating that these substrates are compatible with microfluidics. To limit or reduce the memory effect (carry-over) often related to SERS substrates, we tried to establish a cleaning procedure and found that cleaning with 1.5% HCl in MeOH was the most optimal. However, we do believe that this does not adequately solve the issue of sample carry-over, and more research is needed to obtain a clear view of the reusability of the leaning pillar chips.

Although promising results were obtained with the analysis of solutions using the leaning pillar substrates, they resulted in some confusion regarding the monitoring of the photodegradation of CV. The changes observed in the SERS spectra were roughly in line with the final sample composition after irradiation as measured by LC-MS. It is suspected that the leaning pillar chips influence the photodegradation process, and also may be unable to represent the complete sample mixture due to differences in adsorption between the parent and degradation molecules.

The deposition of silver or gold NPs on CP could be a solution for implementing gas permeability in a microfluidic device for studying the effect of oxygen on photodegradation mechanisms. Clearly, we have only slightly touched upon what is needed for establishing this. The results are promising with regards to the 3D printed substrates; however, more work is required for realizing a gas-permeable microfluidic device allowing in-situ SERS monitoring.

It is clear that the presented results are far from conclusive and raise a number of questions. However, the fact that the photodegradation of CV obtained in the PI cell shows a similar pattern as compared to that obtained inside the LCW is promising. The possibility of simultaneously monitoring the sample by means of SERS shows that the concept is feasible. Some experiments were conducted only once, and therefore, repeats are needed to be able to draw more final conclusions. The results of these exploratory

experiments also illustrate the challenges that we are still facing with implementing SERS as a repeatable detection approach in microfluidic devices.

**Acknowledgments**

We would like to thank several people for contributing to the work presented in this Chapter. First and foremost, Niels Muntjewerf, Lotte van Leuken, and Esther de Graaff for conducting the experiments and SERS analysis described in Sections 8.2, 8.3, and 8.4, respectively. Jasper Smeets and Mimi den Uijl are acknowledged for the development of the PI cell. We would like to thank Ineke Joosten for her help with the SEM analyses, and VSPARTICLE for the donation of the gold-coated carbon paper substrates.

# References

[1] G.L. Johnson, R.M. Machado, K.G. Freidl, M.L. Achenbach, P.J. Clark, S.K. Reidy, Evaluation of Raman spectroscopy for determining cis and trans isomers in partially hydrogenated soybean oil, Org Process Res Dev. 6 (2002) 637–644. https://doi.org/10.1021/op0202080.

[2] C. Krafft, E. Pigorsch, B. Weber, F. Ott, S. Brennecke, G.E. Krammer, R. Salzer, Determination of configurational isomers in cyclic polysulfides by Raman spectroscopy, Vib Spectrosc. 43 (2007) 49–52. https://doi.org/10.1016/J.VIBSPEC.2006.06.009.

[3] A. Gutiérrez-Quintanilla, R. Platakyte, M. Chevalier, C. Crépin, J. Ceponkus, Hidden Isomer of Trifluoroacetylacetone Revealed by Matrix Isolation Infrared and Raman Spectroscopy, Journal of Physical Chemistry A. 125 (2021) 2249–2266. https://doi.org/10.1021/acs.jpca.0c10945.

[4] P.L. Stiles, J.A. Dieringer, N.C. Shah, R.P. van Duyne, Surface-Enhanced Raman Spectroscopy, Annual Review of Analytical Chemistry. 1 (2008) 601–626. https://doi.org/10.1146/annurev.anchem.1.031207.112814.

[5] I. Osticioli, A. Zoppi, E.M. Castellucci, Fluorescence and Raman spectra on painting materials: reconstruction of spectra with mathematical methods, Journal of Raman Spectroscopy. 37 (2006) 974–980. https://doi.org/10.1002/JRS.1587.

[6] E.C. le Ru, E. Blackie, M. Meyer, P.G. Etchegoint, Surface enhanced raman scattering enhancement factors: A comprehensive study, Journal of Physical Chemistry C. 111 (2007) 13794–13803. https://doi.org/10.1021/jp0687908.

[7] S.Y. Ding, E.M. You, Z.Q. Tian, M. Moskovits, Electromagnetic theories of surface-enhanced Raman spectroscopy, Chem Soc Rev. 46 (2017) 4042–4076. https://doi.org/10.1039/C7CS00238F.

[8] S.K. Gahlaut, D. Savargaonkar, C. Sharan, S. Yadav, P. Mishra, J.P. Singh, SERS Platform for Dengue Diagnosis from Clinical Samples Employing a Hand Held Raman Spectrometer, Anal Chem. 92 (2020) 2527–2534. https://doi.org/10.1021/acs.analchem.9b04129.

[9] R.J. Dijkstra, A.N. Bader, G.P. Hoornweg, U.A.T. Brinkman, C. Gooijer, On-Line Coupling of Column Liquid Chromatography and Raman Spectroscopy Using a Liquid Core Waveguide, Anal Chem. 71 (1999) 4575–4579. https://doi.org/10.1021/ac9902648.

[10] R.J. Dijkstra, C.J. Slooten, A. Stortelder, J.B. Buijs, F. Ariese, U.A.Th. Brinkman, C. Gooijer, Liquid-core waveguide technology for coupling column liquid chromatography and Raman spectroscopy, J Chromatogr A. 918 (2001) 25–36. https://doi.org/10.1016/S0021-9673(01)00721-X.

[11] Y.S. Huh, A.J. Chung, B. Cordovez, D. Erickson, Enhanced on-chip SERS based biomolecular detection using electrokinetically active microwells, Lab Chip. 9 (2009) 433. https://doi.org/10.1039/B809702J.

[12] Q. Zhou, G. Meng, P. Zheng, S. Cushing, N. Wu, Q. Huang, C. Zhu, Z. Zhang, Z. Wang, A Surface-Enhanced Raman Scattering Sensor Integrated with Battery-Controlled Fluidic Device for Capture and Detection of Trace Small Molecules, Scientific Reports 2015 5:1. 5 (2015) 1–11. https://doi.org/10.1038/srep12865.

[13] J. Jeon, N. Choi, H. Chen, J. il Moon, L. Chen, J. Choo, SERS-based droplet microfluidics for high-throughput gradient analysis, Lab Chip. 19 (2019) 674–681. https://doi.org/10.1039/C8LC01180J.

[14] X. Zhang, H. Zhang, S. Yan, Z. Zeng, A. Huang, A. Liu, Y. Yuan, Y. Huang, Organic Molecule Detection Based on SERS in Microfluidics, Scientific Reports 2019 9:1. 9 (2019) 1–7. https://doi.org/10.1038/s41598-019-53478-7.

[15] D.R. Hermann, D. Lilek, C. Daffert, I. Fritz, S. Weinberger, V. Rumpler, B. Herbinger, K. Prohaska, In situ based surface-enhanced Raman spectroscopy (SERS) for the fast and reproducible identification of PHB producers in cyanobacterial cultures, Analyst. 145 (2020) 5242–5251. https://doi.org/10.1039/D0AN00969E.

[16] K. Yang, S. Zong, Y. Zhang, Z. Qian, Y. Liu, K. Zhu, L. Li, N. Li, Z. Wang, Y. Cui, Array-Assisted SERS Microfluidic Chips for Highly Sensitive and Multiplex Gas Sensing, ACS Appl Mater Interfaces. 12 (2020) 1395–1403. https://doi.org/10.1021/acsami.9b19358.

[17] Y. Liu, R. Gao, Y. Zhuo, Y. Wang, H. Jia, X. Chen, Y. Lu, D. Zhang, L. Yu, Rapid simultaneous SERS detection of dual myocardial biomarkers on single-track finger-pump microfluidic chip, Anal Chim Acta. 1239 (2023) 340673. https://doi.org/10.1016/J.ACA.2022.340673.

[18] K.G. Stamplecoskie, J.C. Scaiano, V.S. Tiwari, H. Anis, Optimal size of silver nanoparticles for surface-enhanced raman spectroscopy, Journal of Physical Chemistry C. 115 (2011) 1403–1409. https://doi.org/10.1021/jp106666t.

[19] H. Pu, W. Xiao, D.W. Sun, SERS-microfluidic systems: A potential platform for rapid analysis of food contaminants, Trends Food Sci Technol. 70 (2017) 114–126. https://doi.org/10.1016/J.TIFS.2017.10.001.

[20] J. Guo, F. Zeng, J. Guo, X. Ma, Preparation and application of microfluidic SERS substrate: Challenges and future perspectives, J Mater Sci Technol. 37 (2020) 96–103. https://doi.org/10.1016/J.JMST.2019.06.018.

[21] R. Panneerselvam, H. Sadat, E.M. Höhn, A. Das, H. Noothalapati, D. Belder, Microfluidics and surface-enhanced Raman spectroscopy, a win–win combination?, Lab Chip. 22 (2022) 665–682. https://doi.org/10.1039/D1LC01097B.

[22] A. Cesaratto, J.R. Lombardi, M. Leona, Tracking photo-degradation of triarylmethane dyes with surface-enhanced Raman spectroscopy, Journal of Raman Spectroscopy. 48 (2017) 418–424. https://doi.org/10.1002/jrs.5056.

[23] P.C. Lee, D. Meisel, Adsorption and surface-enhanced Raman of dyes on silver and gold sols, Journal of Physical Chemistry. 86 (1982) 3391–3395. https://doi.org/10.1021/j100214a025.

[24] C.C. Chen, H.J. Liao, C.Y. Cheng, C.Y. Yen, Y.C. Chung, Biodegradation of crystal violet by Pseudomonas putida, Biotechnol Lett. 29 (2007) 391–396. https://doi.org/10.1007/s10529-006-9265-6.

[25] M.S. Schmidt, J. Hübner, A. Boisen, Large Area Fabrication of Leaning Silicon Nanopillars for Surface Enhanced Raman Spectroscopy, Advanced Materials. 24 (2012) OP11–OP18. https://doi.org/10.1002/ADMA.201103496.

[26] G. Ochoa-Vazquez, B. Kharisov, A. Arizmendi-Morquecho, A. Cario, C. Aymonier, S. Marre, I. Lopez, Microfluidics and Surface-Enhanced Raman Spectroscopy: A Perfect Match for New Analytical Tools, IEEE Trans Nanobioscience. 18 (2019) 558–566. https://doi.org/10.1109/TNB.2019.2943078.

[27] O. Durucan, T. Rindzevicius, M.S. Schmidt, M. Matteucci, A. Boisen, Nanopillar Filters for Surface-Enhanced Raman Spectroscopy, ACS Sens. 2 (2017) 1400–1404. https://doi.org/10.1021/ACSSENSORS.7B00499.

[28] O. Durucan, K. Wu, M. Viehrig, T. Rindzevicius, A. Boisen, Nanopillar-Assisted SERS Chromatography, ACS Sens. 3 (2018) 2592–2598. https://doi.org/10.1021/ACSSENSORS.8B00887.

[29] Z. Lao, Y. Zheng, Y. Dai, Y. Hu, J. Ni, S. Ji, Z. Cai, Z.J. Smith, J. Li, L. Zhang, D. Wu, J. Chu, Nanogap Plasmonic Structures Fabricated by Switchable Capillary-Force Driven Self-Assembly for Localized Sensing of Anticancer Medicines with Microfluidic SERS, Adv Funct Mater. 30 (2020) 1909467. https://doi.org/10.1002/ADFM.201909467.

[30] J. Plou, M. Charconnet, I. García, J. Calvo, L.M. Liz-Marzán, Preventing Memory Effects in Surface-Enhanced Raman Scattering Substrates by Polymer Coating and Laser-Activated Deprotection, ACS Nano. 15 (2021) 8984–8995. https://doi.org/10.1021/acsnano.1c01878.

[31] A. Kamińska, I. Dzicielewski, J.L. Weyher, J. Waluk, S. Gawinkowski, V. Sashuk, M. Fiałkowski, M. Sawicka, T. Suski, S. Porowski, R. Hołyst, Highly reproducible, stable and multiply regenerated surface-enhanced Raman scattering substrate for biomedical applications, J Mater Chem. 21 (2011) 8662–8669. https://doi.org/10.1039/C0JM03336G.

[32] M. Fan, P. Wang, C. Escobedo, D. Sinton, A.G. Brolo, Surface-enhanced Raman scattering (SERS) optrodes for multiplexed on-chip sensing of nile blue A and oxazine 720, Lab Chip. 12 (2012) 1554–1560. https://doi.org/10.1039/C2LC20648J.

[33] T.A. Meier, E. Poehler, F. Kemper, O. Pabst, H.G. Jahnke, E. Beckert, A. Robitzki, D. Belder, Fast electrically assisted regeneration of on-chip SERS substrates, Lab Chip. 15 (2015) 2923–2927. https://doi.org/10.1039/C5LC00397K.

[34] M. Viehrig, S.T. Rajendran, K. Sanger, M.S. Schmidt, T.S. Alstrøm, T. Rindzevicius, K. Zór, A. Boisen, Quantitative SERS Assay on a Single Chip Enabled by Electrochemically Assisted Regeneration: A Method for Detection of Melamine in Milk, Anal Chem. 92 (2020) 4317–4325. https://doi.org/10.1021/acs.analchem.9b05060.

[35] Z. Wang, J. Zhang, M. Jiang, TiO2/AgNPs SERS substrate for the detection of multi-molecules with a self-cleaning and high enhancement factor using the UV-induced method, Opt Mater Express. 12 (2022) 1010–1018. https://doi.org/10.1364/OME.451734.

[36] P.K. Jain, K.S. Lee, I.H. El-Sayed, M.A. El-Sayed, Calculated Absorption and Scattering Properties of Gold Nanoparticles of Different Size, Shape, and Composition: Applications in Biological Imaging and Biomedicine, J Phys Chem B. 110 (2006) 7238–7248. https://doi.org/10.1021/jp057170o.

[37] S. Singh, A. Bharti, V.K. Meena, Green synthesis of multi-shaped silver nanoparticles: optical, morphological and antibacterial properties, Journal of Materials Science: Materials in Electronics. 26 (2015) 3638–3648. https://doi.org/10.1007/s10854-015-2881-y.

[38] J.F. Lin, J. Wertz, R. Ahmad, M. Thommes, A.M. Kannan, Effect of carbon paper substrate of the gas diffusion layer on the performance of proton exchange membrane fuel cell, Electrochim Acta. 55 (2010) 2746–2751. https://doi.org/10.1016/j.electacta.2009.12.056.

[39] C. Lim, C.Y. Wang, Effects of hydrophobic polymer content in GDL on power performance of a PEM fuel cell, Electrochim Acta. 49 (2004) 4149–4156. https://doi.org/10.1016/J.ELECTACTA.2004.04.009.

[40] Y. Wang, C.Y. Wang, K.S. Chen, Elucidating differences between carbon paper and carbon cloth in polymer electrolyte fuel cells, Electrochim Acta. 52 (2007) 3965–3975. https://doi.org/10.1016/J.ELECTACTA.2006.11.012.

[41] S. Park, B.N. Popov, Effect of a GDL based on carbon paper or carbon cloth on PEM fuel cell performance, Fuel. 90 (2011) 436–440. https://doi.org/10.1016/J.FUEL.2010.09.003.

[42] M.M. Waje, X. Wang, W. Li, Y. Yan, Deposition of platinum nanoparticles on organic functionalized carbon nanotubes grown in situ on carbon paper for fuel cells, Nanotechnology. 16 (2005) S395. https://doi.org/10.1088/0957-4484/16/7/013.

[43] C. te Hsieh, C. Pan, W.Y. Chen, Synthesis of silver nanoparticles on carbon papers for electrochemical catalysts, J Power Sources. 196 (2011) 6055–6061. https://doi.org/10.1016/j.jpowsour.2011.03.087.

[44] E. Nunez-Bajo, M.C. Blanco-López, A. Costa-García, M.T. Fernández-Abedul, Electrogeneration of Gold Nanoparticles on Porous-Carbon Paper-Based Electrodes and Application to Inorganic Arsenic Analysis in White Wines by Chronoamperometric Stripping, Anal Chem. 89 (2017) 6415–6423. https://doi.org/10.1021/acs.analchem.7b00144.

[45] S. Lu, T. You, N. Yang, Y. Gao, P. Yin, Flexible SERS substrate based on Ag nanodendrite–coated carbon fiber cloth: simultaneous detection for multiple pesticides in liquid droplet, Anal Bioanal Chem. 412 (2020) 1159–1167. https://doi.org/10.1007/s00216-019-02344-6.

[46] M. Tran, A. Fallatah, A. Whale, S. Padalkar, Utilization of inexpensive carbon-based substrates as platforms for sensing, Sensors. 18 (2018) 1–11. https://doi.org/10.3390/s18082444.

[47] Z. Luo, L. Chen, C. Liang, Q. Wei, Y. Chen, J. Wang, Porous carbon films decorated with silver nanoparticles as a sensitive SERS substrate, and their application to virus identification, Microchimica Acta. 184 (2017) 3505–3511. https://doi.org/10.1007/s00604-017-2369-y.

[48] M.-L. Cheng, J. Yang, Influences of Composition on Electroless Deposition of Silver Nanoparticles on Glass Substrates for Surface-Enhanced Raman Scattering Measurements, Appl Spectrosc. 62 (2008) 1384–1394. https://doi.org/10.1366/000370208786822232.

[49] M.L. Cheng, B.C. Tsai, J. Yang, Silver nanoparticle-treated filter paper as a highly sensitive surface-enhanced Raman scattering (SERS) substrate for detection of tyrosine in aqueous solution, Anal Chim Acta. 708 (2011) 89–96. https://doi.org/10.1016/j.aca.2011.10.013.

[50] M. Verma, T.K. Naqvi, S.K. Tripathi, M.M. Kulkarni, P.K. Dwivedi, Paper based low-cost flexible SERS sensor for food adulterant detection, Environ Technol Innov. 24 (2021) 102033. https://doi.org/10.1016/J.ETI.2021.102033.

[51] VSPARTICLE, Revolutionizing material development: Nanoporous Printer, VSP-P1 Nanoporous Printer, (2022). https://vsparticle.com/products/vsp-p1-nanoporous-printer (accessed December 4, 2022).

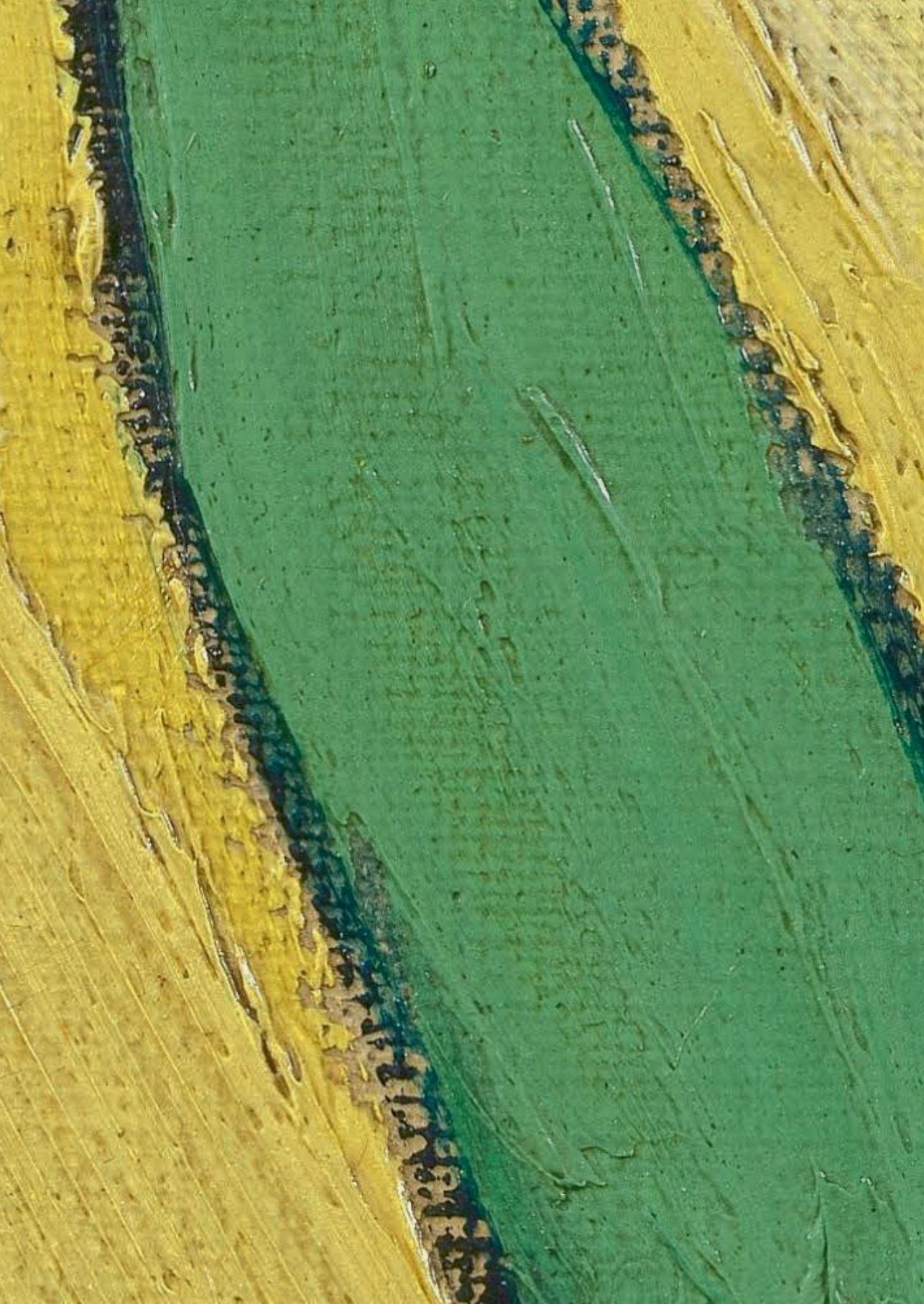

# CHAPTER 9

Conclusions and future perspectives

# Conclusions and future perspectives

The research presented in this thesis was largely performed within the framework of the TooCOLD project (Toolbox for studying the Chemistry Of Light-induced Degradation) in the TTW Open Technology Programme (project number 15506). TooCOLD is a public-private partnership funded by NWO-TTW and several companies. Partners in this collaborative project were the Analytical Chemistry groups of the University of Amsterdam and the Vrije Universiteit Amsterdam, and the companies/institutes DaVinci, Unilever, KWR, PWN, Van Gogh Museum, and Cultural Heritage Agency of The Netherlands. The main goal of TooCOLD was to develop an *"innovative, high-resolution, and fully orthogonal system to study the degradation of a wide range of components, either present as pure components or in mixtures, under the influence of light"*. The work presented here involves the development of a light-exposure cell with in-situ absorption spectroscopy coupled to liquid chromatography with diode-array and mass spectrometric detection (LC-DAD-MS) for the study of light-induced degradation (LID) of dyes and other colored compounds.

The LID cell presented in this thesis was based on a gas-permeable Teflon AF2400 liquid-core waveguide (LCW), which was evaluated by applying it to the photodegradation of Crystal Violet, Riboflavin and Eosin Y (Chapters 5 and 6). Due to the gas permeability of the LID cell, we were able to study the effect of oxygen on the photodegradation of Riboflavin and Eosin Y (Chapter 7) and found that our results were broadly in line with previous reports in literature. Furthermore, the final set-up consists of a MultiPurpose Sampler (MPS) by Gerstel that provides sample injection, sample transfer to the LC system, and cleaning of the LCW. The photodegradation experiments conducted in the LID cell are protected from ambient light by a black box, which is directly connected to an LC-DAD system via an in-built 6-port valve. The LC method using triethylamine as an ion-pairing agent (Chapter 4) showed to be useful for the analysis of the photodegraded samples. We found that the addition of quadrupole time-of-flight (QTOF) MS detection to LC-DAD was indispensable for the identification of newly formed photodegradation products (Chapter 7). In-situ measurement of absorbance spectra was conducted by collecting the transmitted light using a compact spectrometer from Thorlabs covering 350 to 700 nm. Pictures of the complete set-up are included in Chapter 12.

The developed, fully automated LID set-up reduces both time in the lab as well as errors caused by manual sample preparation and handling. The flexible set-up provides the user with the option to vary instrumental parameters, i.e., the light source, type of optical fibers, and the spectrometer or LC system, as well as various parameters that affect photodegradation processes, i.e., light intensity, wavelength, type of solvents and

mixtures, pH, and presence or absence of oxygen. Also, the influence of other additives such as catalysts, inhibitors, or peroxides on the photodegradation of pure analytes as well as mixtures can be studied.

Since the goal of the TooCOLD project was to combine the study of photodegradation with analytical chemistry, the analytical performance of the system was rather important. As reported in Chapter 6, the final LID cell set-up showed high repeatability for photodegradation experiments with an RSD of ≤0.01 for the decrease in Riboflavin concentration after 4 hrs of irradiation (n=5). In-situ absorbance measurements (i.e., in the LCW) of Riboflavin showed acceptable linearity (R=0.98), an LOD of $1.74 \cdot 10^{-7}$ M, and satisfactory repeatability (RSD≤0.13, n=5) for every concentration measured within the linear range of $1\text{-}12 \cdot 10^{-6}$ M. It was possible to create time profiles of the photodegradation of Riboflavin and Eosin Y by irradiating for different periods of time followed by chemical analysis. The same LID cell was successfully incorporated in a comprehensive two-dimensional LC set-up by Den Uijl et al. [1] and applied to study the photodegradation of fuchsin, annatto, and a vitamin B complex. In this study, the compounds of interest were first isolated from a mixture by the first LC dimension, then individually irradiated in the LID cell, followed by chemical analysis of the formed photodegradation products by LC-DAD in the second dimension.

The most essential parts of the TooCOLD goals have been achieved, however, there is still room for further improvements and extensions. In the next paragraphs we will reflect on the matter of light input, photon flux and quantum yield, the influence of oxygen on photodegradation, analyte recovery from and contamination of the LID cell, and the feasibility of applying Raman spectroscopy for monitoring photodegradation in LID cells. Furthermore, the applicability of the LID set-up to the three main areas of interest (i.e., water purification, cultural heritage, and food safety) is discussed and ideas for future research are presented.

**Light input**

The speed of photodegradation is inherently connected to the intensity of irradiation, as was thoroughly described in Chapter 2. Therefore, coupling of the light source into the LCW should be efficient to allow accelerated light aging. There are several places in the set-up where light transfer could be critical: (i) coupling of the light source with an optical fiber, (ii) between the optical fiber and the LID-cell entrance, and (iii) across the length of the LCW.

The light source is connected to the LID cell using an optical fiber, which has an inner diameter of 200 µm. In a free-space configuration, the Xenon light source produces roughly 290 mW, of which about 5 mW (i.e., 1.7%) is emerging from the fiber when

coupled, according to the technical specifications by Thorlabs. The light transfer efficiency from the source to the fiber could be improved by using fibers with larger inner diameters or better optics. Thorlabs provides the same type of UV-resistant optical fibers with an inner diameter of up to 600 µm.

The second optical component that may be improved concerning the efficiency of light transmittance is the connection between the optical fiber and the LID cell entrance. Using a collimator and a lens with a relatively long focal length (35 mm), we already tried to focus the light into the LCW as well as possible. However, the optical components were difficult to properly align with the entrance of the LCW, resulting in losses. Therefore, we added an X-Y optical mount that allowed better alignment of the fiber with the collimator and lens to the entrance of the LCW, increasing the light transmittance. Furthermore, a mechanical issue hindered the efficient propagation of light. Fig. 9.1 shows the front (A) and back (B) of the connection piece that is positioned in the filter wheel and holds the LID cell using a PEEK Fingertight fitting. The quartz optical window allows the coupling of the light coming from the optical fiber into the cell. Fig. D-2 and E-2 in the Appendix show schematic cross-sections of these parts. The diameter of this entrance was kept small (≈500 µm) to reduce dead volume, but could be slightly increased to match the diameter of the focused light beam at that exact point to optimize the light input to the LCW.

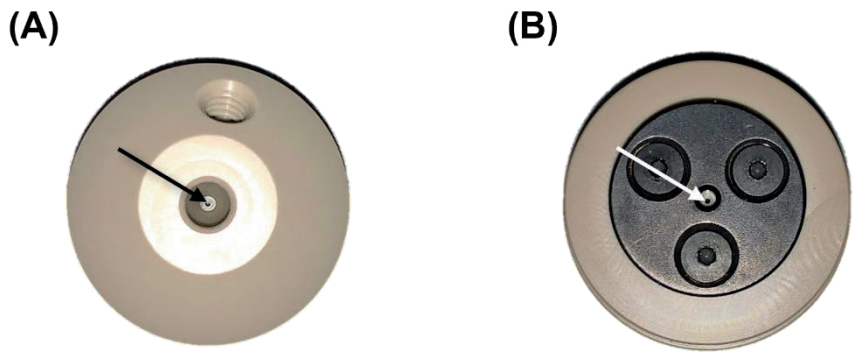


Figure 9.1. The PEEK coupling piece (A) front and (B) back with the quartz optical window in the middle and the light entrance/exit marked by arrows.

Lastly, we found that light is lost across the length of the LCW, probably due to imperfections in the material and pores in the LCW walls [2]. Unfortunately, this cannot be avoided easily as it relies on the material the LCW is made of, but other tubing materials from different manufacturers could potentially be purchased and tested for more efficient light guiding. An interesting option would be Teflon AF1600, which has a lower porosity than AF2400 and, therefore, might have smaller or fewer pores, but also

has a slightly higher refractive index (1.31 versus 1.29). The lower porosity, however, may lead to lower permeability for oxygen and nitrogen, implying a trade-off has to be made.

Another option for improvement is to tune the wavelength and intensity of light by involving the filter wheel. Due to time constraints, we were not able to do the related experiments, although it seems fairly easy to perform. The filter wheel can hold up to six round optical filters and can be turned manually. Therefore, it is simply possible to block or allow certain regions of the lamp spectrum to study their effect on photodegradation.

**Photon flux**

The photon flux in the LCW cell is an important parameter to be able to study the kinetics of photochemical mechanisms. In the preliminary LID set-up, the photon flux was straightforwardly determined inside the LCW with in-situ absorption spectrometry using a diarylethene ether as an actinometer (Chapter 5). This may be important when changes are made to the system. The results closely matched those measured using a power meter [2]. The transmitted light intensity by the LCW was measured at different wavelengths and was found to increase with increasing wavelengths (Fig. 5.2B). Notably, so far this was performed for light of wavelengths >450 nm; transmittance of UV light has not been measured yet. These experiments could be performed in the future using bandpass filters in the UV region.

**Influence of oxygen**

As described in Chapter 7, we were able to study the effect of oxygen on the photodegradation of Riboflavin and Eosin Y using the developed set-up, due to the unique gas permeability of the LCW material. This is not possible for the microfluidic device described in Chapter 8.4. During the initial development of the LID cell, two LCWs were tested that differed in wall thickness: 100 and 220 µm. It was hypothesized that the thick-wall LCW may result in better light guiding, but has a lower gas permeability, decreasing the diffusion rate of oxygen or nitrogen through the LCW walls. For both LCW types, the gas diffusion was assessed by means of the redox reaction between methylene blue and glucose. It was observed that the oxidation of methylene blue occurred much slower for the thick-wall LCW when oxygen was presented to a deoxygenated solution in the LID cell as compared to the thin-wall LCW. This confirmed our oxygen hypothesis, but significant differences in light guiding efficiency were not observed. Therefore, the thin-wall LCW was selected for further work.

In future research, it might be interesting to study the effect of the air/gas flow rate through the LID cell on the observed photodegradation rates. Currently, it is unknown whether a higher gas flow would result in faster gas diffusion into the LCW. Variation in

the oxygen concentration of the added gas could also be studied. Compressed air, which generally contains 20-21% of oxygen, was so far used in the presented work. It has been shown that the percentage of (dissolved) oxygen may affect the rate of photodegradation [3–5]. Both a gas mixer and flow meter could be added to the LID set-up to control, for example, oxygen and nitrogen concentrations to conduct these experiments.

**Sample recovery and contaminations**

Recovery of Riboflavin from the LCW cell was sufficient (89%), and repeatable, however, we have measured lower recoveries for more hydrophobic compounds, such as Crystal Violet, Rhodamine B, and Diamond green G (results not presented here). It is suspected that those compounds either adsorb to the hydrophobic walls of the LCW and/or enter its pores, which evidently decreases the analyte recovery from the LID cell. Transfer of components from the light cell to the LC system is a parameter that should be optimized for each sample, e.g., by varying solvent types or flushing times. For more hydrophobic compounds, the use of less polar solvents, such as 100% MeOH or ACN might be needed. Another strategy might be to increase the LC injection loop volume, which currently is 20 µL. The choice for this volume was made (i) to maintain good compatibility with LC, as a too-large volume of strong solvents (e.g., 100% ACN or MeOH) could result in analyte breakthrough on the RPLC column, and (ii) to avoid the introduction of undegraded compounds that were in the dead volume of the LID system (i.e., tubing in front and after the LCW cell) with a total volume of 10 µL. However, having this relatively small injection volume means that only a third of the content of the 12-cm LCW cell (total volume, 60 µL) can be transferred to the LC system. This in itself should not be a problem since injection is done consistently, however, for hydrophobic compounds this may be the culprit that leads to low recovery. To transfer the content of the LCW to the sample loop, 50 µL of 'transfer solvent' (generally 75% MeOH), is used to 'push' the middle part of the LCW volume to the 20-µL injection loop. When hydrophobic compounds are studied it is preferred to empty the LCW cell with a larger volume to increase analyte recovery. By increasing the LC injection loop to e.g., 200 µL, it would be possible to flush the LID cell with more than three times the volume of the irradiated sample, possibly resulting in higher recoveries, and yielding a more accurate picture of the photodegradation that occurred inside the LCW during irradiation. Large injection volumes, however, may lead to the aforementioned breakthrough and/or band broadening. A possible solution for this would be the use of a trapping column in between the sample loop and the LC column, employing stationary-phase-assisted modulation (SPAM) after online dilution with a weak solvent [6]. The added benefit of SPAM would be that it results in pre-concentration

of the analytes, which is especially important for compounds present at very low concentrations.

Contaminations originating from previous experiments conducted in the LID cell were observed in the mass spectra during LC-DAD-MS of photodegraded pharmaceuticals in water (work done by Ingrida Bagdonaite) and of irradiated Eosin Y and Riboflavin. These contaminations can result in spectral interpretation difficulties when potentially unknown photodegradation products are to be identified. We found that a thorough cleaning procedure resulted in sufficient removal of most of these contaminations, as shown in Fig. 9.2. It shows LC-DAD chromatograms from MQ samples taken from an LID cell that was barely used (A), and from a contaminated LID cell that was frequently used for more than over a year, before (B) and after (C) cleaning. The procedure consisted of flushing the system with 100% ACN for 1 hr at a flowrate of 0.3 mL $min^{-1}$, followed by flushing with MQ. Since the cleaning was successful, it also circumvented the purchase of a replacement in the case of heavy contamination. It is not preferred to conduct the procedure after every analysis, but much like flushing an LC column, it could be performed when a batch of experiments is finished.

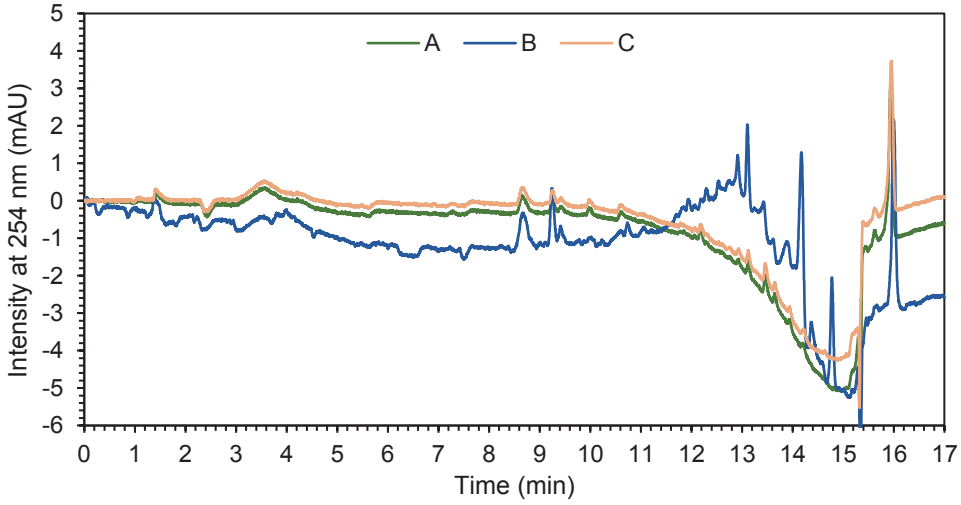


Figure 9.2. LC-DAD chromatograms recorded at 254 nm of MQ samples from (A) an LID cell that was used only several times, (B) an LID cell that was used many times for more than over a year, (C) the same LID cell as (B) after cleaning with 100% ACN for 1 hr. Work done by Ingrida Bagdonaite.

### In-situ monitoring and feasibility of Raman spectroscopy

The in-situ monitoring of the UV/Vis absorbance spectrum of the irradiated sample was found to be an added value for following and understanding photodegradation in real-time. It is a convenient tool to control whether the sample is in the LCW cell, if the

degradation process is still ongoing, and whether the light cell accidentally contains an air bubble, which would hinder proper light guiding and, therefore, the photodegradation process. Additionally, the combination of information obtained from these spectra with those from MS, for example, led to the confirmation of chromophore breakdown of Eosin Y in the presence of oxygen. Without this information, this may have been more difficult to confirm, especially for compounds for which the photodegradation mechanisms are still unknown, unlike that of Eosin Y.

Absorption spectroscopy alone, however, is limited in providing information about (changes in) the chemical structure of the studied compounds, certainly when the chromophore remains largely unchanged. UV-Vis spectra in solution phase tend to be rather broad, and in addition, the in-situ spectra originate from a mixture of which the parent compound is the main component. Therefore, it can be challenging to observe minor components, e.g., as the result of the loss of a methyl group due to photodegradation. To obtain more information about the structural changes that the analyte is undergoing, an online-applicable optical technique like Raman spectroscopy would be attractive. The feasibility of Raman for studying photodegradation in situ was tentatively explored in Chapter 8. Distinct differences were found between the surface-enhanced Raman spectroscopy (SERS) spectra of Crystal Violet and its degradation products, which were isolated by LC fractionation. On-chip monitoring of SERS spectra of Crystal Violet inside a microfluidic device using gold leaning pillar chips as substrate was also attempted. A proof-of-principle experiment showed that it was possible to reveal similar spectral changes for a mixture containing both parent and degradation products employing SERS. Afterward, analysis by LC-DAD-QTOFMS confirmed that the photodegradation products formed were identical to those formed in the LCW, however, the large decrease of CV determined by LC-MS did not reflect the small changes observed in the SERS spectra. It is suspected that the leaning pillar substrate affects either the photodegradation rate or is unable to represent the complete sample mixture due to differences in adsorption between the parent and degradation molecules. Future research may have to focus on different substrates or on a method to prevent this memory effect, for example, by applying a protective layer on top of the substrate, as demonstrated by Plou et al. [7]. For SERS monitoring purposes, a thin layer of poly(lactic-co-glycolic acid) (PLGA) was added on top of a SERS substrate to prevent adsorption of molecules to the substrate. The coating was locally degraded by irradiation with the laser used for SERS measurements at high power, therefore creating small windows that are available for molecules present in solution to adsorb to at a timepoint of interest. Using this technique, they were able to perform 10,000 consecutive measurements per

substrate and showed accurate and continuous monitoring of analytes in microfluidic channels.

Interestingly, LCWs have been used previously as flow cells for Raman spectroscopic detection to enhance sensitivity due to the increased optical path length [8–10]. Considering the LCW-based LID device developed in the present work, one could envisage a similar LID cell that allows in-situ monitoring of the photodegrading sample by Raman spectroscopy (Fig. 9.3). A possible set-up would include a laser for Raman excitation, (a) two mirrors to direct the laser into (b) a microscope objective for focusing and coupling of the laser light into one of the two entrances of a split optical fiber. The other entrance of the split optical fiber is then attached to the photodegradation light source and the exit of the optical fiber is coupled to (d) the LID cell. By using shutters (c), it will then be possible to switch between the laser and the photodegradation light source so that in-situ measurements can be taken during irradiation of the sample. Inside the first filter wheel, a narrow-band laser clean-up filter may be added, and the second filter wheel can hold a notch filter (NF) to block the laser light to allow proper recording of Raman spectra, which is collected by a spectrometer with a CCD detector.

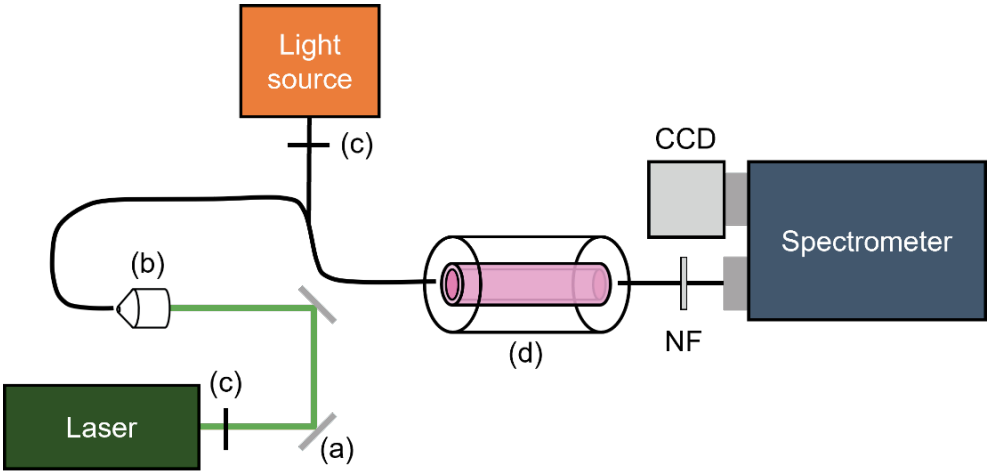


Figure 9.3. Suggestion for a set-up utilizing Raman spectroscopy inside an LCW for studying photodegradation processes, consisting of a laser, (a) silver mirrors to direct the laser into (b) a microscope objective, a split optical fiber, (c) shutters, a light source for irradiation of the sample inside the (d) LID cell, a notch filter (NF) for removal of laser light, and a spectrometer with CCD camera.

### Microfluidic device as a powerful alternative?

It was shown in Chapter 6 that the increased optical pathlength provided by the LCW was optimal for solutions with low concentrations. For higher concentrations, LID cells with shorter optical pathlengths may be better to reduce photodegradation times. Such cells

may be realized by microfluidics. From the photodegradation experiments of Crystal Violet inside the microfluidic device described in Chapter 8, it was found that photodegradation occurred more rapidly, which therefore presents itself as a powerful alternative for the LCW. However, when using the microfluidic device it was not yet possible to study the effect of oxygen on the photodegradation process, whereas this is simple to achieve using the LCW light cell. Incorporating oxygen permeability in a future design of the microfluidic cell would be of great added value. This could potentially be done by adding a gas-diffusive layer, such as carbon paper or a membrane of Teflon AF2400, that creates a barrier between a gas flow channel and the microfluidic channel. Optionally, oxygen-saturated solvents could be used as a medium for the analytes of interest. The solubility of oxygen in freshwater is related to pressure and temperature but reaches approximately 9.1 mg $L^{-1}$ at 20 °C at 1 atm pressure [11], which is equal to $2.8 \cdot 10^{-4}$ M $O_2$. That would mean a maximum of 910 ng of dissolved oxygen (DO) in 100 µL of sample solution (volume of the microfluidic channel) Hypothetically speaking, if oxygen reacts 1:1 with the analyte in question, then it would require a similar mole amount of the analyte to reach oxygen depletion. However, oxygen may also react with other species, e.g., water, additives, and newly formed degradation products, leading to a decrease in the available DO for the parent analyte. Therefore, it is rather complicated to determine if and when oxygen depletion would be reached if this approach is used.

**Relevance of LID cell for real-life photodegradation**

The development of a light exposure cell for studying the chemistry of LID has been successful in several ways: (i) important aspects such as the influence of the light source, wavelength, and oxygen, that affect photodegradation can be studied using the set-up, (ii) coupling with analytical techniques (e.g., LC, LCxLC, and MS) was established, (iii) the system was fully automated and showed satisfactory repeatability. However, with this approach photodegradation is studied in neat solutions, which may deviate from photodegradation situations in real life. Therefore, a critical discussion is provided below on the applicability of the system concerning the three main areas of interest: water purification, cultural heritage, and food.



*Water purification*

In water purification processes, photodegradation of potential contaminants by UV irradiation is a standard procedure. The developed LID system seems well-suited for studying this process on an experimental scale. It is expected that the results obtained using the LCW-based system are representative of the photodegradation reactions during water purification processes. Natural constituents of source water, e.g., NOM, and purification additives, such as peroxides, may influence photodegradation processes,

and with the current LID cell set-up it is possible to study these effects, but a proper comparison with other analytical photodegradation systems still has to be made. Moreover, the applicability of the LID system for this purpose could be improved further. Currently, water purification plants make use of mercury lamps to remove potentially toxic chemicals from water, and it is foreseen that for sustainability reasons these will be replaced by high-intensity UV LEDs in the near future. Therefore, the feasibility of such LEDs with the LID system should be assessed. All optomechanical parts of the TooCOLD system are already suitable for guiding or transmitting deep UV light, which should make the transition from mercury lamps to UV LEDs very well feasible.

An extension of the LID system for water purification studies would be the addition of (in-line) bioassays after LC analysis to study the hazard of the formed degradation products to human or environmental health. LC separation of the photodegraded sample in combination with the aforementioned SPAM would allow pre-concentration of the analytes, and fractionation of the eluent into well plates should make it possible to perform single or multiple bioassays [12].

*Cultural heritage*

There are several methods available for the study of fading and photodegradation in cultural heritage. The two methods most commonly used for textiles and paintings are the Xenotest and the Micro-Fading Tester, which are discussed in more detail in Chapters 1 and 2. An additional approach to studying photodegradation mechanisms much quicker is in-solution photodegradation. It was made clear in Chapter 2 that different outcomes may occur for photodegradation on a substrate and in-solution, as was also known before the start of the TooCOLD project. On the other hand, similar outcomes have also been observed for solid and in-solution photodegradation. Examples of such findings have been presented for Crystal Violet and Eosin Y [13–16]. In this context, it is important to state that the developed LID set-up is not meant to replace the above-mentioned analytical photodegradation methods. It rather is a valuable addition to the existing methods for studying the photodegradation of dyes and pigments in solution, but in a quicker, more repeatable manner. It can, therefore, also be used conveniently to confirm or compare with photodegradation results obtained from solid-state experiments.

For future research, it would be interesting to address these concerns of differences in the matrix by developing an automated system for solid-state photodegradation. This could be realized by combining the irradiation of small, solid samples with automated sample preparation methods coupled with analytical techniques, similar to the LID system. For larger objects, it would require taking small samples, similar to what is done

already, but in an off-line fashion. Another approach could be to dissolve or immerse dyes and/or pigments in a solid phase system that can easily be dissolved in solvents after irradiation, followed by chemical analysis of the formed photodegradation products.

*Food*

The study of photodegradation in foodstuffs may apply approaches used both in water purification and cultural heritage. It shares similarities with water research in the sense that it may deal with liquid foods and drinks, whereas cultural heritage research mostly involves solid materials, comparable to solid food products. The current LID system would be suitable for the study of solutions such as juices and soft drinks, as well as solutions of individual components, e.g., vitamins, anti-oxidants, stabilizers, artificial sweeteners, or food dyes. In addition, the light-protecting properties of food-packaging materials could be studied by placing these as an optical filter in the filter wheel of the developed LID set-up. However, studying photodegradation in solid food products with the new set-up may be challenging. Commonly, food products are placed in a 'light room' where they are illuminated by, e.g., tube lights for prolonged periods to simulate a situation in a supermarket. The current LID system will not be able to replace this method for solid or viscous foodstuffs as these would need elaborate sample pretreatment to prevent clogging of the system and to be compatible with LC analysis.

In the future, complex food matrices may be studied in the LID cell if adjustments are made to the set-up, similar to what is described for cultural heritage. The MPS is capable of moving and mixing samples, and other components may be added to automate sample pretreatment, which would make it more suitable for studying foodstuffs. Since food safety may also be a motivation to study photodegradation in food products, additionally, in-line bioassays could be incorporated similarly as described in the section about water purification.

# References

[1] M.J. den Uijl, Y.J.H.L. van der Wijst, I. Groeneveld, P.J. Schoenmakers, B.W.J. Pirok, M.R. van Bommel, Combining Photodegradation in a Liquid-Core-Waveguide Cell with Multiple-Heart-Cut Two-Dimensional Liquid Chromatography, Anal Chem. 94 (2022) 11055–11061. https://doi.org/10.1021/acs.analchem.2c01928.

[2] I. Groeneveld, S.E. Schoemaker, G.W. Somsen, F. Ariese, M.R. van Bommel, Characterization of a liquid-core waveguide cell for studying the chemistry of light-induced degradation, Analyst. 146 (2021) 3197–3207. https://doi.org/10.1039/d1an00272d.

[3] J.-K. Im, H.-S. Son, Y.-M. Kang, K.-D. Zoh, Carbamazepine Degradation by Photolysis and Titanium Dioxide Photocatalysis, Water Environment Research. 84 (2012) 554–561. https://doi.org/10.2175/106143012X13373550427273.

[4] D. Ren, B. Huang, T. Bi, D. Xiong, X. Pan, Effects of pH and dissolved oxygen on the photodegradation of 17α-ethynylestradiol in dissolved humic acid solution, Environ Sci Process Impacts. 18 (2016) 78–86. https://doi.org/10.1039/C5EM00502G.

[5] X. Zhang, Z. Liu, Q. Kong, G. Liu, W. Lv, F. Li, X. Lin, Aquatic photodegradation of clofibric acid under simulated sunlight irradiation: kinetics and mechanism analysis, RSC Adv. 8 (2018) 27796–27804. https://doi.org/10.1039/C8RA03140A.

[6] M.J. den Uijl, T. Roeland, T.S. Bos, P.J. Schoenmakers, M.R. van Bommel, B.W.J. Pirok, Assessing the feasibility of stationary-phase-assisted modulation for two-dimensional liquid-chromatography separations, J Chromatogr A. 1679 (2022) 463388. https://doi.org/10.1016/J.CHROMA.2022.463388.

[7] J. Plou, M. Charconnet, I. García, J. Calvo, L.M. Liz-Marzán, Preventing Memory Effects in Surface-Enhanced Raman Scattering Substrates by Polymer Coating and Laser-Activated Deprotection, ACS Nano. 15 (2021) 8984–8995. https://doi.org/10.1021/acsnano.1c01878.

[8] R.J. Dijkstra, A.N. Bader, G.P. Hoornweg, U.A.T. Brinkman, C. Gooijer, On-Line Coupling of Column Liquid Chromatography and Raman Spectroscopy Using a Liquid Core Waveguide, Anal Chem. 71 (1999) 4575–4579. https://doi.org/10.1021/ac9902648.

[9] R.J. Dijkstra, C.J. Slooten, A. Stortelder, J.B. Buijs, F. Ariese, U.A.Th. Brinkman, C. Gooijer, Liquid-core waveguide technology for coupling column liquid chromatography and Raman spectroscopy, J Chromatogr A. 918 (2001) 25–36. https://doi.org/10.1016/S0021-9673(01)00721-X.

[10] R.J. Dijkstra, F. Ariese, C. Gooijer, U.A.T. Brinkman, Raman spectroscopy as a detection method for liquid-separation techniques, TrAC - Trends in Analytical Chemistry. 24 (2005) 304–323. https://doi.org/10.1016/j.trac.2004.11.022.

[11] H. Patel, R.T. Vashi, Chapter 2 - Characterization of Textile Wastewater, in: Characterization and Treatment of Textile Wastewater, Elsevier, 2015: pp. 21–71. https://doi.org/10.1016/B978-0-12-802326-6.00002-2.

[12] F.D.L. Leusch, P.A. Neale, A. Hebert, M. Scheurer, M.C.M. Schriks, Analysis of the sensitivity of in vitro bioassays for androgenic, progestagenic, glucocorticoid, thyroid and estrogenic activity: Suitability for drinking and environmental waters, Environ Int. 99 (2017) 120–130. https://doi.org/10.1016/J.ENVINT.2016.12.014.

[13] M.J. den Uijl, A. Lokker, B. van Dooren, P.J. Schoenmakers, B.W.J. Pirok, M.R. van Bommel, Comparing different light-degradation approaches for the degradation of crystal violet and eosin Y, Dyes and Pigments. 197 (2022) 109882. https://doi.org/10.1016/J.DYEPIG.2021.109882.

[14] A. Alvarez-Martin, S. Trashin, M. Cuykx, A. Covaci, K. de Wael, K. Janssens, Photodegradation mechanisms and kinetics of Eosin-Y in oxic and anoxic conditions, Dyes and Pigments. 145 (2017) 376–384. https://doi.org/10.1016/j.dyepig.2017.06.031.

[15] A. Alvarez-Martin, T.P. Cleland, G.M. Kavich, K. Janssens, G.A. Newsome, Rapid Evaluation of the Debromination Mechanism of Eosin in Oil Paint by Direct Analysis in Real Time and Direct Infusion-Electrospray Ionization Mass Spectrometry, Anal Chem. 91 (2019) 10856–10863. https://doi.org/10.1021/acs.analchem.9b02568.

[16] D. Confortin, H. Neevel, M. Brustolon, L. Franco, A.J. Kettelarij, R.M. Williams, M.R. van Bommel, Crystal violet: Study of the photo-fading of an early synthetic dye in aqueous solution and on paper with HPLC-PDA, LC-MS and FORS, J Phys Conf Ser. 231 (2010) 012011. https://doi.org/10.1088/1742-6596/231/1/012011.

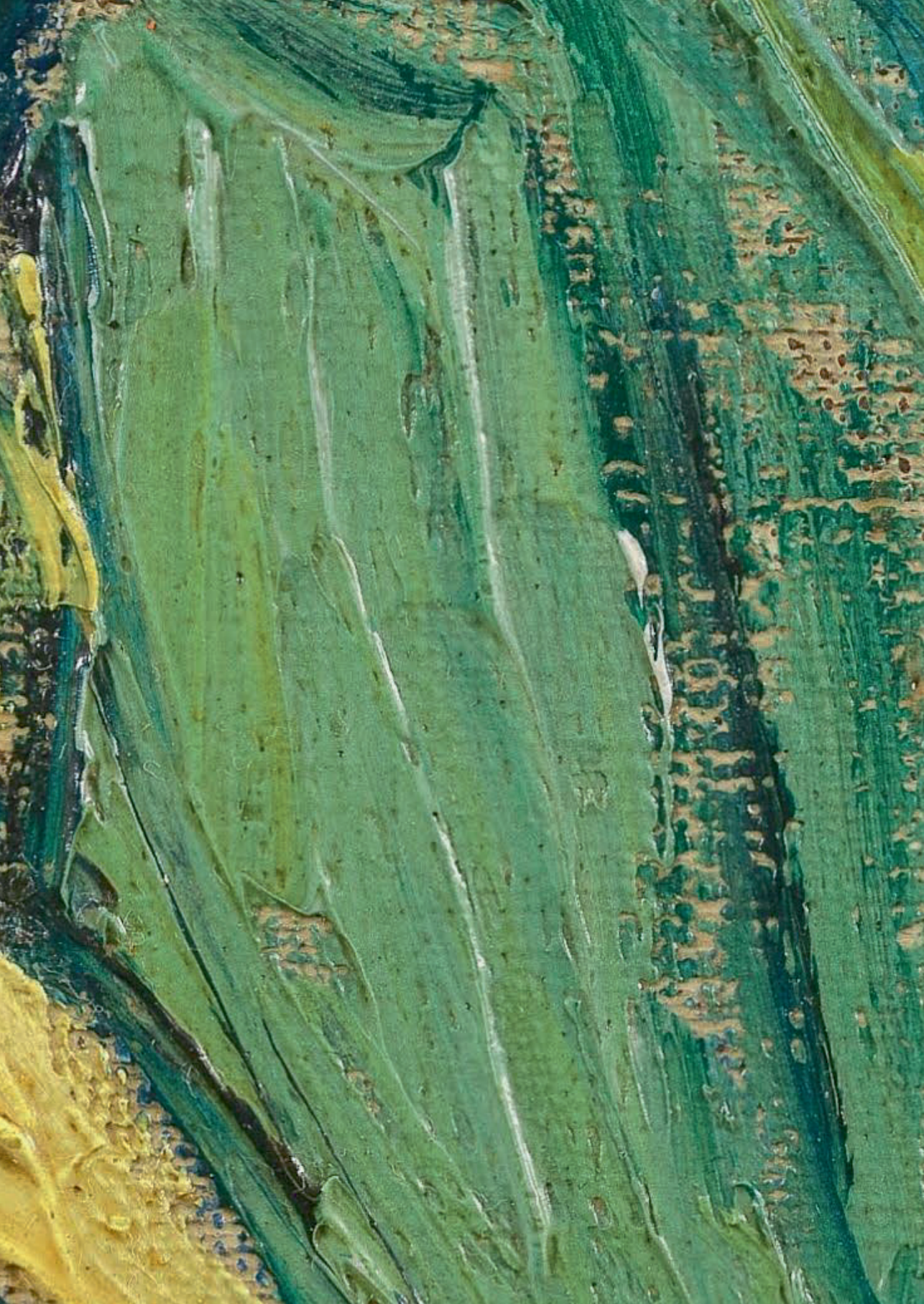

# CHAPTER 10

Summary and samenvatting

# Summary

The study of photodegradation processes concerns many fields, including those of cultural heritage, the food industry, and water purification. In each of these areas, different questions concerning photodegradation arise, but generally, they are related to either (i) the prevention of photodegradation aiming to avoid loss or change of properties, such as color, taste or smell, or (ii) the exploitation of photodegradation for removal of potentially harmful compounds in, e.g., drinking water. Studying light-induced degradation (LID) reactions is challenging and often it is difficult to establish a strong link between the degradation and the starting products. Several techniques and approaches for studying photodegradation had been developed previously, but these can be laborious and prone to errors. A solution to this could be found in a comprehensive, automated device that enables simultaneous sample irradiation of compounds in solution and chemical analysis in real-time and after photodegradation.

The need for such an analytical platform is clarified in **Chapter 1**. The 'Toolbox for studying the Chemistry Of Light-induced Degradation' (TooCOLD) project envisioned to develop an integrated device. It would encompass a light-exposure cell, allow in-situ spectroscopic monitoring of the irradiated sample and on-line coupling to liquid chromatography (LC) with diode array detection (DAD) and mass spectrometry (MS) for direct identification of degradation products formed during irradiation. This thesis describes the step-wise development of such an automated device employing a gas-permeable liquid-core waveguide (LCW) as a light-exposure cell, a sample handler, a spectrograph for in-situ absorption spectroscopy, and switching valves for coupling to LC-DAD-QTOFMS. The full device was applied to study the photodegradation of several compounds to evaluate and demonstrate its analytical performance.

Ideally, parameters that affect photodegradation should be known to aid the design of a system that can be used to study photodegradation in the broadest sense. **Chapter 2** describes the many parameters that can influence the photodegradation of dyes and pigments in solution and on a substrate. Regardless of the sample medium, important parameters that affect photodegradation are the irradiation source (i.e., light dose and wavelength), the presence or absence of oxygen and/or catalysts, and the concentration of the compound of interest. For solutions also the type of solvent and the pH are essential, and for solid-state photodegradation, the type of substrate, the humidity, and the type of mordant used also can play an important role.

The light-exposure cell developed in this thesis project was based on an LCW, which employs the principle of total internal reflection (TIR) to irradiate the entire sample in contrast to conventional cells using perpendicular illumination. LCWs are hollow optical

fibers, which guide light along the length of the tube when filled with a solvent with a refractive index larger than the LCW's material, or by interfering layers in the LCW material itself that cause reflections along the length of the tube. **Chapter 3** reviews the different types of LCWs that are available and applicable as a photoreactor and for chemical analysis. The TIR-based LCWs discussed are polymer-coated capillaries, polymer capillaries (made from Teflon AF), and silica aerogels. In addition, interference-based LCWs are discussed, including photonic crystal fibers (i.e., Bragg, holey, and Kagomé fibers), and anti-resonant reflecting optical waveguides (ARROWs). Most of these waveguides offer the advantage of low light losses and are feasible for coupling with analytical techniques. However, many interference-based LCWs share the disadvantage of being fragile and complicated to design. TIR-based LCWs made of Teflon AF show good light-guiding and are also gas permeable, which would allow the introduction of gases (e.g., oxygen) to the photodegradation experiment.

The analysis of complex mixtures resulting from photodegradation may be challenging as the chemical properties of the components can vary greatly. **Chapter 4** describes the development of a generic LC-DAD method for the analysis of natural and synthetic dyes. A compound library of nearly 130 dyestuff compounds was created and used for LC method evaluation. The use of triethylamine as an ion-pairing agent in the mobile phase proved to be a good approach for the separation of acidic, neutral and basic compounds in a single run. The optimized method was applied to several historical artifacts that were expected to contain photodegradation products and the results were compared to those obtained by comprehensive two-dimensional LC (LCxLC). Most compounds in samples from historical objects, including degradation products, could be assigned using the generic LC method, however, the LCxLC method was more successful in separating photodegradation compounds that were structurally very similar to the parent compound. The developed generic LC method was later used to analyze photodegraded samples (Chapters 5-8).

**Chapter 5** describes the development and overall performance of a low-volume LID cell based on a gas-permeable LCW made of Teflon AF2400 connected to a spectrograph, allowing the collection of spectral data in real-time. The transmission characteristics of the LCW were found to depend mostly on its length, and irregularities induced by manual injection of the sample. Therefore, a medium-length LCW was preferred and the use of an autoinjector is recommended to increase stability and repeatability. The photon flux was successfully determined by actinometry inside the LCW using diarylethene ether (DAE) and in-situ absorption spectroscopy. The gas diffusion rate was assessed by measuring the absorbance in-situ during the 'blue bottle test' where methylene blue undergoes a color change upon oxidation. Within the order of tens of seconds, the

absorbance stabilized, indicating that the system was deoxygenated. The potential of the LID set-up for light-exposure studies was successfully demonstrated by monitoring the degradation of the dyes Eosin Y (EY) and Crystal Violet (CV).

All of the abovementioned results were included in the design of a full prototype of an LID-cell based device. Da Vinci Laboratory Solutions assembled a 'black box' with an integrated 6-port valve for coupling with LC and implemented a liquid handler (MultiPurpose Sampler by Gerstel) for the automated injection of samples into the LID cell. The MPS was also used to transfer the sample after degradation to the LC. **Chapter 6** describes the analytical performance of the fully automated system coupled to LC-DAD. The final LID-cell set-up showed high repeatability for photodegradation experiments with an RSD of ≤0.01 for the decrease of the concentration of Riboflavin after 4 hrs of irradiation (n=5). In-situ absorbance measurements of riboflavin showed good linearity (R=0.98), a limit of detection (LOD) of $1.74 \cdot 10^{-7}$ M, and good repeatability (RSD≤0.13, n=5) for every concentration measured within the linear range of $1\text{-}12 \cdot 10^{-6}$ M. Sample recovery of Riboflavin from the light cell was sufficient (89%), however, lower recoveries were experienced with more hydrophobic compounds. Finally, a time profile of the photodegradation of Riboflavin was presented.

**Chapter 7** describes the study of the effect of oxygen on the photodegradation of Riboflavin and EY using the final prototype of the device coupled to LC-DAD-QTOFMS. According to the literature, both compounds show a decreased photodegradation rate under oxic conditions as the excited (triplet) state is quenched by $^3O_2$. Additionally, these compounds show different photodegradation products under oxic versus anoxic conditions. This could be nicely confirmed by our study, proving that the newly developed tool is a valid addition to the existing methods for studying photodegradation in solution. Additionally, the fully debrominated species of EY (fluorescein) was identified as a photodegradation product in solution for the first time. The fully automated set-up reduced both operator time in the lab as well as potential error, as manual sampling was not required. The results obtained by in-situ monitoring closely resembled the change that the sample was undergoing during irradiation as analyzed by LC-DAD-QTOFMS.



The feasibility of Raman spectroscopy for studying changes in the molecular structure during irradiation was assessed in several exploratory subprojects, discussed in **Chapter 8**. CV was irradiated inside the LID cell and the photodegradation products were isolated by LC, which were subsequently analyzed by surface-enhanced Raman spectroscopy (SERS) using silver colloids. This approach was compared to on-chip SERS monitoring during the photodegradation of CV using leaning pillar chip substrates. Before the comparison was made, several characteristics of the leaning pillar chips were

described, i.e., signal enhancement of the silver and gold coatings in combination with 532 or 785 nm lasers, repeatability, and memory effects after cleaning. Unfortunately, we concluded that SERS substrates do not offer good analytical repeatability due to memory effects. The on-chip SERS spectra showed similarities with the changes observed for SERS spectra of the photodegradation products separated by LC. LC-DAD-QTOFMS analysis confirmed the presence of the same degradation products, however, the gold-coated chips seemed to influence the photodegradation rate. Finally, carbon paper was used as a gas-permeable SERS substrate for the implementation inside a microfluidic device to eventually study the influence of oxygen.

Finally, **Chapter 9** contains conclusions on the work covered in Chapters 1 to 8, discussing several relevant aspects and providing perspectives on future use of the developed system, optimization strategies, and possible new application areas.

# Samenvatting

Het bestuderen van fotodegradatieprocessen heeft betrekking op veel vakgebieden, waaronder dat van cultureel erfgoed, de voedingsindustrie en waterzuivering. In elk van deze gebieden rijzen verschillende vragen op, maar over het algemeen hebben zij betrekking op (i) de preventie van fotodegradatie met als doel het vermijden van verlies of verandering van eigenschappen, zoals kleur, smaak of geur, en/of (ii) het toepassen van fotodegradatie voor het verwijderen van potentieel schadelijke stoffen in bijvoorbeeld drinkwater. Het bestuderen van fotodegradatiemechanismen is uitdagend en het is over het algemeen lastig om een verband te leggen tussen de afbraak- aan startproducten. Verschillende technieken en benaderingen voor het bestuderen van deze mechanismen zijn eerder ontwikkeld, maar deze kunnen arbeidsintensief en tijdrovend zijn. Een oplossing hiervoor zou gevonden kunnen worden in een geautomatiseerd systeem dat toelaat om een stof in oplossing te bestralen en tegelijkertijd te kunnen analyseren voor het verkrijgen van chemische informatie tijdens en na fotodegradatie.

De behoefte aan een dergelijk analytisch platform wordt verduidelijkt in **Hoofdstuk 1**. Het TooCOLD project (Toolbox for studying the Chemistry Of Light-induced Degradation) heeft als doel een systeem te ontwikkelen bestaande uit een lichtcel voor lichtblootstelling met in-situ spectroscopische monitoring. Dit systeem moet vervolgens gekoppeld worden aan vloeistofchromatografie (LC) met diode-array-detectie (DAD) en massaspectrometrie (MS) voor de identificatie van de gevormde afbraakproducten. Dit proefschrift beschrijft de stapsgewijze ontwikkeling van het systeem bestaande uit een lichtcel gemaakt van een gasdoorlaatbare *liquid-core waveguide* (LCW), een auto-injector, een spectrograaf voor in-situ absorptiespectroscopie en koppeling aan LC-DAD-MS. Het systeem werd gebruikt om de fotodegradatie van verschillende verbindingen te bestuderen voor het evalueren en demonstreren van de analytische prestaties.



Om een systeem te ontwerpen dat gebruikt kan worden voor het bestuderen van fotodegradatie in de breedste zin, moet bekend zijn welke parameters fotodegradatie beïnvloeden. **Hoofdstuk 2** beschrijft deze parameters voor kleurstoffen en pigmenten in oplossing en op een substraat. De parameters omvangen de bestralingsbron (d.w.z. lichtdosis en golflengte), de aanwezigheid of afwezigheid van zuurstof en/of katalysatoren, en de concentratie van de te onderzoeken verbinding, ongeacht het medium. Voor verbindingen in oplossing zijn ook het type oplosmiddel en de pH essentieel, en voor fotodegradatie in de vaste vorm of op een substraat kan het type substraat, de vochtigheid en het type mordant ook een belangrijke rol spelen.

Zoals hierboven benoemd, was de ontwikkelde lichtcel gebaseerd op een gasdoorlaatbare LCW, die het principe van totale interne reflectie (TIR) gebruikt om het

monster van binnenuit te bestralen. Dit is in tegenstelling tot conventionele cellen die loodrechte bestraling toepassen. LCW's zijn holle optische vezels die licht over de lengte van de vezel geleiden wanneer deze gevuld is met een oplosmiddel met een brekingsindex groter dan van het materiaal van de LCW. Ditzelfde reflecterende effect kan verkregen worden door interfererende lagen te verwerken in een ander type LCW. **Hoofdstuk 3** geeft een overzicht van de verschillende soorten LCW's die beschikbaar en bovendien bruikbaar zijn als fotoreactor en/of voor chemische analyse. De TIR-gebaseerde LCW's die worden besproken zijn gecoate polymeer-capillairen, polymeer-capillairen (gemaakt van Teflon AF) en silica-aerogels. Daarnaast worden interferentie-gebaseerde LCW's, zoals fotonische kristalvezels (bijv. Bragg-, holey- en Kagomé-fibers) en anti-resonerende reflecterende optische golfgeleiders (ARROW's), onder de loep genomen. De meeste van deze LCW's bieden het voordeel van lage lichtverliezen en zijn geschikt voor de koppeling met analytische technieken. Veel interferentie-gebaseerde LCW's hebben echter als nadeel dat ze fragiel en moeilijk te fabriceren zijn. TIR-gebaseerde LCW's van Teflon AF tonen goede lichtgeleiding en zijn ook gasdoorlaatbaar, waardoor de introductie van gassen (bijv. zuurstof) tot de lichtcel mogelijk is.

De analyse van complexe mengsels als gevolg van fotodegradatie kan ingewikkeld zijn vanwege de grote variatie in chemische eigenschappen van de gevormde componenten. **Hoofdstuk 4** beschrijft de ontwikkeling van een generieke LC-DAD methode voor de analyse van natuurlijke en synthetische kleurstoffen. Er werd een bibliotheek van bijna 130 kleurstofverbindingen gecreëerd en deze werd later toegepast voor de validatie van de methode. Het gebruik van triethylamine als ionpaar in de mobiele fase bleek een goede aanpak te zijn voor de scheiding van zure, neutrale en basische verbindingen in een enkele analyse. De geoptimaliseerde methode werd toegepast op verschillende historische objecten waarvan werd verwacht dat deze fotodegradatieproducten bevatten. De resultaten van de ontwikkelde methode werden vergeleken met die verkregen door middel van tweedimensionale LC (LCxLC). De meeste verbindingen, inclusief fotodegradatieproducten, konden worden toegewezen met behulp van de nieuwe LC methode, hoewel de LCxLC-methode succesvoller was in het scheiden van fotodegradatieverbindingen die structureel sterk op de oorspronkelijke verbinding leken. De ontwikkelde LC methode werd later toegepast om gedegradeerde monsters te analyseren (Hoofdstukken 5, 6 en 8).

**Hoofdstuk 5** beschrijft de ontwikkeling en kenmerken van een lichtcel gebaseerd op een gasdoorlaatbare LCW gemaakt van Teflon AF2400 welke gekoppeld was aan een spectrometer voor het monitoren van de veranderingen in het absorptiespectrum. De transmissie van de LCW bleek voornamelijk afhankelijk te zijn van de lengte en van kleine verschillen in druk die veroorzaakt werden door handmatige injectie. Om die reden werd

een LCW met een middelmatige lengte geprefereerd en werd het gebruik van een auto-injector aanbevolen om de stabiliteit en herhaalbaarheid te verhogen. De fotonflux in de LCW werd bepaald door middel van actinometrie met behulp van diaryletheen ether (DAE) en in-situ absorptiespectroscopie. Vervolgens werden de gasdiffusiesnelheid van zuurstof en stikstof door de LCW wanden gemeten. Dit werd gedaan aan de hand van de *blue bottle test* waarbij methyleen blauw van kleur verandert in een zuurstofrijke omgeving. Deze verandering werd gemonitord door het meten van de absorptie in situ. De absorptie stabiliseerde binnen enkele tientallen seconden, wat betekende dat het systeem vrij van zuurstof was. De potentie van het gepresenteerde systeem werd met succes gedemonstreerd aan de hand van de fotodegradatie van de kleurstoffen Eosin Y (EY) en Crystal Violet (CV).

Alle bovengenoemde resultaten werden opgenomen in het ontwerp van een volledig geautomatiseerd prototype gebaseerd op de LCW-lichtcel. Da Vinci Laboratory Solutions ontwierp een 'black box' met geïntegreerde 6-poorts valve voor koppeling met LC. Een auto-injector (MultiPurpose Sampler van Gerstel) werd geïmplementeerd voor de automatische injectie van monsters in de lichtcel en om het monster na bestraling over te brengen naar het LC systeem. **Hoofdstuk 6** beschrijft de analytische prestaties van het volledig geautomatiseerde systeem gekoppeld aan LC-DAD. De uiteindelijke opstelling vertoonde een hoge herhaalbaarheid voor fotodegradatie experimenten van Riboflavine (RF) met een RSD van ≤0.01 voor de afname na 4 uur bestraling (n=5). In-situ absorptiemetingen van RF vertoonden een goede lineariteit (R=0.98), een detectielimiet (LOD) van $1.74 \cdot 10^{-7}$ M, en een goede herhaalbaarheid (RSD≤0.13, n=5) voor elke gemeten concentratie binnen het lineaire bereik van $1\text{-}12 \cdot 10^{-6}$ M. De recovery van RF uit de lichtcel was voldoende (89%), echter lagere rendementen werden waargenomen voor meer hydrofobe verbindingen. Tot slot werd een tijdsprofiel van de fotodegradatie van RF gepresenteerd.

**Hoofdstuk 7** beschrijft de resultaten van de studie naar het effect van zuurstof op de fotodegradatie van RF en EY door middel van het ontwikkelde systeem gekoppeld aan LC-DAD-QTOFMS. Volgens de literatuur vertonen beide verbindingen een lagere fotodegradatiesnelheid in een zuurstofrijke omgeving, doordat de aangeslagen (triplet) toestand energie uitwisselt met $^3O_2$ en zo terugvalt naar de grondtoestand. Daarnaast tonen deze verbindingen verschillende fotodegradatieproducten onder zuurstofrijke en zuurstofarme omstandigheden. Dit werd bevestigd door deze studie, wat aantoont dat de nieuw ontwikkelde tool een waardevolle toevoeging is aan de bestaande methoden voor het bestuderen van fotodegradatie in oplossing. Bovendien werd voor het eerst de volledig gedebromineerde vorm van EY (fluoresceïne) geïdentificeerd als een fotodegradatieproduct in oplossing. De volledig geautomatiseerde opstelling

verminderde zowel de tijd in het lab als potentieel geïntroduceerde fouten, aangezien handmatige injectie niet nodig was. De resultaten verkregen door in-situ absorptiemonitoring kwamen sterk overeen met de resultaten verkregen door middel van LC-DAD-QTOFMS.

**Hoofdstuk 8** beschrijft de resultaten van verschillende verkennende subprojecten voor het toepassen van Raman spectroscopie om veranderingen in de moleculaire structuur te bestuderen tijdens bestraling. CV werd bestraald in de LCW-lichtcel en de verkregen producten werden gescheiden door middel van LC-DAD die vervolgens werden geanalyseerd door off-line surface enhanced Raman spectroscopie (SERS) met behulp van zilver colloïden. Deze benadering werd vergeleken met on-chip SERS monitoring tijdens de fotodegradatie van CV met behulp van *leaning pillar chips*. Voordat deze vergelijking werd gemaakt, werden verschillende kenmerken van de *leaning pillar chips* beschreven, zoals signaalversterking van de zilveren en gouden coatings in combinatie met 532 of 785 nm lasers, en de herhaalbaarheid en geheugeneffect na reiniging van de substraten. Helaas werd geconcludeerd dat deze SERS substraten (nog) geen goede analytische herhaalbaarheid bieden vanwege geheugeneffecten. Desalniettemin, vertoonden de on-chip SERS spectra tijdens de degradatie van CV overeenkomsten met de off-line SERS spectra van de fotodegradatieproducten gescheiden door LC. LC-DAD-QTOFMS analyse bevestigde de aanwezigheid van dezelfde afbraakproducten, hoewel de goud-gecoate chips van invloed leken te zijn op de fotodegradatiesnelheid van CV. Als laatste werd koolstofpapier getest als een gasdoorlaatbaar SERS-substraat voor de implementatie in een microfluïdisch systeem om uiteindelijk de invloed van zuurstof te bestuderen.

Tot slot bevat **Hoofdstuk 9** conclusies over het werk dat wordt behandeld in Hoofdstukken 1 t/m 8. Ook worden hier verschillende relevante aspecten besproken en worden er perspectieven gegeven over toekomstig gebruik van het systeem, optimalisatiestrategieën en mogelijke nieuwe toepassingsgebieden.

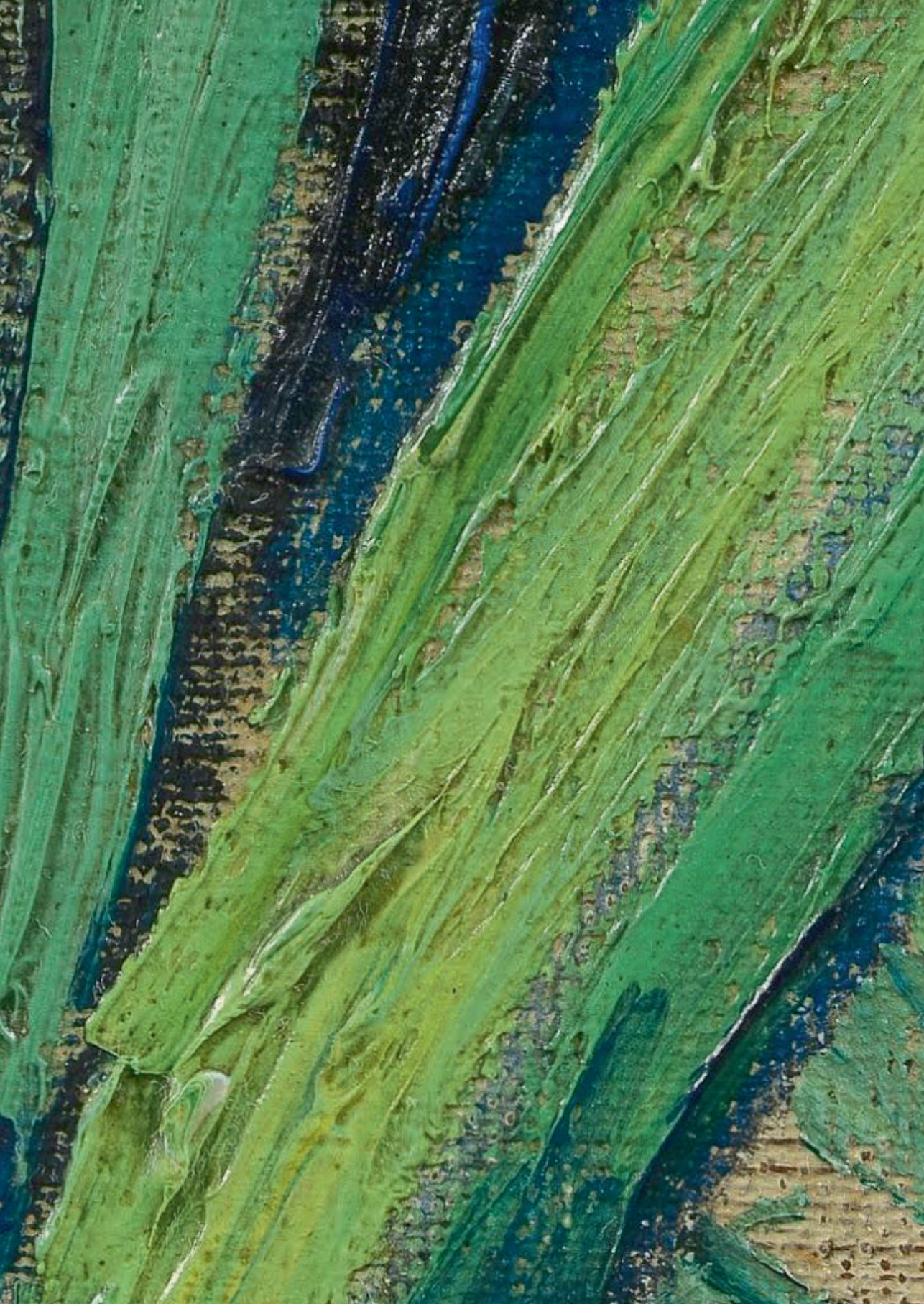

# CHAPTER 11

## Appendices

Appendix A. Supporting Information Chapter 2

Appendix B. Supporting Information Chapter 4

Appendix C. Supporting Information Chapter 5

Appendix D. Supporting Information Chapter 6

Appendix E. Supporting Information Chapter 7

Appendix F. Supporting Information Chapter 8

# Appendix A. Supporting Information Chapter 2

Supporting Information for this Chapter is available via:

**Adapted from:** https://doi.org/10.1016/j.dyepig.2022.110999

# Appendix B. Supporting Information Chapter 4

Supporting Information for this Chapter is available via:



**Adapted from:** https://doi.org/10.1016/j.chroma.2022.463038

# Appendix C. Supporting Information Chapter 5

Supporting Information for this Chapter is available via:

**Adapted from:** https://doi.org/10.1039/D1AN00272D

# Appendix D. Supporting Information Chapter 6

Supporting Information for this Chapter is available via:



**Adapted from:** https://doi.org/10.1021/acs.analchem.2c00886

# Appendix E. Supporting Information Chapter 7

Supporting Information for this Chapter is available via:

**Adapted from:** https://doi.org/10.1016/j.jphotochem.2023.114685

# Appendix F. Supporting Information Chapter 8

Supporting Information for this Chapter is available via:

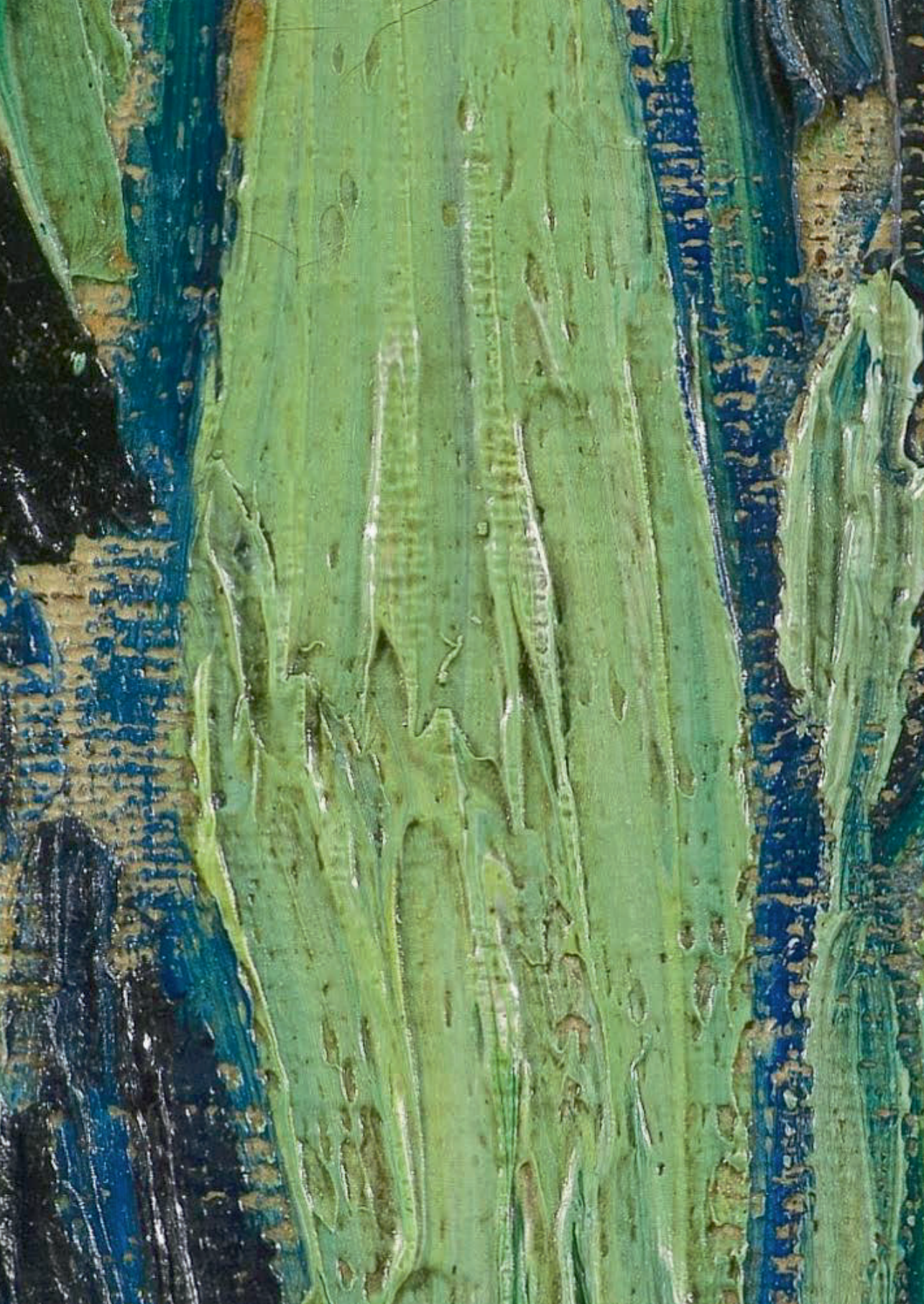

# CHAPTER 12

## Sundries

Pictures set-up

Scientific output

Overview of co-authors' contributions

List of abbreviations

List of symbols

Words of gratitude | Dankwoord

# Pictures set-up

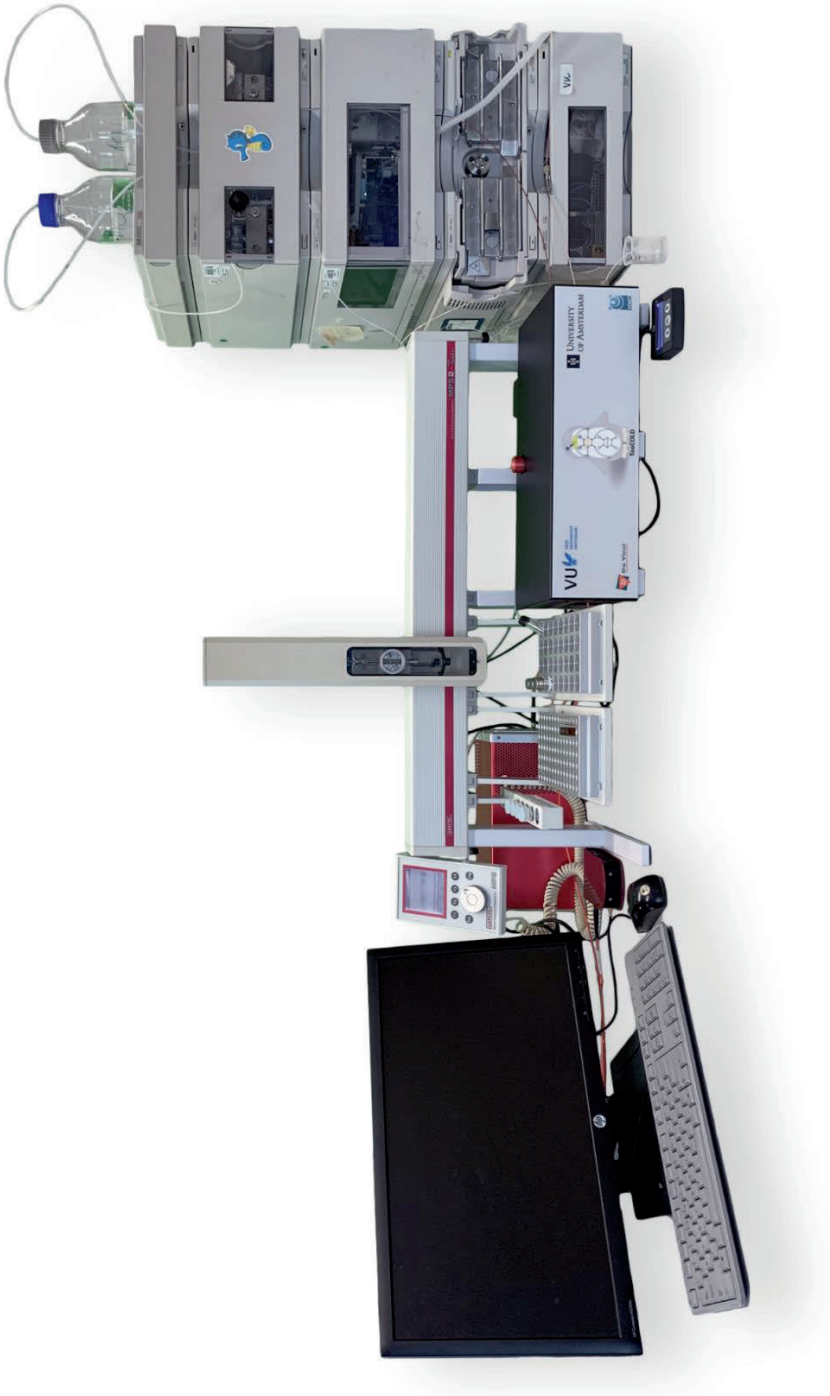


Figure 12.1. The TooCOLD system, including a MultiPurpose Sampler (MPS) (middle) that is controlled by a PC, with the TooCOLD box containing the LID cell coupled to a liquid chromatography (LC) system (far right) with a diode array detector, a Xenon light source (red, behind MPS), and a compact CCD spectrophotometer (red, left of MPS).


Figure 12.2. The MPS with TooCOLD box containing the LID cell, with the Xenon light source (red, behind MPS), and a compact CCD spectrophotometer (red, left of the MPS).

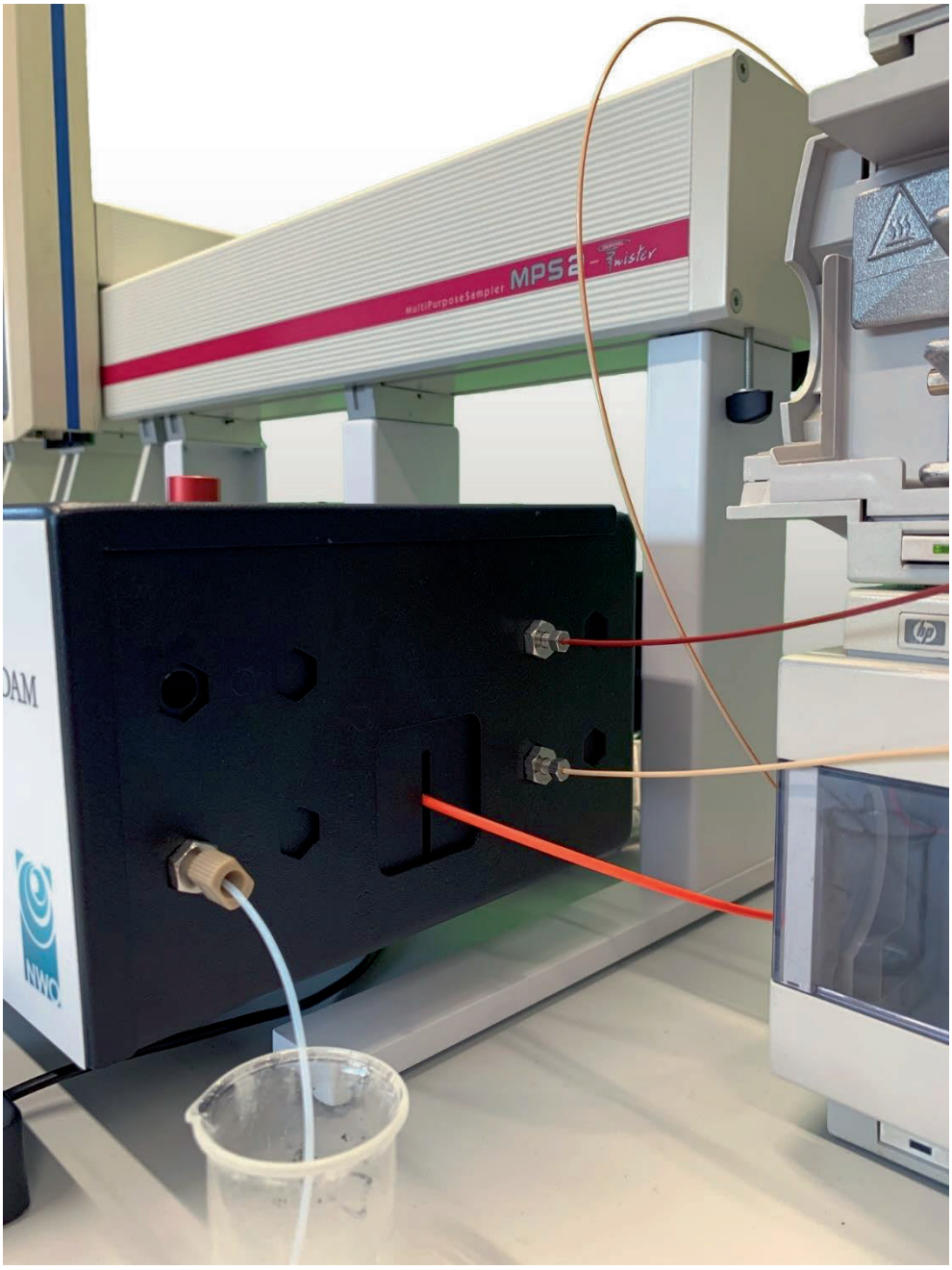


Figure 12.3. The output side of the TooCOLD box (on the right) with the optical fiber for light collection (orange), the tubing from the LC pump (red) and to the LC column (beige). The waste from the LID cell is directed into the small beaker.

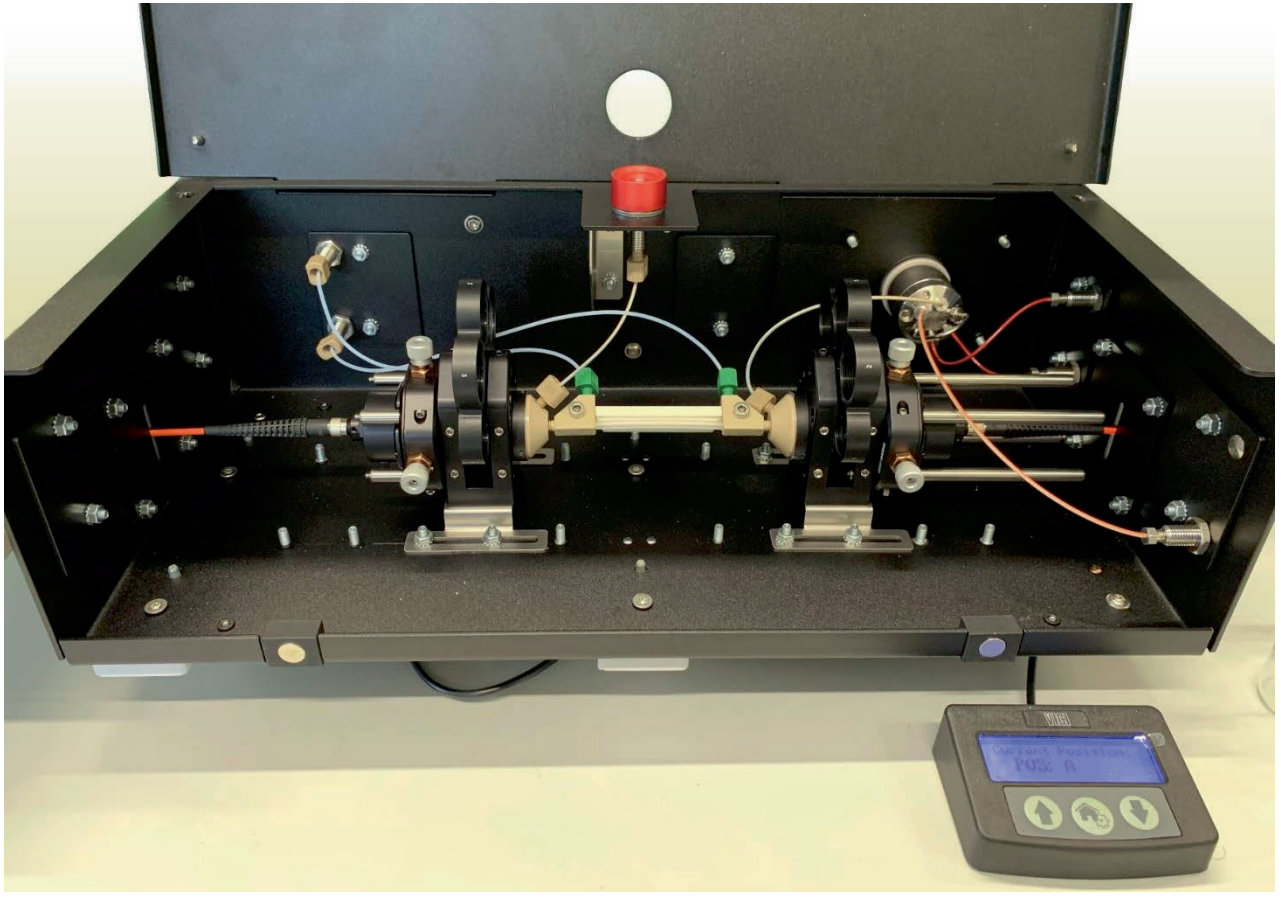


Figure 12.4. Inside of the TooCOLD box with the injection port (red, on top), 6-port valve (right), gas in- and outlets (opaque, left), LID cell (middle) with filter wheels and XY mounts, and optical fibers (orange). The electronic module below on the right can be used to control the switch valve.

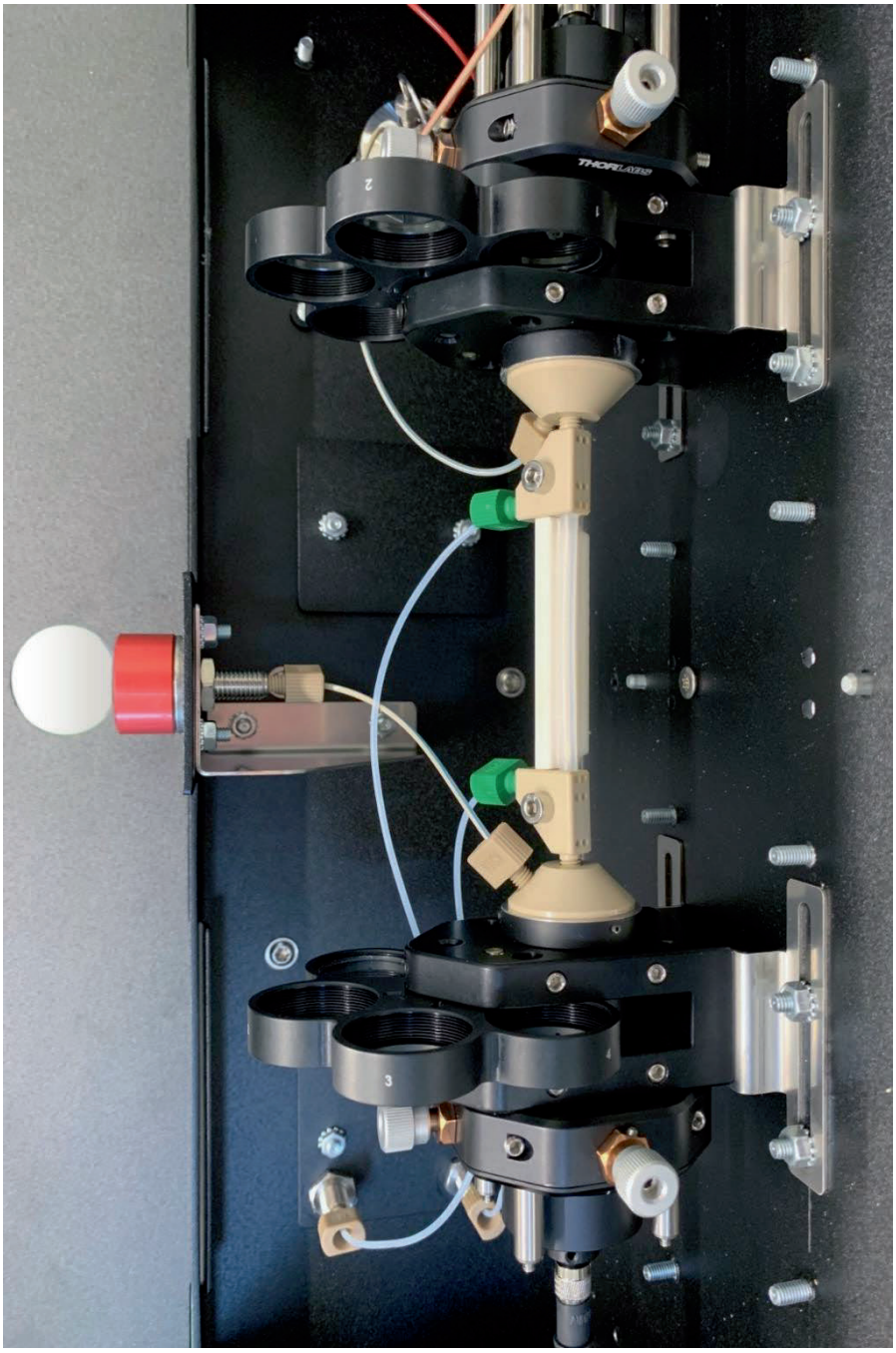


Figure 12.5. Close-up of the LID cell attached to the filter wheels with XY mounts on both sides. Gas in- and outlet attached to the LID cell have green ferrules, sample in- and outlet are positioned on the left and right side of the LID cell, respectively.

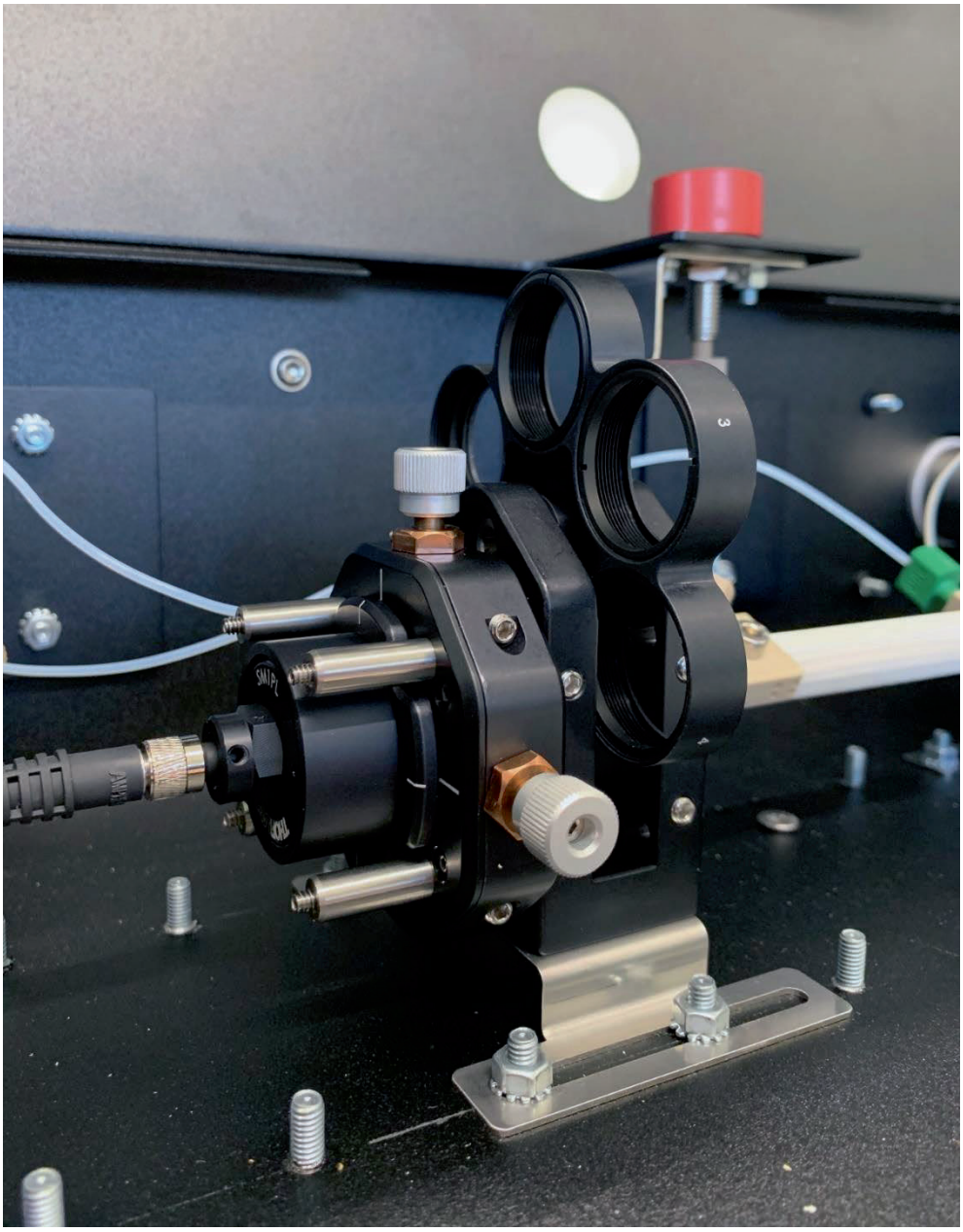

Figure 12.6. Close-up of the connection between (from left to right) the optical fiber for the incoming light, the collimator, adjustable XY mount holding a focusing lens, and the filter wheel. The configuration at the other end is identical.

# Scientific output

## Journal papers

*Included in this thesis*

1. **Characterization of a liquid-core waveguide cell for studying the chemistry of light-induced degradation**
   Iris Groeneveld, Suzan E. Schoemaker, Govert W. Somsen, Freek Ariese, Maarten R. van Bommel
   *Analyst*, **2021**, *146*, 3197
   DOI: 10.1039/d1an00272d
   Covered by Chapter 5

2. **Liquid-core waveguide cell with in-situ absorbance spectroscopy and coupled to liquid chromatography for studying light-induced degradation**
   Iris Groeneveld, Ingrida Bagdonaite, Edwin Beekwilder, Freek Ariese, Govert W. Somsen, Maarten R. Van Bommel
   *Anal. Chem.,* **2022**, 94, 21, 7647–7654
   DOI: 10.1021/acs.analchem.2c00886
   Covered by Chapter 6

3. **The development of a generic analysis method for natural and synthetic dyes by ultra-high-pressure liquid chromatography with photo-diode-array detection and triethylamine as an ion-pairing agent**
   Iris Groeneveld, Bob W.J. Pirok, Stef R.A. Molenaar, Peter J. Schoenmakers, Maarten R. Van Bommel
   *J. Chromatogr. A*, **2022**, *1673*, 463038
   DOI: 10.1016/j.chroma.2022.463038
   Covered by Chapter 4

4. **Parameters that affect the photodegradation of dyes and pigments in solution and on substrate – An overview**
   Iris Groeneveld, Maria Kanelli, Freek Ariese, Maarten R. van Bommel
   *Dyes and Pigments*, **2023**, *210*, 110999
   DOI: 10.1016/j.dyepig.2022.110999
   Covered by Chapter 2

5. **Use of liquid-core waveguides as photochemical reactors and/or for chemical analysis – An overview**
   Iris Groeneveld, Amber Jaspars, Govert W. Somsen, Freek Ariese, Maarten R. van Bommel
   *J. Photochem. and Photobiol.*, **2023**, *14*, 100168
   DOI: 10.1016/j.jpap.2023.100168
   Covered by Chapter 3

6. **Gas-permeable liquid-core waveguide coupled to LC-MS for studying the influence of oxygen on photodegradation processes**
   Iris Groeneveld, Govert W. Somsen, Freek Ariese, Maarten R. van Bommel
   *J. Photochem. Photobiol. A*, **2023**, *441*, 114685
   DOI: 10.1016/j.jphotochem.2023.114685
   Covered by Chapter 7

*Not included in this thesis*

7. **Review of analytical approaches for the identification of non-intentionally added substances in paper and board food contact materials**
   Ruud J.B. Peters, Iris Groeneveld, Patricia Lopez Sanchez, Wouter Gebbink, Arjen Gersen, Monique de Nijs, Stefan P.J. van Leeuwen
   *Trends Food Sci Technol.*, **2019**, 85, 44-54
   DOI: 10.1016/j.tifs.2018.12.010

8. **Combining photodegradation in a liquid-core-waveguide cell with multiple heart-cut two-dimensional liquid chromatography**
   Mimi J. den Uijl, Yorn J.H.L. van der Wijst, Iris Groeneveld,
   Peter J. Schoenmakers, Bob W.J. Pirok, and Maarten R. van Bommel
   *Anal. Chem.*, **2022**, 94, 11055-11061
   DOI: 10.1021/acs.analchem.2c01928

## Interviews & Media

1. ***'Junior-tafelwetenschapper'*** **at** ***'De Avond van Wetenschap & Maatschappij'***, Ridderzaal, Den Haag, 7 October 2019, www.avondwenm.nl

2. **Item about TooCOLD in** ***'Atlas'***, a Dutch scientific tv-show at NPO1, 25 May 2022, www.npo3.nl/atlas/25-05-2022/VPWON_1335387

3. **Instagram account** ***'koolstoftotnadenken'***, a personal page where I intend to share background information on interesting, hot-topic, and common-day science, created on 8 November 2022
   instagram.com/koolstoftotnadenken/

# Overview of co-authors' contributions

| Chapter 1. Introduction | |
|---|---|
| Iris Groeneveld | Wrote the chapter. |
| Maarten R. van Bommel | Reviewed, edited and provided feedback for improvements. |
| Govert W. Somsen | Reviewed, edited and provided feedback for improvements. |
| Freek Ariese | Reviewed, edited and provided feedback for improvements. |

| Chapter 2. Parameters that affect the photodegradation of dyes and pigments in solution and on substrate – An overview | |
|---|---|
| Iris Groeneveld | Supervision and conceptualization of the project. Contributed to the literature research and wrote the manuscript. |
| Maria Kanelli | Conducted a significant part of the literature research. |
| Freek Ariese | Overall supervision of the project. Reviewed, edited and provided feedback for improvements. |
| Maarten R. van Bommel | Conceptualization and overall supervision of the project. Overall supervision of the project. Reviewed, edited and provided feedback for improvements. |

| Chapter 3. Use of liquid-core waveguides as photochemical reactors and/or for chemical analysis – An overview | |
|---|---|
| Iris Groeneveld | Conceptualization and supervision of the project. Contributed to the literature research and wrote the manuscript. |
| Amber Jaspars | Conducted a significant part of the literature research. |
| Imran B. Akca | Made contributions to the content of the manuscript with regards to the interference-based waveguides. Reviewed, edited and made suggestions for improvements. |

| | |
|---|---|
| Freek Ariese | Overall supervision of the project. Reviewed, edited and provided feedback for improvements. |
| Govert W. Somsen | Overall supervision of the project. Reviewed, edited and provided feedback for improvements. |
| Maarten R. van Bommel | Overall supervision of the project. Reviewed, edited and provided feedback for improvements. |

**Chapter 4. The development of a generic analysis method for natural and synthetic dyes by LC-DAD and triethylamine as an ion-pairing agent**

| | |
|---|---|
| Iris Groeneveld | Conceptualization, conducted the experiments, processed the data and wrote the manuscript. |
| Stef R.A. Molenaar | Developed and wrote the PIOTR code, contributed with advice and suggestions throughout the study with regards to PIOTR results. |
| Bob W.J. Pirok | Overall supervision of the project. Contributed to the work by providing advice and suggestions for improving the manuscript. Reviewed and edited the manuscript. |
| Peter. J. Schoenmakers | Made contributions to the content of the manuscript, reviewed, edited and made suggestions for improvements. |
| Maarten R. van Bommel | Overall supervision and conceptualization of the project. Reviewed, edited and made suggestions for improvement of the manuscript. |

**Chapter 5. Characterization of a liquid-core waveguide cell for studying the chemistry of light-induced degradation**

| | |
|---|---|
| Iris Groeneveld | Conceptualization, conducted transmittance and gas diffusion experiments. Wrote the manuscript. |
| Suzan E. Schoemaker | Conducted actinometry and power measurement experiments and data processing thereof, including calculations. |
| Freek Ariese | Overall supervision and conceptualization. Reviewed, edited and made improvements to the manuscript. |

| | |
|---|---|
| Govert W. Somsen | Overall supervision and conceptualization. Reviewed, edited and made improvements to the manuscript. |
| Maarten R. van Bommel | Overall supervision and conceptualization. Reviewed, edited and made improvements to the manuscript. |

**Chapter 6. Liquid-core waveguide cell with in-situ absorbance spectroscopy and coupled to liquid chromatography for studying light-induced degradation**

| | |
|---|---|
| Iris Groeneveld | Supervision of the project, conceptualization, data processing. Wrote the manuscript. |
| Ingrida Bagdonaite | Conducted a great part of the experiments and data processing thereof. |
| Freek Ariese | Overall supervision and conceptualization. Reviewed, edited and made improvements to the manuscript. |
| Govert W. Somsen | Overall supervision and conceptualization. Reviewed, edited and made improvements to the manuscript. |
| Maarten R. van Bommel | Overall supervision and conceptualization. Reviewed, edited and made improvements to the manuscript. |

**Chapter 7. Gas-permeable liquid-core waveguide coupled to LC-MS for studying the influence of oxygen on photodegradation processes**

| | |
|---|---|
| Iris Groeneveld | Conducted all experiments and the data processing thereof. Wrote the manuscript. |
| Maarten R. van Bommel | Overall supervision and conceptualization. Reviewed, edited and made improvements to the manuscript. |
| Govert W. Somsen | Overall supervision and conceptualization. Reviewed, edited and made improvements to the manuscript. |
| Freek Ariese | Overall supervision and conceptualization. Reviewed, edited and made improvements to the manuscript. |

**Chapter 8. Exploring the feasibility of Raman spectroscopy for in-situ monitoring of photodegradation processes**

| | |
|---|---|
| Iris Groeneveld | Overall supervision and conceptualization of the project. Performed experiments regarding the coating of carbon paper, LC-DAD analyses and fractionation experiments of crystal violet, and data processing thereof. Wrote the chapter. |
| Niels Muntjewerf | Conducted off-line SERS experiments of photodegraded crystal violet fractions with silver colloids, and data processing thereof. |
| Lotte van Leuken | Conducted all experiments regarding the sensitivity, repeatability and cleaning procedure for the leaning pillar chips, and data processing thereof. |
| Esther de Graaff | Conducted on-chip photodegradation experiments of crystal violet, and data processing thereof. |
| Freek Ariese | Overall supervision and conceptualization. Reviewed, edited and made improvements to the chapter. |
| Govert W. Somsen | Overall supervision and conceptualization. Reviewed, edited and made improvements to the chapter. |
| Maarten R. van Bommel | Overall supervision and conceptualization. Reviewed, edited and made improvements to the chapter. |

**Chapter 9. Conclusions and future perspectives**

| | |
|---|---|
| Iris Groeneveld | Wrote the chapter. |
| Freek Ariese | Reviewed, edited and provided feedback for improvements. |
| Govert W. Somsen | Reviewed, edited and provided feedback for improvements. |
| Maarten R. van Bommel | Reviewed, edited and provided feedback for improvements. |

# List of abbreviations

| Abbreviation | Meaning |
|---|---|
| ACN | Acetonitrile |
| CDRF | Cyclodehydroriboflavin |
| CMF | Carboxymethylflavin |
| CP | Carbon paper |
| CV | Crystal violet |
| CV-Me | Mono-demethylated crystal violet |
| CV-2Me | Di-demethylated crystal violet |
| CV-3Me | Tri-demethylated crystal violet |
| CV-4Me | Tetra-demethylated crystal violet |
| CV-5Me | Penta-demethylated crystal violet |
| CV-6Me | Hexa-demethylated crystal violet |
| DAD | Diode array detection |
| DAE | Diarylethene |
| DAE-c | Closed form of diarylethene |
| DAE-o | Open form of diarylethene |
| DMSO | Dimethyl sulfoxide |
| DP | Degradation product |
| DQ | 1,2,3,4-tetrahydro-1-methyl-2,3-dioxo-quinoxaline |
| EIC | Extracted-ion chromatogram |
| EtOH | Ethanol |
| EY | Eosin Y |
| EY-Br | Mono-debrominated eosin Y |
| EY-2Br | Di-debrominated eosin Y |
| EY-3Br | Tri-debrominated eosin Y |
| FA | Formic acid |
| FMF | Formylmethylflavin |
| FWHM | Full-width-at-half-maximum |
| HCl | Hydrochloric acid |
| HDPE | High-density polyethylene |
| ID | Internal diameter |
| IEC | Ion-exchange chromatography |
| IP | Ion pair |
| IR | Infrared |
| KA | 1,2-dihydro-1-methyl-2-keto-3-quinoxaline carboxylic acid |

| Abbreviation | Meaning |
|---|---|
| KOH | Potassium hydroxide |
| LC | Liquid chromatography |
| LCW | Liquid-core waveguide |
| LCxLC | Comprehensive two-dimensional liquid chromatography |
| LED | Light-emitting diode |
| LF | Lumiflavin |
| LID | Light-induced degradation |
| LMC | Lumichrome |
| LOD | Limit of detection |
| MB | Methylene blue |
| $MB_{ox}$ | Oxidized methylene blue |
| $MB_{red}$ | Reduced methylene blue |
| MeOH | Methanol |
| MK | Michler's ketone |
| MK-Me | Mono-demethylated Michler's ketone |
| MPS | Multi-Purpose Sampler |
| MQ | Ultrapure milli-Q water |
| MS | Mass spectrometry |
| NaOH | Sodium hydroxide |
| NPs | Nanoparticles |
| OD | Outer diameter |
| PDD | 2,2-bis(trifluoromethyl)-4,5-difluoro-1,3-dioxole |
| PEEK | Polyether ether ketone |
| PIOTR | Program for Interpretive Optimization of Two-dimensional Resolution |
| PO | Pareto optimization |
| QTOF | Quadrupole time-of-flight |
| RF | Riboflavin |
| RhB | Rhodamine B |
| RI | Refractive index |
| RP | Reversed phase |
| RPLC | Reversed-phase liquid chromatography |
| RSD | Relative standard deviation |
| S/N | Signal-to-noise ratio |
| SD | Standard deviation |
| SERS | Surface-enhanced Raman scattering |

| Abbreviation | Meaning |
|---|---|
| TBA | Tetrabutylammonium |
| TEA | Triethylamine |
| TFA | Trifluoroacetic acid |
| TFE | Tetrafluorethylene |
| TIR | Total internal reflection |
| TMA | Tetramethylammonium |
| TooCOLD | Toolbox for studying the Chemistry Of Light-induced Degradation |
| UPLC | Ultra-performance liquid chromatography |
| UV | Ultraviolet |
| Vis | Visible |

# List of symbols

| Symbol | Meaning |
|---|---|
| $^1O_2$ | Singlet excited state oxygen |
| $^3O_2$ | Triplet state oxygen |
| $A$ | Absorbance |
| $C$ | Concentration |
| $F$ | Flow rate |
| $I$ | Transmitted signal intensity |
| $I_0$ | Reference signal intensity |
| $k$ | Retention factor |
| $k_0$ | k for φ=0 |
| $l$ | Optical path length |
| $Q$ | Quantum yield |
| $S$ | Slope of ln k-φ curve |
| $t_G$ | Duration of gradient |
| $t_{init}$ | Starting time of the gradient |
| $t_R$ | Retention time |
| $\varepsilon$ | Absorption coefficient |
| $\lambda_{max}$ | Absorption maximum wavelength |
| $\varphi$ | Organic modifier fraction |
| $\varphi_{final}$ | Final organic modifier fraction |
| $\varphi_{init}$ | Initial organic modifier fraction |

# Words of gratitude | Dankwoord

Thank you for getting this far through my thesis, or for the people who just arrived to this specific part: welcome! It is difficult to describe in a few words what a PhD entails, but it definitely includes pushing scientific boundaries, which is achieved by a lot of teamwork. Surely, the work presented here could not have been made possible without all the people supporting me in one way or another. This is the moment they receive the credits they deserve.

Allereerst wil ik mijn promotoren **Maarten** en **Govert**, en mijn copromotor **Freek** bedanken voor hun sturing, support en aanmoedigingen gedurende mijn PhD traject. Jullie inzichten en expertise zijn van onschatbare waarde geweest en ik ben jullie dankbaar voor al het vertrouwen en geduld dat jullie mij hebben gegeven. Naast een kritische noot was er altijd ruimte voor humor. Het moet ook leuk blijven! Op persoonlijk vlak was het niet altijd makkelijk, maar jullie gaven mij altijd alle tijd en ruimte zodat ik mij daarna weer op mijn werk kon focussen. Dankjulliewel hiervoor!

**Maarten**, we hebben elkaar in 2017 leren kennen toen ik op zoek was naar een onderzoeksproject voor mijn master. Ik heb toen een fantastische tijd gehad bij het RCE waar ik nog steeds met veel plezier op terugkijk. Tijdens die periode wist je mij ook te vertellen dat er zeer binnenkort twee PhD posities vrijkwamen in een leuk project. Voordat ik hiervan hoorde, wist ik nog niet eens of ik überhaupt een PhD wilde gaan doen, maar het onderwerp sprak mij erg aan en door mijn positieve ervaring bij het RCE wist ik zeker dat ik er voor moest gaan. Eenmaal begonnen aan het PhD avontuur wist je mij steeds weer met beide benen op de grond te houden als ik te enthousiast was en mij al zorgen maakte over de volgende stap. De eerste periode van experimenteren met de LCW verliep niet altijd soepel, maar je wist mij vertrouwen te geven door je ervaring van tijdens je eigen PhD te delen: “soms lukken dingen heel lang niet en dan opeens wel, en daar moet je dan maar geen vragen meer over stellen”. En jawel, opeens stond het als een huis! Bedankt voor alle lol die we hebben gehad met TooCOLD, de Avond van Wetenschap & Maatschappij (hoogtepuntje!) en voor het toevertrouwen van dit project!

**Freek**, wij gaan nog verder terug naar 2015 toen ik solliciteerde voor een onderzoeksproject bij AkzoNobel om bacteriën in verf te detecteren. Ik denk dat dit het moment was dat je mijn liefde voor spectroscopie aanwakkerde. Je enthousiasme, creativiteit en kennis vond ik toen al bewonderend. Naast spectroscopie leerde je mij ook over geduld en dat het best handig kan zijn om dingen +20 jaar te bewaren. Tijdens onze reis naar Californië hebben we onze band nog verder kunnen verdiepen, waar ik erg dankbaar voor ben. De vele prachtige uitzichten, Castle Hearst, de verbrande voorhoofden door de Jeep-cabrio, de otters en de walvissen die we hebben gespot, zal ik

nooit vergeten. En ohja, er was volgens mij ook nog een conferentie waar we beide een leuk praatje mochten geven. Dankjewel voor al je wijze (levens)lessen. Ik hoop dat we elkaar in de toekomst nog vaak tegen het lijf mogen lopen.

**Govert**, we konden het al gauw met elkaar vinden op het gebied van sport. Hoewel het gewichtheffen je niet zo bekend was, vond ik het ontzettend leuk dat je altijd interesse toonde en je mij bovendien de tijd en ruimte gaf om in mijn sportcarrière te steken. Dankjewel voor alle gezellige gesprekken in de wandelgangen, de trein en tijdens de borrels, je continue support en voor de lessen die je mij hebt geleerd op het gebied van onderzoek. Ik moest steeds een beetje grinniken als ik een manuscript volledig gemarkeerd terugkreeg, maar natuurlijk altijd goed bedoeld. Ik heb het altijd erg fijn gehad binnen BAC en daar heb jij natuurlijk ook een rol in gespeeld. Bedankt voor deze fantastische tijd!

Dit project was niet compleet geweest zonder het werk van **Mimi**, aka mijn partner in crime! We ontmoetten elkaar al tijdens onze studie en zaten samen in het MSc+ programma. Misschien was je het vergeten, maar we hebben zelfs ons literatuuronderzoek op dezelfde dag gepresenteerd. Was het een voorteken van een hele goede samenwerking? Zonder jouw vertrouwen in mij was de TooCOLD box misschien wel niet zoals die nu is. Ik ben ontzettend trots op hoe we elkaar wisten te motiveren en samen gegroeid zijn, zowel op professioneel als persoonlijk vlak. Ik kan niet wachten om te zien wat de toekomst je nog meer brengt en ik hoop dat we de koffietjes samen nog lang mogen doorzetten.

Iemand die als een bonus-mentor voor mij was, is **Peter**. Er is een grote kans dat ik deze PhD niet was gaan doen als je Maarten niet had verteld “dat ik wel graag een PhD wilde gaan doen” (wist ik trouwens niks van af). Ik mocht al van je leren als broekie in het tweede jaar van mijn HBO opleiding toen ik werd toegelaten bij ASTP (2013!). Gedurende de vele jaren ben je altijd motiverend, behulpzaam en geduldig geweest. Bedankt voor al je kritische vragen die mij verder hielpen in mijn onderzoek. Ik zal overigens nooit de borrels en feestjes vergeten waar jij altijd één van de gangmakers was!

There were three other members that played a significant role in this project, **Ingrida**, **Carl**, and **Rick**. After one year, **Carl** fulfilled the postdoc position within TooCOLD. I am grateful for your help with Matlab (amongst other subjects) and I enjoyed the conversations we had, even though it was short. **Rick**, jouw kennis en ervaring waren een enorme toevoeging voor TooCOLD. Ik vind het prachtig om te zien hoe jouw software zo goed toegepast kan worden op de data die we binnen TooCOLD hebben gegenereerd. The third member had been with TooCOLD for over two years! First as a student and later as a research assistant. **Ingrida**, your curiosity and hard work undoubtedly contributed to the

success of this project. It was a pleasure to work with you and it is great to see how you have grown over the years.

**Bob**, hoewel we elkaar vooral in het eerste jaar regelmatig spraken bij de tweewekelijkse meetings, wil ik je bedanken voor al je wijze input, steun en aanmoedigingen de afgelopen jaren. Je kwam voor me op, op de momenten dat ik het zelf niet kon opbrengen. Bovendien wist je mij door jouw enthousiasme er altijd aan te herinneren hoe goed het project eigenlijk verliep.

De uitbreiding van de research group sloot zich eens per maand aan bij de meeting. **Hans-Gerd**, **Pim** en **Thomas**, ik wil jullie bedanken voor jullie waardevolle input en vertrouwen. Zonder jullie expertise was het misschien wel niet gelukt om de TooCOLD box zo breed inzetbaar te maken als nu. **Hans-Gerd**, bedankt voor al je vragen en grensverleggende ideeën. LID van ketchup zal vast eens gaan lukken! **Pim** en **Thomas**, ik vond het erg leuk om meer te leren over de uitdagingen binnen de waterzuivering en het waarborgen van de waterkwaliteit. Behalve de research group, hadden we bij het TooCOLD project ook een **user group**. Ik wil alle leden van deze groep bedanken voor de nuttige meetings, hun input, enthousiasme en voor het organiseren van de halfjaarlijkse meetings op inspirerende locaties.

Een belangrijk onderdeel van mijn opdracht binnen het TooCOLD project was het ontwikkelen van een prototype. Dat had ik niet kunnen doen zonder de hulp van **Da Vinci Laboratory Solutions B.V.**. In het speciaal wil ik **Edwin** bedanken voor het meedenken en realiseren van dit prototype. Ik heb hier enorm veel van geleerd. Ook **de werkplaats** van de Vrije Universiteit speelde hier een grote rol in. **Dick**, hoewel je halverwege mijn PhD met pensioen ging, heb je ontzettend veel betekent voor het ontwerp van de toolbox. Ook **Lars**, jouw aanpassingen aan het design waren van grote toegevoegde waarde. Bedankt daarvoor!

No thesis can be defended without feedback and critical questions by the **committee**. I am grateful that we found five people willing to spend their time assessing my thesis. I genuinely hope you enjoyed reading this thesis as much as I enjoyed creating it.

During the course of my PhD, I have had the privilege to work with many amazing and inspiring people within the BAC department at the VU. **Anouk**, **Jeroen**, **Isabelle**, **Rob**, **Henrik**, **Melissa**, as the senior staff at BAC, thank you for guiding me through my PhD journey. **Anouk**, halverwege mijn PhD sloot je je aan bij onze groep en natuurlijk klikten we meteen door onze passie voor sport, maar ook vanwege onze gedeelde liefde voor spectroscopie. Ik heb enorm genoten van onze gesprekken over beide en ik ga ze zeker missen. Voor mij ben je een rolmodel en ik hoop dat we in de toekomst nog regelmatig

ideeën mogen uitwisselen. **Jeroen**, bedankt dat je mij kennis hebt laten maken met de wonderlijke wereld achter slangengif. Ik zal de jaarlijkse opruimbuien (soms spontaan wat vaker) niet snel vergeten. **Isabelle**, your spirit and drive to fight for more diversity and gender equality in research is admirable and above all, very much needed. In a male dominated field this is not always the popular opinion, making your work even more impressive. Thank you for inspiring me. **Melissa**, thank you for always being more than happy to answer all my MS-related questions. **Henrik**, thank you for introducing me to the heavenly sweet combination of chocolate and liquorice. A sweet that is definitely underappreciated. Thank you for all your advice during the course of my PhD, and also afterwards.

Most people know the Dutch proverb "beter een goede buur dan een verre vriend", and I think that also goes for my many fellow PhD students and colleagues from the BAC department. **Agathe**, **Annika**, **Arif**, **Bas**, **Carlos**, **Chuck**, **Chunfang**, **Dave**, **Dina**, **Hany**, **Haifeng**, **Iuliia**, **Jesper**, **Jonatan**, **Jordy**, **Joshka**, **Julien**, **Kristina**, **Ludovica**, **Luis**, **Mátyás**, **Peng**, **Raya**, **Robert**, **Sjors**, **Tijmen**, **Valeriia**, and **Xiaoyi**. You all contributed to me wanting to travel to work every day.

**Kristina** and **Raya**, you have surely become a bit more than good neighbors in my opinion. You were there from the start and we have shared many similar challenges during our time together (have I mentioned COVID already?). Both of you know how to be the life of the party, literally and figuratively, and I wish for both of you to stay that way. **Kristina**, bedankt voor al je liefde, geschaterlach, dansjes en steun tijdens de diepte- en hoogtepunten. We konden elkaar al gauw vinden in onze openheid, interesses en blijkbaar deelden we dezelfde kledingkast. Je bent een kei van een mens en ik weet zeker dat je nog hele mooie momenten te wachten staan! **Raya**, it is extremely empowering to see how you have handled the past couple years. Combining the demanding job of a lab technician and doing a PhD at the same time is something most people would not even think about. You have made yourself indispensable within the BAC department and beyond. Thank you for all your love, laughter, and support over the years!

**Jordy**, **Peng**, and **Tijmen**: my office buddies! Well, it was more like an office island without a door. Thank you for all your gezelligheid, support, and shared happiness over the years. **Tijmen**, na jouw komst in 2019 was het geen onbewoond eilandje meer. Hoewel we meer van de stille gesprekken waren, konden we elkaar ook erg goed vinden in onze PhD-struggles. Ik ben je super dankbaar voor al je hulp met mijn eindeloze vragen over Matlab (and beyond). **Jordy**, jij kwam erbij vlak voordat de hele boel op slot moest vanwege het welbekende virus. Met jou als buurman heb ik nooit aan lachtherapie hoeven doen: jij hebt de meest aanstekelijke lach in de wereld (thanks!). And then **Peng**, the person who

has probably seen more of The Netherlands within 2 years than I have all of my life. Thank you for all the fun conversations we have had over the years and for teaching me about your home country. I'm confident you will succeed in completing your PhD. Just remember: one breath at a time.

**Hany**, altijd gezellig als je weer eens op de VU te vinden was. In de tijden dat ik meer op de 6e verdieping werkte hebben we elkaar ook beter leren kennen. Had veel eerder moeten gebeuren! Bedankt voor als je hulp, de gedeelde koffietjes, je openheid en gezelligheid. **Bas**, jij kwam ons team versterken als technician. Dat vond ik persoonlijk heel fijn, want nu was er iemand anders dan Raya wie ik kon lastigvallen met stomme vragen. Hoewel het van korte duur was, ben ik je ontzettend dankbaar voor je geduld en hulp op het lab. Doet het NFI ook aan karoke? **Robert**, bedankt voor al je flauwe grappen en de muziek die ik door je kantoordeur heen hoorde in de ochtend. Ik wist niet dat ik het zo zou gaan missen toen je vertrok. **Julien** and **Ludovica**, after 3+ years, we finally became gym buddies! Clearly something I wish I could have done much earlier. **Julien**, jij stond bijna altijd als eerste klaar als ik weer eens iets vroeg in de groepsapp. Topper! Bedankt voor de gezelligheid en de leuke gesprekken over van alles en nog wat. Ik ben trots dat ik je nog even hard heb mogen laten zweten bij het trainen van de beentjes! **Ludovica**, thank you for letting me get to know you! You are an awesome person and I hope to see you again soon in the future. **Mátyás**, door jouw enthousiasme over je werk vroeg ik mij soms af of ik niet biologie had moeten studeren. De manier waarop jij je passie kan overbrengen op mensen is aanstekelijk. En hoe fijn is het dat je enkele weken lang mijn tv-entertainment verzorgde?! Bedankt voor al je mooie verhalen en gezelligheid! **Joshka**, ik vond het heel leuk om je als zorgzame en behulpzame, maar ook gedisciplineerde en sterke vrouw te leren kennen. Ik heb altijd enorm genoten van onze gesprekken over wetenschap en feminisme, en ook over ons persoonlijke leven konden we bij elkaar terecht. Bedankt daarvoor!

I cannot forget the people from the MS-Laserlab of course! **Agathe**, **Dave**, **Iuliia**, and **Sjors**, thank you for all the fun conversations we have had during and after work. **Dave**, ik vind het jammer dat we elkaar later pas beter leerden kennen. Je bent een schat van een mens en ik weet zeker dat je mooie resultaten zult behalen in je PhD! **Iuliia**, thank you for wanting to be a part of the 'borrel committee' with me. It was a pleasure to work together on this very important task. **Sjors**, bedankt dat je altijd weer klaar stond met een laser, een inbussleutel of een bout als ik daarnaar op zoek was. Iedereen zou een Sjors op zijn lab moeten hebben!

**Annika**, **Chuck**, **Dina**, **Haifeng**, **Jesper**, **Jonatan**, **Luis**, and **Xiaoyi**, although quite brief, I enjoyed our contact very much and I wish you all the best in the next steps of your career!

I am also grateful for the big group of talented students who I have had the pleasure to work with. This thesis would definitely not be here without their help. First of all, **Amber J**, **Amber K**, **Gerben**, **Karan**, and **Maria**, who worked on literature theses with me. Thank you for joining me in this important, although sometimes tiring, task. The work done by **Amber J** and **Maria** even led to the publication of two review articles, which are covered by Chapters 2 and 3. There were other students who did practical work. **Suzan**, je was de eerste student die ik mocht begeleiden, dus eigenlijk kreeg je meteen een moeilijk klusje. Bedankt dat ik al die moeilijke berekeningen aan jou heb mogen overlaten en wat staat het mooi in Hoofdstuk 5! **Niels**, hoewel COVID al na een maand roet in het eten gooide, heb je uiteindelijk toch vele interessante Raman metingen kunnen genereren. Knap gedaan! **Ingrida** basically helped me with taking the houtje-touwtje set-up to the level of an actual prototype. Your hard work (I had to slow you down every now and then) was trivial in reaching the final result. It is a shame that COVID resulted in the delay of many processes, which meant you were not able to apply the system as well, but you have made up for that during your time with Mimi and Rick! **Ibtissam**, na een korte inleiding op het TooCOLD systeem kreeg jij de moeilijke opdracht om het systeem te testen op twee kleurstoffen. Hoewel het veel moeilijker bleek dan gedacht, heb je toch een mooi verslag neergezet! Het duo **Lotte** en **Esther** hielp met de ontwikkeling van een Raman detectiemethode. Uiteraard ging ook dit niet vanzelf, maar ik was erg blij dat jullie het goed met elkaar konden vinden. Samen experimenten plannen en uitvoeren, daarna vergelijken en verder gaan met het volgende experiment. Dat ging best soepel! Uiteindelijk denk ik dat we een mooie eerste stap hebben gezet in de ontwikkeling van deze methode. Bedankt voor jullie gezelligheid en enthousiasme en natuurlijk de Limburgse vlaai! Als laatste wil ik ook **Jasper** bedanken voor de ontwikkeling van de PI cell. Jij deed je project natuurlijk onder de supervisie van Mimi, maar er moest ook regelmatig overlegd worden met het VU-front, zodat de Raman metingen netjes uitgevoerd konden worden. Bedankt voor al je harde werk!

CASA would not be complete without the members from the University of Amsterdam. **Alina**, **Andrea**, **Arian**, **Bob**, **Garry**, **Iro**, **Leon**, **Liana**, **Lotte**, **Mirjam**, **Nino**, **Noor**, **Pascal**, **Peter**, **Rianne**, **Rick**, **Saer**, **Stef**, **Suhas**, **Tom**, **Wouter**, thank you for always making me feel welcome whenever I visited. I especially enjoyed all the dances, drinks, and good talks we have shared during the CASA social events. **Stef**, ontzettend bedankt voor jouw bijdrage aan Hoofdstuk 4. **Suhas**, thank you for taking the time to teach us about the art behind the creation of a 3D printed light cell.

Ieder mens met gezond verstand weet hoe belangrijk het is om af en toe wat stoom af te blazen. Al voor een hele lange tijd is **UnScared** een tweede huis en uitlaatklep voor mij. Ik werd er als 20–jarig broekie lid, heb daar een groot deel van mijn vrienden ontmoet, mijn

passie voor gewichtheffen ontdekt en bovendien heel veel gratis koffie gedronken. Bedankt voor het sponsoren van mijn cafeïneverslaving en voor het creëren van een plek waar een gestrest mens zijn ei kwijt kan. Ook bedankt aan iedereen die daar aan bij heeft gedragen.

The last part of the acknowledgements has a place for a couple of very special people that I call my **friends and family**. I would not have been here without their endless support, inspiration, and the joy they bring to my life. It is difficult to describe in words how much you all mean to me.

In special, I would like to thank a couple of my best friends (not in a specific order, because I love you all equally much). Dearest **Meike** and **Nirit**, it is a special thing when one can feel entirely at peace and completely themselves around others. I would say we are a perfect triangle, each corner equally skewed at 60°. Your love and support throughout this 4-year journey and in all other moments of my life mean the absolute world to me. אני אוהב אותך. **Nirit**, thank you also for supporting me during the preparations for my ceremony by being my paranymph. **Sanne**, mijn allersterkste vriendin! Ook jij hebt een grote bijdrage geleverd aan dit boekje. Gewoon door er te zijn wanneer ik je nodig had. Jij weet als geen ander dat het antwoord soms simpelweg ligt in het gooien van wat gewichten. Voor eeuwig bedankt dat je mijn vriendinnetje bent. Lieve **Joyce**, jij bent één van de redenen dat ik dit avontuur ben aangegaan. Ik kan me ons gesprek na een intense workout bij UnScared nog goed herinneren. Zoals altijd wist je toen de juiste vragen te stellen: "wat wil *jij* nou doen?", "waar word *jij* gelukkig van?". Ik hoop dat we nog heeel lang dit soort mooie gesprekken met elkaar mogen voeren en koffietjes mogen drinken. Wel tikkie sturen hè. **Quynh**, my big weirdo! We only met a year ago during a summer school, but I really wish we could have met earlier on in life. It has been an amazing year with many laughs, coffees, cookies, and also some science. Thank you for being so wonderful and for letting me share all my weird energy with you! **Imme** en **Bri**, ik ben zo blij dat we vorig jaar ons kneuterige knutselclubje zijn gestart! Ik kijk ernaar uit om jullie nog veel beter te leren kennen! Lieve **Britt**, **Nienke**, **Paula** en **Rianne**. Het feit dat we elkaar sinds ons MSc+ traject in 2018 nog steeds een aantal keer per jaar opzoeken, zegt veel over onze vriendschap. Ik vind het waanzinnig leuk om wetenschappelijke ideeën te delen en inspiratie op te doen met een groep ambitieuze vriendinnen. Ik ben trots op jullie!

**Anneke** en **Wilbert**, jullie wil ik bedanken voor jullie gastvrijheid, de leuke avondjes in de pizzahut die mij hielpen ontspannen tijdens deze periode en het bieden van een luisterend oor wanneer nodig. **Anne**, **Pieter** en **Josephine**, jullie zijn de leukste schoonzusjes en zwager die ik me kan wensen. Bedankt voor al jullie liefde.

Lieve **papa**, ook zonder jou zou dit proefschrift er niet zijn geweest. Het is vroeger zeker niet altijd makkelijk geweest, maar ik ben erg dankbaar voor hoe we de laatste 10 jaar meer naar elkaar toe zijn gegroeid. Over de jaren krijg ik steeds meer inzicht en respect voor hoe je ons hebt opgevoed. Zonder die vrijheid op de boerderij was ik misschien wel niet zo eigenwijs (dwars?) en creatief als nu. Bedankt voor het stimuleren van mijn nieuwsgierigheid en de steun die ik altijd van je heb mogen ervaren. **Lian**, hoewel ik het niet vaak in woorden uitdruk, ben ik erg blij dat jij nu onderdeel uitmaakt van onze familie. Je maakt pa gelukkig en brengt hem (en ons) wat rust in zijn leven. En dan mijn lieve, stoere zussen **Carola**, **Laura**, **Anne**, en **Eline**. We hebben veel meegemaakt met elkaar en ben ontzettend dankbaar dat ons dit alleen maar dichter bij elkaar heeft gebracht. Hoewel we vroeger best wel eens ruzie hadden (sorry voor het pikken van dat ene kledingstuk), komen we nu bij elkaar om volwassen mensen dingen te bespreken (oef). Misschien hebben jullie het niet door, maar stuk voor stuk zijn jullie enorme rolmodellen voor mij. **Carola**, ik heb het altijd bijzonder gevonden hoe jij mensen naar je toetrekt. **Laura**, jouw doorzettingsvermogen is bewonderenswaardig. **Anne**, het is echt prachtig om je te zien opbloeien de afgelopen jaren. **Eline**, jouw talent voor het overbrengen van je ideeën op papier is in-sane. Zonder jou was die hele cover er niet geweest! Bedankt dat je dit voor mij wilde doen. Ook **Falk** en **Sven** horen daar natuurlijk bij. Bedankt voor jullie bijdrage aan slechte grappen en gedeelde liefde voor mijn zussen. Lieve, kleine **Dax**, hoewel je dit nog niet kan lezen, ben ik super trots om jouw tante te mogen zijn. Lieve **mama**, hoewel je er al zoveel jaren niet meer bij bent, denk ik nog iedere dag aan je. Alles wat ik doe, denk en voel, is een resultaat van jou. Ik hou van jou.

Natuurlijk kan ik mijn twee lieve kattenmonsters niet vergeten. **Casper** en **Coco**, bedankt voor de dagelijkse dosis serotonine en het verzorgen van menig typefouten in mijn proefschrift. Jullie zijn te schattig om er echt een probleem van te maken.

En dan als laatste, **Maarten**, mijn allergrootste cheerleader. We kenden elkaar nog maar 2 maanden toen je mij al had geholpen met 4(!!!) verhuizingen. Dat was blijkbaar een goed voorteken. Als je één ding van mij hebt geleerd dan is 't dat ik alles graag zelf doe, want hallo, ik ben toch een zelfstandige vrouw. Van jou mocht ik leren dat samen doen ook helemaal niet erg is en misschien zelfs wel veel leuker. Je herinnerde mij er ook aan hoe belangrijk het was om af en toe te pauzeren en de natuur in te gaan. Bedankt dat je mij respecteert, vrij laat in mijn doen en laten, en me aanmoedigt om mijn grenzen te blijven verleggen. Ik kijk uit naar alle avonturen die we nog gaan meemaken!

*Veel liefs,*

*Iris*